LRP 728/02 August 2002

Papers presented at the

29th EPS CONFERENCE ON CONTROLLED FUSION AND PLASMA PHYSICS

Montreux, Switzerland
17th - 21st June 2002

Available in colour on the web at
crppwww.epfl.ch/conferences

ISSN 0458-5895

LIST OF CONTENTS

Bootstrap Current Destabilisation of Ideal MHD Modes in 3D Reactor Configurations

W. Anthony Cooper, S. Ferrando i Margalet, S. J. Allfrey
Centre de Recherches en Physique des Plasmas,
Association Euratom/Confédération Suisse, EPFL, 1015 Lausanne, Switzerland
M. Yu. Isaev, M. I. Mikhailov, V. D. Shafranov, A. A. Subbotin
Russian Research Centre "Kurchatov Institute", Moscow, Russia
Y. Narushima, S. Okamura, C. Suzuki, K. Yamazaki
National Institute for Fusion Science, Toki-shi, Japan
G. Y. Fu, L. P. Ku, D. A. Monticello, M. Redi, A. Reiman, M. Zarnstorff
Princeton Plasma Physics Laboratory, Princeton, NJ, USA
J. Nührenberg
Max Planck Institut für Plasma Physik-Euratom Association, Greifswald, Germany
T. N. Todd
UKAEA Dounreay, Caithness, Scotland, United Kingdom

Abstract

In current-free stellarators, the parallel current density is normally too weak to drive global external kink modes. However, at finite values of β, the bootstrap current (BC) can provide sufficient free energy to trigger this class of mode in some stellarator systems. The effect of the BC in the collisionless $1/\nu$ regime has been investigated in several different types of stellarator reactor systems all with a volume $V \sim 1000m^3$. In quasiaxisymmetric and quasihelically symmetric stellarators, the BC is large at finite β and this can cause low order resonances to move into and emerge out of the plasma which in turn can destabilise global internal and external kink modes. In a 6-field period system with poloidally closed contours of the magnetic field strength B, the BC is small and decreases the rotational transform only slightly. As a result, only intermediate to high n modes can become weakly destabilised. Furthermore, it is demonstrated in this system that the contours of the second adiabatic invariant $\mathcal{J}_{\|}$ close poloidally for all trapped particles at finite $\beta^* \sim 6\%$. This condition leads to the loss of a very small fraction of the collisionless $\alpha-$particle orbits. In sphellamak configurations with peaked toroidal currents required to generate nearly isodynamic maximum-B confining field structures, the BC accounts only for a small fraction of the total current. The loss of $\alpha-$particles born within the inner quarter of the plasma volume is negligible while about 1/3 of those born at half volume escape the device within a slowing down time.

1. Introduction

Stellarator devices do not normally operate with induced toroidal plasma currents like Tokamaks and Reversed Field Pinches. However, at finite β, stellarators and other three-dimensional (3D) configurations can develop a bootstrap current due to variations in the frictional forces experienced by the different trapped particle species interacting with circulating particles. If the bootstrap current becomes sufficiently large, it can impact the ideal magnetohydrodynamic (MHD) stability properties by providing free energy to drive internal and external kink modes. In advanced stellarators like Wendelstein WVII-X [1], the bootstrap current is expected to be small, consequently the ideal MHD stability investigations have been limited to the current-free case. It has been shown for this system that the mode structures that can be destabilised at high values of $\beta > 5\%$ are internal rather than external [2]. A detailed survey of the stability properties of different possible configurations attainable with the WVII-X coil set has been reported in Ref. [3]. The investigation of ideal MHD stability including the effect of the bootstrap current has been previously considered in the proposed National Compact Stellarator Experiment (NCSX) [4] where all ideal modes were found to be stable at $\beta = 4.1\%$.

The impact of the bootstrap current on global kink mode stability is investigated in this paper using a quasi-analytic model valid in the collisionless $1/\nu$ regime [5] that is applied to various 3D plasma confinement systems currently under consideration. We concentrate our modelling on reactor-sized devices with a volume $V \sim 1000m^3$. 2 and 3-period quasiaxisymmetric (QAS) stellarator configurations, a 6-period $\mathcal{J}_{\|}$-optimised quasipoloidally symmetric (QPS) stellarator and a compact 10-period Sphellamak system are specifically examined in some detail. We illustrate the mod-B^2 distribution on cross sections at the beginning, at one quarter and at half of a field period for each of the 3D systems we investigate in Fig. 1. We also evaluate the confinement of α-particles in the QPS and Sphellamak reactors.

Quasiaxisymmetric stellarators [6, 7] are magnetic confinement systems in which the magnetic field strength in Boozer coordinates (s, θ, ϕ) [8] is predominantly axisymmetric very much like in tokamaks although their physical appearance is fully 3D. In these coordinates where $0 \leq s \leq 1$ is the radial variable, θ is the poloidal angle and ϕ is the toroidal angle, the magnetic field lines are straight and the poloidal and toroidal components of the magnetic field $\mathbf{B}$ in the covariant representation correspond to the toroidal and poloidal current fluxes, respectively. Experimental devices are proposed to test this concept in the USA [4] and Japan [9]. The 6-period $\mathcal{J}_{\|}$-optimised QPS stellarator is a concept that has evolved from the Wendelstein WVII-X design. The criteria for optimisation of the second adiabatic invariant $\mathcal{J}_{\|} = \int v_{\|} d\ell$ constitutes the basis for the quasi-isodynamic stellarator system [10].

In this system, the contours of $\mathcal{J}_\parallel$ close poloidally in a $(\sqrt{s}, \theta)$ polar representation, where s is proportional to the toroidal magnetic flux. An almost identical concept is that of the quasiomnigenous stellarator [11] which has been explored in a very compact setting with a small number of periods [12] which is now identified as a QPS system. The further optimisation of a quasi-isodynamic device with respect to criteria of pseudosymmetry leads to the $\mathcal{J}_\parallel$-optimised QPS [13] in which the good confinement properties are extended to all trapped particles. The pseudosymmetry condition corresponds to the absence of closed contours of the magnetic field strength B on a specified flux surface (typically at midradius) in a plane defined by the Boozer angular variables [14]. The Sphellamak concept [15] is a coreless device with helical coils wound on a spheroidal surface. A large toroidal current is required to generate the confining fields. The dynamo effect associated with plasma turbulence is not required as the magnetic field structure imposed is 3D. Paramagnetic enhancement of the toroidal magnetic field is an important feature of the concept as it allows peaked currents to produce a maximum-B system with nearly isodynamic properties in the central core of the plasma.

2. The Bootstrap Current Model in the $1/\nu$ Regime

The bootstrap current model in the $1/\nu$ regime that has been used in this work has been very compactly described in Ref. [5]. The formulas presented there have evolved from previous research on the subject [16, 17, 18]. The specific equations can be summarised as

$$\begin{aligned}
2\pi J(s) &= 2\pi \int_0^s ds \frac{< \boldsymbol{j} \cdot \boldsymbol{B} >}{< B^2 >} \Phi'(s) \\
< \boldsymbol{j} \cdot \boldsymbol{B} > &= -G_b \Big(L_1 \frac{dp}{d\Phi} + L_2 \rho \frac{dT}{d\Phi} \Big) \\
G_b(s) &= \frac{1}{f_t} \Big[< g_2 > - \frac{3 < B^2 >}{4 B_{max}^2} \int_0^1 d\lambda \lambda \frac{< g_4 >}{< g_1 >} \Big] \\
f_t &= 1 - \frac{3 < B^2 >}{4 B_{max}^2} \int_0^1 d\lambda \frac{\lambda}{< g_1 >} \\
g_1 &= \sqrt{(1 - \lambda B / B_{max})} \\
\boldsymbol{B} \cdot \boldsymbol{\nabla} (g_2 / B^2) &= \boldsymbol{B} \times \boldsymbol{\nabla} \Phi \cdot \boldsymbol{\nabla} B^{-2} \\
\boldsymbol{B} \cdot \boldsymbol{\nabla} (g_4 / g_1) &= \boldsymbol{B} \times \boldsymbol{\nabla} \Phi \cdot \boldsymbol{\nabla} g_1^{-1} \\
g_2(B_{max}) &= g_4(B_{max}) = 0
\end{aligned}$$

where $2\pi J(s)$ and $2\pi\Phi(s)$ are the toroidal current and magnetic fluxes, respectively, G_b is a geometric factor, L_1 and L_2 are viscosity and friction coefficients, f_t is the trapped particle fraction, λ is the pitch angle and g_1 is the normalised parallel velocity. In these expressions, we identify the average $< A > \equiv \int d\theta d\phi \sqrt{g} A / V$ with

$V \equiv \int \sqrt{g} d\theta d\phi$ corresponding to the plasma volume enclosed. The pressure and temperature profiles are labelled with $p(s)$ and $T(s)$, respectively. For all the calculations presented, we assume a single ion and electron plasma of equal temperatures. The normalised density profile is prescribed as $(1 - 0.9999s^2)$, while the temperature is given by the pressure to density ratio.

The quasi-analytic solution of the moment of the drift kinetic equation that determines the bootstrap current corresponds to the equations listed above. It should be noted that certain approximations are invoked in this quasi-analytic solution that may give rise to differences compared with more precise numerical solutions of the drift kinetic equation. Nevertheless, the full collision operator including pitch angle scattering and slowing down is employed, which may not be the general case in the numerical approach. This neoclassical model has been tested with experimental discharges in the Compact Helical System (CHS) where it gives reasonable agreement in L-mode discharges [19], but appears to scale incorrectly in discharges with internal transport barriers.

3. Equilibria with Finite Bootstrap Current

The 3D VMEC code [20] is employed to generate equilibria with nested magnetic surfaces. To compute equilibria in which the toroidal currents are solely due to the bootstrap effect, we iterate between calculations from VMEC and from the bootstrap current (BC) algorithm until a converged BC profile is achieved [21]. We have implemented in the local modules of the TERPSICHORE code [22] (which perform the mapping to Boozer coordinates) the bootstrap current model described in the previous section. In a QAS stellarator, the BC is large at $\beta^* \geq 5\%$ and increases the rotational transform ι by almost a factor of 2. In a quasihelically symmetric stellarator (QHS) [23], the finite BC decreases the rotational transform significantly from about unity in the absence of BC to a minimum of nearly 1/2 at midvolume and 3/4 at the edge at $\beta^* \simeq 3\%$. For higher values of β^*, the BC algorithm failed to adequately produce a converged profile. In a WVII-X-like device, the BC at $\beta^* \simeq 5\%$ increases the edge transform by about 7%. This translates to about $400kA$ in a reactor-scaled system which is a factor of about 4 larger than predictions obtained with a numerical drift kinetic solver. This discrepancy can be attributed to a combination of the approximations made in the quasi-analytic approach and the effect of the collision operator. In this work, we employ the definition $\beta^* \equiv 2\mu_0\sqrt{<p^2>}/<B^2>$ because this parameter may be more relevant in a fusion power producing environment.

4. The Ideal MHD Stability Energy Principle

The 3d ideal MHD code TERPSICHORE is employed to investigate the impact of the BC on internal and external kink modes. The relevant equations are expressed as

$$\delta W_p + \delta W_v - \omega^2 \delta W_k = 0$$

$$\delta W_p = \frac{1}{2}\int\int\int d^3x \left[C^2 + \Gamma p|\nabla\cdot\xi|^2 - D|\boldsymbol{\xi}\cdot\boldsymbol{\nabla}s|^2\right]$$

$$\mathbf{C} = \nabla\times(\xi\times\mathbf{B}) + \frac{\boldsymbol{j}\times\boldsymbol{\nabla}s}{|\boldsymbol{\nabla}s|^2}(\boldsymbol{\xi}\cdot\boldsymbol{\nabla}s)$$

$$D = \frac{j^2}{|\boldsymbol{\nabla}s|^2} - \frac{p'(s)(\nabla\cdot\nabla s)}{|\boldsymbol{\nabla}s|^2} - \frac{(\boldsymbol{j}\times\boldsymbol{\nabla}s)\cdot\boldsymbol{\nabla}\times(\boldsymbol{B}\times\boldsymbol{\nabla}s)}{|\boldsymbol{\nabla}s|^4},$$

where δW_p, δW_v and $-\omega^2\delta W_k$ correspond to the potential, vacuum and kinetic energies, respectively. Γ is the adiabatic index. The vacuum surrounding the plasma is treated as a shearless and pressureless pseudoplasma. The structure of the matrix that describes the vacuum is identical to that of the plasma. A model kinetic energy is employed that annihilates the parallel component of the perturbed displacement vector. As a result, this component can be eliminated analytically from the energy principle. Although the eigenvalue $\omega^2 = \lambda$ is unrelated to the physical growth rate, the marginal points of stability are correct.

5. 2-Period QAS Stellarator Reactor

Virtually all the pressure profiles we have chosen in this work have vanishing edge gradients to avoid current profile discontinuities at the plasma-vacuum interface. Previously, we have found that the BC with either peaked $p(s) = p(0)(1-s)^2$ or box-like broad $p(s) = p(0)[1-s^2-0.2(1-s^{10})]/0.8$ pressure profiles was significantly larger than a nearly parabolic $p(s) = p(0)[1-s-0.1(1-s^{10})]/0.9$ profile in real space in a 2-period QAS reactor at $\beta^* \simeq 5\%$. This suggested that the search of profiles in the neighbourhood of the parabolic type could yield a set in which the edge rotational transform ι_e could fall below the critical value $\iota_e = 1/2$. Consequently, in this section we prescribe $p(s) = p_0[1-s-0.1(1-s^{10})] + p_1[1-s-0.2(1-s^5)]$ which recovers the nearly parabolic case when $p_1 = 0$ and is more peaked (broader) when p_1 is positive (negative). The pressure profiles and corresponding bootstrap current profiles are displayed in Fig. 2. The apparent BC discontinuities at $s \sim 2/3$ may be related to a change in θ and ϕ for which B is maximum, but this issue is still under investigation, As we vary p_1, we adjust p_0 to maintain $\beta^* \simeq 5\%$. The rotational transform ι profiles for $p_1 = -1.68$, 0 and 0.84 appear in Fig. 3a. With finite BC (at $\beta^* = 5\%$), we have been unable to obtain a profile for which $\iota_e \leq 1/2$. Thus the 2-period QAS reactor system under consideration is unstable to a low order $m/n = 2/1$ external kink at this value of β^*. The unstable eigenvalue as a function of p_1 as shown in Fig. 3b demonstrates that the most favourable profile is realised with $p_1 \simeq 0.42$ for which the BC and ι_e reach minimal values in the scan with respect to this parameter. For the nearly parabolic pressure profile ($p_1 = 0$), we have artificially enhanced and suppressed the bootstrap current by a constant factor T. We find that for $T \leq 0.8$, the value of $\iota_e \leq 1/2$ and the $m/n = 2/1$ external kink is stabilised. For $T > 1.5$, we get $\iota_e \geq 3/4$ resulting in the destabilisation of a $m/n = 4/3$ external kink. With a peaked pressure profile of the form $p(s) = p(0)(1 - s)^2$, we have observed the destabilisation of internal $m/n = 4/3$ kink modes. These results suggest that a modest level of counter current drive of the order of $1MA$ may be required to reduce $\iota \leq 1/2$ to maintain the ideal MHD stability with respect to external kink modes in the 2-period QAS stellarator reactor we have studied. Low shear stellarators are usually designed to avoid low order resonant surfaces, but the large BC in QAS systems may not reliably prevent this scenario.

6. 3-Period QAS Stellarator Reactor

We consider in this section a 3-period QAS stellarator reactor with a finite BC generated with a nearly parabolic $p(s) = p(0)[1 - s - 0.1(1 - s^{10})]/0.9$ profile. This profile, the corresponding bootstrap current profile and the ι-profile when $\beta^* = 5\%$ are plotted in Fig. 4a. With the BC model we have applied, the edge transform exceeds the critical value $\iota_e = 3/4$ and a global $m/n = 4/3$ external kink mode is destabilised. Artificially suppressing the bootstrap current by multiplying its profile be a factor T yield a set of ι-profiles presented in Fig. 4b. For $T < 0.95$, we find $\iota_e < 3/4$ and for $T < 0.73$, the entire ι-profile falls below 3/4. In Fig. 5a, we obtain that the eigenvalue of the external kink decreases rapidly almost reaching marginal conditions for $T = 0.95$ but then increases before stabilising completely at $T = 0.73$ when $\iota < 3/4$ everywhere. In Fig. 5b, we plot the profiles of the $m/n = 4/3$ component of the radial displacement vector for different values of T. The amplitude of the external mode drops rapidly in the range $0.95 \leq T \leq 1$, but for $T < 0.95$ it becomes an internal mode increasing in amplitude and displacing itself radially inwards into the plasma. The destabilisation of this internal $m/n = 4/3$ mode can be attributed to a decrease in the global shear $(s/\iota)d\iota/ds$ with diminishing T at the $\iota = 3/4$ resonant surface as shown in Fig. 5a. The eigenvalue of the internal mode starts to decrease only for $T < 0.8$ when the global shear starts to increase again. These results suggest that a small amount of counter current drive $\sim 400kA$ may be necessary to stabilise the external kink in the 3-period QAS stellarator reactor considered. To tackle the residual internal kink, either pressure profile control that would alter the BC profile or localised electron cyclotron current drive may be required to enhance the global shear at the critical $\iota = 3/4$ surface. Although NCSX is similar in shape to the reactor system studied here, the BC that is calculated in that device contributes only about 1/4 of the rotational transform and thus evades the issue of the resonant $\iota = 3/4$ surface emerging from the plasma.

7. 6-Period $\mathcal{J}_{\|}$-optimised QPS Stellarator Reactor

The 6-fold periodic $\mathcal{J}_{\|}$-optimised QPS stellarator configuration we investigate in this section corresponds to the result of a maximisation of the fraction of poloidally closed contours of the second adiabatic invariant $\mathcal{J}_{\|} = \int v_{\|} d\ell$ in a $(\sqrt{s}, \theta)$ polar representation (quasi-isodynamicity) [10] in conjunction with a minimisation of the fraction of closed mod-B contours in a plane defined by the Boozer angular coordinates on a specific flux surface, typically at midradius (pseudosymmetry) [14].

We have examined pressure profiles that are peaked $p(s) = p(0)(1-s)^2$, nearly parabolic $p(s) = p(0)[1 - s - 0.1(1 - s^{10})]/0.9$ and broad $p(s) = p(0)[1 - s^2 - 0.2(1 - s^{10})]/0.8$ and find that the bootstrap current at $\beta^* \simeq 6\%$ is very small, typically of the order of $100kA$ in the reactor system under consideration. As a result, the rotational transform profiles are not significantly altered by the existence of the BC. The pressure profiles studied and the corresponding ι-profiles are presented in Fig. 6. To underscore the weak impact of the BC, we also show the ι-profile for the broad pressure profile under zero net current conditions. To verify how closely we satisfy the conditions of pseudosymmetry, we plot in Fig. 7 the mod-B contours in a plane defined by the Boozer angles on the surface $s = 0.234375$ to demonstrate that only a small fraction of these contours are closed near the maxima of B for the range of pressure profiles we have studied when $\beta^* \simeq 6\%$. This figure also illustrates the feature of quasipoloidal symmetry because for fixed Boozer toroidal angle, the magnetic field strength is almost constant as a function of the Boozer poloidal angle. Another characteristic of this system is that the magnetic field structure achieves minimum-B conditions towards the magnetic axis in the vicinity of the up-down symmetric cross section where the magnetic field strength is minimum. Correspondingly, closed B-contours are realised about this cross section. The $\mathcal{J}_{\|}$-optimised QPS system are also characterised by nearly vanishing magnetic field line curvature on the cross sections not only where B is minimum but also where it is a maximum. The $\mathcal{J}_{\|}$ contours for peaked and broad pressure profile in a polar $(\sqrt{s}, \theta)$ representation are displayed in Fig. 8 and show that as the pressure profile broadens, the $\mathcal{J}_{\|}$ contours extend closer to the edge of the plasma. This demonstrates that quasi-isodynamicity improves with pressure profile width and augurs favourable conditions for particle confinement. In fact, the collisionless orbit loss analysis of 1000 α-particles born at midradius ($s = 1/4$) shows no particles escaping the plasma in a time interval of

$5s$, well beyond the typical slowing down expected. For α-particles born at approximately 2/3 the plasma radius ($s = 0.44$), a loss pattern is detected. About 6% of the trapped α-particles are lost after $5s$ when the pressure profile is peaked while the loss reduces to 1.5% with the nearly parabolic pressure profile. For the broad pressure profile examined, only 2 of the 1000 particles followed were lost. This loss pattern as a function of pressure profile width can be attributed to the improved quasi-isodynamicity obtained with broader pressure profiles.

The weak bootstrap current also implies favourable ideal MHD stability conditions with respect to current driven kink modes. In the absence of a BC, the plasma was stable to all modes computed with TERPSICHORE. With finite BC at $\beta^* \simeq 6\%$, intermediate to high mode number structures were weakly destabilised. However, the mode structures calculated were sufficiently localised that they would be subject to finite Larmor radius stabilisation.

8. 10-period Sphellamak Reactor

We concentrate in this section on a Sphellamak reactor system with $V \sim 1000m^3$ at $\beta^* \simeq 8\%$ with a peaked toroidal plasma current prescribed by $2\pi J'(s) = 2\pi J'(0)[3(1-s)^5 + (1-s^5)^2]/4$ such that the total toroidal current is $2\pi J(1) = 20MA$. This type of current profile produces a maximum-B configuration in the central region of the plasma so that conditions that are close to isodynamic in the core are achieved. For various sets of pressure profiles and ratios of helical winding currents to toroidal current, we find that the bootstrap current provides only about a 10% fraction of the total current required in the system at $\beta^* \simeq 8\%$. We also find that the pressure profile $p(s) = p(0)(1-s^2)^4$ is favourable with respect to localised ballooning stability. However, the system remains weakly unstable to a low order $m/n = 1/1$ kink mode because the edge ι approaches the critical value of unity. The $\sqrt{g}\delta B^s$ structure of this mode near the edge of the plasma in Fig. 9a shows the dominating $m/n = 1/1$ mode modulated by higher order toroidal components. The perturbed radial magnetic field is designated by δB^s. The orbit confinement loss of trapped α-particles born at midradius ($s = 0.24$) is negligible because they reside in the domain in which the mod-B contours are poloidally closed on all cross sections. The bulk of the trapped α-particles born at midvolume ($s = 0.5$) become lost within a slowing down time because they experience the full 3D structure of the magnetic fields at the edge of the plasma. The α-loss patterns for particles with orbits originating at midvolume as a function of time are displayed in Fig. 9b for pressure profiles $p(s) = p(0)[0.9(1-s)^2 + 0.1(1-s)]$ and $p(s) = p(0)(1-s^2)^4$.

9. Conclusions

The global ideal MHD kink stability properties of 3D reactor configurations with volume $V \sim 1000m^3$ driven by finite bootstrap currents in the collisionless $1/\nu$ regime have been investigated. The systems examined in some detail are 2 and 3-period quasiaxisymmetric stellarators, a 6-period $\mathcal{J}_{\parallel}$-optimised quasipoloidally symmetric stellarator and a compact Sphellamak device. Furthermore, the α-particle properties were evaluated in the QPS and Sphellamak systems.

As expected, we find that the BC in QAS stellarators is large and increases the edge rotational transform as in Tokamak devices. In QHS stellarators, the BC is also large but decreases the rotational transform. In a system with vacuum transform of the order of unity, we find that the rotational transform with finite BC approaches the critical value $\iota = 1/2$ when $\beta^* \sim 3\%$ while for higher β^* values, the BC algorithm fails. In a reactor-scaled version of WVII-X, the BC at $\beta^* \simeq 5\%$ is relatively small enhancing ι_e by about 7% with the model we have applied.

We have analysed in some detail pressure profiles that minimise the BC in a 2-period QAS at $\beta^* \simeq 5\%$. A profile that is nearly parabolic yields the smallest BC. However, this is insufficient to keep the edge transform below the critical value $\iota_e = 1/2$. As a result, a global external $m/n = 2/1$ kink mode is destabilised. Artificially suppressing the BC by 20% decreases $\iota_e < 1/2$ and the mode becomes stabilised. This suggests that modest counter current drive of the order of $1MA$ could realise the goal of stable operation in this type of reactor.

In a 3-period QAS reactor system, the BC and the rotational transform are larger than in the 2-period device. Using a nearly parabolic pressure profile, the BC model we have applied causes $\iota_e > 3/4$ at $\beta^* \simeq 5\%$ and this triggers the destabilisation of a $m/n = 4/3$ mode. Artificially suppressing the BC by 5% displaces the critical $\iota = 3/4$ surface into the plasma and the external mode structure almost reaches marginal conditions. A further suppression of the BC, however, causes an internal $m/n = 4/3$ dominated structure to appear that is correlated with a reduction of the global shear at the $\iota = 3/4$ surface. Eventually this mode is stabilised when the entire profile falls below $\iota = 0.75$. We can expect that a more optimally chosen pressure profile that causes the BC to locally enhance the global shear at the $\iota = 3/4$ surface or localised electron cyclotron current drive to achieve the same goal with respect to the shear would stabilise the internal mode structure.

The BC in a 6-period $\mathcal{J}_{\parallel}$-optimised QPS stellarator reactor system is small in the order of $100kA$ at $\beta^* \simeq 6\%$. It has the effect of decreasing the rotational transform by less than 5%. This type of configuration is achieved by maximising the fraction of poloidally closed contours of the second adiabatic inavariant $\mathcal{J}_{\|}$ in a $(\sqrt{s}, \theta)$ polar representation and minimising the fraction of closed mod-B contours on a flux surface near halfradius. This type of system is characterised by weak normal curvature at both up-down symmetric cross sections where the magnitude of B is an extremum and by the appearance of a minimum-B structure at the cross section where the magnetic field strength is weakest. The poloidally closed contours of $\mathcal{J}_{\|}$ guarantee good confinement of α-particles. These closed $\mathcal{J}_{\|}$ contours extend closer to the edge of the plasma with broad pressure profiles which improves the confinement of α-particles born at larger plasma radii. The small BC weakly destabilises relatively high toroidal mode number internal structures that are very localised and thus susceptible to finite Larmor radius stabilisation.

In a Sphellamak reactor device with peaked toroidal current to ensure a maximum-B configuration with nearly isodynamic properties in the central core of the plasma, the BC contributes a rather minor 10% of the total current required at $\beta^* \simeq 8\%$. For this range of β^*, the plasma becomes weakly unstable to a global $m/n = 1/1$ current driven kink due to the proximity of the critical $\iota = 1$ surface near the edge of the plasma. The orbits of α-particles within the region of closed mod-B contours are very well confined. On the other hand, α-particles born in the outer half of the plasma volume experience the full 3D structure of the magnetic fields near the edge of the plasma and the bulk of the trapped population drifts out within a slowing down time.

Acknowledgements

This research was partially sponsored by the Fonds National Suisse de la Recherche Scientifique, Euratom and INTAS Grant No. 99 – 00592. We thank Dr. S.P. Hirshman for the use of the VMEC code. The numerical calculations were primarily performed on a NEC/SX5 platform at the Centro Svizzero di Calcolo Scientifico, Manno, Switzerland.

References

[1] G. Grieger, C.D. Beidler, H. Maassberg, E. Harmeyer, F. Herrnegger, J. Janker, J. Kisslinger, W. Lotz, P. Merkel, J. Nührenberg, F. Rau, J. Sapper, F. Sardei and H. Wobig, Plasma Physics and Controlled Nuclear Fusion Research 1990, (International Atomic Energy Agency, Vienna 1991), Vol. 3, p. 525. Plasma Physics and Controlled Nuclear Fusion Research 1990,

[2] W.A. Cooper, G.Y. Fu, C. Schab, U. Schwenn, R. Gruber, S. Merazzi and D.V. Anderson, (International Atomic Energy Agency, Vienna 1991), Vol. 2, p. 793.

[3] C. Nührenberg, Phys. Plasmas **3**, 2401 (1996).

[4] M.C. Zarnstorff. L.A. Berry, A. Brooks, E. Fredrickson, G.Y. Fu et al., Plasma Phys. Control. Fusion **43**, A237 (2001).

[5] J.L. Johnson, K. Ichiguchi, Y. Nakamura, M. Okamoto, M. Wakatani and N. Nakajima, Phys. Plasmas **6**, 2513 (1999).

[6] J. Nührenberg, W. Lotz and S. Gori, Proc. Joint Varenna-Lausanne Int. Workshop on Theory of Fusion Plasmas, Editrice Compositori, Bologna (1994) 3.

[7] P.R. Garabedian, Phys. Plasmas **3**, 2483 (1996).

[8] A.H. Boozer, Phys. Fluids **23**, 904 (1980).

[9] S. Okamura et al., J. Plasma Fusion Res. **1**, 164 (1998).

[10] S. Gori, W. Lotz and J. Nührenberg, Proc. Joint Varenna-Lausanne Int. Workshop on Theory of Fusion Plasmas, Editrice Compositori, Bologna (1996) 335.

[11] J.R. Cary and S.G. Shasharina, Phys. Rev. Lett. **78**, 374 (1998).

[12] D.A. Spong, S.P. Hirshman, J.C. Whitson, D.B. Batchelor, B.A. Carreras, V.E. Lynch and J.A. Rome, Phys. Plasmas **5**, 1751 (1998).

[13] A.A. Subbotin, W.A. Cooper, M.Yu. Isaev, M.I. Mikhailov, J. Nührenberg, M.F. Heyn, V.N. Kalyuzhnyj, V.S. Kasilov, W. Kernbichler, V.V. Nemov, M.A. Samitov, V.D. Shafranov and R. Zille, (2002) Proceedings of 29*th* EPS Conference on Plasma Physics and Controlled Fusion, Montreux.

[14] M.I. Mikhailov, W.A. Cooper, M.Yu. Isaev, V.D. Shafranov, A.A. Skovoroda and A.A. Subbotin, Proc. Joint Varenna-Lausanne Int. Workshop on Theory of Fusion Plasmas, Editrice Compositori, Bologna (1998) 185.

[15] W.A. Cooper, J.M. Antonietti and T.N. Todd, Proc. 17*th* IAEA Conf. on Fusion Energy, Yokohama, Japan (1998).

[16] K.C. Shaing and J.D. Callen, Phys. Fluids **26**, 3315 (1983).

[17] N. Nakajima and M. Okamoto, J. Phys. Soc. Jap **61**, 833 (1992).

[18] K.Y. Watanabe et al., Nucl. Fusion **35**, 335 (1995).

[19] M. Isobe et al., Plasma Phys. Control. Fusion **44**, A189 (2002).

[20] S.P. Hirshman et al., Comput. Physics Commun. **43**, 143 (1986).

[21] K. Ichiguchi, N. Nakajima and M. Okamoto, Proc. Joint Varenna-Lausanne Int. Workshop on Theory of Fusion Plasmas, Editrice Compositori, Bologna (1996) 45.

[22] D.V. Anderson et al., Int. J. Supercomp. Appl. **1**, 34 (1990).

[23] J. Nührenberg and R. Zille, Phys. Letters **A129**, 113 (1988).

Figures

FIG. 1. The mod-B^2 distribution in Boozer magnetic coordinates for a 2-field period QAS stellarator reactor (first column from the left), a 3-period QAS stellarator reactor (second column from the left), a 6-period $\mathcal{J}_\parallel$ QPS stellarator reactor (third column from the left) and a 10-period Sphellamak reactor (last column on the right) on cross sections at the beginning of a field period (top row), at one quarter of a field period (middle row) and at midperiod (bottom row).

FIG. 2. (a) The pressure profiles investigated in a 2-period QAS stellarator reactor (left) and (b) the corresponding bootstrap currents in the $1/\nu$ regime at $\beta^* = 5\%$ (right).

FIG. 3. (a) The rotational transform ι profiles for each input pressure at $\beta^* = 5\%$ (left) and (b) the eigenvalue of a global $m/n = 2/1$ external kink (multiplied by 25), ι_e and the toroidal component of the bootstrap current (multiplied by $\mu_0/15$) as a function of the pressure profile parameter p_1 (right) in a 2-period QAS reactor.

FIG. 4. (a) The pressure, rotational transform ι and bootstrap current profiles (left) and (b) the ι-profiles for different values of the bootstrap current suppression factor T imposed (right) at $\beta^* = 5\%$ in a 3-period QAS reactor.

FIG. 5. (a) The eigenvalue of a global kink dominated by the $m/n = 4/3$ mode component and the global magnetic shear at the $\iota = 3/4$ surface as a function of the bootstrap current suppression factor T (left) and (b) the profile of the dominating $m/n = 4/3$ component of the radial displacement vector for different suppression factors T (right) at $\beta^* = 5\%$ in a 3-period QAS reactor.

FIG. 6. (a) The pressure profiles prescribed (left) and (b) the corresponding rotational transform ι profiles at $\beta^* \simeq 6\%$ (right) in a 6-period $\mathcal{J}_\parallel$-optimised QPS reactor. Also shown is the ι-profile when the effect of the bootstrap current is neglected for the broad pressure profile case (right).

FIG. 7. The mod-B contours on a flux surface labelled with $s = 0.234375$ at $\beta^* \simeq 6\%$ with (a) a peaked $p(s) = p(0)(1-s)^2$ profile (left) and (b) a broad $p(s) = p(0)[1 - s^2 - 0.2(1 - s^{10})]/0.8$ profile (right) in a 6-period $\mathcal{J}_\parallel$-optimised QPS reactor. The system displays pseudosymmetric features because the fraction of closed contours is small.

FIG. 8. The $\mathcal{J}_\parallel$ contours where $\mathcal{J}_\parallel \propto \int d\theta \left(\frac{B_{ref}-B}{B^2}\right)^{1/2}$, in a 6-period $\mathcal{J}_\parallel$-optimised QPS reactor at $\beta^* \simeq 6\%$ for (a) a peaked $p(s) = p(0)(1-s)^2$ profile (left) and (b) a broad $p(s) = p(0)[1-s^2-0.2(1-s^{10})]/0.8$ profile (right). The indices ℓ on each figure identify $B_{ref} = B_{min} + \ell\delta B$ with $\delta B = (B_{max} - B_{min})/7$ and B_{max}, B_{min}

correspond to the maximum and minimum values of B, respectively, on the flux surface labelled with $s = 0.234375$.

FIG. 9. (a) The edge structure of $\sqrt{g}\delta B^s$ corresponding to a global $m/n = 1/1$ kink modulated by higher order toroidal components at $\beta^* \simeq 8\%$ with a pressure profile $p(s) = p(0)[0.9(1-s)^2 + 0.1(1-s)]$ (left) and (b) the α-particle losses as a function of time for particles born at midvolume ($s = 0.5$) for pressure profiles $p(s) = p(0)[0.9(1-s)^2 + 0.1(1-s)]$ (red trace) and $p(s) = p(0)(1-s^2)^4$ (blue trace) (right) in a Sphellamak reactor.

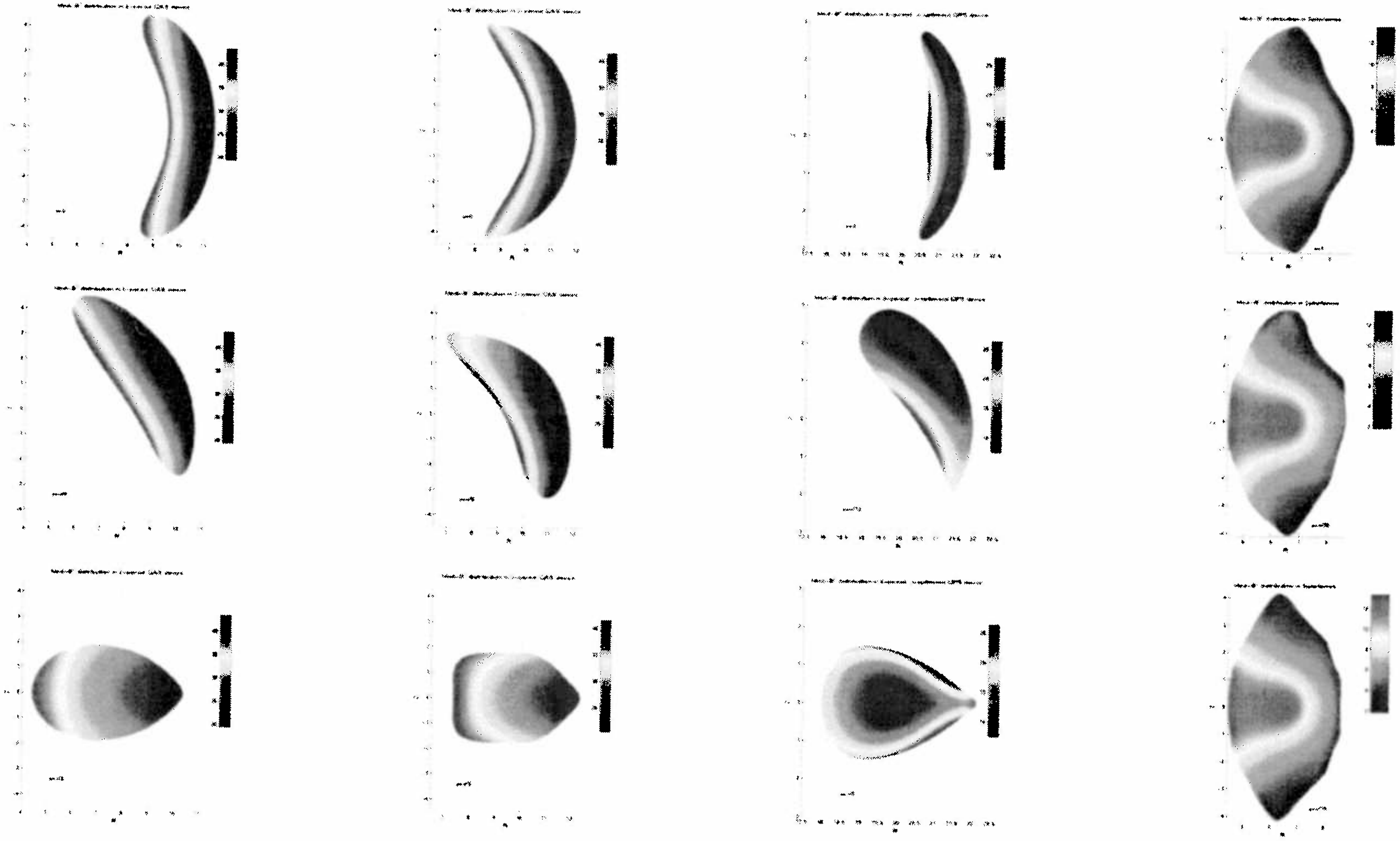

Fig. 1

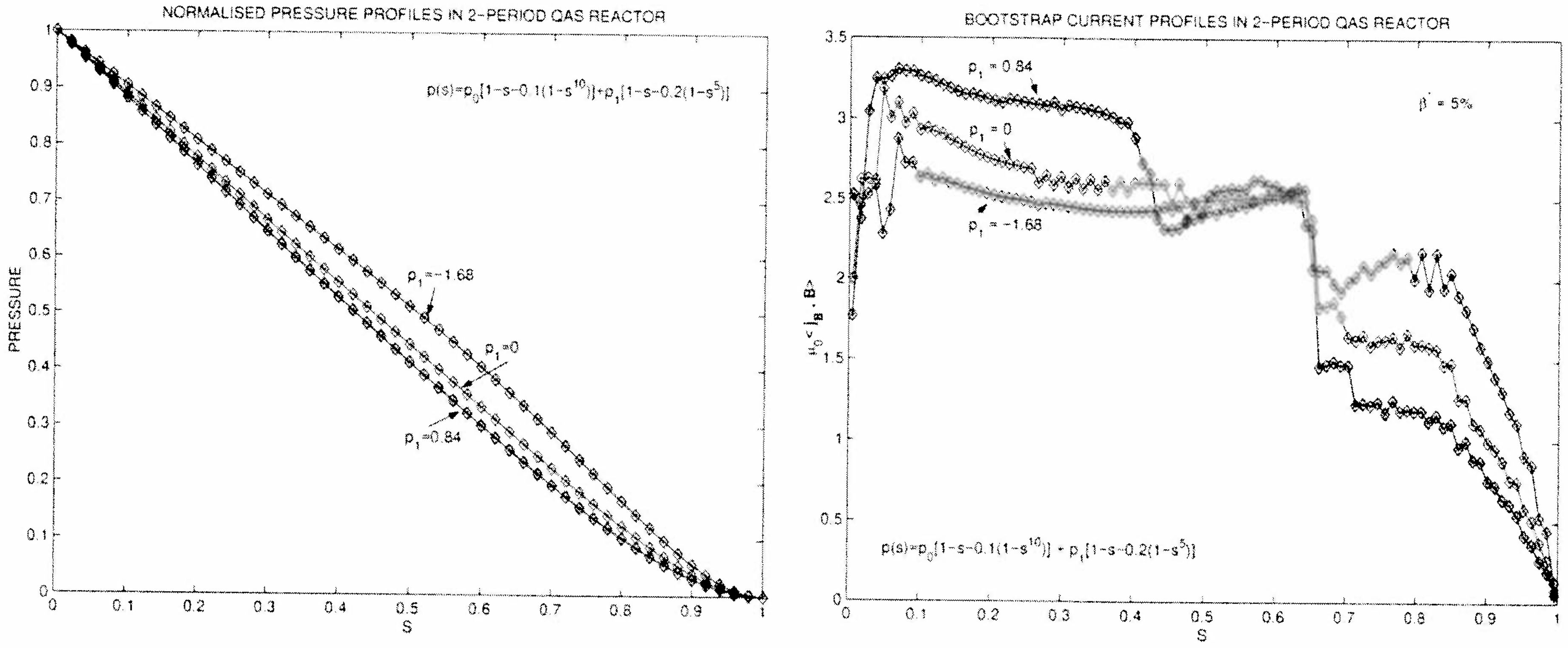
NORMALISED PRESSURE PROFILES IN 2-PERIOD QAS REACTOR
PRESSURE
S
0
0.1
0.2
0.3
0.4
0.5
0.6
0.7
0.8
0.9
1
p(s)=p0[1-s-0.1(1-s^10)]+p1[1-s-0.2(1-s^5)]
p1=-1.68
p1=0
p1=0.84
BOOTSTRAP CURRENT PROFILES IN 2-PERIOD QAS REACTOR
μ0<jB · B>
0.5
1
1.5
2
2.5
3
3.5
p1 = 0.84
p1 = 0
p1 = -1.68
β* = 5%
p(s)=p0[1-s-0.1(1-s^10)] + p1[1-s-0.2(1-s^5)]

Fig. 2

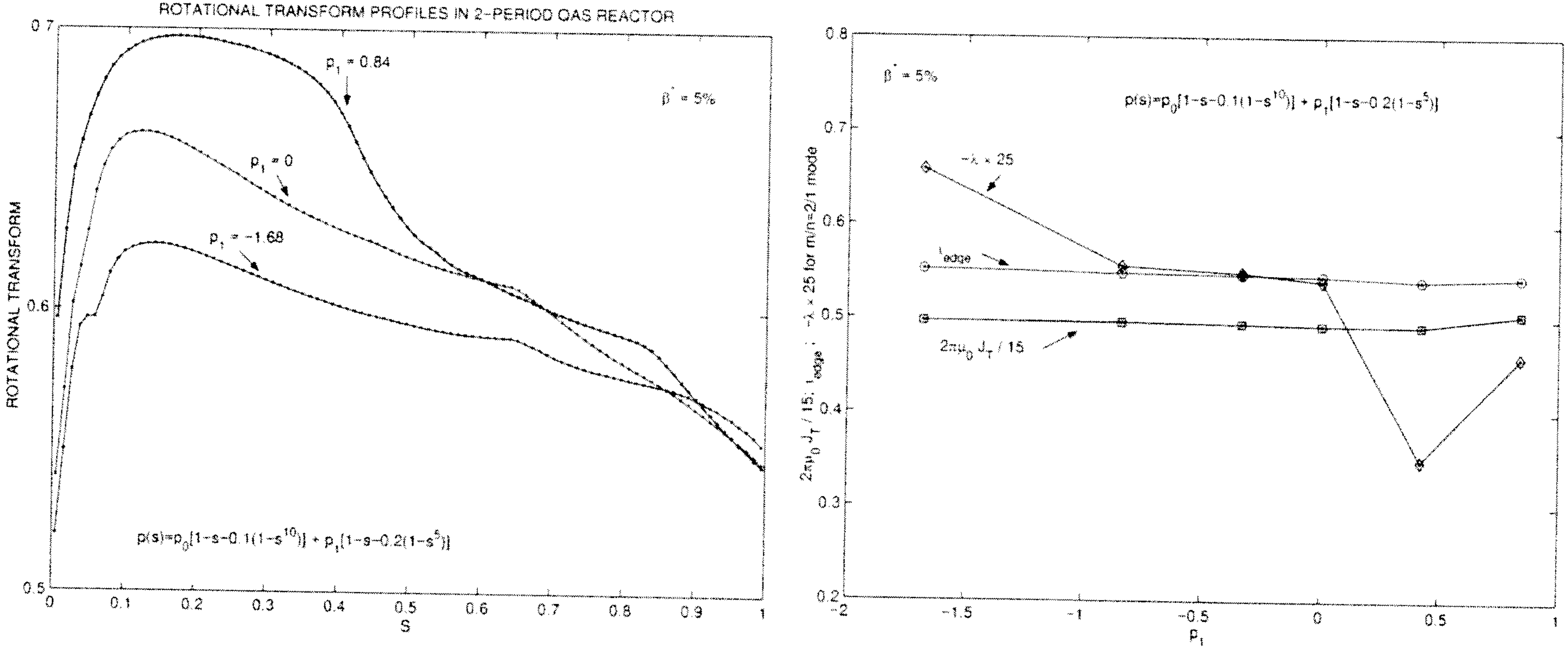
ROTATIONAL TRANSFORM PROFILES IN 2-PERIOD QAS REACTOR
ROTATIONAL TRANSFORM
S
$p_1 = 0.84$
$p_1 = 0$
$p_1 = -1.68$
$\beta^* = 5\%$
$p(s)=p_0[1-s-0.1(1-s^{10})] + p_1[1-s-0.2(1-s^5)]$
0.5
0.6
0.7
0
0.1
0.2
0.3
0.4
0.5
0.6
0.7
0.8
0.9
1
$2\pi\mu_0 J_T / 15$; ι_{edge} ; $-\lambda \times 25$ for m/n=2/1 mode
p_1
$\beta^* = 5\%$
$p(s)=p_0[1-s-0.1(1-s^{10})] + p_1[1-s-0.2(1-s^5)]$
$-\lambda \times 25$
ι_{edge}
$2\pi\mu_0 J_T / 15$
0.2
0.3
0.4
0.5
0.6
0.7
0.8
-2
-1.5
-1
-0.5
0
0.5
1

Fig. 3

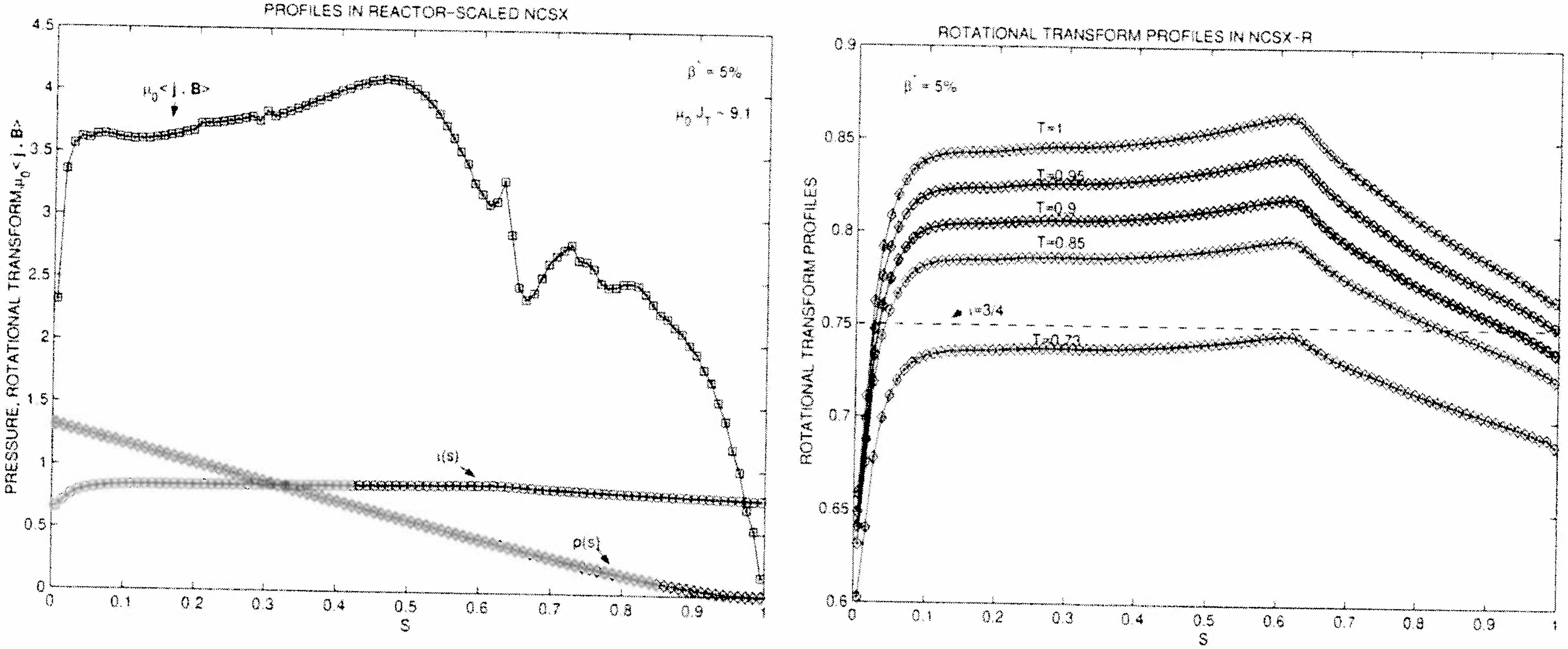
PROFILES IN REACTOR-SCALED NCSX
PRESSURE, ROTATIONAL TRANSFORM,μ_0< j . B>
μ_0< j . B>
β^* = 5%
$\mu_0 J_T$ ~ 9.1
ι(s)
p(s)
S
0
0.1
0.2
0.3
0.4
0.5
0.6
0.7
0.8
0.9
1
0.5
1.5
2
2.5
3
3.5
4
4.5
ROTATIONAL TRANSFORM PROFILES IN NCSX-R
ROTATIONAL TRANSFORM PROFILES
β^* = 5%
T=1
T=0.95
T=0.9
T=0.85
ι=3/4
T=0.73
0.6
0.65
0.7
0.75
0.8
0.85
0.9

Fig. 4

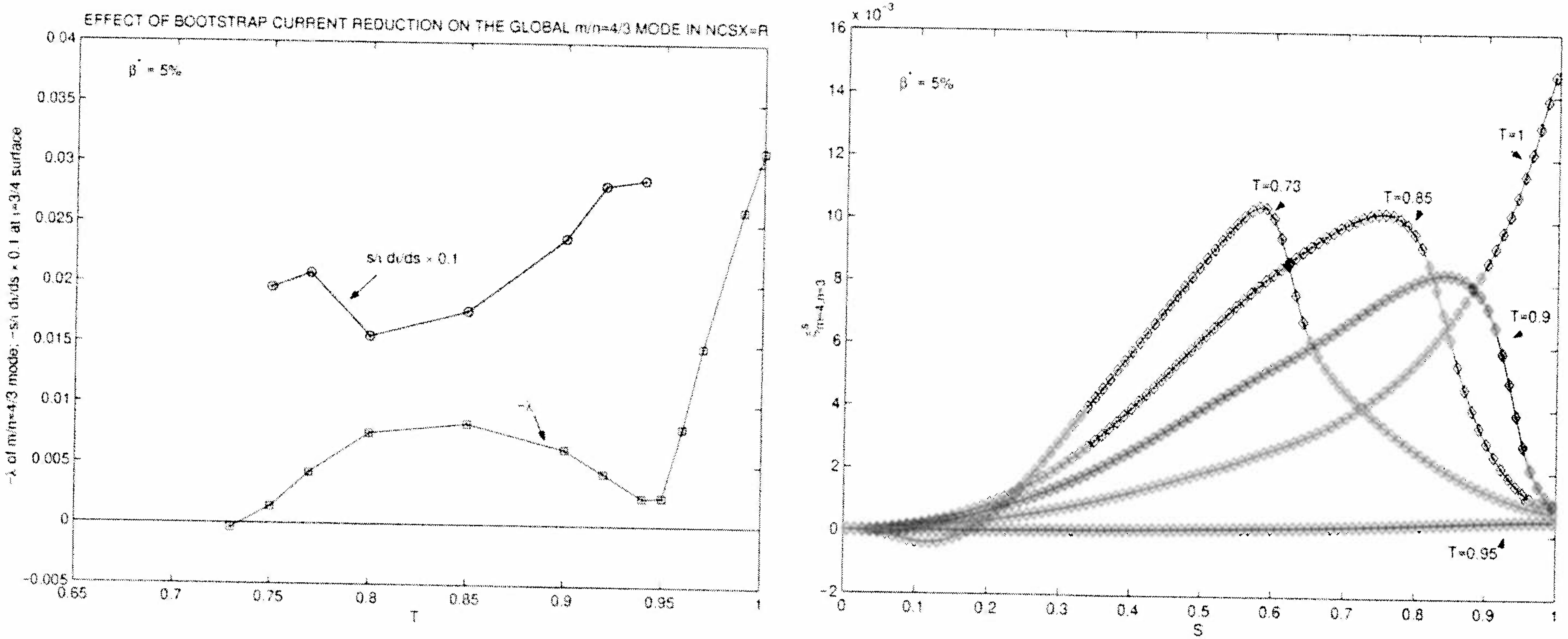
EFFECT OF BOOTSTRAP CURRENT REDUCTION ON THE GLOBAL m/n=4/3 MODE IN NCSX=R
β* = 5%
−λ of m/n=4/3 mode; −s/ι dι/ds × 0.1 at ι=3/4 surface
s/ι dι/ds × 0.1
−λ
0.04
0.035
0.03
0.025
0.02
0.015
0.01
0.005
0
−0.005
0.65
0.7
0.75
0.8
0.85
0.9
0.95
1
T
x 10⁻³
β* = 5%
ξˢ m=4,n=3
T=0.73
T=0.85
T=1
T=0.9
T=0.95
16
14
12
10
8
6
4
2
0
−2
0
0.1
0.2
0.3
0.4
0.5
0.6
0.7
0.8
0.9
1
S

Fig. 5

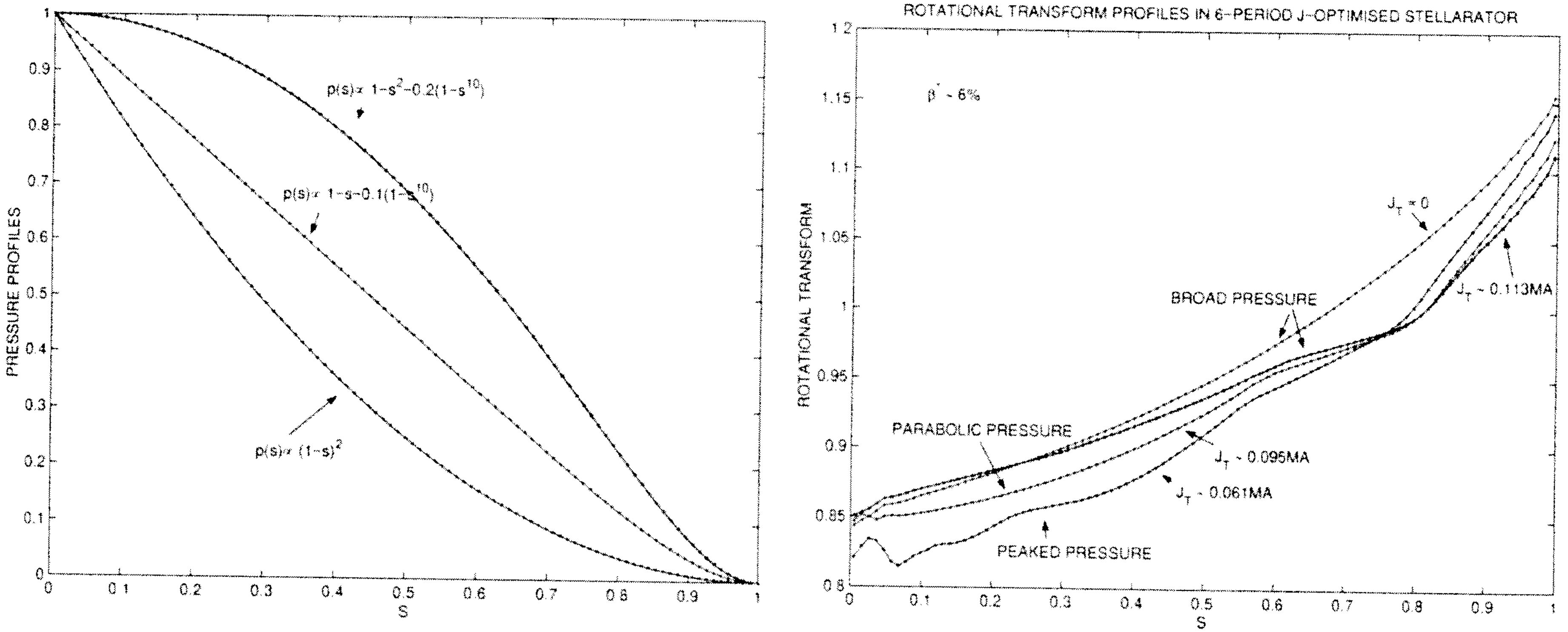
PRESSURE PROFILES
S
p(s)∝ 1-s²-0.2(1-s¹⁰)
p(s)∝ 1-s-0.1(1-s¹⁰)
p(s)∝ (1-s)²
0
0.1
0.2
0.3
0.4
0.5
0.6
0.7
0.8
0.9
1
ROTATIONAL TRANSFORM PROFILES IN 6-PERIOD J-OPTIMISED STELLARATOR
ROTATIONAL TRANSFORM
β* ~ 6%
J_T = 0
BROAD PRESSURE
J_T ~ 0.113MA
PARABOLIC PRESSURE
J_T ~ 0.095MA
J_T ~ 0.061MA
PEAKED PRESSURE
0.8
0.85
0.9
0.95
1
1.05
1.1
1.15
1.2

Fig. 6

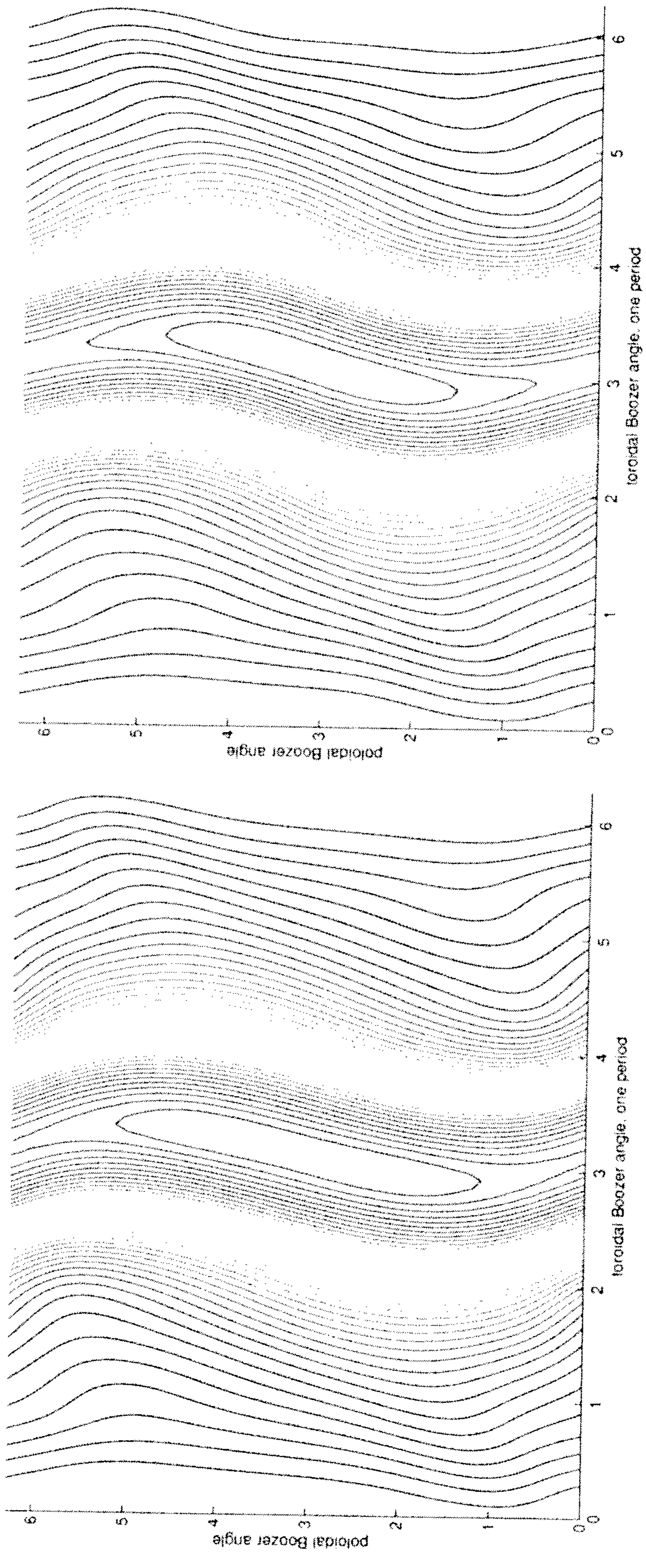
poloidal Boozer angle
0
1
2
3
4
5
6
toroidal Boozer angle, one period
0
1
2
3
4
5
6
poloidal Boozer angle
0
1
2
3
4
5
6
toroidal Boozer angle, one period
0
1
2
3
4
5
6

Fig. 7

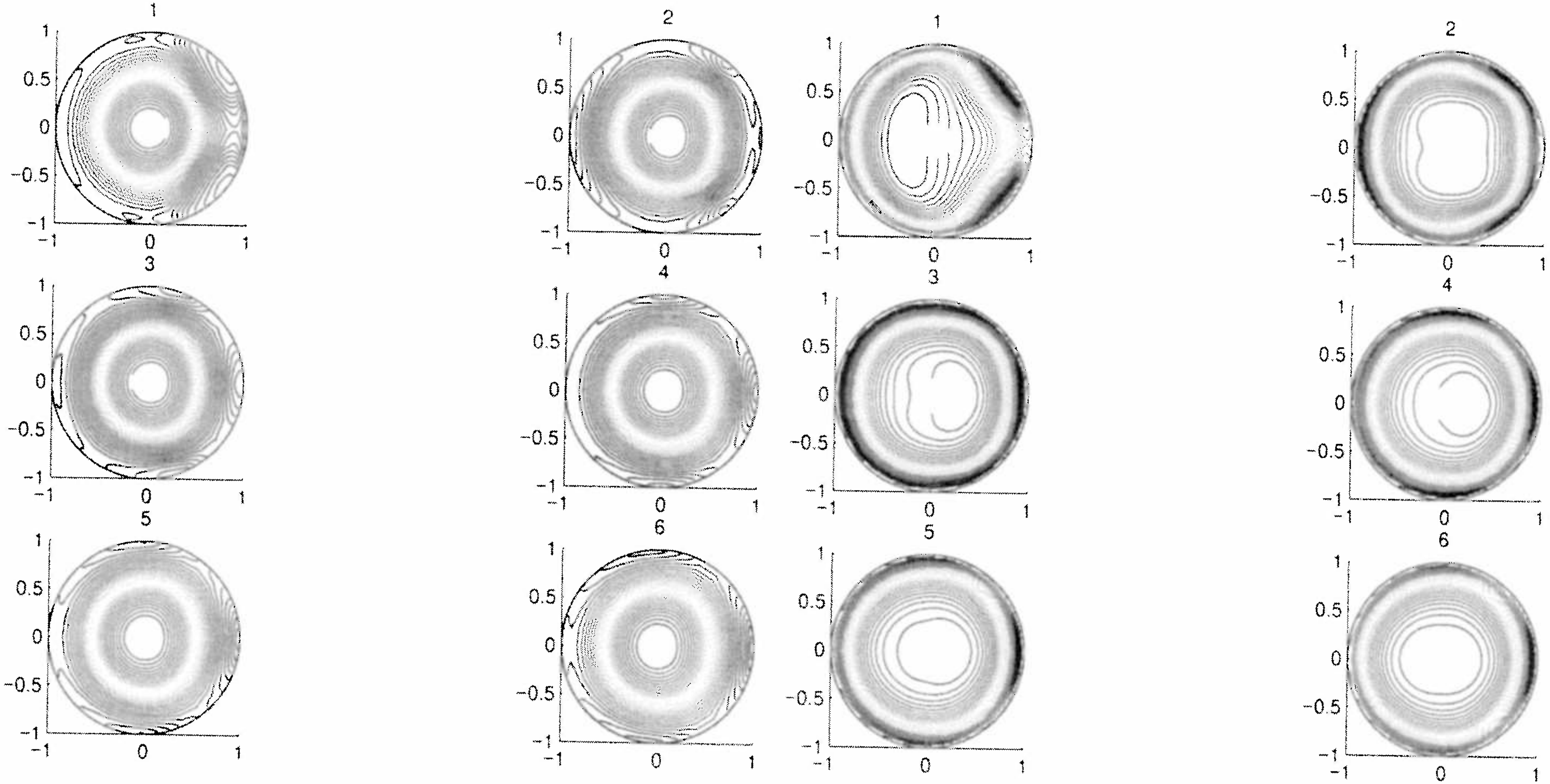

Fig. 8

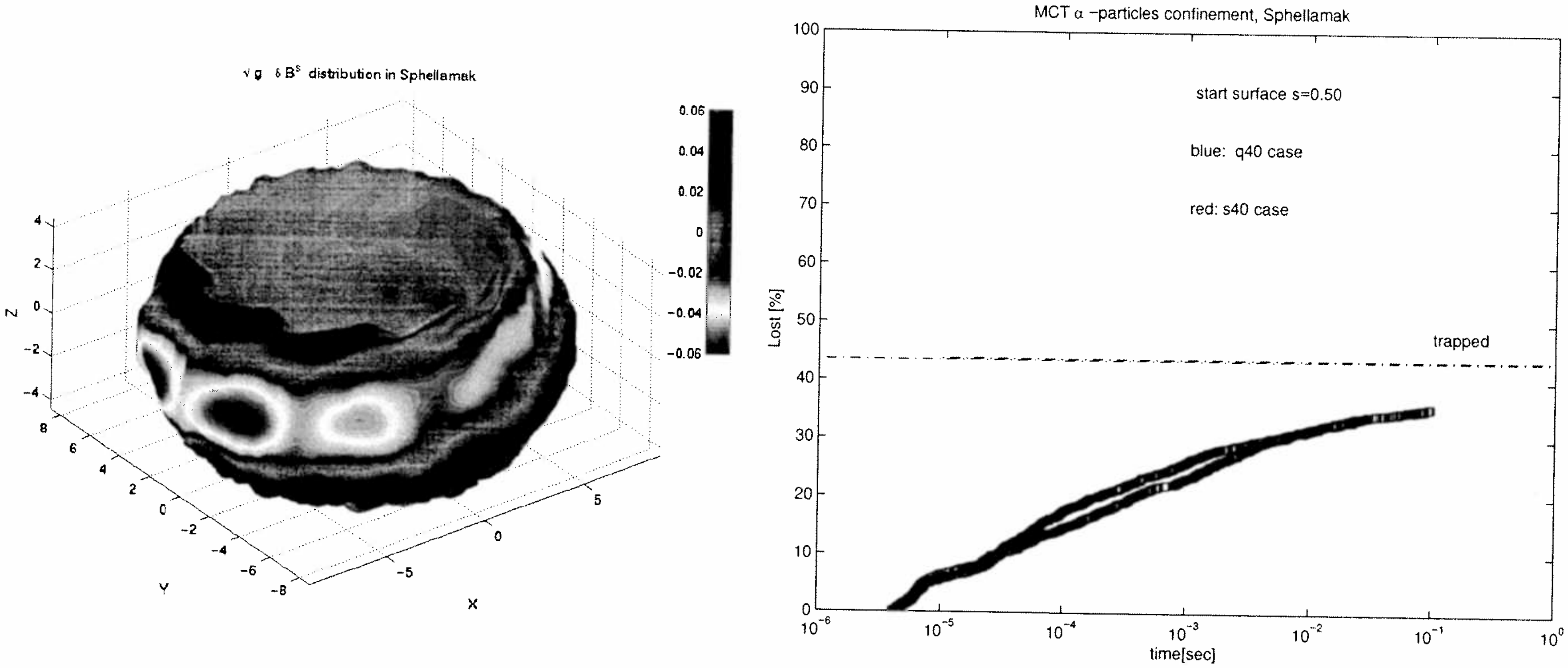
√g δB^S distribution in Sphellamak
Z
4
2
0
-2
-4
Y
8
6
4
2
0
-2
-4
-6
-8
X
-5
0
5
0.06
0.04
0.02
0
-0.02
-0.04
-0.06
MCT α -particles confinement, Sphellamak
Lost [%]
100
90
80
70
60
50
40
30
20
10
0
start surface s=0.50
blue: q40 case
red: s40 case
trapped
time[sec]
10^-6
10^-5
10^-4
10^-3
10^-2
10^-1
10^0

Fig. 9

MHD Spectroscopy

A.Fasoli[1,2], D.Testa[2], S.Sharapov[3], H.L.Berk[4], B.Breizman[4], A.Gondhalekar[3], R.F.Heeter[5],
M.Mantsinen[3], and contributors to the EFDA-JET work programme[**]

[1]*CRPP-EPFL, Association EURATOM-Confédération Suisse, 1015 Lausanne, Switzerland*
[2]*Plasma Science and Fusion Center, MIT, Cambridge, MA 02139, USA*
[3]*EURATOM-UKAEA Fusion Association, Culham Science Center, Abingdon, UK*
[4]*Institute for Fusion Studies, University of Texas at Austin, Texas 78712, USA*
[5]*Lawrence Livermore National Laboratory, CA 94550, USA*

Abstract

Experiments are conducted on the JET tokamak to demonstrate the diagnostic potential of MHD spectroscopy, for the plasma bulk and its suprathermal components, using Alfvén Eigenmodes (AEs) excited by external antennas and by energetic particles. The measurements of AE frequencies and mode numbers give information on the bulk plasma. Improved equilibrium reconstruction, in particular in terms of radial profiles of density and safety factor, is possible from the comparison between the antenna driven spectrum and that calculated theoretically. Details of the time evolution of the non-monotonic safety factor profile in advanced scenarios are reconstructed from the frequency behaviour of ICRH-driven energetic particle modes. The plasma effective mass is inferred from the resonant frequency of externally driven AEs in discharges with similar equilibrium profiles. The stability thresholds and the nonlinear development of the instabilities give clues on energy and spatial distribution of the fast particle population. The presence of unstable AEs provides lower limits in the energy of ICRH generated fast ion tails. Fast ion pressure gradients and their evolution are inferred from the stability of AEs at different plasma radial positions. Finally, the details of the AE spectrum in the nonlinear stage are used to obtain information about the fast particle velocity space diffusion.

---

[*] *see Appendix of J.Pamela et al., Fusion Energy 2000 (Proc. 18th International Conference, Sorrento, 2000), IAEA Vienna (2001).*

1. Introduction

Collective modes are a special property of the plasma state. In fusion research, they are commonly studied for two reasons. First, to assess and limit their negative effect on the plasma performance, in particular on the confinement and transport of energy and particles. Conditions in which the modes are either stable or can be kept at amplitudes that are too low to affect the plasma behavior are sought. Second, to find ways to couple energy via electromagnetic waves from external antennas in order to heat the plasma. Here we discuss a third aim for investigating the properties of collective plasma modes in fusion devices, namely on how to extract information on the plasma. Because of the low frequency range of the modes that are used for diagnostic purposes, this approach is referred to as Magneto-Hydro-Dynamics (MHD) spectroscopy [1].

To serve diagnostic purposes for the plasma bulk as well as for suprathermal components of the plasma, the collective modes must satisfy a number of requirements. Their dispersion relation should depend on the macroscopic properties of the plasma, separate from the instability drive, which should come from non-thermal components or fast particles. The modes should not be subject to strong damping, with their phase velocity well separated from both the ion and electron thermal speeds, and should exist in a frequency range that is naturally free of significant background turbulence. It should be possible to drive and detect the modes at amplitudes that are low enough to avoid significant perturbations to the plasma equilibrium and transport. The above requirements are satisfied by modes in the Alfvén wave range of frequencies.

In toroidal plasmas, the dispersion relation for Alfvén waves is locally satisfied point by point along the radial profile, giving rise to the so-called Alfvén continuum, described by $f_A(r)=k_{||}(r)v_A(r)/2\pi$, which in cylindrical approximation reads

$$f_A(r)=\frac{v_A(r)}{2\pi R}\left(n+\frac{m}{q(r)}\right)\;;v_A=\frac{B}{\sqrt{4\pi n_i m_i}} \tag{1}$$

Here v_A is the Alfvén speed, n and m the toroidal and poloidal mode numbers, R the torus major radius, and q(r) the safety factor profile. Due to the continuous dependence of the frequency on position, continuum modes are strongly damped. The coupling of different poloidal harmonics produces gaps within which weakly damped Alfvén Eigenmodes (AEs) exist [2], such as Toroidal AEs, in the gap centered at $f_{TAE}=v_A/(4\pi qR)$, and Elliptical AEs, with $f_{EAE}\sim 2f_{TAE}$.The drive for these modes stems from the free energy source associated with the radial pressure gradient of particles with energies such that their velocities are of the order of the Alfvén speed. For passing particles the resonance condition is expressed in terms of the velocity parallel to the magnetic field, $v_{||}\sim v_A$ for the primary resonance and $v_{||}\sim v_A/3$, $v_A/5$, etc. for higher order resonances, of decreasing significance. For trapped particles, the resonance occurs between the wave and the bounce or precession motions, corresponding to particle velocities $|v|=v_A/2(R/r)^{1/2}$ and $|v|=v_A/2qk_\theta\rho_L$, respectively [3].

In JET different sources for non-thermal ions exist, including Neutral Beam Injected (NBI) and fusion reactions generating 3.5MeV α's in Deuterium-Tritium plasmas. However, in this Paper we will focus on fast ions generated by Ion Cyclotron Resonance Heating (ICRH). The most commonly used scheme is Hydrogen minority heating in Deuterium plasmas, in which the H^+ ions typically resonate with Alfvén waves for ion energies of the order of 0.5 MeV.

The resonance condition is a necessary but not sufficient condition to drive AEs unstable. A strong fast particle pressure gradient is necessary to overcome the Landau damping due to the fast particles themselves and the damping coming from the background plasma. The drive from the fast particles leads to a growth rate of the AE instability that can be expressed as

$$\gamma = \int \left[\omega \frac{dF}{dE} - const \times n \frac{dF}{dr} \right] F_{resonance}(v, v_A) dv \qquad (2)$$

where F is the fast particle distribution function, E the particle energy, and $F_{resonance}(v,v_A)$ expresses the resonance condition discussed above.

Figure 1 (right) presents a characteristic Alfvén Eigenmode spectrum in a JET discharge with about 4MW of ICRH additional heating in the H-minority heating scheme. As expected, TAEs and EAEs appear in a turbulence free zone of the spectrum in the corresponding gaps of the Alfvén continuum. Their amplitude, $\delta B/B \sim 10^{-6}$ as measured at the plasma edge, does not seem to produce any significant effect in the plasma, nor to affect the ICRH power deposition process significantly. Each mode measured in the laboratory frame is subject to Doppler shift due to the plasma rotation, with $f_{meas}=f_{AE}+nf_{rot}^{tor}(r_{AE})$ $[+mf_{rot}^{pol}(r_{AE})]$. Here r_{AE} is the position of the Eigenmode. The term with the poloidal rotation appearing in brackets is neglected as is usually small in comparison with the toroidal rotation term.

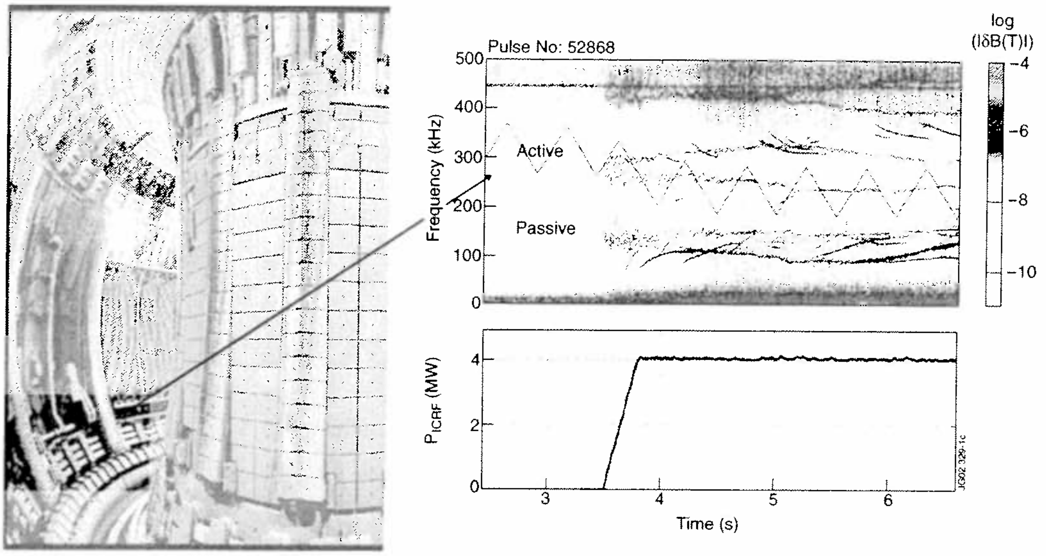

Figure 1 Example of co-existence of active and passive MHD spectroscopy. Here and in the following figures the plasma is started at 40s.

We will discuss the experimental methods to investigate the AE properties, passive and active MHD spectroscopy, in Section 2. Section 3 is dedicated to the extraction of information on the plasma bulk, namely on the plasma equilibrium density and safety factor profiles, and on the plasma effective mass, from the measurement of the mode frequency. Section 4 explores the possibility of inferring properties of the suprathermal ion distribution, both in real and in configuration spaces, from the mode stability limits and from the nonlinear evolution of unstable modes. A summary of the results and an outlook for future experiments are included in the Section 5.

2. Experimental Method

Two experimental methods, passive and active MHD spectroscopy, are used at JET to obtain information on the plasma and its non-thermal components.

2.1 Passive MHD spectroscopy

Passive MHD spectroscopy simply consists in observing collective modes in the Alfvén frequency range driven unstable by fast particles using edge and internal fluctuation measurements. Magnetic probes measuring $d\delta B_{pol}/dt$ at the plasma edge provide the clearest signals. For simplicity, only spectral data from this system will be used throughout this Paper. The fluctuation signals are digitized for 4s at 1MHz, with 12 bits resolution, by the 8-channel KC1F system. The distribution of the probes connected to KC1F allows us to reconstruct toroidal mode numbers in the range from n =-17 to n=+17 and to measure local poloidal phases. All magnetic probe channels are calibrated remotely; the calibration is implemented as a digital filter applied to the raw data [4]. Unstable modes with amplitudes as low as $|\delta B|\sim 10^{-8}$ T can be detected.

2.2 Active MHD spectroscopy

Active MHD spectroscopy refers to the technique of driving low amplitude perturbations in the plasma using external antennas, and extracting the plasma response using synchronous detection. At JET, signals from magnetic coils, electron cyclotron emission (ECE), reflectometer and X-ray cameras are employed. Different combinations of antenna phasing for 1, 2 or 4 saddle coils can be chosen to excite specific low toroidal mode numbers (n=0,1,2). Maximum current and voltage are of the order of 30 A and 1000 V, corresponding to core magnetic perturbations ($\delta B/B<10^{-5}$) too weak to produce significant effects on the bulk plasma or on the fast particle confinement.

The plasma collective modes appear as resonances in the measured plasma response. Their frequency, mode structure and background damping rate can therefore be measured in the absence of resonant fast particles. When resonant particles are present, but the instability drive is insufficient to drive the modes unstable, active spectroscopy still provides estimates of fast particle drive and background plasma damping separately [5].

Figure 1(left) highlights one of the four saddle coils presently installed inside the JET vacuum vessel. The spectrogram of a magnetic probe at the plasma edge shown in Figure 1(right) illustrates both active and passive spectroscopic methods in action in a plasma discharge. The trace labeled ‘active’ corresponds to the magnetic perturbation driven in the plasma by the saddle coils, and is well visible on the spectrogram before any fast particles are present. Once the ICRH power exceeds the threshold for driving AEs unstable, the magnetic signals corresponding to ICRH-driven TAEs and EAEs are visible and coexist with the active signal.

When time resolved measurements of properties of the driven mode are needed, a digital real time control system is used to perform individual resonance tracking. The controller of the exciter frequency, run at a 1 ms clock rate, varies the frequency linearly around the initial guess for the AE resonance, generally at the center of the AE gap. When the AE resonance is met, the exciter frequency is swept back and forth around it. The time taken to cross each resonance, typically of the order of 30 ms, represents the typical time resolution of the measurement of frequencies and damping rates. As the simple estimate of frequency and damping rate from the center and width of the driven resonance follows closely the value obtained from a full fit [6], these quantities can be evaluated in real time. Figure 2 illustrates an example of tracking an individual collective mode in a plasma in the absence of AE instability drive. On the right, the magnitude of the synchronously detected magnetic probe signal is plotted as a function of frequency and time. The signal peaks when the frequency of the exciter crosses the calculated center of TAE gap, f_{TAE}, allowing an unambiguous identification of the driven modes as n=1 TAEs. The detail shows a single peak corresponding to an n=1 TAE resonance crossing. The magnetic spectrogram on the left for the time interval 53-57s confirms that the antenna driven perturbation completely dominates the fluctuation spectrum in the AE frequency range.

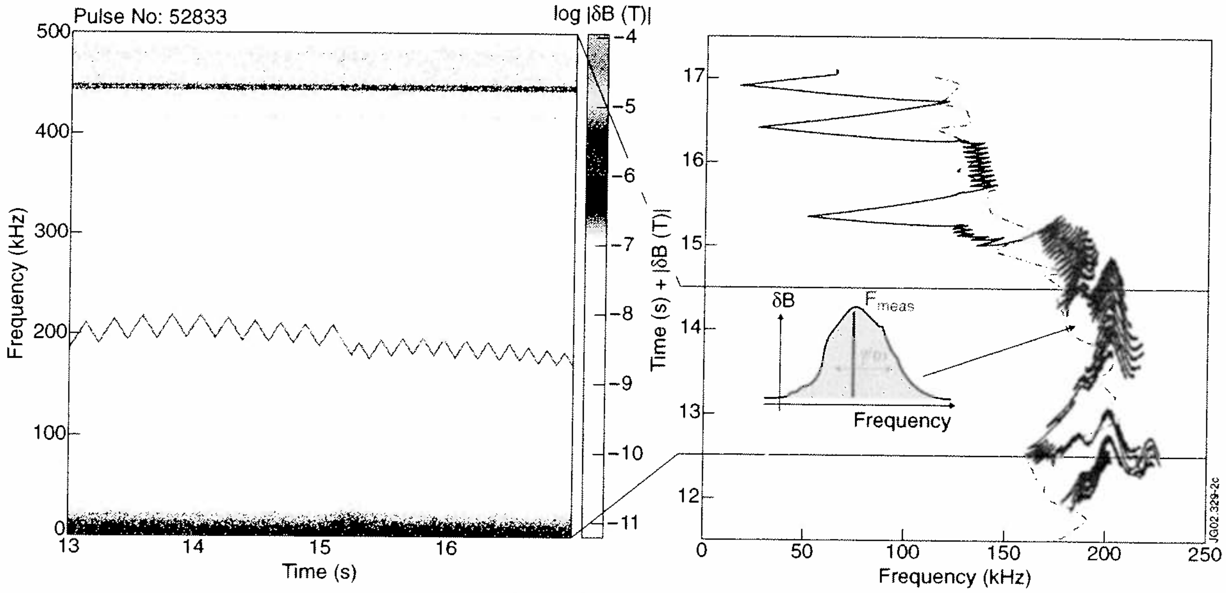

Figure 2 Tracking of an individual AE (an n=1 TAE) in the absence of fast particle drive in the limiter phase of a JET ohmic discharge, with the synchronously detected signal (right), and the spectrogram of the directly digitized magnetic perturbation (left).

The low toroidal mode numbers that can be driven by the JET saddle coils are strongly damped in plasmas of high elongation and edge magnetic shear, hence becoming undetectable during the divertor phase of the discharge [7]. Although this finding represents a positive piece of news for future burning plasma experiments, in most cases it prevents the use of MHD spectroscopy in the high performance phase of the JET discharges. In addition, intermediate or high toroidal mode numbers characterize the most unstable AEs detected in JET and predicted for ITER. A direct excitation and tracking of the same modes would therefore be of interest for preparing the next step experiments.

To overcome these limitations, a structure optimized for the excitation and detection of AEs with n≤15 is being designed for future applications in JET. Eight antennas in two groups of four are foreseen. Each antenna is made of 7-turns of conductor, of a size of about 20cmx20cmx15cm, separated from each other by about 15cm, and is characterized by a static self-inductance for each antenna of the order of L~15 μH. The distance between the antennas and the last closed flux surface is the order of 10 cm. A sketch of the proposed design is shown in Figure 3. Four of the eight antennas will be driven at the same time, chosen to obtain the specific toroidal mode number spectrum needed for a given experiment. The un-energized antennas will be used as detectors.

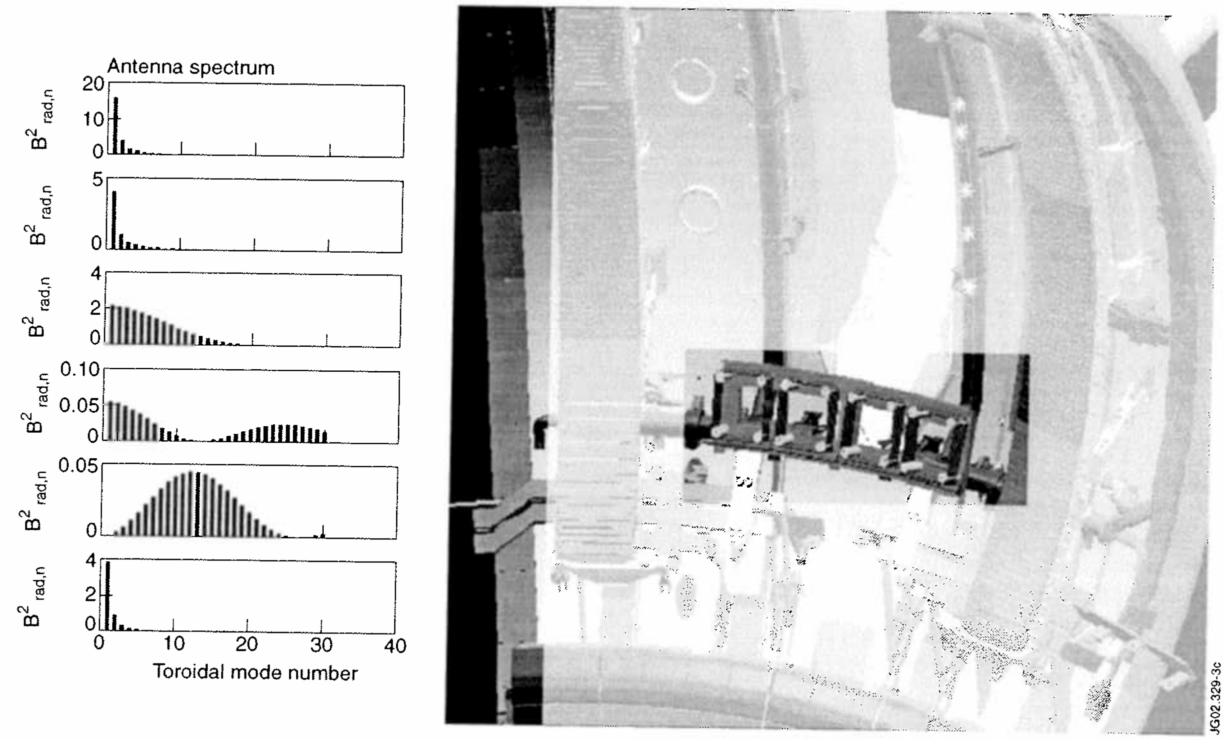

Figure 3 A sketch of four of the eight new AE antennas designed for JET-EP, along with the expected geometrical toroidal mode number spectrum for a number of possible phase combinations. A second block of four antennas will be installed diametrically opposed in the vacuum vessel.

3. From the wave frequency to plasma bulk properties

The measurement of the mode frequency performed in the laboratory frame is subject to Doppler shift due to plasma rotation, which can be significant in the presence of NBI additional heating. By measuring the Doppler shift in the frequency of the ICRH-driven AEs with different n, the value of the plasma rotation velocity at the mode location is inferred. Such measurements indicate that a significant difference in the rotation of the bulk and impurity ions exists in the presence of strong pressure gradients [8].

As shown in Eq. (1), the dispersion relation of Alfvén waves in a torus depends on the safety factor profile q(r), and the plasma effective mass, in addition to the magnetic field and density. In the following we will show examples of information obtained on q(r) from active and passive spectroscopy, and on the plasma isotopic mix from active mode tracking in D-T plasmas.

3.1 Static q-profile from active MHD spectroscopy: improvement of equilibrium reconstruction

In addition to weakly damped Eigenmodes in the gap, external antennas can drive the Alfvén continuum and measure the structure of the corresponding plasma response. As the structure of the Alfvén continuum in a tokamak depends on q(r) and the density profile, $n_e(r)$, information on these can be gathered. Relatively cold JET ohmic plasmas, in the limiter phase of the discharge, are considered, as in this case kinetic effects such as the creation of multiple AEs at the top of the relevant gap are not observed to play an important role [9]. The experimental curve is compared to the results of a numerical calculation based on the fluid model CASTOR [10]. In order for the two curves to match, the standard equilibrium reconstruction has to be modified, namely the central part of the safety factor profile and the edge portion of the density profile [11].

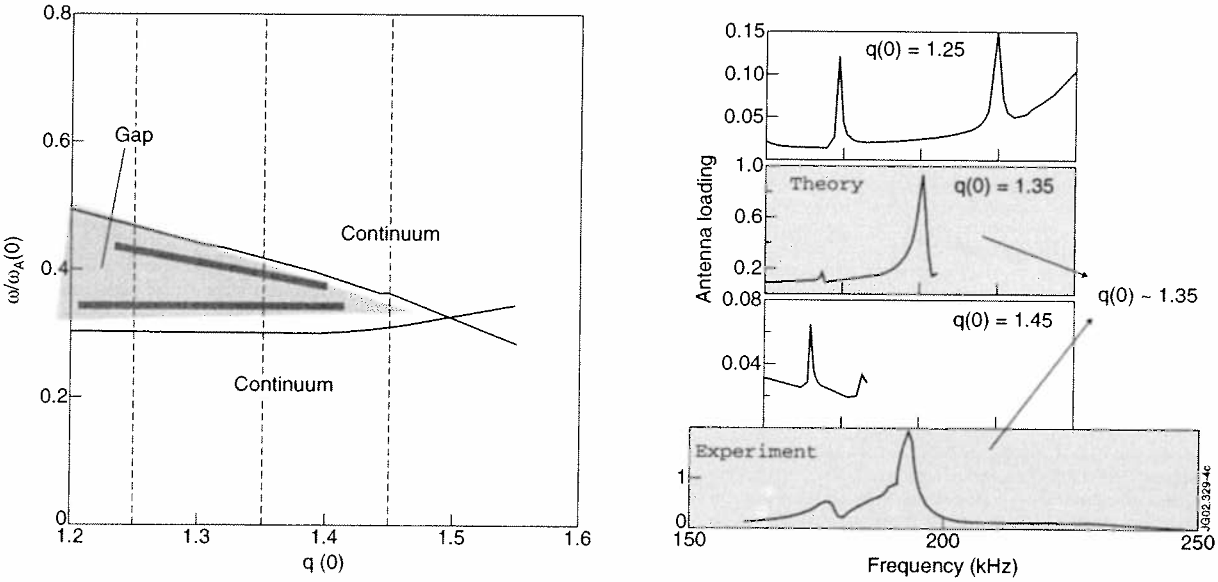

Figure 4 Comparison of data and fluid theory results on the antenna loading for a case in which two core-localized n=1 TAEs are present on the gap [11]. The dependence of the gap width and mode frequency on q(0) is shown on the left, while the adjustment of q(0) to obtain a good fit of the data appears on the right; the calculated and measured spectrum is plotted on the same frequency axis in terms of the antenna loading, i.e. the power absorbed in the plasma per period of the driving frequency, and of the amplitude of the magnetic perturbation at the plasma edge, respectively.

When more than one core localized TAE exist for a given mode number, the frequency separation of the modes is related to the width of the Alfvén gap in the core. As this depends on the value of q at the plasma center, as shown in Figure 4 (left), the comparison of the measured antenna driven spectrum with that calculated from fluid theory leads to a good estimate of the value of q(0). This is demonstrated in Figure 4 (right), which shows on the same frequency axis the calculated and measured mode spectrum in terms of the antenna loading, i.e. the power absorbed in the plasma per period of the driving frequency, and of the magnitude of the magnetic perturbation at the plasma edge, respectively.

The accuracy of this method can be rather good, up to ±10% for q(0), but it depends critically on the quality of the initial guess for the equilibrium and requires a laborious comparison between the data and the results of numerical codes. As the frequency range that the antenna has to cover to measure the continuum plasma response and/or several modes in the gap is rather large, the intrinsic time resolution is limited to no less than 100-200 ms.

3.2 Dynamic q-profile: determination of q_{min} from Alfvén Cascades

In advanced scenarios it is important to obtain information on the time evolution of the safety factor profile. Details of q(r,t) are in fact related to the creation of regions in the plasma core within which the turbulence-induced transport can be significantly reduced, improving the plasma performance [12]. Passive MHD spectroscopy on modes that are excited by ICRH can be used to this purpose.

The experimental observations indicate that in the presence of a non-monotonic q-profile, generated by Lower Hybrid current drive in the pre-heating phase of the discharge, a new class of Alfvén waves is driven by ICRH [13,14]. As their existence, in addition to their drive, is associated with supra-thermal ion populations, these modes belong to the general class of Energetic Particle Modes (EPM) [15, 16]; owing to their fast frequency sweep in time, those observed in the JET reversed shear discharges are named Alfvén Cascades (ACs) [16].

Each cascade consists of several modes with different toroidal mode numbers, typically from n=1 to n=6. The different frequencies are subject to upward sweeping, starting from 20 to 60 kHz, below the TAE gap, and increasing up to the frequency of the TAE gap. The rate of increase in the frequency is proportional to the mode number, as apparent from Figure 5 (right), where a typical sequence of cascades is shown in terms of the measured toroidal mode numbers as a function of frequency and time.

The AC frequency sweeping shows a very close correlation with the time evolution of the local extremum, or *tip* of the Alfvén continuum, where $df_A/dr=0$, which in turn is associated with the minimum of the q-profile, q_{min}. This suggests that the observations correspond to a new type of EPMs found theoretically just above the *tip* of continuum, localized at the radial position of q_{min}, with an eigenfrequency given by [17]

$$f_{AC}(t) \simeq \left| \frac{m}{q_{\min}(t)} - n \right| \cdot \frac{v_A(t)}{R_0} + \delta f\left(\beta_{hot}, \frac{d^2 q}{dr^2} \right) + \Delta f \; . \tag{3}$$

Here Δf is a fixed offset and δf is a small deviation of the cascade frequency from the Alfvén continuum, depending on the fast ion pressure and the second derivative of q(r) at the point of zero magnetic shear. The finite value of δf allows ACs to avoid strong continuum damping.

Modes of different n satisfy the condition $m-nq_{min}=0$ at different times at which q_{min} passes different rational magnetic surfaces. Thus, the observation of the cascade frequencies provides information on $q_{min}(t)$. For example, the n=1 rational surfaces occur when q_{min} passes integer values 1, 2, 3...; the n=2 rational surfaces occur when q_{min} passes integer and half-integer values 1, 3/2, 2, 5/2..., and so on.

Figure 5 illustrates this principle in a JET discharge with deeply reversed q-profile due to LH pre-heating. The Alfvén continuum structure for n=1 is shown on the left for different times corresponding to the evolution of the value of q_{min}. The curves labeled 1 through 8 on the figure are also identified by the values of q_{min} indicated on the plot, from 3 to 2.5 The arrows indicate the correlation with the observed n=1 AC frequency evolution. At the point where the AC frequencies tend to cross their minimum value, for example around t=43.7, we can infer that q_{min} passes an integer value. A single equilibrium reconstruction, performed including data from the motional Stark effect diagnostics for t=47s, is sufficient to determine which value of q_{min} is crossed at that time ($q_{min}=3$), as well as at the subsequent ones, as indicated. The accuracy with which the value of q_{min} is determined at a precise time is very high and provides a novel tool to investigate the dynamics of the creation of internal transport barriers (ITBs), as ITB triggering events are often associated with integer q_{min} surfaces.

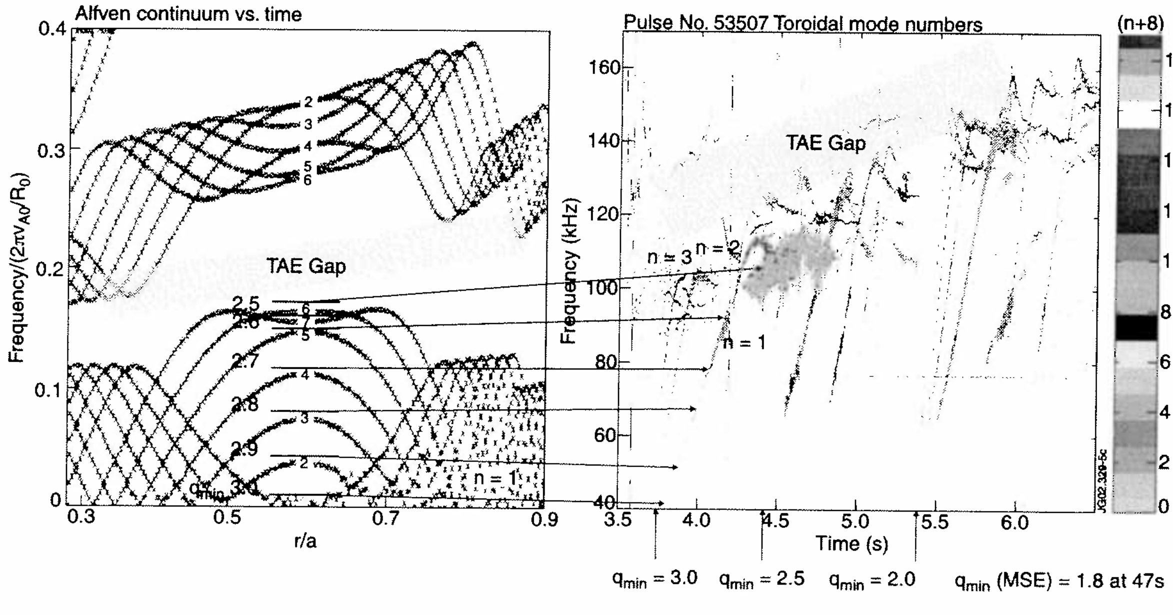

Figure 5 Correspondence between the evolution of the Alfvén continuum and the appearance of Alfvén Cascades of different toroidal mode numbers driven by ICRH ions in JET advanced scenarios with non-monotonic q-profile. The exact time of the crossing of the q_{min} rational values can be determined with great accuracy.

3.3 Plasma mass determination from active AE measurements

The square root dependence on the plasma mass has suggested since the early experiments on Alfvén waves in tokamaks the diagnostic potential of the AE frequency measurements for determining the plasma isotopic mix [18]. Local measurements of Global AEs, existing just below a local minimum of the Alfvén continuum in the plasma core, were proposed [19]. After the discovery of new classes of AEs, including TAEs and EAEs, the same principle was further investigated [20] and tested on the JET D-T plasmas. An example of the results is shown in Figure 6, where the measurement of the plasma effective mass, i.e. the D/T ratio, is performed in a series of discharges with similar equilibrium characteristics [21]. In this case direct estimates can be obtained purely from experimental measurements. Focusing on relative changes of the ion mass, we can neglect the contribution from impurities and obtain [22]

$$n_T/(n_D + n_T) = A_{eff} - 2 \tag{4}$$

$$n_T/(n_D + n_T) = 2\,[\,(f_{TAE}^{\;D\text{-}D}\,K(n)\,/\,f_{measured})^2 - 1] \tag{5}$$

$f_{TAE}^{D\text{-}D}$ is calculated from the average density $<n_e>$, $q=1.5$ and $A_{eff}=2$; $K(n)$ is a calibration factor obtained from similar D-D shots, accounting for the difference between the actual density and q values at the TAE location, $n_e(r_{TAE})$ $q(r_{TAE})$, and $<n_e>$ and $q=1.5$. Figure 6 suggests a good agreement with edge spectroscopic measurements for two discharges with different D/T relative concentrations, although with a somewhat different time evolution. This method may be useful in a reactor, where the same plasma configuration will repeatedly be employed.

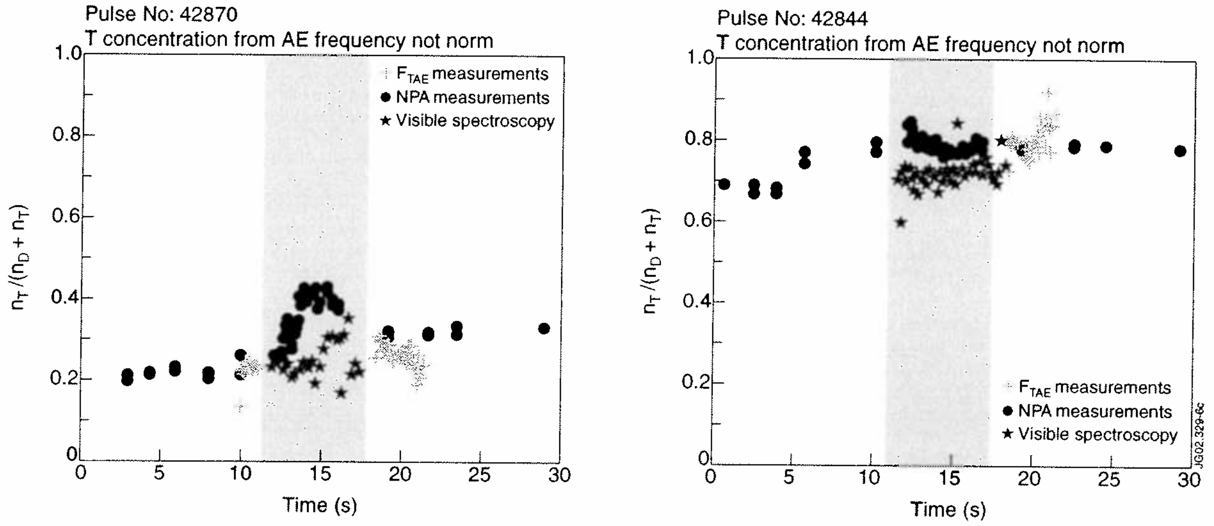

Figure 6 Estimate of D-T ratio from the measured frequency of an externally excited n = 1 TAE compared with visible spectroscopic data (intensity ratio of T_α to D_α lines) and with results from the neutral particle analyzer [5].

Direct measurements are possible in real time for similar equilibria, with a time resolution of the order of 30 ms, the time needed to scan across a resonance. Spatially, we can consider that the measurement is averaged over the global mode structure, encompassing the core region, to which conventional spectroscopic methods are not sensitive. The overall accuracy depends on the reproducibility of the equilibrium. When the equilibrium is significantly varied from shot to shot along with the isotopic mix, one must rely upon a full theoretical analysis, losing the real time capability.

The new multiple antenna system discussed above (see Fig.3), which will be able to drive higher n harmonics, could enable us to perform tracking of individual resonances throughout plasma discharges, possibly including the divertor phase. The possibility of following more than one toroidal harmonic at a time will also be explored, to strengthen the constraint on the mass determination and correct for the Doppler shift due to plasma toroidal rotation in the high performance phase of the discharges.

4. From AE stability to fast particle properties

As shown in Eq. (2), two conditions must be satisfied for AE instabilities to exist: fast particles must resonate in their motion with the phase velocity of the wave, and the free energy source for the instability, their radial pressure gradient, must be sufficiently strong. In this Section we will illustrate examples of how the observation of unstable AEs can provide information on the fast ion energy content and their pressure gradient. The fast ions are produced by ICRH in JET conventional scenarios. In the case of H-minority heating in D plasmas, for a relative concentration of H of less than 10%, an ICRH power of 5 MW, corresponding to about $1W/cm^3$, produces a H^+ tail up to at least 0.5MeV, as calculated by the PION code [23].

4.1 Fast particle energy tail

In addition to the ICRH power, a factor determining the creation of a tail in the H^+ distribution in D plasmas is the H/D relative concentration. For a given ICRH scenario, the AE stability limits therefore depend on this value. To illustrate this, we show in Figure 7 a discharge in which the plasma equilibrium is maintained stationary, with a fully relaxed current profile.

The ICRH power is kept above a level of 8MW, but the H/D ratio is varied. The measured H/D ratio is shown at the bottom, while the top shows a detail of the magnetic spectrogram, corresponding to the TAE gap. When the H/D concentration ratio exceeds the value of about 13%, as measured at the plasma edge by optical spectroscopy, the ICRH-driven AE instabilities disappear, indicating that the ion tail does not reach resonant energies. Based purely on experimental observations, we can establish a link between H/D ratio and tail energy content; as the H/D ratio exceeds 13%, the number of fast ions with energies in the MeV range, resonating with the AEs, is significantly reduced. Such reduction is confirmed by NPA data.

A second example comes from experiments in which third harmonic ICRH heating of He^4 in He^4 plasmas is used to create high-energy tails of α-particles, of interest for investigating the physics of burning plasmas in present devices [24]. The use of third harmonic is needed as the absorption at the fundamental would be too small, and at the second and the fourth harmonics would be too strongly affected by residual H-amounts in the vessel. As the absorption at $f=3f_{ci}$ is a finite Larmor radius effect, ions with a relatively large initial energy must be created by NBI injection. The measurements reported in Figure 8 show that an important difference exist between NBI ions at 70 keV and at 120 keV. In the lower energy case the absorption is much weaker. Effects typically associated with fast particle tail in the plasma core, such as strong electron heating and stabilization of sawteeth, are observed only in the higher energy case.

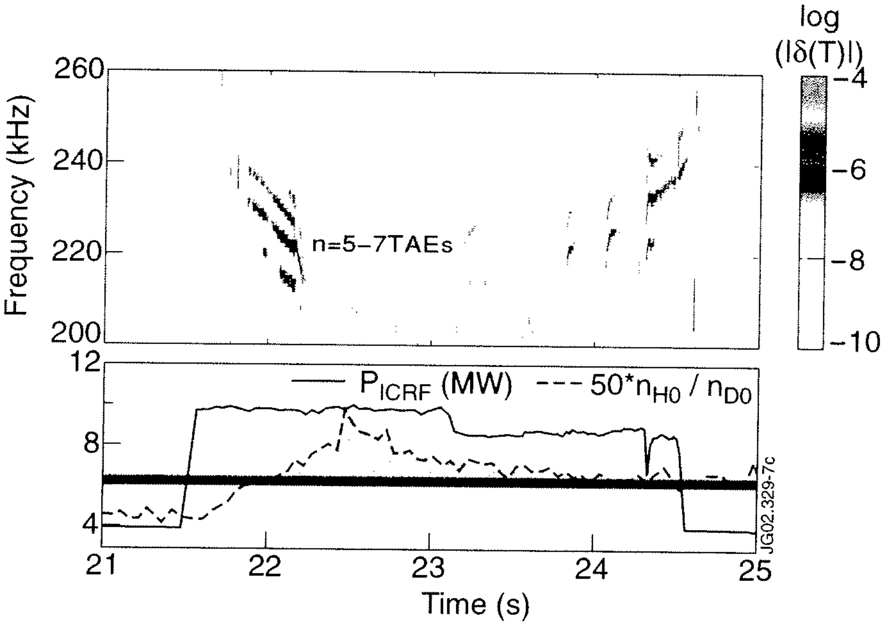

Figure 7 Suppression of the AE instability driven by ICRH power by the increase in the H minority concentration. This result shows that the AE stability limits can be used to infer in this case the tail ion energy content.

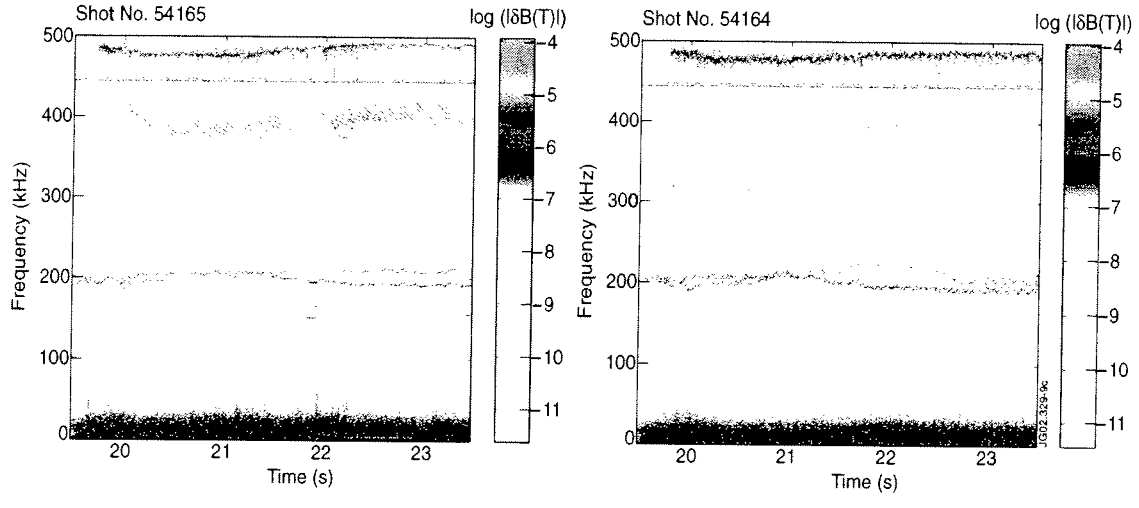

Figure 8 Comparison of magnetic spectrograms from two similar discharges with f ≈ $3f_{ci}(^4He)$ ICRH, one with 120 keV, relatively low density and $\rho_{beam}\sim$ 2.2cm (left), and the other with 70 keV beams, higher density and $\rho_{beam}\sim$ 1.4cm (right). Only the higher energy case shows TAE and EAE instabilities in the 150-200kHz and 360-420kHz ranges, signature of the production of α-tails in the MeV range [24].

The measured unstable AEs shown in Figure 8, the first α-driven AEs observed on JET, indicate that only in the case of 120 keV NBI α's reach energies in the MeV range. Note that, due to a larger value of the ratio v_A/v_{thi}, the ion Landau damping is reduced and AE collective effects are easier to observe than in equivalent D-T plasmas. In the neutron-free He^4 plasma, this result can be confirmed by γ-rays spectroscopy of threshold nuclear reaction $^9Be(\alpha, n\gamma)^{12}C$ [25], which suggests the presence of ^4He ions in the energy range 2 MeV. The scenario of third harmonic ICRH on He^4 plasma heated by 120keV NBI is therefore suitable to produce significant α-particle tails in JET [24].

4.2 Fast particle pressure gradient

The possibility of obtaining information on the static fast particle pressure gradient has been illustrated in a number of past experiments on JET. It has been shown for example that due to the sign of the destabilizing term for AEs, appearing in Eq. (2), the presence of unstable negative mode numbers reveals the existence of a non-monotonic fast particle profile [26]. It has also been demonstrated experimentally that unstable AEs could be associated with a phasing of ICRH antennas that would produce an inward fast particle pinch, while no AEs were observed in the opposite case [27]. Here we show that such information can also be related to the dynamical evolution of the fast particle pressure gradient. We consider a case in which the current profile is monotonic and completely relaxed, with central q values just below unity, producing regular sawteeth events. TAEs and EAEs are driven unstable by 8MW of ICRH power, with a H/D relative concentration of about 10%.

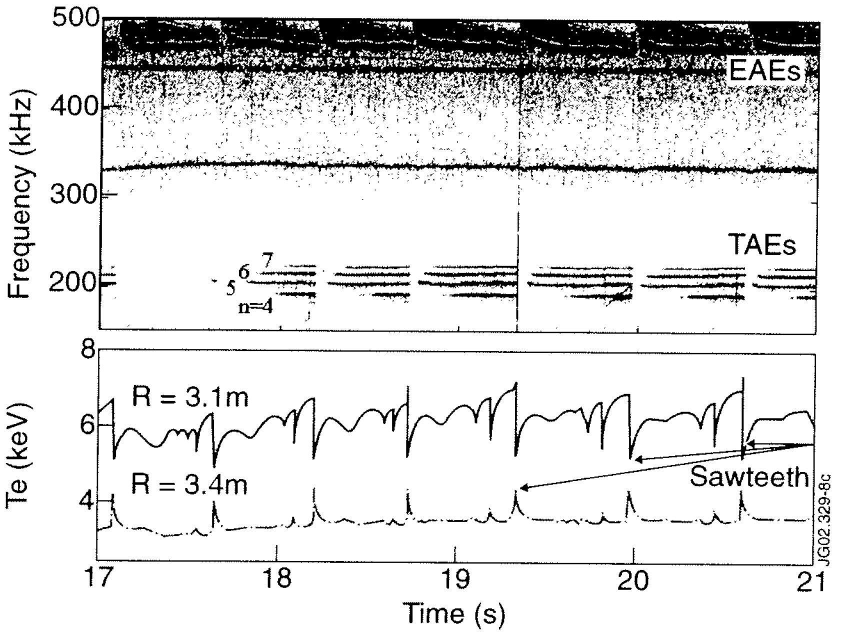

Figure 9 Effect of saw tooth crashes on the TAE and EAE stability in the presence of H-minority heating ICRH, with P_{ICRH}~8MW, and H/D~10%.

We note that at each saw-tooth crash, the TAE instability disappears for a short period of time (Figure 9). This time interval is of the order of 100ms, shorter than the slowing down time for ~0.5MeV ions. It is therefore related to a rapid radial redistribution of fast ions associated with each saw tooth crash. The amplitude of the EAE instabilities is not affected significantly. This is due to the fact that for the equilibrium of the discharge under consideration, the TAE mode structure is core localized, peaking around r/a~0.3, while the EAE peaks at a larger radial position, around r/a~0.45, as reconstructed from the MISHKA MHD code [28]. Such an argument is supported by the fact that the Doppler shift of different toroidal harmonics, visible in the spectrogram, is larger for TAEs than for EAEs, corresponding to regions of strong and weak toroidal rotation, respectively. Note that the EAE frequency is affected by a sudden variation in the density and possibly in the local value of q [29].

4.3 Fast particle phase space local diffusion

A piece of information that the study of the AE spectrum can bring, which is inaccessible to any other diagnostic method, is the effective collision frequency in the phase space for particles resonating with the AEs [30]. This can be extracted from a detailed comparison of the AE spectra in the nonlinear phase of their evolution with the results of a general theory based on a model equation for the AE amplitude evolution A(t) [31]:

$$\exp(-i\phi)\frac{dA}{dt}=\frac{\gamma}{\cos\phi}A-\frac{\gamma_L}{2}\int_0^{t/2}\tau^2 d\tau\int_0^{t-2\tau}d\tau_1\exp\left[-\nu_{eff}^3\tau^2(2\tau/3+\tau_1)\right]A(t-\tau)A(t-\tau-\tau_1)A^*(t-2\tau-\tau_1) \tag{6}$$

The amplitude evolution, and in particular the nonlinear regime that A(t) falls into, is determined by a competition between the mode growth from the net drive (γ) and the replenishment of the distribution function in the region of the resonance with the mode. The latter mechanism is quantified by ν_{eff}, the effective collision frequency for the particles that resonate with the mode. All regimes predicted from Eq. (6) have been observed at JET for ICRH driven AEs in conventional and advanced scenarios of plasma operation [32,33]. For the case of transition to a limit cycle behavior, quantitative estimates of γ and ν_{eff} are obtained. Considering the example of a n=7 TAE, we find that the value of γ (~8.5×10^3 s^{-1}) is in agreement with the expectations from the linear stability theory and with the direct measurements of damping and fast particle drive using active MHD spectroscopy. The measured ν_{eff} (1.75×10^4 s^{-1}), on the other hand, is too large to be explained by classical collisions, and is suggestive of a direct effect of the ICRH power on the energetic particles. These estimates open the way to an evaluation of phase space transport for fusion-produced α's, important for plasmas on their way to ignition.

5. Conclusions and further developments

The investigation of the properties of collective modes in magnetized plasmas is used to extract information on the plasma from the measurement of the modes. Alfvén waves are the collective modes with the largest diagnostic potential both for the plasma bulk and the energetic particle population, as their frequency range is essentially free of incoherent fluctuations, waves can be exempt from strong damping, and non-perturbative, small amplitudes modes can be detected.

Active and passive MHD spectroscopy, based on external antenna excitation and fast particle intrinsic drive, have been used to reveal a number of properties of the JET plasmas. Plasma bulk characteristics are extracted from the mode frequency. The examples discussed herein include equilibrium quantities, such as q(r) in the plasma core and $n_e(r)$ at the edge, and the fast evolution of the minimum value of the q-profile in advanced scenarios with non-monotonic q profile. The plasma effective mass can also be extracted form the frequency of externally driven modes; for reproducible plasma equilibria, such information can be available in real time during a discharge. Information on fast ion energies and pressure gradients, including their dynamical evolution, can be obtained by observing the AE stability limits. The nonlinear development of AEs, if compared with fundamental nonlinear theory, can also provide information on the phase space dynamics of fast particles.

In principle, both active and passive spectroscopy can be employed in next step devices, such as ITER. The passive method of observing intrinsically unstable modes will benefit from the recent developments in fast data acquisition and storage and from the fact that in ITER or other plasmas with significant production of α's by fusion reaction, AEs of benign nature are expected to be present in most plasma conditions. The active method would necessitate an antenna structure able to drive low amplitude modes in the range 10-1000kHz, perhaps making use of in-vessel components having a different main application, such as ICRH antennas. To test the possibility of driving intermediate toroidal mode numbers in the plasma core throughout plasma discharges using a small in-vessel structure, and the active MHD diagnostic potential for future experiments such as ITER, a new AE antenna for JET is being designed.

Use of MHD spectroscopy is not limited to fusion and laboratory plasmas. MHD waves are predicted to exist in a number of astrophysical plasmas, such as accretion disks [34] or coronal loops. For example, recent theoretical developments indicate that AEs induced by the density stratification along the loop can exist in coronal loops [35]. Remote observation of the properties of these modes could be used to extract information on the plasma local parameters.

This work was partly conducted under the European Fusion Development Agreement and some of the experiments were carried out within a JET-CRPP Task Agreement and within a JET-MIT collaboration supported by DoE Contract DE-FG02-99ER5-456.

References

[1] J.P.Goedbloed et al., *Plasma Phys. Controlled Fusion* **35**, B277 (1994).
[2] C.Z.Cheng, L.Chen and M.S.Chance, *Ann. Phys.* (New York) **161**, 21 (1985).
[3] K.L.Wong, *Plasma Phys. Contr. Fusion* **41**, R1 (1999).
[4] R.F.Heeter, A.Fasoli, S.Ali-Arshad and J.M.Moret, *Rev. of Sci. Instrum.* **71**, 4092 (2000).
[5] A.Fasoli et al., *Plasma Phys.Contr.Fusion* **39**, B287 (1997).
[6] A.Fasoli et al., *Phys. Rev. Lett.* **75**, 645 (1995).
[7] A.Jaun, et al., *Plasma Phys. Contr. Fusion* **43**, A207 (2001).
[8] D.Testa et al., *Phys. Plasmas* **9**, 243 (2002).
[9] A. Fasoli et al., *Phys. Rev. Lett.* **81**, 5564 (1998).
[10] G.T.A.Huysmans et al., *Phys. Plasmas* **2**, 1605 (1995).
[11] H.Holties, A.Fasoli, J.P.Goedbloed, *Phys. Plasmas* **4**, 709 (1997).
[12] C.Gormezano et al., *Phys. Rev. Lett.* **80**, 5544 (1998).
[13] S.Sharapov et al., *Phys. Lett. A* **289**, 127 (2001).
[14] H.Kimura et al., *Nucl. Fusion* **38**, 1303 (1998).
[15] F.Zonca et al., *submitted to PoP* (2002).
[16] H.L.Berk et al., *Phys. Rev. Lett.* **87**, 185002 (2001).
[17] S.Sharapov et al., *Phys. Plasmas* **9**, (2002).
[18] G.A.Collins et al., *Plasma Phys. Contr. Fusion* **29**, 323 (1987).
[19] P.Descamps et al., *Phys. Lett A* **143**, 311 (1990)
[20] J.B.Lister, L.Villard and G.de Ridder, *Plasma Phys. Contr. Fusion* **40**, 1635 (1998).
[21] P.R.Thomas et al., *Phys. Rev. Lett.* **80**, 5548 (1998).
[22] A.Fasoli et al., *Physics of Plasmas* **7**, 1816 (2000).
[23] L.-G.Eriksson, T.Hellsten and U.Willen, *Nucl. Fus.* **33**, 1037 (1993).
[24] M.J.Mantsinen et al., *Phys. Rev. Lett.* **88**, 105002 (2002).
[25] V.G.Kiptily, *Fusion Technol.*, **18**, 583 (1990).
[26] R.F.Heeter, *Ph.D. Thesis*, Princeton University (1999).
[27] L.Ericksson et al., *Phys. Rev. Lett.* **81**, 1231 (1998).
[28] S.Sharapov et al., *Nucl. Fusion* **39**, 373 (1999).
[29] M.Saigusa et al., *Plasma Phys. Control. Fusion* **40**, 1647 (1998).
[30] R.F.Heeter, A.Fasoli, S.Sharapov, D.Testa, submitted for publication on *Phys. Plasmas* (2002)
[31] H.Berk, B.N.Breizman and M.S.Pekker, *Plasma Phys. Rep.* **23**, 778 (1997).
[32] A.Fasoli et al., *Phys. Rev. Lett.* **81**, 5564 (1998).
[33] R.F.Heeter, A.Fasoli and S.Sharapov, *Phys. Rev. Lett.* **85**, 3177 (2000).
[34] R. Keppens, F. Casse and J.P. Goedbloed, *Astrophys. J. Letters* **569**, L121 (2002).
[35] A.J.C.Beliën, S. Poedts and J.P. Goedbloed, *Phys. Rev Lett.* **76**, 567 (1996).

ECH physics and new operational regimes on TCV

J.-M. Moret, S.M. Ahmed, S. Alberti, Y. Andrebe, K. Appert, G. Arnoux, R. Behn, P. Blanchard, P. Bosshard, Y. Camenen, R. Chavan, S. Coda, I. Condrea, A. Degeling, B.P. Duval, D. Fasel, A. Fasoli, J.-Y. Favez, T. Goodman, M. Henderson, F. Hofmann, J.-P. Hogge, J. Horacek, P. Isoz, B. Joye, A. Karpushov, I. Klimanov, J.B. Lister, X. Llobet, T. Madeira, J.-C. Magnin, A. Manini, B. Marlétaz, P. Marmillod, Y. Martin, A. Martynov, J.-M. Mayor, J. Mlynar, E. Nelson-Melby, P. Nikkola, P.J. Paris, A. Perez, Y. Peysson*, R.A. Pitts, A. Pochelon, L. Porte, O. Sauter, A. Scarabosio, E. Scavino, S.-H. Seo, U. Siravo, A. Sushkov**, G. Tonetti, M.Q. Tran, H. Weisen, M. Wischmeier, A. Zabolotsky, G. Zhuang

Centre de Recherches en Physique des Plasmas
Association EURATOM-Confédération Suisse, EPFL, 1015 Lausanne, Switzerland

**Département de Recherches sur la Fusion Contrôlée, Association EURATOM-CEA*
CEA-Cadarache, 13108 St Paul-lez-Durance, France

***Russian Research Centre Kurchatov Institute*
123182 Moscow, Russian Federation

The physics of tokamak plasmas, in which electrons are heated by electron cyclotron heating (ECH) and whose current is driven by electron cyclotron current drive (ECCD), is investigated in this paper together with applications on TCV (Tokamak à Configuration Variable) using modifications of the pressure and current profiles to improve the operational regimes. In order to explain the experimentally determined current drive efficiency and hard X-ray and electron cyclotron emission measurements, it is shown that quasi-linear effects and radial transport of the suprathermal electrons are necessary. Plasmas with fully non-inductively driven currents were obtained with 0.9MW of off-axis ECCD and 0.45MW of on-axis counter ECCD. The combination of the driven current and the bootstrap current, accounting for 50% of the total current and peaking off-axis, yields a reversed safety factor profile and a wide and stable electron internal transport barrier. This barrier leads to an enhancement in the energy confinement by a factor of 4.5. ECH is also used to broaden the current profile of high elongation, low normalised-current plasmas whose vertical position would otherwise be uncontrollable on TCV, but whose MHD stability properties should allow high β values. Elongation of 2.47 at a normalised-current of 1.05MA/mT is obtained with off-axis ECH absorbed at an optimised normalised radius between 0.55 and 0.7. Finally, third harmonic ECH

is tested in various scenarios, all using vertical beam launching. In particular high density ohmic target and preheating with second harmonic ECH are presented. The fraction of third harmonic power absorbed reaches 65% and 85% respectively.

Introduction

The flexibility in the configuration of the TCV plasmas is complemented by an electron cyclotron heating (ECH) and current drive (ECCD) system with a power capability of 4.5MW and an adaptable launching geometry. This makes TCV a unique tool for investigating advanced scenarios potentially relevant to burning reactor plasmas in which electron α-heating is dominant and does not supply direct momentum input. In these advanced modes of operation the interplay between the safety factor profile and the electron transport and the complementarity of the bootstrap and driven current require tailoring of the pressure profile and the current distribution through localised heating and current drive.

When ECH and ECCD are used for this purpose, these mechanisms strongly depend on the suprathermal electron dynamics. The electron distribution function has been extensively studied on TCV, using a hard X-ray camera [1] and a high field side electron cyclotron emission radiometer [2], and modelled with a quasi linear Fokker-Planck code which includes radial particle transport. The latter has been found necessary to correctly determine the driven current profile and current drive efficiency [3].

Fully non inductive plasma currents of 90kA have been sustained on TCV using a combination of central ECH and off-axis ECCD [4] with a total power of 1.35MW. This yields a regime with a wide and steep internal electron transport barrier and a bootstrap current fraction of over 50%. This fraction can be increased to $80\% \pm 10\%$ by injecting 2.2MW of EC power at higher plasma densities. The energy confinement time increases with central heating power, reaching 4.5 times the Rebut-Lallia-Watkins (RLW) scaling law prediction[19]. The time evolution of the electron temperature in different heating schemes shows that the creation of the transport barrier is related to modifications in the current profile, and that the barrier can be sustained at the same position for periods considerably longer than the energy confinement time and even the current redistribution time. Calculation of the current components yields a hollow current profile and a reversed safety factor profile with a minimum value at the barrier location.

The quest for high β plasmas around the optimal value of the elongation, $\kappa = 2.4$, and a normalised current $I_N \cong 2$ has motivated the development of high elongation, low current (300kA) configurations [5]. Here, off axis ECH is used to broaden the current profile during plasma elongation to improve the vertical stability. By tuning the launching geometry, it was possible to create plasmas with an overdense central density ($6\times10^{19}m^{-3}$) that can be heated with vertically launched third harmonic X-mode ECH (X3-ECH).

TCV has up to 1.5MW of ECH power at the third harmonic of the electron cyclotron frequency, whose higher cut off extends the density range up to $10^{20}m^{-3}$, giving access to higher β plasmas and H-mode regimes. Heating schemes include low field, lateral and vertical launching possibilities. The absorption is found to be strongly sensitive to the launching geometry and is enhanced in the presence of a suprathermal electrons which are created by second harmonic ECCD [7]. Scenarios that maximise the X3-ECH absorption were tested, in particular using a vertical beam to increase the path length, an optimised launching angle, high density and preheating with second harmonic X-mode ECH (X2-ECH). On an ohmic target with central density of $4.5\times10^{19}m^{-3}$ single-pass absorption as high as 65% was achieved. Using X2-ECH preheating, the fraction of X3-ECH power absorbed reaches ~85%, and X3-ECH alone was able to maintain the energy content of the plasma, even at densities well above the second harmonic cut off. This opens the possibility to heat high density plasmas with ECH.

After a brief presentation of the TCV tokamak and the ECH heating system, each of these topics will be developed, namely ECCD modelling, fully driven plasmas with off-axis ECCD, high elongation plasmas with off-axis ECH and X3-ECH heating.

The TCV tokamak and its ECH system

TCV has the following main parameters: major radius, 0.88m, minor radius, 0.25m, axial magnetic field, 1.5T, maximum plasma current, 1MA, maximum elongation, 2.8 [8]. Its shaping system consists of 16 independently controlled shaping coils. A high aspect rectangular vessel equipped with fast internal coils for vertical position control provide a high elongation capability. This is complemented by an ECH system with an adaptable launching system with real time control. There are 6 gyrotrons at a frequency of 82.7GHz with a unit power of 0.5MW, which correspond to the second harmonic of the electron cyclotron frequency. They are connected to 6 independent lateral launchers [9] with a fast movable mirror that can sweep the beam in real time in a given plane, which can be rotated around its horizontal axis between shots. TCV is also equipped with 3 gyrotrons at 117.8GHz, corresponding to the third harmonic, also with a unit power of 0.5MW [10]. The beams enter the TCV plasma vertically to maximise path length via a mirror that can be tilted poloidally during a plasma discharge and displaced radially between discharges. This combination of flexibility in the plasma shape configuration and powerful additional heating with a highly controllable geometry offers a wide spectrum of ways of tailoring the spatial distribution of plasma parameters to obtain increased performance.

ECCD modelling

Current profile tailoring used to optimise plasma performances in advance scenarios is based on the generation by ECCD of suprathermal electrons. Modelling of the ECCD efficiency and of the driven current profile thus requires a good comprehension of the mechanisms governing the suprathermal electron population. On TCV, fast electrons are diagnosed by a multi-element CdTe hard X-ray (HXR) pinhole camera, on loan from CEA Cadarache, and a high field side (HFS) electron cyclotron emission (ECE) radiometer. The HXR camera is sensitive to bremmstrahlung radiation from which a "photon temperature" can be derived. It features 14 vertical chords each with 8 energy channels in the 10-200keV range [1]. The ECE is a superheterodyne radiometer with 24 frequency channels on a horizontal line of sight [2]. Relativistic downshift of the radiation in the energy in the region of 10keV leads to a displacement of the emitting region towards the HFS, beyond the cold plasma resonance; unlike low field side detection, the radiation then propagates freely to the HFS antenna. Interpretation of the ECE with a bi-Maxwellian model gives an estimation of the temperature and density of the fast electrons [2]. Both diagnostics indicate suprathermal electron temperatures between 10-50keV with densities in the range $1\times10^{17}-6\times10^{18}\mathrm{m}^{-3}$.

The modelling of the electron distribution function is performed with the CQL3D code [11]. This solves the bounce averaged Fokker-Planck equation in perpendicular and parallel velocity space and along the radial dimension, using a relativistic collision operator, quasi-linear wave damping and a radial transport model. The exact experimental flux geometry and ray paths from TORAY-GA [12,13] are used. To use CQL3D in linear mode, the ECCD power is downscaled by a factor 10^{-3} and the computed driven current multiplied by 10^{3}. Such a linear simulation gives a driven current profile limited to the deposition region, comparable to that obtained with TORAY-GA, with a current drive efficiency around 50% of that determined experimentally in zero loop voltage conditions. This can be seen in Figure 1 for an off-axis ECCD fully driven plasma. Here the driven current, estimated by taking into account the bootstrap current, is 40kA for an ECCD power of 0.9MW. The simulation with the real ECCD power and therefore including the quasi-linear effects, yields an overestimation by an order of magnitude as seen in Figure 1. This is due to a built-up of the fast electron population in the absorption region by quasi-linear effects at such a high power density.

To make the model more complete, a radial transport operator is introduced in the Fokker-Planck equation [9,14]:

$$\nabla \cdot \left(D_0 \cdot \frac{1 + 27\rho^3}{n_e / n_{e0}} \cdot h(v_{//}) \cdot \nabla f + V f \right) \tag{1}$$

where the magnitude of the radial diffusion coefficient is given by D_0, combined with a radial profile and a dependence on the parallel velocity $v_{//}$. Two transport models were tested, one with $h(v_{//}) = 1$ corresponding to small scale length electrostatic turbulence, and one with $h(v_{//}) \sim v_{//}$, simulating transport due to long scale length electromagnetic turbulence [15,16]. In both cases D_0 and the convection velocity V were adapted to reproduce the total measured driven current and the density profile, respectively. For both models, the value of the diffusion coefficient for the velocity range of the current carrying electrons is comparable to that commonly observed for anomalous transport, in the range of $2 - 5\,\mathrm{m}^2/\mathrm{s}$. The calculated driven current profiles shown in Figure 1 are similar in both cases, indicating that the calculation does not depend significantly on the transport model.

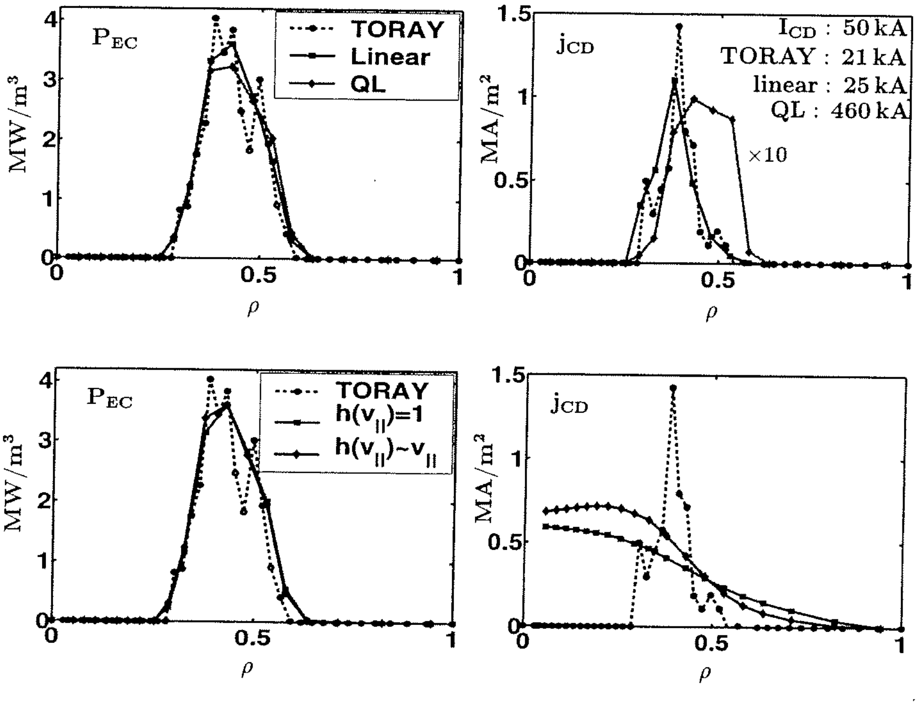

Fig. 1: Simulation of the absorbed power and driven current profiles for off-axis ECCD (#21657). Top: TORAY, CQL3D in linear mode and CQL3D with quasi-linear effects. Bottom: TORAY and CQL3D with two transport models.

The simulation also provides a calculation of the bremsstrahlung spectrum and its associated photon temperature and intensity profile. A comparison with the experimental profiles shows good agreement between the experimental and simulated temperatures, with high photon temperature extending over the entire plasma radius, not localised in the absorption region, as drawn in Figure 2 [1,2].

These results highlight the important role of the radial transport in the fast electron dynamics and in the profile and intensity of the driven current.

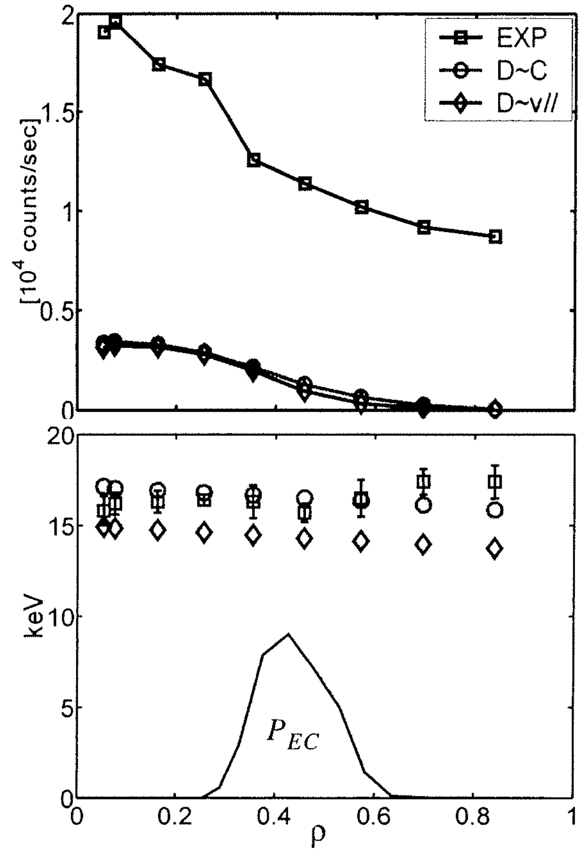

Fig. 2: Profiles of the photon temperature and intensity of the bremsstrahlung during off-axis ECCD (#21657) as measured with the hard X-ray camera and as simulated with CQL3D with two transport models. These are line integrated profiles as a function of the normalised distance from the chord to the magnetic axis.

Fully driven plasmas with off-axis ECCD

Good confinement properties have been previously obtained in TCV by modifying the current and pressure profile with off-axis ECH combined with central counter ECCD, yielding central temperature of 10keV and a confinement enhancement factor, $H_{RLW} = \tau_{Ee}/\tau_{RLW}$, between 3 and 4 [17,18]. Here the experimental electron energy confinement time τ_{Ee} is compared with the Rebut-Lallia-Watkins (RLW) scaling law predictions [19], which was observed to reproduce TCV confinement over a wide range of L-mode regimes [20]. It was argued that this enhanced confinement originated from a reversed central magnetic shear which was limited by peaking of the inductive current due to the increase in central electrical conductivity with temperature. This limitation would disappear in the absence of an inductive electric field and fully non-inductive plasmas are routinely obtained with ECCD in TCV [21,22].

Starting from an improved central electron confinement regime, off-axis ECH is replaced by off-axis co-ECCD with constant currents both in the ohmic transformer and in the shaping coils, ensuring zero loop voltage. The line average electron density is $\bar{n}_e = 0.5\times10^{19}\text{m}^{-3}$ and the elongation $\kappa = 1.6$. Some relevant time traces are drawn in Figure 3. Two EC wave beams absorbed at a normalised radius (square root of normalised volume) of $\rho_{abs} = 0.35$ and 0.47, launched with an angle of $\varphi_T = 23°$ (with respect to the normal to the toroidal field, in the electron drift direction) giving a total power of $P_{EC} = 0.9\text{MW}$. The ECCD power drives a current I_{CD} which attains 70% of the total plasma current, $I_p = 70\text{kA}$, the remaining 30% consisting of 20kA of bootstrap current, I_{BS}, as derived from the experimental pressure profile. The current drive efficiency in this situation, $\eta_{CD} = I_{CD}n_e/P_{EC}$, is three times lower than typical values with central ECCD due the lower temperature and the presence of trapped electrons in the off-axis absorption region. As shown in Figure 4, the electron temperature profile evolves on a resistive time scale (0.2s) from a parabolic shape at the beginning of the ECCD phase to a profile with a steep gradient at a normalised radius $\rho = 0.4$. This is a possible indication of the formation of an electron internal transport barrier (eITB).

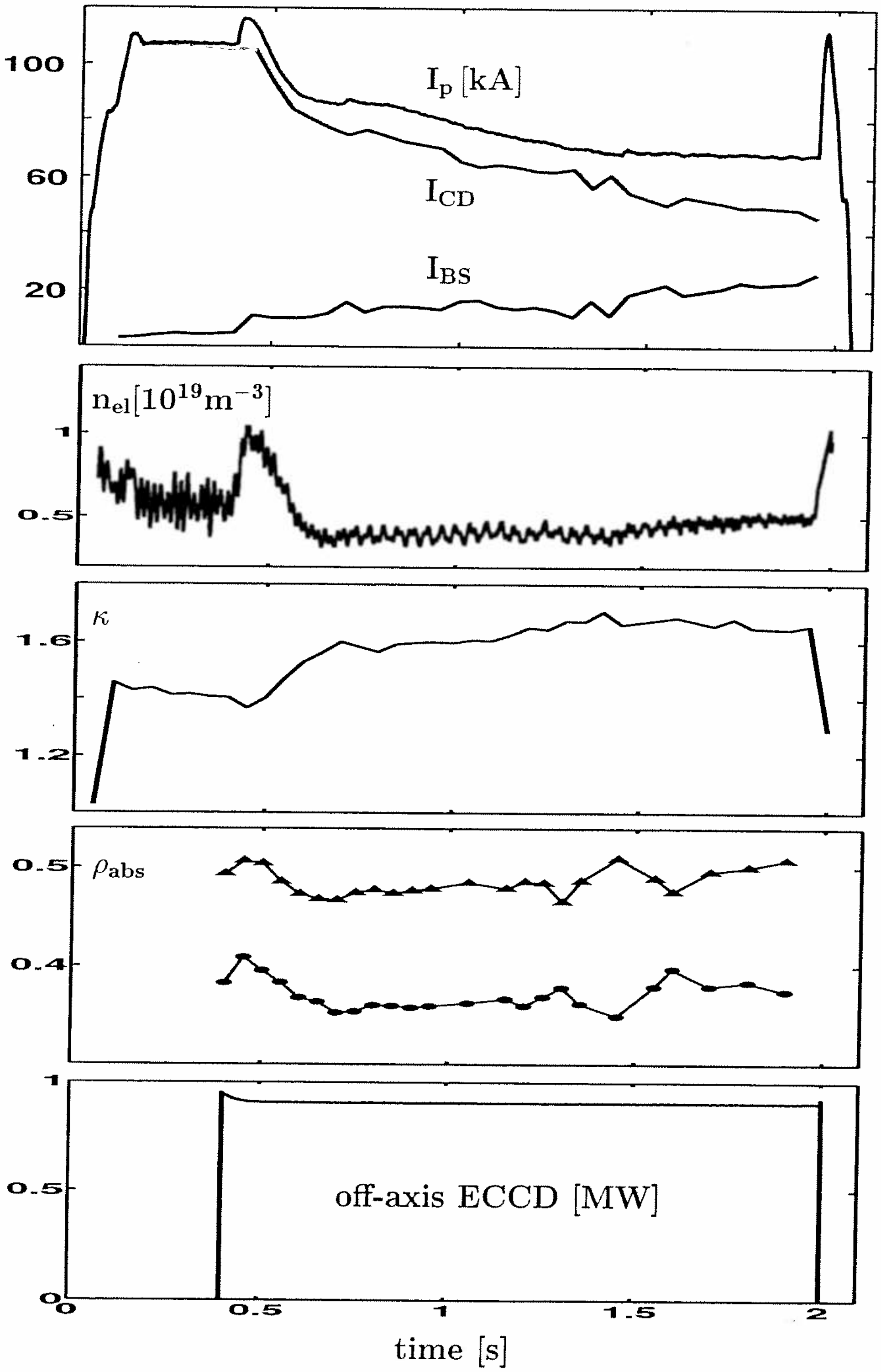

Fig. 3: Time traces for off-axis ECCD in a fully driven plasma (#21657). From top to bottom: total current, bootstrap current and driven current; line average electron density; plasma elongation; power deposition radii§; ECCD power.

To evaluate the confinement properties of this transport barrier, an ECH wave beam of 0.45 MW was added with a central deposition, $\rho_{abs} \leq 0.3$ after the barrier was fully formed. The temperature profile thus obtained are shown in Figure 4. It is similar to the case of off-axis ECCD only, but with a steeper gradient and a higher central energy content. No energy confinement degradation is observed even though the input power has been increased by a factor of 1.5. The confinement enhancement factor H_{RLW} rises from 2 to 3.5, as seen in Figure 5. These observations confirm the formation of an electron internal transport barrier, which remains at $\rho = 0.4$ for over 1 s, i.e. over $500\tau_{Ee}$ or 10 current redistribution periods. To verify that the creation of the eITB is related to a modification of the current profile, the start time of the central ECH relative to that of the off-axis ECCD was varied: as shown in Figure 5, if applied simultaneously, the central electron temperature rapidly reaches an intermediate level and then evolves slowly on a redistribution current time scale to an asymptotic value, while if ECH is applied 0.65 s after the ECCD, the central temperature rises rapidly on a confinement time (1.5 ms) scale from an intermediate level to the same final value.

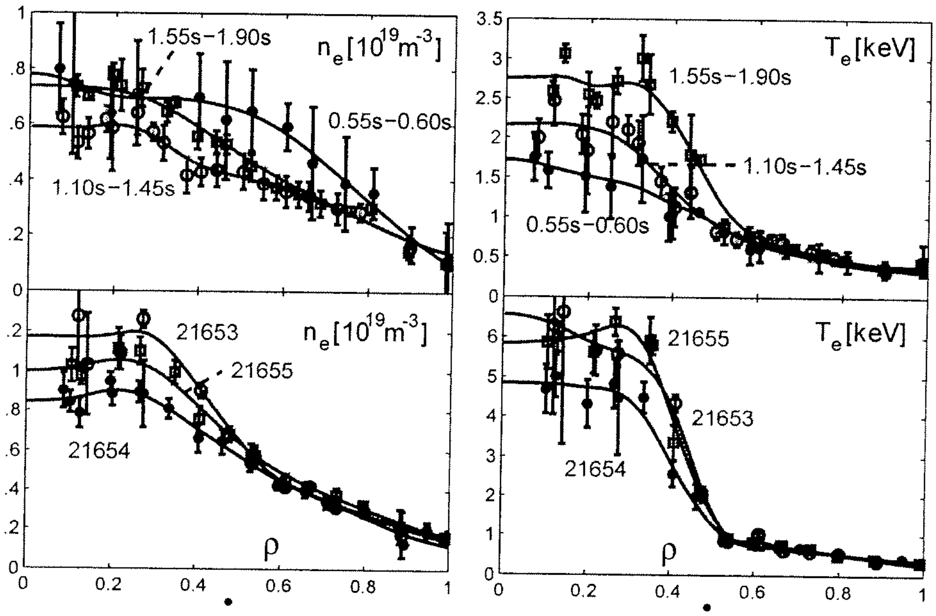

Fig. 4: Electron density and temperature profiles measured by Thomson scattering. Top: off-axis ECCD for three different times (#21657). Bottom: off-axis ECCD combined with central ECH or counter ECCD with varying launching angle φ_T (#21553, #21554, #21555).

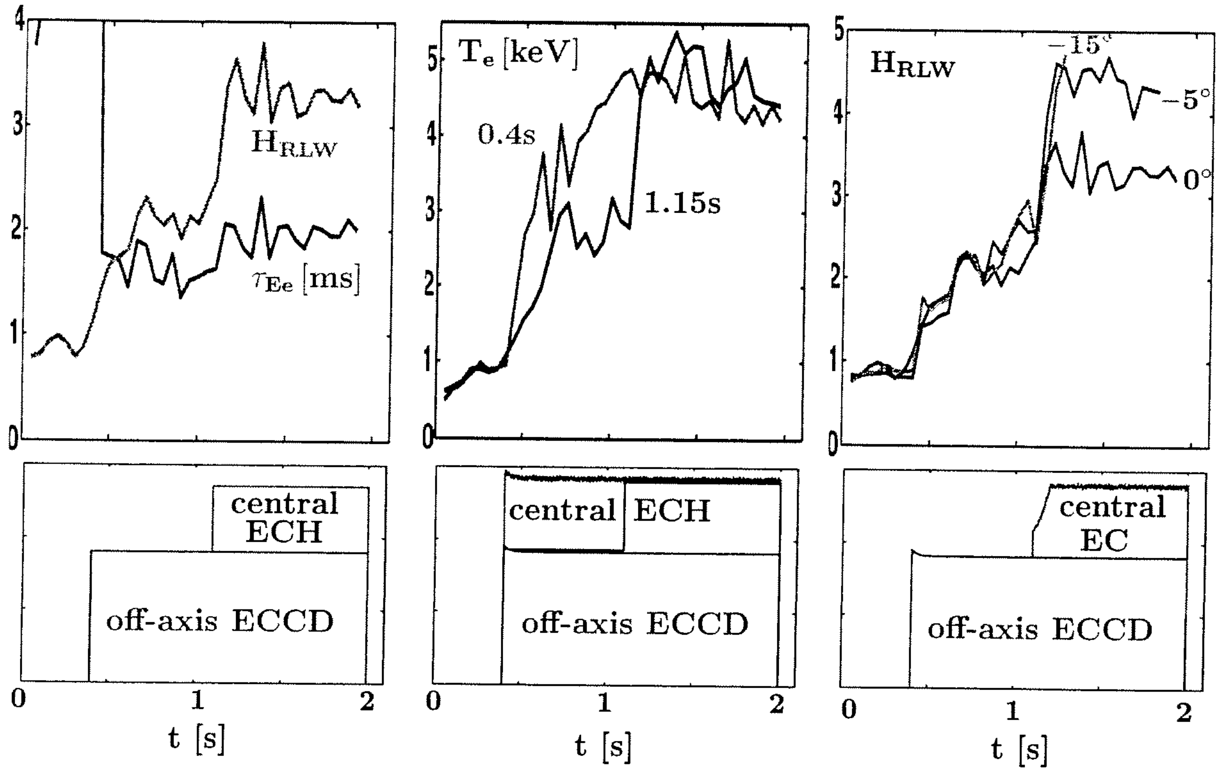

Fig. 5: Time evolution of confinement parameters. Left: confinement enhancement factor and electron energy confinement time for off-axis ECCD combined with central ECH (#21654). Centre: central electron temperature for different starting time of the central ECH with respect to that of off-axis ECCD. Right: confinement enhancement factor for off-axis ECCD combined with central ECH or counter ECCD with varying launching angle φ_T (#21553, #21554, #21555).

Optimisation of the performance in this regime can be achieved by further tuning the current profile with counter central ECCD, going from ECH with $\varphi_T = 0°$ to ECCD at -5° and -15°. In both central ECCD cases a confinement enhancement factor of $H_{RLW} = 4.5$ is obtained, as shown in Figure 5, with a central temperature of 6keV. However, with the largest negative injection angle, the pressure profile becomes over-peaked and MHD unstable, while at -5° a steady state is achieved. In these conditions the bootstrap fraction I_{BS}/I_p increases to ~50%. Working at higher electron density $n_{e0} = 2\times10^{19}\mathrm{m}^{-3}$ decreases the driven current and increases the pressure gradient, increasing the bootstrap current. With a total EC power of 2.2MW, a bootstrap fraction estimated between 75% and 90% was obtained in this way.

The driven current profile j_{CD} was modelled with the Fokker-Planck code CQL3D described above. Due to radial transport of fast electrons, the driven current is not localised in the absorption region but is characterised by a flat profile inside the absorption radius, presented in Figure 6. Combining a bootstrap current that peaks around the pressure gradient associated with the eITB and the driven current profile, a hollow total current profile is obtained. The corresponding safety factor profile is reversed with a minimum value at the barrier location.

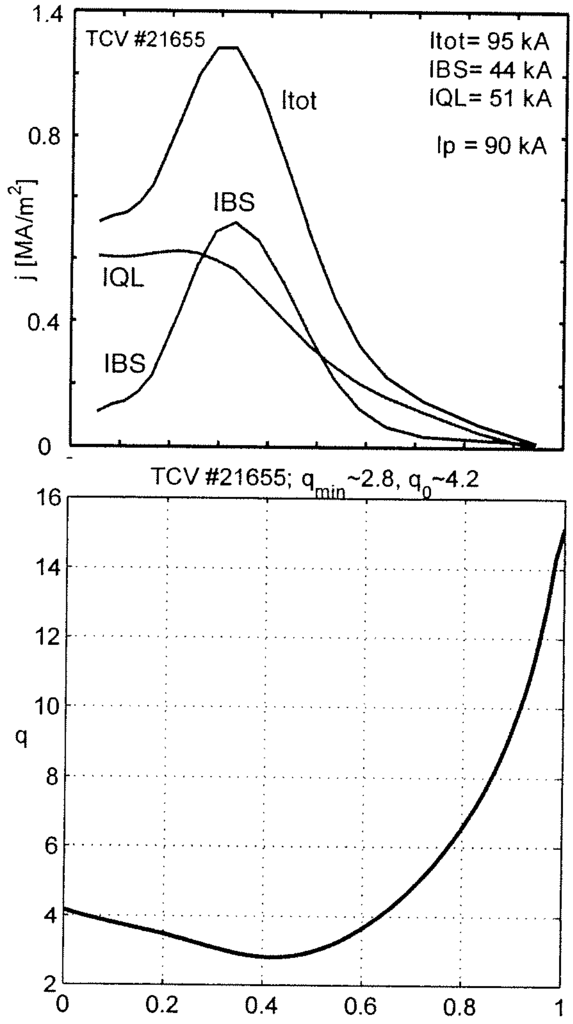

Fig. 6: Radial profiles of the driven current j_{CD}, of the bootstrap current j_{BS}, the total current j_{tot} and the safety factor q for off-axis ECCD combined with central counter ECCD with $\varphi_T = -5°$ (#21655).

High elongation plasmas with off-axis ECH

The main advantage of an elongated plasma cross-section is that, for a given safety factor, the plasma current increases with the elongation κ as $I_p \sim (\kappa^2 + 1)/2$, and according to the Troyon limit, the maximum achievable β is proportional to the normalised current $I_N = I_p/(aB_T)$. MHD stability calculations also suggest that the β limit does indeed increase with elongation, but only up to a limit. For a conventional aspect ratio, $R/a = 3-4$, the optimal elongation lies between 2.2 and 2.4 and the maximum β is attained for intermediate $I_N \cong 2$ [23]. In ohmic conditions, such a high elongation configuration at low current is vertically uncontrollable, even with a well tuned vertical control using fast internal coils, since the natural current profile is too peaked. By broadening the current profile with off-axis ECH, this limitation can be overcome [24].

Off-axis ECH was applied to an ohmic plasma with an elongation of $\kappa = 1.7$, with deposition in the region of $\rho_{abs} > 0.7$; the temperature and consequently the current profile broadened, and the plasma elongated since the quadrupole magnetic field was maintained constant. Figure 7 shows the time evolution of the relevant plasma parameters. The effect of off-axis ECH on current broadening is quantified by the change in the internal inductance normalised to account for the effect of the shape Δl_i^* [5,6]. The most critical parameters are the power level and the power deposition location. Scans of these parameters together with simulations with the transport code PRETOR using RLW model and power deposition from TORAY-GA are illustrated in Figure 8. The optimal deposition location clearly lies at a normalised radius between $\rho_{abs} = 0.55$ and $\rho_{abs} = 0.7$. Energy deposited outside this region is no longer well confined and has less effect. The deposition width and the toroidal launching angle had little influence on the current broadening, the latter because the current drive efficiency in this outer region is small. In this scenario the central plasma density can be increased by a factor 1.5 above the 2nd harmonic cut-off, since absorption is peripheral. At these optimised launching parameters, an elongation of 2.47 was obtained with a plasma current of 390kA, corresponding to a normalised current of $I_N = 1.05$. The extension of the operating space in terms of κ and I_N is shown in Figure 9 where ohmic conditions, ECH and off-axis ECH are presented. These overdense plasmas of high elongation are good candidates for heating by vertically launched X3-ECH and obtaining high β values.

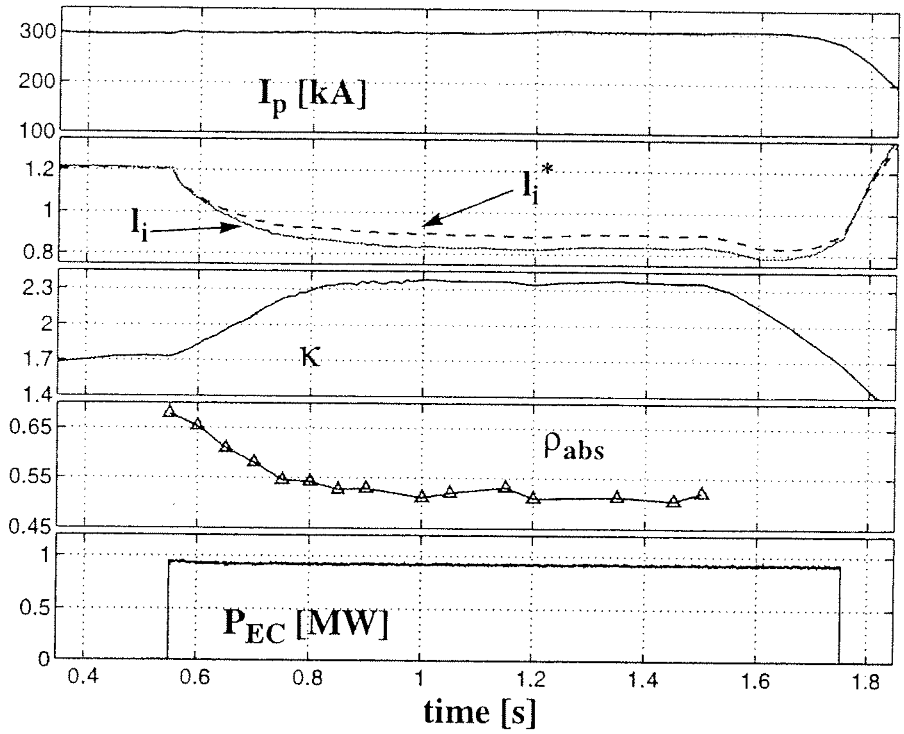

Fig. 7: Time traces for off-axis ECH in a high elongation plasma (#22295). From top to bottom: plasma current, internal inductance, elongation, absorption radius and ECH power.

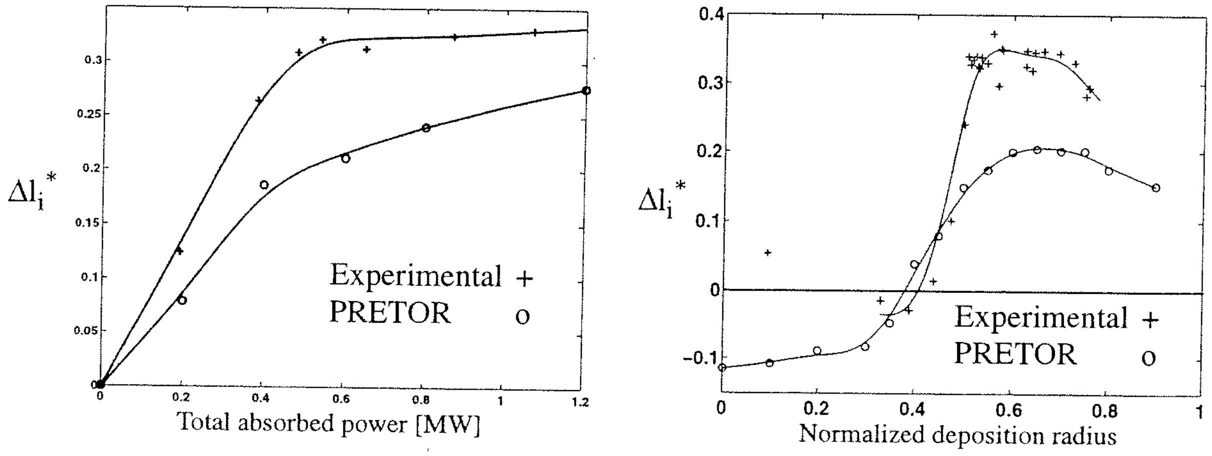

Fig. 8: Change in the internal inductance due to off-axis ECH in elongated plasmas as a function of the deposition radius, both deduced from the experimental equilibrium and simulated with PRETOR.

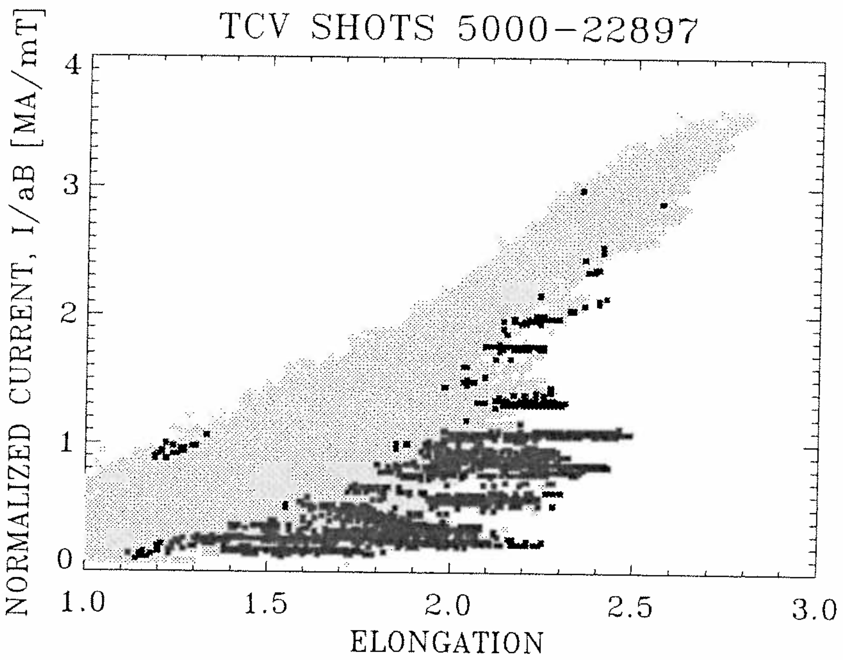

Fig. 9: Operating space in the elongation versus normalised current plane for ohmic (gray), ECH and off-axis ECH (black) conditions.

Third harmonic ECH

The main advantage of using X3-ECH on TCV is its ability to heat higher density plasmas, since the cut-off density at the third harmonic is $10^{20}\mathrm{m}^{-3}$, 2.5 higher than the second harmonic. However wave absorption is considerably lower and care must be taken to ensure high first path absorption. Besides operating at higher density, there are other ways to improve absorption: the beam can be launched vertically into the plasma to maximise the path length along the resonance layer; preheating of the plasma by X2-ECH offers a way to improve third harmonic efficiency since the absorption coefficient is proportional to the electron temperature; it was shown experimentally that absorption is greatly enhanced by the presence of a suprathermal electron tail, produced for example by second harmonic ECCD [25].

Two scenarios that use these methods are reported. First a high density ohmic target plasma, with $n_{e0} = 4.5\times10^{19}\mathrm{m}^{-3}$, is heated by 1MW of X3-ECH. The time traces of relevant plasma parameters are plotted in Figure 10. In particular the HFS-ECE channel compared to the central temperature measured by Thomson scattering indicates the formation of a fast electron population. Since refraction of the beam is very sensitive to the launching geometry, the optimal launching angle has been determined experimentally with a mirror sweep. The absorbed power fraction was 65%. This was deduced from the diamagnetic flux response to a modulation at 273 Hz of the gyrotron power [26]. In the second scenario, the plasma is preheated by 0.45 MW of centrally absorbed X2-ECH only to avoid the generation of suprathermal electrons. Figure 11 shows the time evolution of the main plasma parameters. During the combined second and third harmonic phase, an absorption fraction as high as 85% was measured. Later in the discharge, X2-ECH is turned off and the density is increased up to n_{e0} = $5 \times 10^{19} m^{-3}$. Here, X3-ECH alone can maintain the thermal energy content at the same level, as demonstrated by the diamagnetic trace. These two examples indicate that almost complete absorption of the X3-ECH can be achieved in tailored scenarios combining high density, high temperature plasmas and the supplementary absorption by the suprathermal electrons.

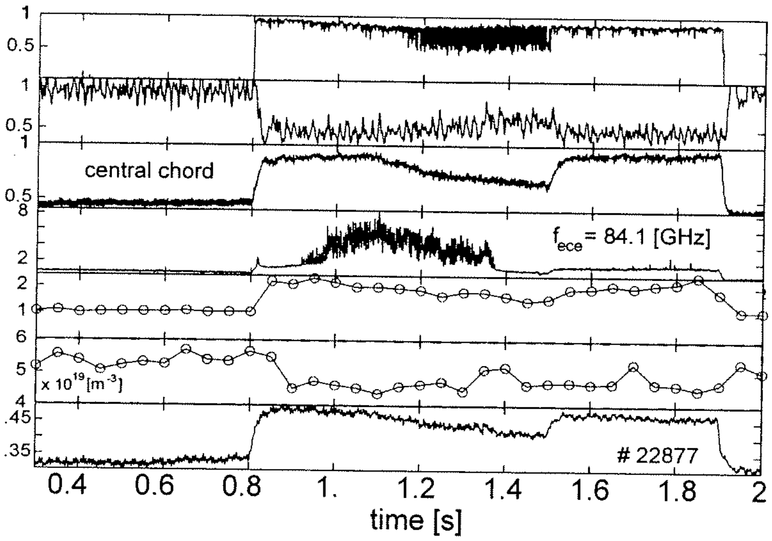

Fig. 10: Time traces for X3-ECH on a ohmic target plasma. From top to bottom: EC power [MW], loop voltage [V], central soft X-ray emission, HFS-ECE temperature, central temperature [keV] from Thomson scattering, central electron density [$10^{19} m^{-3}$] and β_p from diamagnetic flux.

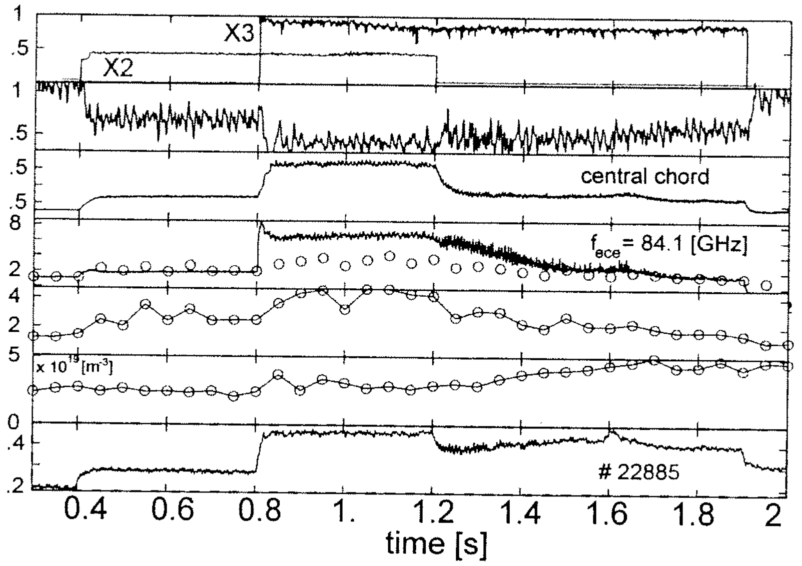

Fig. 11: Time traces for X3-ECH on a preheated plasma, as in Figure 10.

Conclusions

The pairing of a versatile plasma configuration and ECH heating on TCV provides a unique set of tools to modify the spatial distribution of the pressure and the current density, with the goal of controlling the MHD instabilities and turbulence responsible for anomalous transport. This is illustrated by the simultaneous attainment on TCV of fully non-inductively driven plasmas with a high bootstrap current ratio and a wide stable internal transport barrier, using off-axis ECCD. In particular, a non-monotonic safety factor profile can be sustained by the bootstrap current only. Another example are the high elongation low current configurations which are promising for increasing the β limit. Their vertical control was obtained with the help of overdense off-axis ECH to broaden the plasma current profile. X3-ECH in configurations that optimise the power absorption in high density, high temperature plasmas obtained near full absorption. The role of suprathermal electrons, generated either by second or by third harmonic, in the absorption of EC waves is of primary importance by providing ECH access on TCV to high density, high β plasmas.

A thorough analysis of these experiments was possible by combining measurements probing the suprathermal electron population generated by intense EC waves and simulations of its dynamics. In particular, it was shown that radial transport of the fast electrons plays a crucial role in widening the profile of the driven current from the deposition region, resulting in the correct evaluation of the current drive efficiency.

This work was partly supported by the Swiss National Science Foundation.

References

[1] S. Coda et al., this conference.

[2] P. Blanchard et al., submitted for publication in Plasma Phys. Control. Fusion.

[3] T.P. Goodman et al. this conference

[4] O. Sauter, R. Behn, S. Coda, this conference

[5] Y. Camenen et al., Proc. 12th Joint Workshop on Electron Cyclotron Emission and Electron Cyclotron Resonance Heating, Aix-en-Provence, 2002.

[6] A. Pochelon et al., this conference

[7] S. Alberti et al., this conference

[8] F. Hofmann et al., Plasma Phys. Control. Fusion **36** (1994) B277.

[9] T.P. Goodman et al., Fusion Technology (Proc. 19th Symp.on Fusion Technology, Lisbon, 1996) **1** (1997) 565.

[10] J.-P. Hogge et al., Proc. 12th Joint Workshop on Electron Cyclotron Emission and Electron Cyclotron Resonance Heating, Aix-en-Provence, 2002.

[11] R.W. Harvey et al., Proc. IAEA Tech. Conf. on Advances in Simulation and Models of Thermonuclear Plasmas, IAEA, Vienna, 1992

[12] K. Matsuda, IEEE Trans. Plasma sci. PS-17 (1986) 6.

[13] R.H. Cohen, Phys. Fluids **30** (1987) 2442.

[14] P. Nikkola et al., Proc. 12th Joint Workshop on Electron Cyclotron Emission and Electron Cyclotron Resonance Heating, Aix-en-Provence, 2002.

[15] A.B. Rechester, M.N. Rosenbluth, Phys. Rev. Lett. **40** (1978) 38.

[16] R.W. Harvey et al., Phys. Rev. Lett. **47** (1981) 102.

[17] Z.A. Pietrzyk et al., Phys. Rev. Lett. **86** (2001) 1530.

[18] R. Behn et al., Proc. 28th EPS Conf. on Cont. Fusion and Plasma Phys., Funchal, Madeira, 2001, Europhys. Conf. Abstr. (2001).

[19] P.H. Rebut, P.P. Lallia, M.L. Watkins in Proc. 12th Int. Conf. on Plasma Phys. and Contr. Fusion Research, Nice, 1988, IAEA Vieanna, **2** (1989) 191.

[20] A. Pochelon et al., Nucl. Fusion **39** (1999) 1807.

[21] O. Sauter et al., Phys. Rev. Lett. **84** (2000) 3322.

[22] S. Coda et al., Plasma Phys. Control. Fusion **42** (2000) B311.

[23] F. Hofmann et al., Plasma Phys. Control. Fusion **43** (2001) A161.

[24] A. Pochelon et al., Nucl. Fusion **41** (2001) 1663.

[25] S. Alberti et al., Nucl. Fusion **42** (2002) 42.

[26] A. Manini et al., Plasma Phys. Control. Fusion **44** (2002) 139.

Top Launch 3rd Harmonic X-mode Electron Cyclotron Heating in the TCV Tokamak

S. Alberti, L. Porte, G. Arnoux, T.P. Goodman, M.A. Henderson, J.P. Hogge,
E. Nelson-Melby

*Centre de Recherches en Physique des Plasmas,
Association EURATOM-Confédération Suisse,
EPFL, 1015 Lausanne, Switzerland.*

Introduction

Additional heating in TCV tokamak has been recently upgraded to a total of 4.5 MW of installed ECH power with 3MW 2nd harmonic ECH-ECCD at 82.7 GHz and 1.5 MW 3rd harmonic ECH at 118 GHz. The additional power at the 3rd harmonic allows the electron density range of ECH heated plasmas to be extended to 1. 10^{20} m^{-3}. Access to these higher densities with additional heating will considerably extend the parameter range of confinement and transport already studied in TCV. It will also permit achievement of H-modes at power levels significantly exceeding the L-H transition power thus allowing the full shape flexibility of TCV to be used in studying the high confinement, ELMing regime.

The choice of the top-launch scheme results as a compromise between heating of high density plasmas and the maximisation of single-pass absorption in ohmically heated target plasmas. The resonance layer is approximately a vertical surface on the high field side of the cold resonance and maximum absorption is obtained when the ray path within the resonance layer is longest. The strong sensitivity of the absorption to the launching geometry is experimentally studied with a top launch injected power as high as 0.9 MW in a variety of plasma configurations and comparisons between the experimental results with predictions from the ray tracing/absorption code TORAY-GA are presented.

Experimental results and Discussion

A preliminary study performed by Hogge et al. [1] was mainly dedicated to the commissioning of the X3 system and in particular to the steering capabilites of the top-launcher together with a study of the sensitivity of the plasma response to the launcher injection angle. In the same configuration for the X3 system as reportedin [1], with 2 X3 gyrotrons connected to the top-launcher and 1 X3 gyrotron connected to a X2-Low Field Side launcher, it has been demonstrated that the ray-tracing/absorption code TORAY-GA gives accurate predictions of the absorbed power at moderate densities (< 5 10^{19} m^{-3}) and low temperatures (<1.5-1.7 keV). However, at larger densities, the agreement deteriorates andfurther study is required.

The experiments reported here were aimed at more detailed and quantitative studies of the ECRH capabilities of the X3 top-launch in terms of single-pass absorption in a variety of plasma conditions with plasma densities significantly higher than the X2 cutoff limit ($n_{ecutoff}$ = 4 10^{19} m^{-3}). The target plasmas used in these experiments have the following parameters: major radius R = 0.88m; minor radius, a = 0.25m; toroidal magnetic field, B_T = 1.45 T; elongation, κ = 1.55; triangularity, δ = 0.1-0.15; peak electron densities ranging from 2 to 6 10^{19} m^{-3}. The main diagnostics used are: the Thomson scattering for the measurement of both the bulk electron temperature and densitiy (every 50ms), for suprathermal electrons the high field side ECE radiometer (ECE-HFS)[2] and for the evolution of the total plasma energy the

DML diagnostic[3]. The absorbed RF power, P_{in}, is measured during a modulated period of the X3 RF pulse using the diamagnetic loop[3, 4].

Two different scenarios were studied: the first with X3 top-launch heating only on an ohmic target plasma with density ranging from 2 to 6 10^{19} m^{-3}. The second scenario uses X2 central preheating at various power levels combined with X3 top-launch ECRH. In this scenario, the X2 aiming in pure ECRH does not produce a suprathermal tail during the X2 preheating phase and therefore allows the measurement of the X3 absorption on the bulk of the electron distribution. In an earlier study [5], with the X3 RF-power injected from the LFS in presence of a suprathermal tail generated by X2 CO-ECCD, it was shown that full single-pass X3 absorption was measured with approximately 50% absorbed on the bulk and 50% absorbed on the suprathermal tail generated by the X2 wave.

For the first scenario, the launching geometry as well as time traces of the relevant plasma parameters is shown in Fig.1.

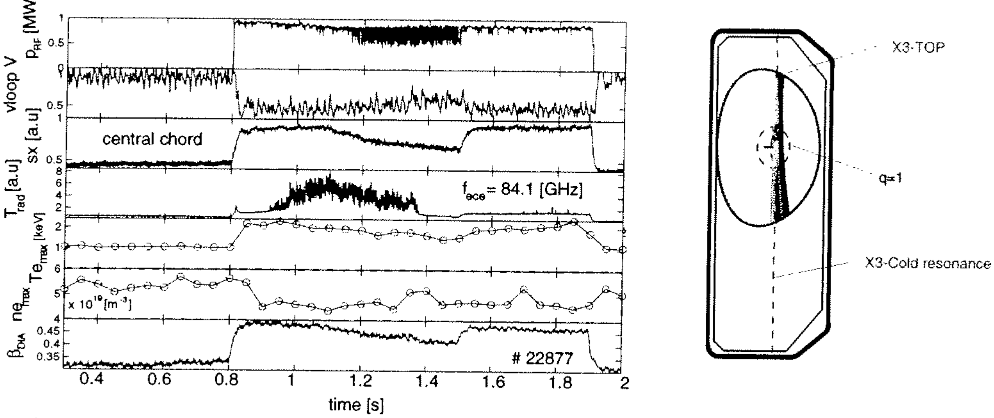

Figure 1. From top to bottom: RF power for X3 corresponding to 0.9 MW of injected power, loop voltage, soft X-ray signal (central chord), non-calibrated radiation temperature from one channel of the ECE-HFS radiometer, peak temperature and density from Thomson scattering (every 50ms) and diamagnetic β. Plasma current: Ip = 230 kA. On the right part, the plasma cross-section with the ray-tracing calculated with the TORAY-GA code.

For this shot, the central electron density, n_{e0} = 4.5-5 10^{19} m^{-3}, is above the cutoff density for the X2 system (4 10^{19} m^{-3}) and the aiming of the top launcher mirror was kept fixed at an angle of 46.2 degrees (measured from the vertical clockwise). The optimum angle was determined in an earlier shot with same plasma parameters, but with an injection angle swept between 45.5 and 47.5 degrees. At n_{e0} = 4.5 10^{19} m^{-3}, the ECE-HFS radiometer channel is in cutoff and the observed deviation of the signal (0.9s – 1.3s) from its base level is to be associated with the presence of suprathermal electrons generated by the X3 wave. The fast electrons are spatially located outside the normalized radius of r/a > 0.2; the q=1 radius of this plasma is located at r/a = 0.3.

The absorption measurement with the DML is made during the RF power modulation of only one gyrotron (square wave at 237Hz) between t =1.2s and 1.4s. The measured absorbed power of the modulated gyrotron is P_{abs} = 290kW which corresponds to an absorbed fraction of the X3 wave of 65% . Preliminary analysis shows that this value corresponds to single-pass absorption. When the top-launcher is swept during the shotover a wide anglular range, whenever the aiming is far form the optimum angle, the main plasma parameters remain at the same level as without X3 power injection. As shown in Figure 2, with this launching geometry the deposition profile calculated with the TORAY-GA code gives a central deposition with the RF power deposited inside a normalized radius of r/a = 0.45 and an absorbed fraction of 32% which is significantly lower than the measured fraction of 66%.

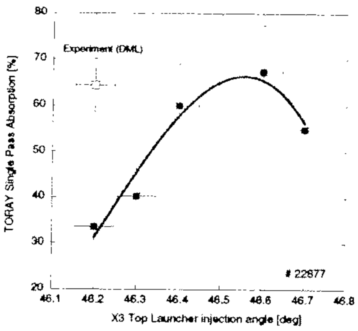

Figure 2. For this shot the X3 launch angle was fixed at 46.2°and the measured absorbed power was 66%. Using a launch angle of 46.2° TORAY-GA underestimates the absorbed power by 33%. By forcng TORAY-GA to use a launch angle of 46.55° agreement is obtained between the measured absorbed power and that predicted by TORAY-GA. Reasons for the discrepancy are being investigated. See main text for details.

The discrepancy between the two values might be explained by the sensitivity of the absorption on the launcher injection angle. By increasing the injection angle to 46.55° the deposition profile shape remains unchanged, but the total absorption predicted by the TORAY-GA code is significantly increased to 66%, in agreement with the measured value. The mechanical accuracy of the top-launch mirror setting is better than 0.1° degrees and we believe that the discrepancy is to be found in the accuracy of the ray-tracing calculation on the reconstructed equilibrium. This effect, as well as other effects like beam diffraction (beam tracing [6]) or hot plasma effects on the refraction [7], are being investigated. In order to cope with the high sensitivity of the absorption on the launcher injection angle, plans to implement a real time feedback on the top-launcher mirror are underway.For the second scenario, which includes a X2 preheating phase (central with deposition within r/a = 0.15) before the turn on of the X3 wave, the launching geometry as well as time traces of the relevant plasma parameters are shown in Fig.3. In this shot the timing of the X2 (0.45 MW) is such that after the X2 turn-off (1.2s) the plasma density is increased from 2.2 10^{19} m^{-3} to 4.7 10^{19} m^{-3} within 500ms. The aiming of the top launcher mirror was kept fixed at an angle of 46.5 degrees. The predicted single-pass absorption by the TORAY-GA code depends, as expected, on the time evolution of the temperature and density profiles and ranges between a maximum of 85% at t = 1.1s followed by a slight decrease at 71% to t =1.6s were X3 only is still on.

The stored energy variation, shown by the the diamagnetic signal (β_{DIA}), clearly shows that with 0.9 MW of RF power, the X3 top launch at high density (4.5 10^{19} m^{-3}) is able to maintain the same level of stored energy as for the combined X2-X3 phase with a significantly lower density (2.2 10^{19} m^{-3}). In this type of scenario with varying density, the absorption sensitivity on refraction could be optimized by a real-time feedback on the top-launcher mirror using for instance the diamagnetic signal.

As for the previous shot, during the combined X2-X3 phase the X3 RF beam generates a suprathermal population which subsequently decays, at X2 turn-off, to the thermal level on a fairly long time scale (> 200ms). In an experiment where the mirror is swept during the shot, withthe absorption location moving form the X3 cold resonance toward the high field side, one observes that the X3 top-launch selectively couples to the electron energy. This can be extremely useful for suprathermal electron dynamics studies. This observation is illustrated in Figure 4 where the soft-x ray signal (sensitive to the bulk) and one channel of the ECE-HFS radiometer are plotted against the top-launch aiming angle.

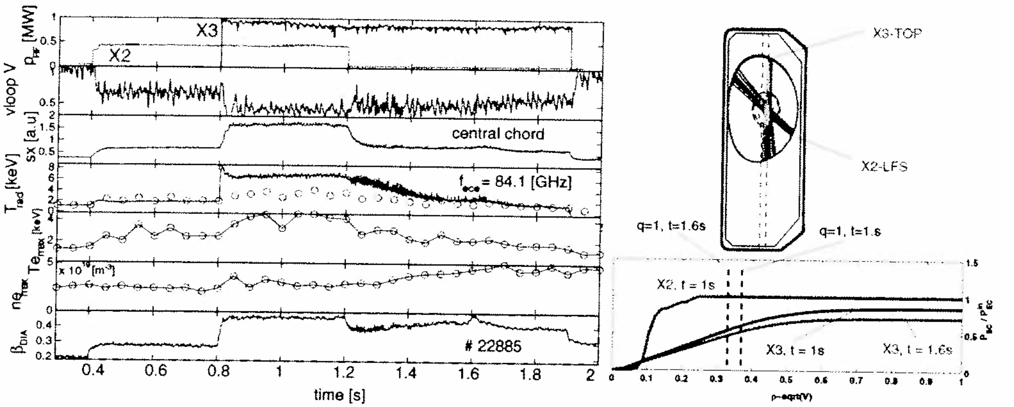

Figure 3. Same traces as in Figure 1 with in addition the calibrated radiation temperature (ECE-HFS) with the Thomson points at the corresponding radii of the ECE-channel. On the right part of the figure (top), the plasma cross section with the ray tracing for the X2 and X3 RF beams. On the right part of the figure (bottom), absorbed power versus normalized minor radius for the X2 beam (t=1s) and for the X3 beams at two different times (1s and 1.6s).

P-2.074

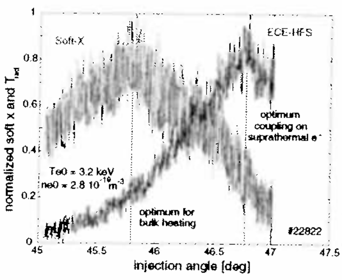

Figure 4. Presented here are a SXR signal (green) and an ECE signal (blue) from the same discharge plotted as a function of launcher angle. In this experiment the launcher angle is scanned. The SXR signal reflects heating on the bulk while the ECE signal reflects heating on the fast electron tail. As the mirror is scanned from the cold resonance to the high field side X3 power is selectively coupled to the bulk (SXR signal peak) and subsequently to the tail (ECE signal peak).

Conclusions

The X3 top-launch system significantly extends the operational regime of the TCV Tokamak. With X2 ECH preheating, single pass X3 absorptions as high as 90% have been measured. In a scenario where a density ramp is imposed after the X2 shutoff it is demonstrated that the stored plasma energy remains at the same level as for the X2 phase but with twice as high electron density. On a purely ohmic plasma at a density of 5.5 10^{19} m^{-3} a single-pass absorption as high as 66% has been measured. With the completion in the near future of the X3 top-launch system with 1.5MW of injected power, with higher electron temperatures, nearly full single-pass absorption is expected. Access to these higher density with additional heating will considerably extend the parameter range of confinement and transport already widely studied in TCV. The X3 top-launch flexibility has shown the possibility to selectively couple to different electron energies and could be used as a diagnostic for studies of the suprathermal electron dynamics.

References

[1] J.-P. Hogge, S. Alberti, L. Porte, G.Arnoux, EC12
[2] P. Blanchard, S. Alberti, S. Coda, H. Weisen, at this coneference
[3] G. Arnoux, A. Manini, S. Alberti, J.-M. Moret at this conference
[4] A. Manini, et al., Plasma Phys. Control. Fusion (2002),
[5] S. Alberti et al., Nucl. Fusion 42 (2002), 42.
[6] S. Nowak and A.Orefice, Phys. Plasmas 1 (1994), 1242.
[7] M.D. Tokman et al, EC12

Global Gyrokinetic Simulations of Nonlinear Interaction of Zonal Flows with ITG Modes

S.J. Allfrey, R. Hatzky[1], A.Bottino and L.Villard

Centre de Recherches en Physique des Plasmas, Association EURATOM-Confédération Suisse, EPFL, 1015 Lausanne, Switzerland

[1]Max-Planck-Institut für Plasmaphysik, Teilinstitut Greifswald, D-17491 Greifswald, Germany

1. Introduction

The δf particle-in-cell (PIC) method provides an approach to solving the nonlinear gyrokinetic equations governing the ion-temperature-gradient-driven (ITG) instabilities commonly held responsible for core plasma transport. The method is, however, rather demanding with respect to current typically available computational resources. The TORB[1] code implements this method in a straight Θ-pinch geometry. The code now employs an adiabatic electron response within surfaces of constant r. Thus the equations governing the $m_\theta = 0, n_z = 0$ Fourier component of the electrostatic potential, ϕ_{00}, which gives rise to zonal $\mathbf{E} \times \mathbf{B}$ flows, are as for the case of finite rotational transform. The underlying equations obey an energy conservation principle allowing for an intrinsic check on the quality of simulation. This has been well satisfied ($\sim$20% deep into the nonlinear stage) though optimising the phase space sampling provided by the markers.

2. The model

Under the geometry considered the equations of motion are

$$\frac{d\mathbf{R}}{dt} = v_\parallel \mathbf{e}_\parallel - \frac{\nabla\langle\phi\rangle}{B} \times \mathbf{e}_\parallel \,, \tag{1}$$

$$\frac{dv_\parallel}{dt} = -\frac{\Omega_i}{B}\mathbf{e}_\parallel \cdot \nabla\langle\phi\rangle \,. \tag{2}$$

Along these characteristics δf evolves according to

$$\frac{d\,\delta f}{dt} = -f_0 \left[\frac{\langle\mathbf{E}\rangle \times \mathbf{e}_\parallel}{B} \cdot \frac{\nabla f_0}{f_0} + \frac{\Omega_i}{B}\mathbf{e}_\parallel \cdot \langle\mathbf{E}\rangle \frac{1}{f_0}\frac{\partial f_0}{\partial v_\parallel} \right] . \tag{3}$$

The quasineutrality equation with linearised polarisation density is

$$\langle n_i \rangle - n_0 = \frac{e n_0}{T_e}\left(\phi - \bar{\phi}\right) - \nabla_\perp \left(\frac{n_0}{B\Omega_i} \nabla_\perp \phi \right) . \tag{4}$$

Here $\Omega_i = q_i B/m_i$ is the ion cyclotron frequency, $\langle\phi\rangle$, $\langle\mathbf{E}\rangle$ and $\langle n_i\rangle$ and the gyro-averaged potential, electric field and ion density and , $\bar{\phi}$ is the magnetic surface average of the potential. The quantity $\bar{\phi}$ is given by ϕ_{00} in this geometry. The quasineutrality equation is subject to the boundary conditions,

$$\left.\frac{\partial}{\partial r}\phi_{n,m=0}\right|_{r=0} = \left.\phi_{n,m\neq 0}\right|_{r=0} = \left.\phi\right|_{r=r_a} = 0, \tag{5}$$

which simply impose a vanishing tangential electric field at r_a, the outer boundary of the plasma. Retaining the parallel nonlinearity in equation (1) allows for an energy conservation principle to be satisfied

$$\frac{d}{dt}(\mathcal{E}_{kin} + \mathcal{E}_{field}) = 0 \; , \tag{6}$$

$$\mathcal{E}_{kin} = \int \frac{1}{2} m_i v^2 f \, d\mathbf{R} d\mathrm{v} \qquad \mathcal{E}_{field} = \int \frac{q_i}{2} \left(\langle n_i \rangle - n_0 \right) \phi \, d\mathbf{x} \; . \tag{7}$$

3. Results

The simulations used 134 million (2^{27}) markers over a cubic finite element basis of dimension $n_r = 64, n_\theta = 256, n_z = 32$. The time step was $\Delta t = 40\Omega_i$. Fourier modes in θ and z in the range $-96 \leq m \leq 96$ and $0 \leq n \leq 6$ were retained in the filter. The initial ion temperature profile $T_i(r)$ is show in figure 3. A flat density (n_0) and electron temperature profile ($T_e = T_i(0.5) = 5keV$), were used. The radius of the pinch was $r_a = 135\rho_{i0}$ and the periodicity length $20\pi r_a$ with ρ_{i0} the thermal Larmor radius at $r = 0.5$. The magnetic field was taken as 2.5T and the ions to be deuterium, $q_i/m_i = 4.79 \times 10^7 C/kg$, giving $\Omega_i = 1.20 \times 10^8$ s.

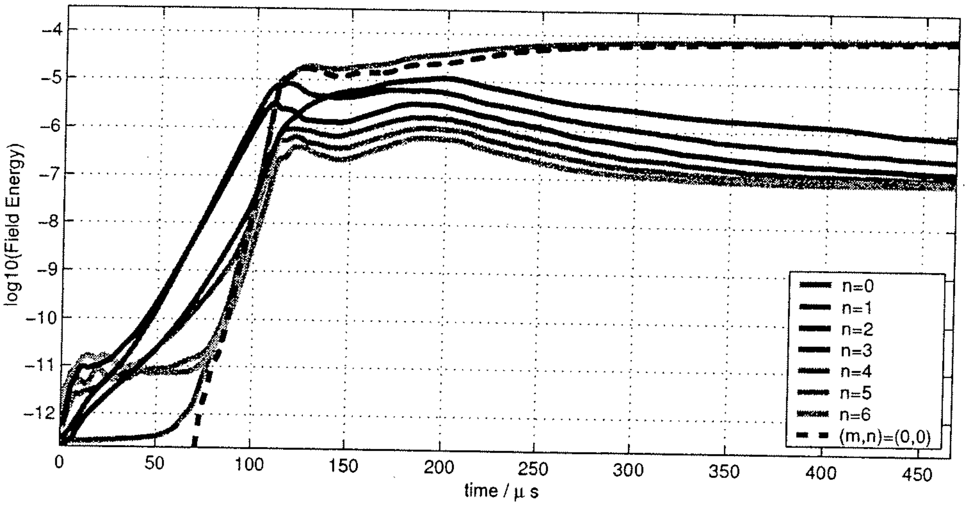

Figure 1. A log plot of the Fourier decomposition of the electrostatic field energy vs. time

Figure 1 shows the evolution of the ITG turbulence toward a saturated nonlinear state. The most unstable linear modes are in the ranges $(n, m) = (2, \sim 48), (3, \sim 55), (1, \sim 30)$ and $(4, \sim 60)$, with $n = 0, 5$ and 6 linearly stable. Initially we see just the linear instabilities, but at $60\mu s$ the nonlinear destabilisation of $n = 0, 5$ then 6 begins. Nonlinear feedback begins with a first roll over at $100\mu s$ followed by a second at $200\mu s$. Finally past $400\mu s$ the system is seen to be approaching a steady state with the expected inverse cascade in n dominated by an $(n, m) = (0, 0)$ mode.

The top two traces in figure 2 show the absolute values of kinetic and electrostatic energy of the perturbation. By equation 6 they should be equal for a perfect simulation. Energy is seen to be well conserved with a relative error of $\sim$ 33% at the end of the simulation. The Fourier filter contains $\geq$ 98% of the signal throughout the nonlinear phase.

Seen in the bottom trace of figure 2 is the heat flux,

$$Q = \frac{1}{V} \int \frac{1}{2} m_i v^2 \frac{\langle \mathbf{E} \rangle \times \mathbf{e}_{||}}{B} \cdot \frac{\nabla r}{|\nabla r|} f \, d\mathbf{R} d v \tag{8}$$

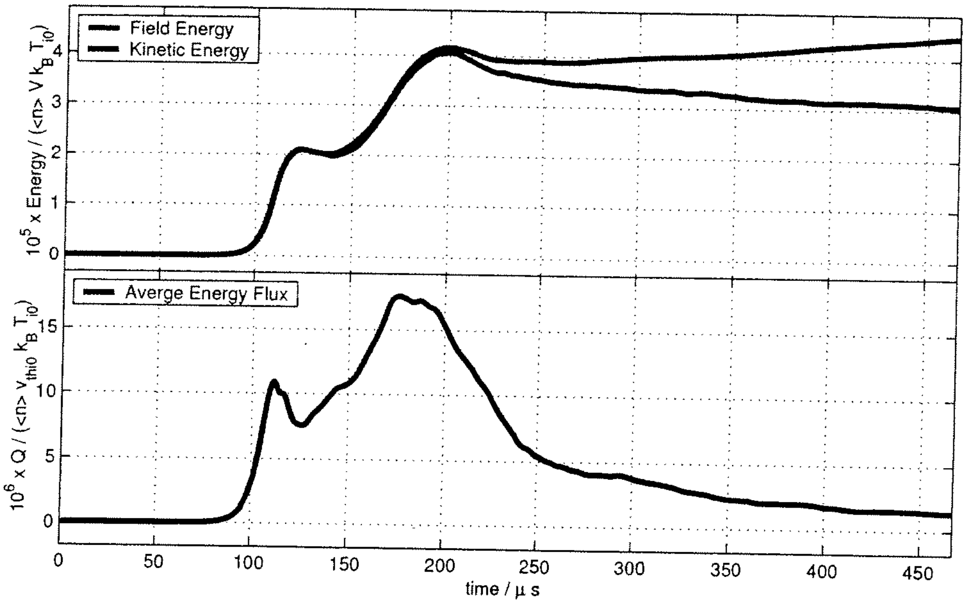

Figure 2. Top, the absolute value of the kinetic and electrostatic field energy (eq.7) of the perturbation normalised to the thermal energy of the plasma and bottom, the normalised average radial energy flux Q (eq.8) vs. time

Previous equivalent simulations [1] did not retain the $\bar{\phi}$ term in equation 4, corresponding to a volume adiabatic electron response. In the previous simulations Q in the late nonlinear stage was an order of magnitude larger than the value found here, with the field energy of comparable magnitude. This is due to fact the the electron model used now allows for the generation of zonal flows [3].

Figure 3 shows the radial profiles at $470\mu s$. In orange and blue are shown the initial and final effective temperature $T_{eff} = \langle v_{thi}^2 \rangle$ profiles. What is immediately striking are the plateau regions of low gradient/ high transport directly, corresponding with the regions of ITG turbulence which are shown in red. In black is shown $-\partial\Phi_{00}/\partial r$ which is proportional to the zonal $\mathbf{E} \times \mathbf{B}$ flow.

We now describe in detail the evolution of the radial envelope of ITG modes. In the linear stage the ITG modes are centred around the maximum temperature gradient at $r = 0.5$. As the modes spread radially and increase in magnitude the zonal flow becomes strong enough to shear the primary ITG envelope radially in two. This is responsible for the first roll over at $100\mu s$ seen in figure 1. This region now settles into an essentially steady state consisting of a central positive flow region in which ITG modes are suppressed, flanked by two bands of negative flow in which they persist. The evolution continues on the inner and outer boundaries of this envelope, where the initial sequence of events is repeated, the roll over at $200\mu s$, leading now to four regions of ITG activity. At $470\mu s$ this bifurcation process is in the course of repeating itself once more, with the splitting more advanced on the outer boundary.

We note that not only are the ITG convective cells restricted to the $\mathbf{E} \times \mathbf{B}$ stream they lie in (shear flow suppression), they are suppressed throughout those streams rotating in a positive sense. In purple is shown a histogram of the heat flux Q in 5 radial bins. It is clear that it is only at the boundaries of the ITG turbulence, which are still evolving, that a significant flux is driven. In the middle of the envelope (bins 3 and 4) the flux levels have remained at a constant low level since $\sim 380\mu s$ having peaked $\sim 200\mu s$ earlier. Presumably the large fluxes seen at boundaries will follow the same behaviour as the entire radial interval reaches saturation.

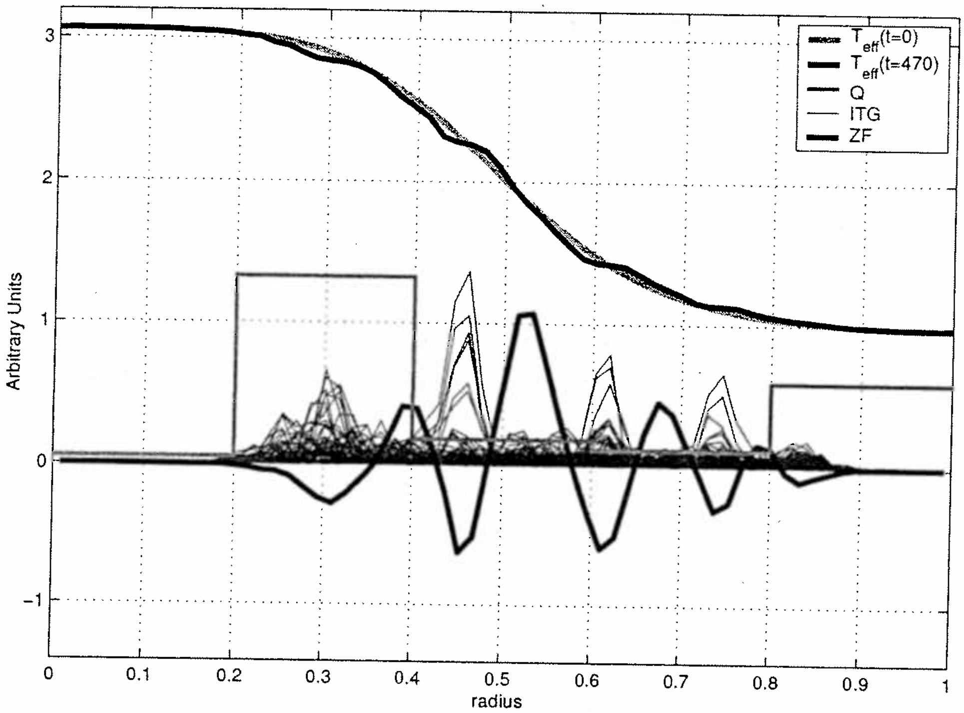

Figure 3. Radial profiles of the effective temperature T_{eff}, ITG mode spectrum, $\mathbf{E} \times \mathbf{B}$ zonal flow and binned heat flux Q. . Profiles have been rescaled for illustrative purposes

4. Conclusions

We have presented simulation of the suppression of ITG driven turbulence by zonal flows in straight Θ-pinch geometry with very good energy conserving properties. The system is seen to approach a steady state in the absence of any collisional terms. The use of an optimised phase space sampling is crucial in attaining energy conservation. Finite rotational transform needs to be introduced to be consistent with the electron model used. Further simulations will examine the dependence of the radial scale-length of the zonal flows and the concomitant scaling of driven flux.

This work was partly supported by the Swiss National Science Foundation. Simulations were executed on the IBM Regatta of the Rechenzentrum, Max-Planck-Gesellschaft, Garching and the SGI Origin 3800 of the Ecole Polytechnique Fédérale de Lausanne.

References

[1] R. Hatzky, T.M. Tran, A. Könies, R. Kleiber, and S.J. Allfrey, Phys. Plasmas **9**, 898 (2002).

[2] L. Villard, A. Bottino, O. Sauter and J. Vlaclavik, Phys. Plasmas **9**, June (2002).

[3] A. Hasegawa, C.G.Maclennan and Y.Kodama, Phys. Fluids **27**, 2122 (1979)

Understanding Sawtooth Period Behaviour with Electron and Ion Cyclotron Resonance Heating and Current Drive

C. Angioni[†], T.P. Goodman, M.A. Henderson, M.J. Mantsinen[1], O. Sauter
Centre de Recherches en Physique des Plasmas,
Association EURATOM - Confédération Suisse, EPFL, 1015 Lausanne, Switzerland
[1] *Helsinki University of Technology, Association EURATOM-Tekes, Espoo, Finland*
[†] Present address: *Max-Planck Institut für Plasmaphysik, IPP-EURATOM Association,*
D-85748 Garching bei München, Germany

1. Introduction

Sawtooth activity has strong effects on plasma profiles and plasma performance. Sawtooth stabilisation, although favourable in producing peaked profiles, can create seed islands capable of triggering neoclassical tearing modes [1] and prevents the removal of impurities from the plasma core. Therefore the sawtooth period should play a non–negligible role in determining the plasma performance in a burning plasma and should be controlled during the reactor operation in order to maximize the fusion yield. For these reasons, the physical understanding of the sawtooth period behaviour must be considered of major importance, particularly in the presence of radiofrequency heating. This can indeed modify the local plasma parameters in such a way to allow the control of the sawtooth period [2, 3, 4, 5].

In particular in the present paper the sawtooth period responses to localized heating and current drive obtained in two different tokamaks, TCV and JET, and with two different auxiliary heating systems, electron cyclotron resonance heating (ECH) and ion cyclotron resonance heating (ICRH) respectively, are analyzed, compared and simulated with a sawtooth period model. This is done using the transport code PRETOR [6], including a sawtooth period model [7, 8] first introduced to predict the sawtooth period in a ITER burning plasma. This model provides sawtooth crash triggers from the linear stability thresholds of the internal kink in both ideal and non–ideal regimes and prescriptions for the post–crash relaxed profiles following the Kadomtsev complete reconnection model. The model was found consistent with the experimental behaviour in ECH discharges in TCV [9] and in NBI discharges in JET [10].

Recent new experimental results in TCV have motivated a set of simulations which clearly identify the separate effects of localized heating (Section 2) and current drive (Section 3) along the full plasma minor radius. It is shown that the effects so identified are consistent with the complex sawtooth period response observed in a JET discharge with ICRH and ICCD [5] as the resonance moves through the inversion radius (Section 4).

2. TCV ECH discharges: stabilisation and destabilisation with localized heating

The stabilizing effect of ECH close to the $q = 1$ surface was observed for the first time at our knowledge in Ref. [11] and the stabilizing location was roughly identified ouside the $q = 1$ surface. More recently, previous TCV experiments [3, 4], performing vertical sweeps of the ECH beam in the poloidal cross section, have pointed out that the sawtooth period (τ_{saw}) and amplitude strongly increase when the power deposition crosses a given flux surface, located very close to the $q = 1$ surface. The sawtooth period behaviour obtained in those experiments was found consistent with the simulations obtained applying the previously mentioned sawtooth period model [9]. In the simulations the radial position of the heating location maximizing τ_{saw} was found to be located just outside the radius ρ_1 of the $q = 1$ surface.

In the present work we show results obtained in recent shots in which the higher plasma current and the slow beam sweep in a very narrow plasma layer in the vertical direction allow us to more easily compare the inversion radius ρ_{inv}, experimentally identified with ρ_1, and the ECH deposition location, computed with the ray–tracing code TORAY–GA [12]. To obtain visible heating effects on τ_{saw} in the case of plasmas with higher Ohmic heating power density, it was necessary to apply three beams of 0.45 MW each, one on top of the other (limiter plasmas, $I_p = 350$ kA, $B_t = 1.45$ T, line averaged density $n_{el} = 1.6\ 10^{19}$ m^{-3}, $q_{edge} = 3$).

The results obtained in shot ♯21103 are shown in Figure 1. In Figure 1(a), circles show the evolution of τ_{saw} as a function of the power deposition. The power deposition is identified with the barycentre of the power density profile as computed with TORAY–GA. The normalized radial coordinate is $\rho = (V/V_{edge})^{1/2}$, where V is the volume enclosed by the corresponding flux surface. With triangles we have plotted τ_{saw} as computed by a PRETOR simulation performed using smoothed TORAY–GA power deposition profiles. The heating power density

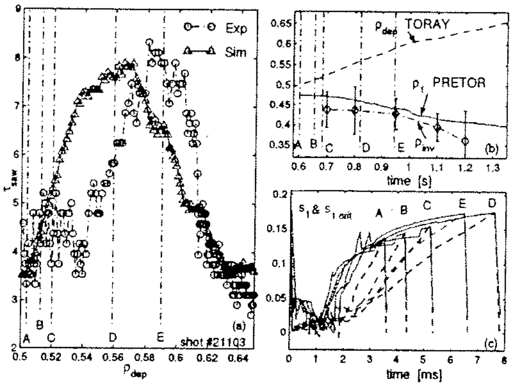

Figure 1. *Experiment and simulation which identify the heating location maximizing τ_{saw}*

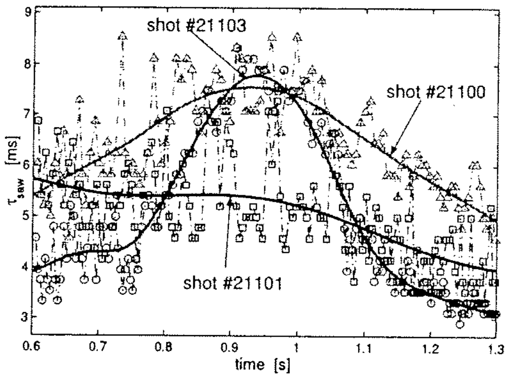

Figure 2. *Experimental traces which show the presence of a heating location destabilizing sawteeth*

profile has a maximum ranging from 8 MW/m^3 at $\rho_{dep} \simeq 0.5$ to 6 MW/m^3 at $\rho_{dep} \simeq 0.65$, with a corresponding deposition width $\Delta\rho_{dep} \simeq 0.08$. The simulation reproduces rather well the variation of the sawtooth period, and provides a location maximizing τ_{saw} (ρ_{max}) which is shifted as compared to the experimental trace by only $\Delta\rho \simeq 0.025$, that is 0.6 cm, below the errorbars on both the TORAY–GA deposition profile and the equilibrium reconstruction.

In Figure 1(b) the barycentre of the TORAY–GA power density profile ρ_{dep} is plotted versus time and compared with the before crash ρ_1 computed by the PRETOR simulation as well as with the experimental inversion radius ρ_{inv}, determined from the soft X-ray (SXR) emissivity profiles. Note that at the time of maximum τ_{saw}, both in the experiment and in the simulation, ρ_{dep} is clearly outside ρ_{inv} and the computed ρ_1, by $\Delta\rho \simeq 0.15$ (more than 3 cm), which is larger than the possible errorbars. Moreover both the PRETOR ρ_1 and the experimental ρ_{inv} have the same behaviour during the power sweep. This shows a general behaviour: ρ_1 moves inward when heating power is deposited outside this surface.

In Figure 1(c) we have plotted the time evolution of the relevant terms determining τ_{saw} in the simulation [7, 8, 9], that is the shear s_1 and the critical shear $s_{1\,\mathrm{crit}}$ at ρ_1. We have chosen 5 sawteeth at five time slices during the simulation. These are identified in Figures 1(a) and 1(b) by dash–dotted vertical lines. The key role in determining τ_{saw} is played by the speed at which s_1 grows up during the sawtooth ramp (for graphical purposes the time quoted in x–axis has been rescaled to zero at the start of each sawtooth).

Although all the plasma parameters of the model are computed at ρ_1, it results that the heating location which most efficiently stabilizes sawteeth is located outside $q = 1$. This is because plasma profiles respond to transport equations, and so a desired effect to be obtained on a given flux surface is not necessarily obtained when heating exactly on that surface. We emphasize also that this heating location does not correspond to any specific physical surface.

In Figure 2 we compare the τ_{saw} time trace of shot ♯21103 with the time traces of shots ♯21101 and ♯21100. These two discharges have been obtained with the same set–up and the same plasma of shot ♯21103, but a fourth ECH beam has been added during the vertical sweep of the other three beams. In the case of shot ♯21101 the fourth beam was aiming at a fixed location just inside ρ_1, whereas in shot ♯21100 the fourth beam was aiming almost at the plasma centre. Only shot ♯21101 does not present a maximum of τ_{saw} around 0.95 s. We deduce that localized heating at the location just inside ρ_1 used in this shot, $\rho_{dep} \simeq 0.35$ ($\rho_{dep} \simeq 75\%\rho_{inv}$) has a destabilizing effect on sawteeth. We have performed a PRETOR simulation looking for this location with the following set–up (Figure 3). The equivalent of three gyrotron beams, 1.35 MW, is deposited at ρ_{max} and we add the sweep of one beam of 0.45 MW along the full minor radius. An experiment of power sweep starting from Ohmic conditions allows us to identify stabilizing heating locations, a sweep performed starting from heating conditions in which τ_{saw} is maximized allows us to explore the existence of destabilizing locations.

The results provided by the model agree with the expectations derived from the previous analysis of the experiments. A destabilizing region between $\rho_{dep} = 0.25$ and 0.42 and a τ_{saw} minimum at $\rho_{dep} = 0.33$ are found. This location is almost coincident with the one experimentally identified in shot ♯21101. When the swept beam crosses ρ_{max} a maximum is obtained, in agreement with the experimental result that τ_{saw} increases with increasing power density [4].

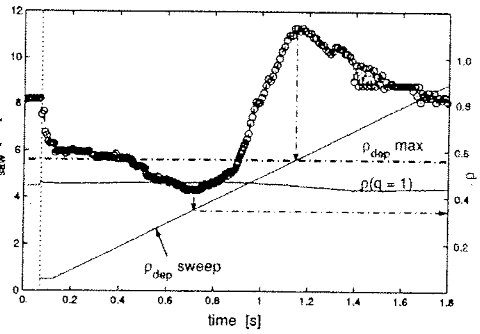

Figure 3. *Simulation which identifies the heating location minimizing* τ_{saw}

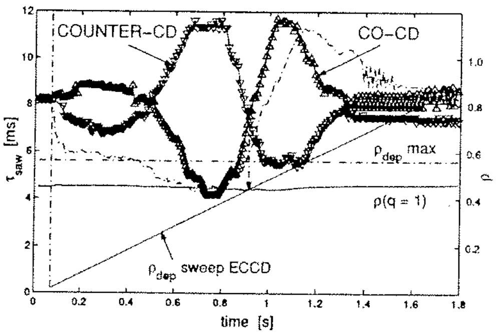

Figure 4. *Simulations showing the effects of co– and counter–CD on* τ_{saw}

The destabilizing effect of localized heating just inside $q = 1$ completely clarifies why maximum stabilisation is obtained when the power is deposited outside $q = 1$ and not exactly on $q = 1$. Since the fraction of the power which is absorbed inside $q = 1$ has a destabilizing effect, the location of ρ_{max} depends on the width of the power density profile, broad profiles providing most efficient stabilisation when ρ_{max} is largely outside $q = 1$ (roughly $\rho_{max} - \rho_1 \simeq 0.5\Delta\rho_{dep}$).

3. Stabilisation and destabilisation with current drive

The same simulation set–up described in the previous section has been used to explore effects due to CD. We keep 1.35 MW of heating power fixed at ρ_{max} and we add the sweep of a small amount of localized CD, 3.5 kA, along the full minor radius (at the plasma centre the local maximum driven current density (0.92 MA/m^2) is about 32% of the local current density, whereas at ρ_1 (0.11 MA/m^2) is less than 4% of the local current density). The results are shown in Figure 4. The τ_{saw} time trace obtained with co–CD (+3.5 kA) is plotted with triangles pointing up, whereas the τ_{saw} time trace obtained with counter–CD (-3.5 kA) with triangles pointing down. When considered alone, that is not accompanied by an amount of heating at the same location, co– and counter–CD have opposite effects at symmetric locations with respect to ρ_1. In particular the stabilizing effect of co–CD and destabilizing effect of counter–CD when applied outside ρ_1 is in agreement with experimental observations in TCV [4]. We observe also that in particular counter–CD has opposite and competitive effects at the same locations as compared with localized heating (Figure 3 and dash–dotted line in Figure 4). Therefore we must expect that in experimental conditions when co–, counter–CD, and localized heating are simultaneously present, very complex time traces can result. JET shot ♯51800 with ICRH and ICCD provides an interesting example in this sense.

4. Analysis of a JET shot with ICRH/ICCD

A set of shots have been performed in JET with ICRH and ICCD at $\omega \approx 2\omega_{cH}$ producing a ramp in B_t and I_p in order to change the ICRF resonance location with respect to ρ_{inv}, while keeping q and ICRF power constant [5]. The time trace of τ_{saw} as well as of the $\omega \approx 2\omega_{cH}$ resonance location and of R_{inv} obtained in shot ♯51800 are shown in Figure 5. We observe that τ_{saw} has a complex behaviour as the resonance moves through the inversion radius, with a sequence of two maxima and minima in the time interval between 23.7 s and 25.5 s.

The different ICRF–related quantities have been computed and analyzed [5] with the codes PION [13] and FIDO [14]. In particular the three–dimensional Monte Carlo code FIDO allows the detailed modelling of the resonating ion distribution and the ICCD density profile, taking into account the effects of finite orbit width and of trapped resonating ions. The collisional electron heating power density and the current density driven by ICRF–accelerated protons as computed by FIDO for shot ♯51800 at 24.5 seconds are shown in Figure 6. The calculated current is dominated by the current of diamagnetic type [15], caused by the large orbit widths of the resonating trapped high–energy protons. Thereby the driven current density profile is bipolar, and the counter– and co–CD components are at shifted locations with respect to the position of the maximum of the collisional heating power density profile. This is particularly interesting since, differently from cases with ECH and ECCD, both counter–CD and co–CD are simulataneously involved and at different locations with respect to the heating power. Note that direct fast particle effects on τ_{saw} are negligible in the time interval we are considering. They become relevant only when the resonance approaches the magnetic axis and are likely to be responsible of the observed increase of τ_{saw} up to 230 ms [5].

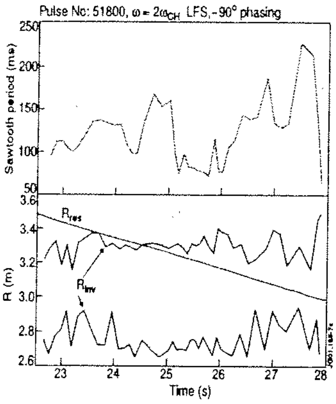

Figure 5.

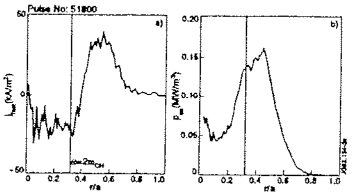

Figure 6. (↑) *ICCD (a) and collisional electron heating power (b) densities at 24.5 s (FIDO results)*

Figure 5. (←) *Time traces of* τ_{saw}*, of the ICRF resonance and of* R_{inv} *(JET shot ♯51800)*

Figure 7. (→) *Corresponding simulation in the interval t = 22.5s-26.0s*

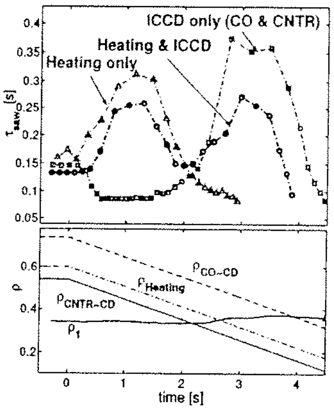

Figure 7.

We have performed simulations of the sawtooth period behaviour of this shot in the mentioned time interval (Figure 7), considering first separately the effects due to electron localized heating (triangles) and due to the co– and counter–ICCD components (squares), and then taking into account both ICRH and ICCD (circles). Time t = 0 s in the simulation corresponds to time t = 22.5 s in the discharge. The profiles of co– and counter–CD as well as the electron heating power density used in the simulation are derived from the results obtained by FIDO for several time slices. The barycentre of these density profiles have been plotted and compared with the time evolution of ρ_1 as obtained in the simulation in which both ICH and ICCD effects have been taken into account (Figure 7). The separate effects due to heating and current drive are consistent with those shown in Figures 3 and 4, and with the related TCV experimental results (Figures 1, 2 and Refs. [3, 4, 9]). The superimposition of these separate effects provides the sequence of maxima and minima observed in the experimental trace of the JET shot.

5. Conclusions

Strong experimental effects due to localized heating and current drive have been identified and explained with the help of transport simulations involving a sawtooth period model. A specific and complex sawtooth period time trace observed in JET in the presence of ICRH and ICCD has been explained and shown consistent with the superimposition of separate effects due to localized heating and current drive as identified by simulations and experiments with ECH/ECCD in TCV.

This work was partly conducted under the European Fusion Development Agreement, and was supported in part by EURATOM and the Swiss National Science Foundation.

References

[1] Sauter O *et al* 2002 *Phys. Rev. Lett.* **88** 105001
[2] Hanada K *et al* 1991 *Phys. Rev. Lett.* **66** 1974
[3] Goodman T P, Henderson M A *et al* 1999 *Proc. 26th EPS Conf. on Control Fusion and Plasma Physics (Maastricht, 1999)* ECA Vol. **23J** 1101
[4] Henderson M A, Goodman T P *et al* 2001 *Fusion Eng. Des.* **53** 241
[5] Mantsinen M J *et al* 2001 *Proc. 28th EPS Conf. on Control. Fusion and Plasma Physics, (Madeira, 2001)*, ECA Vol **25**, P 2.083; submitted to *Plasma Phys. Control. Fusion* (2002)
[6] Boucher D and Rebut P H 1993 *Proc. IAEA Tech. Com. on Advances in Simulation and Modell. of Thermonuclear Plasmas (Montreal, 1992)* p 142
[7] Porcelli F *et al* 1996 *Plasma Phys. Control. Fusion* **38** 2163
[8] Sauter O *et al* 1999 *Theory of Fusion Plasmas (Proc. Joint Varenna–Lausanne Int. Workshop)* Varenna 1998, eds Connor Sindoni Vaclavik, ISPP-18 (Compositori Bologna) 403
[9] Angioni C *et al* 2001 *Theory of Fusion Plasmas (Proc. Joint Varenna–Lausanne Int. Workshop)* Varenna 2000, eds Connor Sauter Sindoni, ISPP-19 (Compositori Bologna) 73
[10] Angioni C *et al* 2002 *Plasma Phys. Control. Fusion* **44** 205
[11] Sillen R M J *et al* 1986 *Nucl. Fusion* **26** 303
[12] Lin-Liu Y R *et al* 1999 *Proc. 26th EPS Conf. on Control Fusion and Plasma Physics (Maastricht, 1999)* ECA Vol. **23J** 1245
[13] Eriksson L-G, Hellsten T, and Willén U 1993 *Nucl. Fusion* **33** 1037
[14] Carlsson J *et al* 1995 *Theory of Fusion Plasmas (Proc. Joint Varenna–Lausanne Int. Workshop)* Varenna 1994, eds Connor Sindoni Vaclavik, ISPP-16 (Compositori Bologna) 351
[15] Hellsten T, Carlsson J, Eriksson L-G 1995 *Phys. Rev. Letters* **74** 3612

Modulated ECH Power Absorption Measurement with a Diamagnetic Loop in TCV Tokamak

G. Arnoux, A. Manini, J.-M. Moret, S. Alberti

Centre de Recherches en Physique des Plasmas
Association EURATOM-Confédération Suisse, EPFL, CH-1015 Lausanne, Switzerland

1. Introduction

The power absorption of additional plasma heating can be determined from the time derivative of the total plasma energy, which can be estimated from the diamagnetic flux of the plasma using a DiaMagnetic Loop (DML). A method based on the temporal variations of the diamagnetic flux of the plasma during Modulated Electron Cyclotron Heating (MECH) has been developed and applied to absorption measurements of second (X2) and third (X3) harmonic X-mode ECH in TCV [1]. A MECH frequency scan has allowed the determination of an optimum modulation frequency situated at about 200-250 Hz. For low field side launching configuration, full single-pass absorption of X2 has been measured and, during X3 low field side launching in plasmas preheated by X2 CO-ECCD, full single-pass absorption has been measured as well. In this paper, X3 absorption measurements with the recently installed top launch injection system is analyzed. The X3 ECH allows heating at plasma densities significantly higher than the X2 cutoff. With these higher density plasmas, additional electron-ion coupling must be taken into account in the MECH-DML analysis. In this model, the power balance equation contains a term describing the energy transfer between electrons and ions. The influence of these effects are discussed by modelling the power balance equation and preliminary X3 top launch absorption measurement are presented.

2. Experimental configuration and frequency response of the DML

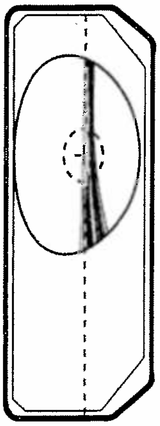

Figure 1 : X3 beam trajectory following the cold resonnance (dashed line). The circular dashed line is the q = 1 surface

The typical ohmic target plasmas and the launching geometry are shown in the figure 1. Two X3 beams are injected from the top launcher of TCV. The launching mirror allows to adjust the poloidal injection angle in real-time to optimize the absorption.The target plasmas have major radius $R_0 = 0.88$ m, minor radius $a = 0.25$ m, elongation $\kappa = 1.53$, triangularity $\delta = 0.15$, toroidal field $B_{0t} = 1.42$ T and plasma current $I_p = 240$ kA.

The DML is a 1-turn loop fixed on the vessel encircling it poloidally. in order to measure the diamagnetic flux, compensations are needed. The achieved frequency response of the DML of up to 1 kHz was obtained by a second order analogue compensation of the vessel image currents; without this, the bandwidth of the diagnostic would be limited to around 30 Hz which is given by the decay time constant of the vacuum vessel current. This large bandwidth, together with the negligible poloidal flux contribution to the DML flux modulation, allows a direct interpretation of the signals without requiring additional data analysis. As described in [1], these effects can be summarized in a system of three equations relating the voltages on the DML, on the compensation loop CL (Figure 2) and the diamagnetic flux $\Delta\phi$ itself. The diamagnetic flux is obtained through a hardware and digital treatment of these signals. The relation between the modulated diamagnetic flux and the modulated plasma energy is given in Fourier space by

$$\tilde{W} = \frac{3\pi}{\mu_0} B_{t0} R_0 \cdot \Delta\tilde{\phi},$$

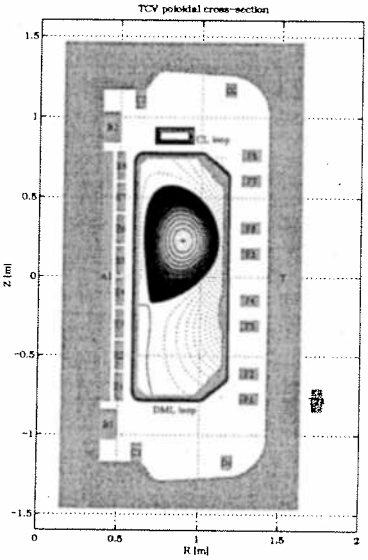

Figure 2 : The DML fixed around the vessel and the compensation loop CL above the vessel

The Shafranov integral terms contributing to the plasma energy can be neglected, since as shown in [1], they do not contribute to the modulation part of the plasma energy.

3. Dynamic response with electron-ion coupling

In reference [1], only the global power balance of the electrons was considered. The electron-ion coupling was negligible because of the temperature difference between electrons and ions and the operating densities were such that the two populations could be considered as uncoupled. Since the ECH waves couple to the perpendicular momentum of the electrons, a term describing the pitch angle scattering is included in the power balance equation. The analysis has shown that for these ECH discharges, the plasma can be considered as being isotropic. In reference [1] and for the optimum modulating frequency of 237 Hz, the plasma can be considered as being isotropic and transport effects can be neglected. In the present paper, the model is implemented by including a term which describes the electron ion coupling. for the same reason as before, the pitch angle scattering on the electrons can also be neglected. Under these assumptions, the power balance equation can be written as:

$$\frac{dW_e}{dt} = -\frac{W_e}{\tau_e} + P_{OH} + P_{RF} - \frac{1}{\langle\tau_{ei}\rangle}(W_e - W_i)$$

$$\frac{dW_i}{dt} = -\frac{W_i}{\tau_i} + \frac{1}{\langle\tau_{ei}\rangle}(W_e - W_i)$$

W_i is the ion energy, W_e the electron energy, P_{OH} the ohmic power and P_{RF} the ECH power. The energy confinement time of the electrons takes into account the heating power dependence by [2] $\tau_e \propto (P_{OH} + P_{RF})^{-0.7}$. The ion energy confinement time τ_i is kept constant. The global equipartition time is given by [3]

$$\langle \tau_{ei} \rangle = \frac{3 m_i}{8 \sqrt{2\pi} \langle n_e \rangle Z_{eff} \ln(\Lambda)} \cdot \frac{\langle T_e^{3/2} \rangle}{m_e^{1/2}},$$

where $\langle \ldots \rangle$ is a volume average of the corresponding quantity, m_i the ion mass, m_e the electron mass, T_e the electron temperature and n_e the electron density. The volume averages are taken on a circular plasma and assume parabolic temperature and density profiles. The power balance equations are linearized with respect to the modulated RF power $\tilde{P}_{RF}$ around an equilibrium point defined by the average input power $P_{OH0} + P_{RF0}$. The Fourier transformation of the linearized system allows to write this system of equations as: $\tilde{W} = H(\omega, \tau_{ei}, \tau_i, \tau_e) \cdot \tilde{P}_{RF}$ where H is the complex transfer function and $\tilde{W} = \tilde{W}_e + \tilde{W}_i$ is the total energy. In Figure 3, the amplitude and phase of the complex transfer function H are shown. The asymptotic limit is defined by $\lim_{\omega \to \infty} H \propto 1/\omega$. For a density of 5×10^{19} m^{-3} the total amplitude ($H_{\mathrm{ion}}+H_{\mathrm{e}}$) stays lower than the asymptotic transfer function $1/\omega$. This means that, if the asymptotic limit $1/\omega$ of the transfer function is used, the measured power absorption is underestimated if no ion-electron coupling is considered.

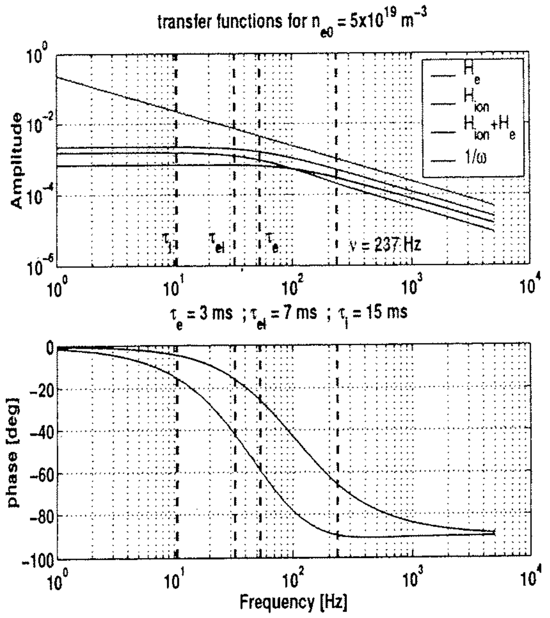

Figure 3 : The phase and amplitude of the transfer function calculated with a $Z_{\mathrm{eff}} = 2$ and an ECH power of 1 MW. $Z_{\mathrm{eff}} = 2$ means that the ionic density is equal to 70 % of the electron density

4. Preliminary results

The DML measurements are compared with the linear ray-tracing absorption code TORAY-GA. The experimental configuration is shown in Figure 1, while the most relevant traces are shown in Figure 4. Two X3 beams carrying 450 kW each are injected from the top of TCV during 1.1 s. Only one of the power sources is modulated at a frequency of 237 Hz during 350 ms. The absorption predicted by TORAY-GA is of 40 %, while the DML measurement results in 65 %. We believe that the discrepancy is to be found in the accuracy of the ray-tracing calculation, which is based on the equilibria calculated by the magnetic reconstruction code LIUQE. This effect together with other effects like diffraction and/or hot plasma effects are presently investigated. More details on experimental results during X3 ECH on ohmic target plasmas can be found in [4]

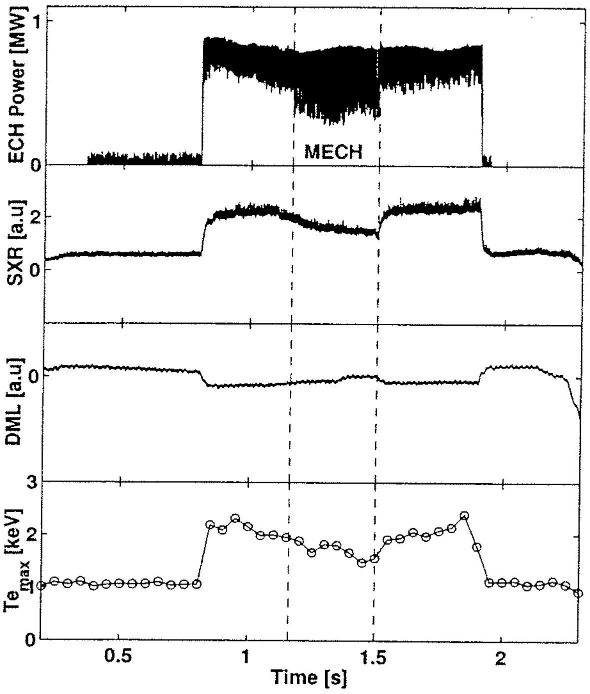

Figure 4 : Temporal traces of a typical shot with X3 MECH. From top to bottom: ECH power, soft-X ray emission, DML signal and Thomson maximum electron temperature.

5. Reference

[1] A. Manini et al., *Plasma Phys. Control. Fusion*, 44, 2002
[2] A. Pochelon et al., *Nucl. Fusion*, (39) 1807, 1999
[3] L. Spitzer Jr., *Physics of Fully Ionised Gases*, (New York: Interscience, 1962)
[4] S. Alberti et al., This conference, poster P-2.073

Plasma Deposition of p-i-n Devices using a Single PECVD Chamber: Study of the Boron Contamination

J. Ballutaud[a], A.A. Howling[a], L. Sansonnens[a], Ch. Hollenstein[a], U. Kroll[b], I. Schönbächler[b], C. Bucher[b], M. Poppeller[c], J. Weichart[c], A.Buechel[c] and F. Jomard[d]

[a]*EPFL-Centre de Recherches en Physique des Plasmas, Lausanne, Switzerland*
[b]*Institut de Microtechnique, Neûchatel, Switzerland*
[c]*Unaxis Displays, Trübbach, Switzerland*
[d]*Laboratoire de Physique du Solide et Cristallogénèse, CNRS Meudon-Bellevue, France*

Plasma-enhanced chemical vapour deposition (PECVD) of photovoltaic p-i-n solar cells in a single plasma reactor offers advantages of time and cost compared to multi-chamber processes which use separate reactors for production of the p-, i- and n-layers. The p-layer is a boron-doped silicon thin film deposited by plasma in a gas mixture containing silane and a boron source gas. In a single chamber PECVD reactor, the silane plasma subsequently used to deposit the undoped silicon intrinsic film (i-layer) leads to the recycling of impurities [1]. It can cause boron contamination from the reactor walls, pumping ducts or layer itself. The resulting boron contamination of the i-layer degrades the performance of the final solar cell (Fig. 1). Therefore, for mass production of solar cells in a single chamber reactor, it would be practical if some plasma treatment applied between the deposition of the p- and i-layers could reduce the boron contamination and so maintain the cell quality.

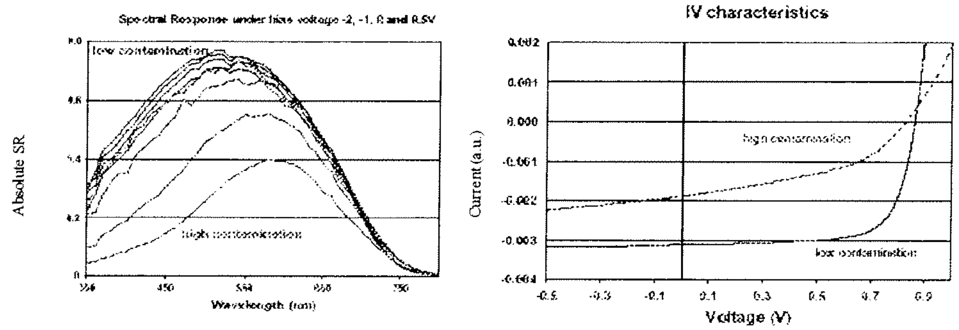

Fig. 1 : Deterioration of cell performance with boron contamination : spectral response and IV characteristics

In this work, various techniques to reduce the boron contamination were investigated. Their effectiveness was evaluated by means of Secondary Ion Mass Spectroscopy (SIMS), to study the boron concentration depth profile across the p-i interface. For the purposes of p-i-n solar cell fabrication, the boron contamination of the i-layer should not exceed 10^{17} atom/cm^3. Trimethylboron (TMB), $B(CH_3)_3$, instead of diborane, B_2H_6, was used as the boron source gas because it has superior thermal stability in the hot reactor and causes less contamination

[2]. The experimental apparatus is a modified version of the industrial KAI-S reactor commercialised by Unaxis Displays. It is a parallel plate capacitively-coupled reactor of dimensions 47 cm width × 57 cm length with 2.4 cm height between RF electrode and ground electrode. A loadlock chamber was used to introduce substrates in the reactor without breaking vacuum. Sequences of p-i layers were deposited on silicon wafers put on a glass substrate 47 cm × 37 cm × 1 mm to test different procedures between the p- and i-layers. The gas parameters used for the p-layer were: flow rates 70/60/1/50 sccm of SiH_4/CH_4/ TMB/H_2 at 0.4 mbar; for the i-layer: flow rates 160/40 sccm of SiH_4/H_2 at 0.5 mbar. The excitation frequency was 27.12 MHz at 60 W RF power for an i-layer deposition rate of approximately 0.3 nm/s at substrate temperature of 200 °C. The procedures investigated were: pumping between p-layer deposition and i-layer deposition, gas purging, and various plasma treatments of the p-layer.

First, it was checked if physisorption or backstreaming of the TMB dopant gas was a source of contamination [2]. The substrate was exposed to a TMB gas flow in the reactor, without plasma, for 20 minutes before plasma deposition of an i-layer. This i-layer was found not to be contaminated, showing that the boron contamination is not simply due to traces of TMB gas which are desorbed from the reactor walls, pumpline, or pumps but is due to boron-containing radicals created during p-layer deposition. However, following plasma deposition of a p-layer, flushing with an inert gas (Fig. 2) or pumping for several minutes were both ineffective in preventing boron contamination of the i-layer. All-night pumping did reduce the contamination to an acceptable level (Fig. 2), which suggests that the boron source was slowly desorbed, or that the boron was slowly transformed and eventually immobilised in the p-layer.

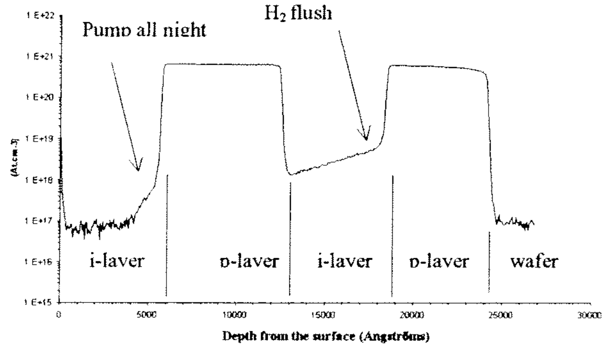

fig. 2 : Boron SIMS profile H2 flush and pump all night

The boron contamination is trapped in the reactor with a confinement time much longer than the plasma processing time of a solar cell, which means that some procedure must be found to reduce the release of boron during i-layer deposition to maintain a high throughput.

Two types of plasma treatment were found to give i-layers with sufficiently low contamination, although it was necessary to remove the substrate into the loadlock to protect the deposited p-layer, otherwise the solar cell performance was degraded. The first treatment was 10 minutes of plasma etch cleaning (using a SF_6, O_2 and He gas mixture) which removed the p-layer deposit from the reactor walls and eliminated almost all boron contamination (Fig. 3) of the subsequent i-layer. This may appear a trivial result, but the implication is that the boron from the p-layer of the substrate itself does not contribute to i-layer contamination. This is also the case in multi chamber processing.

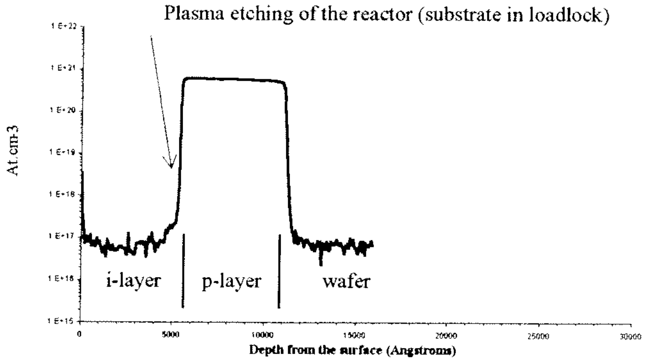

Fig. 3 : Boron SIMS profile, etch (substrate in loadlock) between p-layer and i-layer

The second strategy is to immobilise the boron in the p-layer on the reactor walls by means of an oxidising plasma: 10 minutes of plasma treatment with CO_2 [3] or O_2 (Fig.4) between the p-layer and i-layer (always with substrate in the loadlock) was observed to eliminate almost all boron contamination. Exposure to O_2 gas alone would be expected to oxidise boron in the top monolayer, but flushing with O_2 gas was in fact ineffective. Therefore, efficient oxidation requires plasma-produced radicals, and/or oxidation of sub-surface boron assisted by ion bombardment. Boron desorption by ion bombardment alone is insufficient because the same procedure using an argon or hydrogen plasma, instead of oxygen, did not reduce boron contamination of the i-layer.

Contamination was reduced, but not eliminated, by buring the boron on the reactor walls by a thin i-layer deposited while the substrate was in the loadlock. This shows that the boron source is in the reactor, not in the pumping line or pumps, because the pathlength of silane radicals out of the reactor is not more than a few cm. From the industrial point of view, however, an *in situ* plasma treatment which does not require moving the substrate to the loadlock would be preferable. It was clear that i-layer deposition at 60 W RF power, corresponding to 0.3 nm/s, caused too much plasma-induced desorption of boron from the previous p-layer. But when the RF power was reduced to 30 W to deposit at only 0.05 nm/s, the boron desorption rate was low enough to avoid excessive contamination, presumably due to the decrease in ion flux and energy in the low power plasma. Moreover, since a thin intrinsic buffer layer was sufficient to bury the boron in the p-layer from the higher power plasma, a satisfactory procedure was to initially deposit a 10 nm i-layer at 0.05 nm/s before accelerating to 0.3 nm/s. This procedure prolongs the process time by 3 minutes, and offers an alternative to removing the substrate to the loadlock. The time penalty could be minimised by finding a compromise between the RF power ramp rate and the level of contamination which can be tolerated.

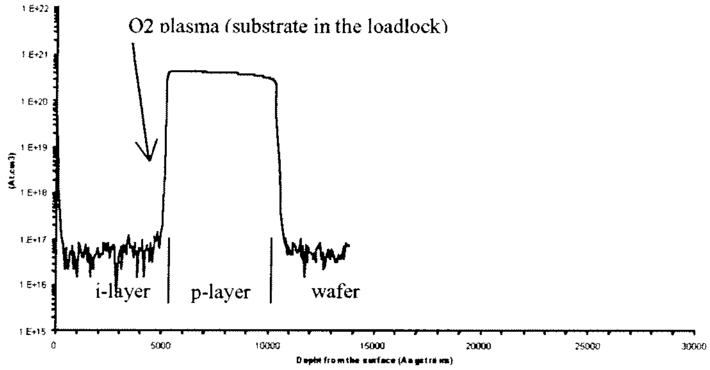

Fig. 4 :Boron SIMS profile, O_2 plasma (substrate in loadlock) between p-layer and i-layer

To conclude, various plasma treatments between the deposition of the p- and i-layers were investigated to avoid boron contamination during fabrication of photovoltaic solar cells in a single chamber reactor. Plasma etch cleaning and plasma oxidation are both effective provided that the substrate is removed to the loadlock during the treatment. Alternatively, the i-layer can be deposited directly after the p-layer provided that the plasma power is strongly reduced during the deposition of a shielding layer to prevent desorption of the boron from the underlying film.

Acknowledgement: This work was financially supported by Swiss Federal Research Grant CTI no. 4559.1.

[1] P. Roca i Cabarrocas, S. Kumar, and B. Drévillon, J. Appl. Phys. **66** (1989) 3286

[2] A. Lloret, Z.Y. Wu, M.L. Thèye, I. El Zawawi, J.M. Siéfert, and B. Equer, Appl. Phys. A **55** 573 (1992).

[3] M. Kubon, N. Schultz, M. Kolter, C. Beneking, and H. Wagner, Proc.12th European Photovoltaic Solar Energy Conference, Amsterdam (1994), p. 1268

Analysis of the Electron Cyclotron Emission from the Non-Thermal Electron Population Generated by ECRH and ECCD

P. Blanchard, S.Alberti, S.Coda, H.Weisen,

Centre de Recherches en Physique des Plasmas
Association EURATOM - Confédération Suisse, EPFL, 1015 Lausanne, Switzerland

Abstract: Measurements of Electron Cyclotron Emission (ECE) from the high field side (HFS) of the TCV tokamak have been made on plasmas heated by second and third harmonic X-mode Electron Cyclotron Heating (ECH) and Electron Cyclotron Current Drive (ECCD). The ECE increases sharply with the local toroidal incidence angle of the X2 EC beams and with the X2 injected power. The measured ECE spectra are modelled using a bi-Maxwellian describing the bulk and the suprathermal electron populations. Suprathermal temperatures between 10 and 50keV and densities in the range $1\cdot10^{17}$ - $6\cdot10^{18}$ m^{-3} are obtained. Good agreement between ECE suprathermal temperatures and energetic photon temperatures, measured by a hard X-ray (HXR) camera, is found. For optically thin X3 LFS ECH injection, reflection of the beam on the inner wall and absorption on the suprathermal electron population partly explain the discrepancy between global energy deposition measurements and first pass calculations.

Introduction

The TCV tokamak (R=0.88m, a<0.24m, B_T<1.54T, I_p<1.2MA) is equipped with six 0.45MW gyrotrons at the second electron cyclotron frequency (X2) and three 0.47MW gyrotrons at the third harmonic (X3). In the case of a Maxwellian plasma, the optical thickness τ^{Xn}, for the X-mode at the n-th harmonic ($n \geq 2$), is proportional to $n_e(k_BT_e/m_ec^2)^{n-1}$[1]. X3 absorption is hence much weaker than X2 absorption. In the thermal bulk of TCV plasmas, X2 is optically thick, while X3 is optically thin. Injection of high power electron cyclotron waves in extraordinary polarisation mode in X2 ECCD and/or in X3 ECH injection configuration creates a non-thermal electron population, which increases the single-pass absorption for X3 Low Field Side (LFS) injection[2]. In X2-ECCD preheated plasmas, a seed suprathermal tail is generated and for LFS X3 injection, the X3 EC beam is first partly absorbed on the thermal bulk at the cold resonance and then interacts with the suprathermal population by increasing this non-thermal population and by increasing its absorption efficiency.

Experimental setup

To study suprathermal electron populations, TCV has been equipped with an ECE radiometer working in the X2 frequency range and connected to a choice of two receiving antennae, on the High Field Side (HFS) of the torus, placed at Z=0m and Z=0.21m. The ECE radiometer is a X-mode 24 channels super-heterodyne radiometer. It covers the frequency range from 78.5GHz to 114.5GHz, corresponding to the second harmonic of the electron cyclotron frequency at the HFS. The frequency bandwidth of each channel is 750MHz, corresponding to a spatial resolution between 0.4 (edge) and 1 cm (center) for the cold resonance.The radiometer is cross calibrated from Thomson scattering measurements during the ohmic phase of the discharge, prior to ECH and ECCD injections.

The flexibility of the EC heating system allows both the toroidal and the poloidal injection angles to be adjusted[2]. The target plasmas used in the experiments reported here have the following parameters: I_p=200kA, q_{95}=3.8, κ=1.31,δ=0.06, B_T=1.45T. The X3 power (P_{X3}=0.47 MW) and the launching angles (ECH heating) are kept constant, whereas the toroidal and poloidal launching angles of the X2 ECH/ECCD are varied.

For typical densities and temperatures of TCV ($n_e(0)$~$2.5\text{x}10^{19}\text{m}^{-3}$, $T_e(0)$~2keV), the plasma is optically thick (the bulk optical depth $\tau_b^{X2} > 10$) and the ECE radiometer provides a measurement of the electron temperature profile if the distribution function is Maxwellian. In these conditions, the plasma behaves like a black body. The radiation temperature T_r is defined by $T_r = 8\pi^3 c^2 I_\omega/\omega^2(1 - e^{-\tau_b})$, where I_ω is the intensity of the EC radiation at the frequency ω. For an optically thick Maxwellian plasma in thermal equilibrium T_r=T_e: the radiation temperature corresponds to the electron temperature. Concerning the ECE, we will refer to the directly measurable quantity $T_{ece} = 8\pi^3 c^2 I_\omega/\omega^2$ as the (apparent) ECE temperature.

Non thermal ECE measurements on TCV

If the plasma is not Maxwellian, e.g. if non-thermal electrons are produced by heating the plasma with EC waves, or if the bulk optical depth is optically thin for the considered radiation, T_r is no longer equal to the bulk temperature. For plasmas heated by central X2 ECCD, P_{X2}=450kW and X3 ECH, T_{ece} up to six time T_b have been measured when the X2 local toroidal angle at the resonance is +35°[2]. Under the assumption of a bi-Maxwellian (bulk+suprathermal) electron distribution function, an expression for the local intensity can be obtained as[3]:

$$I_\omega = \frac{\omega^2}{8\pi^3 c^2}\left[T_b\left(1 - e^{-\tau_b}\right)e^{-\tau_s} + T_s\left(1 - e^{-\tau_s}\right)\right] \qquad (1)$$

with T_b and T_s the electron bulk and suprathermal temperatures, τ_b and τ_s the respective optical depths.

The ECE from suprathermals is frequency-downshifted by the relativistic factor γ. If the radiation is observed from the HFS, this downshifted radiation does not pass through the EC cold resonance and

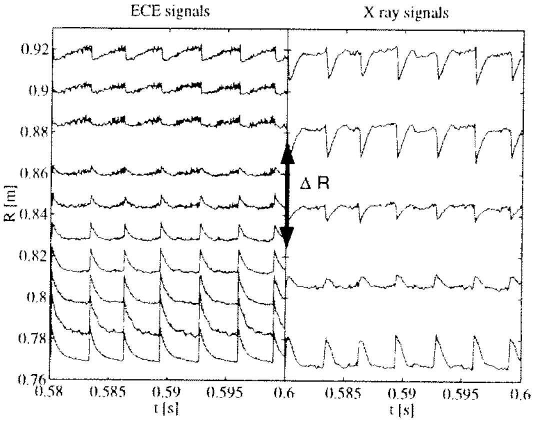

***Figure 1**: Temporal evolution of ECE signals (left) and soft X-ray measurements (right) of shot #21668 with 0.45MW X2 CO-ECCD +17° local angle and 0.47MW X3 ECH injections. The y-axis represents the radial position of these emissions; in the ECE case, this is calculated considering the cold resonance. The amplitude of the signals is arbitrary. The horizontal gray lines shows the position of the inversion radii for both diagnostics.*

is unaffected by the bulk absorption. At any given observation frequency, the intensity of the EC radiation is then the result of a sequence of emission and absorption by electrons from different populations, occurring in different plasma regions. The non-thermal origin of the ECE spectra, in the presence of EC heating, is also clearly demonstrated by the sawtooth activity on the ECE radiometer signals. Comparison of the spatial location of the sawtooth inversion radius, obtained with the ECE radiometer signals and with soft X-ray measurements, clearly shows the effect of the relativistic downshift of the ECE signals emitted by non-thermal population as illustrated in Fig.1. For a radial shift ΔR, where R is the spatial location of the non-shifted event, we obtain the characteristic energy of the non-thermal electrons by $E=m_ec^2(\Delta R/R)$. Based on this relation, for the typical heated plasma studied for this paper, the energy estimation of such non-thermal electrons in the X2+X3 phase is between 30 and 45keV while in the X2 phase alone, the energy is between 15 and 35keV.

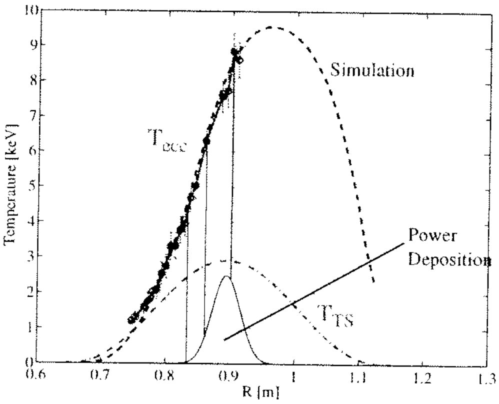

Figure 2: Bi-Maxwellian simulation of the ECE spectra for shot # 21732 with 0.45MW X2 CO-ECCD @+15^o and 0.47MW X3 ECH injections. $\alpha=0$, $\beta=8$. *We used $T_s(0)=11keV$ and $n_s(0)=1.7\cdot10^{18}m^{-3}$.*

We simulate the ECE spectrum considering the electron distribution function as a linear combination of two Maxwellians. One of these characterizes the thermal electrons, the other characterizes the suprathermals. The bulk is determined by Thomson scattering measurements while the shapes of the suprathermal temperature and density are obtained by HXR measurements. We assume $T_s(r)=T_s(0)(1-(r/a)^2)^{\alpha}$, $n_s(r)=n_s(0)(1-(r/a)^2)^{\beta}$, $\alpha \in [-0.5, 0.5]$, $\beta \in [6, 10]$. The central values $T_s(0)$ and $n_s(0)$ are the two free parameters that need to be determined in order to satisfy Eq.1. In this equation, the optical depths are calculated in the hot plasma approximation taking into account finite density effects with intermediate temperature effect corrections[1]. A result of the application of this method is shown on Fig.2.

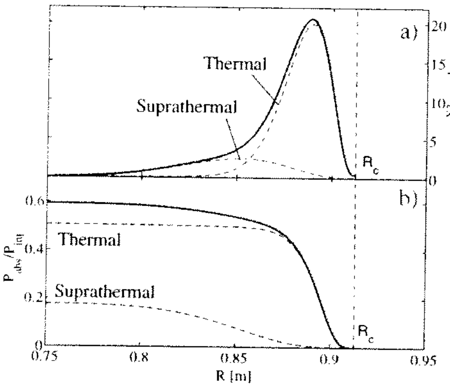

***Figure 3**: **a)** Absorption coefficient for the third harmonic at 118GHz for thermal et suprathermal populations. **b)** Spatial evolution of the X3 absorption by both populations. The thick lines are calculated considering both populations effects.*

The study of optically thin X3 absorbed fraction has shown that the global X3 absorption measured by a diamagnetic loop is larger than predicted by linear calculations made by the code TORAY-GA based on a thermal plasma[5]. In particular, a scan of the X2 toroidal injection angle has shown a maxima in the X3 absorbed fraction for an X2 local toroidal angle of +25^o with global absorption measurements of 100% and simulated absorption of 50% indicating a bulk optical depth $\tau_b^{X3} = 0.7$. The bi-Maxwellian simulation of the corresponding ECE spectra gives $T_s(0)=14\pm6$keV and $n_s(0)=1.3\pm0.4\cdot10^{18}m^{-3}$ corresponding to a suprathermal optical depth $\tau_s^{X3} = 0.2 \pm 0.06$. The X3 absorption on the thermal and suprathermal populations is $1-\exp(-(\tau_s^{X3}+\tau_b^{X3})) = 60 \pm 2.5\%$.

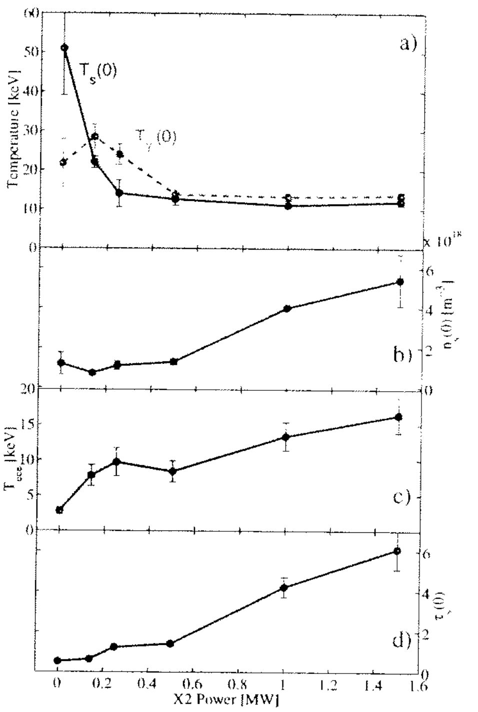

Figure 4**: Results from the bi-Maxwellian simulations applied on a X2 power scan with 0.47MW X3 ECH power.* ***a) *Central suprathermal temperature Ts(0) and photon temperature Tg(0).* ***b)*** *Central suprathermal density.* ***c)*** *Central ECE temperature.* ***d)*** *Second harmonic central optical depth for the suprathermals* $\tau_s(0) \propto n_s T_s$

To study the influence of the EC power on the ECE spectra we carried out a shot-to-shot X2 central power scan from 0 to 1.35MW with +15° toroidal launcher injection angle before 0.47MW X3 central ECH injection. With X2 heating, $T_s(0)$ is approximately 7keV and does not depend significantly on the X2 power while $n_s(0)$ increases linearly from $1\cdot10^{17}m^{-3}$ with P_{X2}=0.25MW to $2\cdot10^{18}m^{-3}$ with P_{X2}=1.35MW. By contrast $n_b(0)=1.6\cdot10^{19}m^{-3}$ for all shots. Results of the bi-Maxwellian approximation method during X2+X3 combined heating are shown in Fig.4. As the X2 power is increased from 0 to 1.35MW, $n_s(0)$ increases from $1.2\cdot10^{18}m^{-3}$ to $5.4\cdot10^{18}m^{-3}$; at the same time $T_s(0)$ decreases from 51keV to 12keV. Moreover, $T_s(0)$ is nearly constant for P_{X2}>0.45MW. The suprathermal temperature during X2+X3 injection is in fair agreement with the photon temperature from the HXR camera. We also see that, as the X2 power increases from 0 to 1.35MW with constant X3 power, the central suprathermal optical depth $\tau_s(0)$ increases from 0.5 to 6.1: the suprathermal population becomes more and more optically thick. The fraction of the electron energy carried by the suprathermals i.e. $\int n_s T_s dV / \int (n_s T_s + n_b T_b) dV$ is 15% with 0.15MW X2 and increases up to 40% with 1.35MW X2 power.

Acknowledgments

This work was partly funded by the Swiss National Science Foundation.

References

[1] M.Bornatici *et al Nucl.Fusion* **23** 1983

[2] S. Alberti *et al* Nuclear Fusion **42** 42 2002

[3]P.Blanchard *et al* Proc. of the 28th EPS conference on Controlled Fusion and Plasma Physics, Europh. Conf. Abstr. **23J** 2001

[4]M.Bornatici & F.Engelmann, Phys Plasmas 1 (1994) 189-198

[5]A.Manini *et al* 2002 Plasma Phys. Control. Fusion **44** 139

Ion Temperature Behaviour and Ion Contribution to the Power Balance Measured by CXRS in Ohmic and ECR Heated Plasmas on TCV

P. Bosshard, B. P. Duval, A. Karpushov, J. Mlynar
Centre de Recherches en Physique des Plasmas
Association EURATOM - Confédération Suisse, EPFL, 1015 Lausanne, Switzerland

1. INTRODUCTION

This paper reports on the first measurements of the ion temperature profile in TCV. These measurements help to improve the understanding of different physics phenomena obtained using the TCV capabilities, such as the dependence of the energy confinement on the plasma shape or the plasma behaviour in presence of additional ECR heating, especially for advanced scenarios with ITB creation by off-axis heating. Some information on the upgrade of the Charge eXchange Recombination Spectroscopy (CXRS) diagnostic performance are also reported.

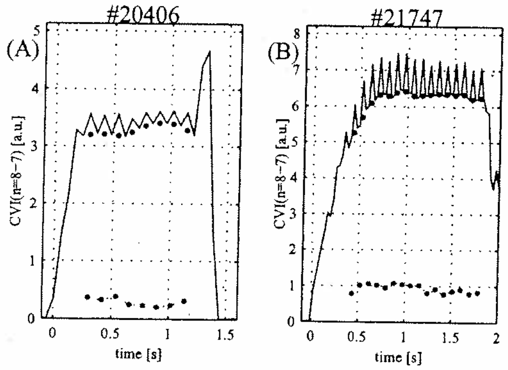

Figure 1. C/X CVI(n=8→7) line (λ=5291Å) intensity for two ohmic shots with $\bar{n}_e$~$6.10^{19}m^{-3}$. Dots represent interpolated passive and calculated active intensities. (A) Before DNBI upgrade: A/P~12%. (B) After upgrade: A/P~20%.

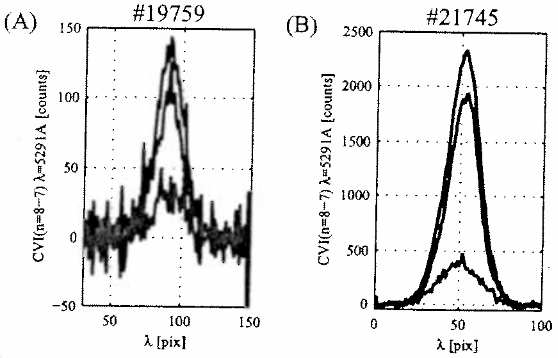

Figure 2. C/X CVI(n=8→7) lines @ 5291Å ($\bar{n}_e$~$3.10^{19}m^{-3}$). The photon collection has been enhanced by ~20x, corresponding to an increase of S/N ratio by ~5x.

2. CXRS AND DNBI UPGRADES

The Charge eXchange Recombination Spectroscopy diagnostic of TCV was limited in two main ways 1): low active / passive signal ratio (A/P) due to low DNBI current and to the high thermal neutral density, which is probably a consequence of the size of the TCV device. The DNBI extracted current has been increased from ~1.7A up to ~3A, increasing the A/P by ~70% at $n_e = 1.5.10^{19}m^{-3}$ and ~20% at $6.10^{19}m^{-3}$ (see figure 1). 2) low S/N ratio due to poor photon statistics. The S/N has been increased by ~5x by enhancing the spectroscopic system throughput. The collected photon flux has been increased by ~20x (see figure 2) following numerous modifications: 1) the number of chords /

radial position has been doubled; the observation volume has been increase by ~4x without significant loss of spatial resolution (limited by the flux surface curvature to ~3cm at the plasma edge); the monochromator (f/~9 @5300Å, F=0.75m) collecting mirror size has been maximised leading to an increase ~2x in the signal level and the slit width has been increased which is accounted for in the spectral analysis by numerical deconvolution of the measured instrumental function.

3. ION CONTRIBUTION TO THE POWER BALANCE AND ION ENERGY CONFINEMENT IN OHMIC PLASMAS

Ion temperature profiles have been measured in ohmic discharges where shape parameters (elongation κ, triangularity δ, in limited and diverted configurations) and plasma density have been modified. T_i profiles are usually flatter than T_e profiles measured with Thomson scattering, the typical peaking factor being of k ~0.2-0.5 ($T_i(\rho) \cong T_i(0) \cdot (1-\rho^2)^k$). Measured central ion temperatures vary from 100eV to 900eV with increasing n_e and total energy content. Measured $T_i(0)/T_e(0)$ ratios may reach values up to 80 - 90% at average plasma densities of ~ 6.10^{19}m^{-3}. Preliminary CXRS measurements of the carbon density (the main impurity of the

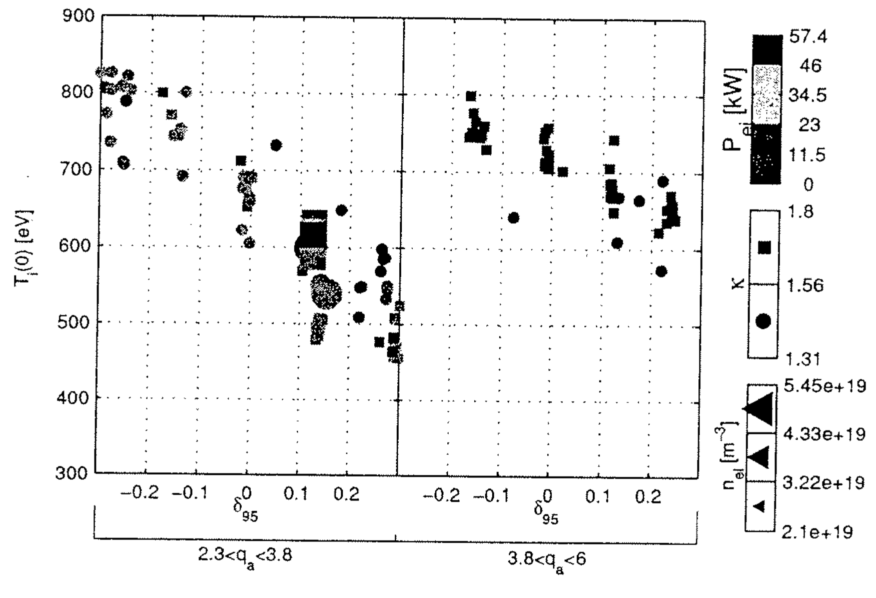

Figure 3. $T_i(0)$ is plotted as a function of the plasma triangularity. Left and right hand side plots correspond to two different I_p scans, where q_{edge} has been maintained roughly constant. Colors represent the e^- - ions equipartition power P_{ei} ; the marker style the elongation, and its size the average electron density. The strong dependence of the ion confinement on triangularity is clearly shown by the decreasing of $T_i(0)$ of 25% - 40% with increasing δ, independently from the ion heating power and any other plasma parameters.

TCV plasmas) give concentrations typically of 3 - 5%. Consequently, the deuterium contribution to the power balance $\frac{W_D}{W_D + W_e}$ is in the range 15 - 40%.
The ion temperature behaviour has been studied as a function of the plasma shape to complete previous studies on the influence of the plasma shape on the energy transport, performed on TCV [2]. Plasma elongation and triangularity have been varied from 1.3 to 1.8 and -0.3 to 0.3 respectively. A current scan from 150kA to 450kA, corresponding to q_{edge} values from 2.3 to 6, has been performed to examine the influence of the plasma shape on the confinement from any intrinsic dependence on I_p. The triangularity is found to be the parameter that most strongly affects the ion and electron confinement. Figure 3 shows that $T_i(0)$ decreases strongly when δ ranging from negative to positive values. This behaviour is not related to the variation of the e^- - ion equipartition power $P_{ei} = W_e.\nu_{ei}$ (where ν_{ei} is e^- - ion collision time), nor to the electron density. As explained in [2], two main phenomena are responsible of this confinement loss: the sawteeth activity disparition at negative triangularities and the thermal conduction $q = -n\chi\nabla T$ rise as flux surface compression increases with δ, leading to more extended regions with high temperature gradients.

4. ION TEMPERATURE BEHAVIOUR IN ECR HEATED PLASMAS

T_i profiles have been measured in second (X2 82.7 GHz) and third (X3 118 GHz) harmonic EC heated plasmas. X2 heated plasmas often have low densities to stay within the density cutoff ($n_{e,X2\text{-cutoff}} = 4.2.10^{19}m^{-3}$) and to limit the refraction of the EC beams. In these conditions e^- - ion coupling is weak and T_i mostly reacts to the density changes caused by gas injection or EC caused desorption on the TCV carbon walls, since the e^- - ion equipartition power P_{ei} is proportional to n_e [3]:

$$P_{ei} \propto n_e \cdot \frac{(T_e - T_i)}{T_e^{-3/2}} .$$

X3 EC allows operation at higher densities ($n_{e,X3\text{-cutoff}} = 11.10^{19}m^{-3}$) where the e^- - ions coupling is expected to be stronger. Figure 4 shows an example of a discharge where X3 heating has been applied on an off-axis X2-preheated plasma [4]. T_i not only reacts to the density variations, but also to the changes of T_e resulting from the additional heating. With X3 heating, $T_e(0)$ rises abruptly before relaxing on a time scale of ~200ms with an increase of n_e. $T_i(0)$ decreases by ~30% from the $T_e^{-3/2}$ dependence of P_{ei} and then rises again following the n_e increase.

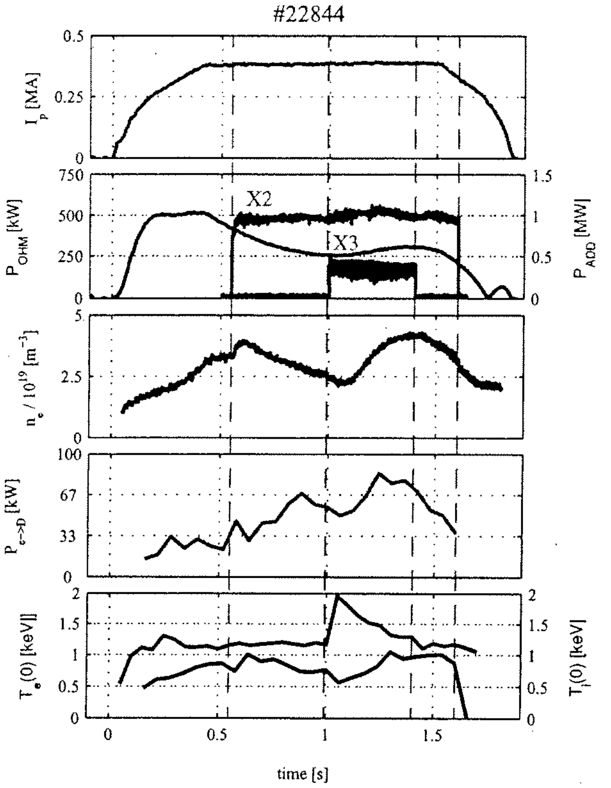

Figure 4. Discharge #22844 has been pre-heated with X2 ECR off-axis heating, before vertical injection of X3 at 1s. $T_e(0)$ rises of ~80% at the X3 injection whereas $T_i(0)$ decreases of 30% following the ion heating power (P_{ei}) evolution. After injection both temperatures relaxe on the same time scale as the density increase.

5. CONCLUSIONS

Investigations of the ion temperature behaviour in ohmic plasmas show that the ion contribution to the power balance is not negligible ($W_i/W_e \leq 60\%$) even in the absence of additional ion heating on TCV. Ion and electron energy confinement degrade strongly with triangularity increasing from negative to positive values. This dependence is explained by the geometrical effect on the temperature gradients at the plasma edge and by the reduction of sawteeth activity at negative triangularities. In EC heated plasmas, T_i follows the evolution of the e^- - ion equilibration power. At low density, as in the case of X2 heating scenarios, only its linear dependence on n_e is observed on T_i. In X3 heated discharges, with average densities reaching $8.10^{19}m^{-3}$, e^- - ion coupling is stronger and T_i also becomes sensitive to the temporal evolution of T_e.

Acknowledgments

This work was partly funded by the Swiss National Science Foundation.

References

[1] P. Bosshard, B. P. Duval, J. Mlynar, H. Weisen, proceedings of EPS 2001, Madeira.
[2] J.-M. Moret, S. Franke and al., Phys. Rev. Letters **79** (11), 1997
[3] J. Wesson, Tokamaks, 2nd edition, p.68, Clarendon Press, 1997
[4] Y. Camenen, F. Hofmann & al., this conference - P-2.075

E × B Flow Effects on ITG Modes in Reverse Shear ASDEX Upgrade Discharges

A. Bottino, S.J. Allfrey, A.G. Peeters[1], O. Sauter, L. Villard and ASDEX Upgrade Team

Centre de Recherches en Physique des Plasmas,
Association EURATOM - Confédération Suisse, EPFL, 1015 Lausanne, Switzerland
[1] *Max-Planck Institut für Plasmaphysik, IPP-EURATOM Association,*
D-85748 Garching bei München, Germany

1. Introduction

Recent experiments with Internal Transport Barriers (ITB) have shown that the anomalous transport is considerably reduced by a radial electric field in the plasma [1]. Several theoretical models predict a strong stabilizing effect on toroidal Ion Temperature Gradient (ITG) modes due to the $\mathbf{E_r} \times \mathbf{B}$ flow. If the plasma rotation is sheared then a decorrelation in the mode structure appears, which tends to stabilize ITG modes. On the other hand, in some plasma discharges the shearing rate criterion does not predict a complete stabilization of the modes even if the criteria for identifying an ITB are satisfied.

In this paper we present a linear stability analysis for electrostatic microinstabilities in high confinement conditions by using the global electrostatic linear PIC code LORB5. This code can directly simulate the effect of the $\mathbf{E_r} \times \mathbf{B}$ drift induced by an imposed radial electric field. In particular we show results obtained using equilibria and equilibrium profiles of the ASDEX Upgrade discharge 13149 in which an Ion Internal Transport Barrier (ITB) was identified.This discharge has a reverse shear configuration and a relatively strong radial electric field.

2. The model

The code LORB5 follows the linear time evolution of quasi-neutral electrostatic perturbations of the local Maxwellian distribution function in a 2D magnetic configuration. In LORB5 the ion dynamic is described by a gyrokinetic model derived by Hahm [2] based on a Vlasov-Poisson system in which the fast ion cyclotron motion has been averaged out. Trapped electrons are modeled using drift-kinetic equations, no finite electron Larmor radius effects are retained. Passing electrons are supposed to respond adiabatically to the perturbation. The time evolution of the perturbed ion distribution function $\tilde{f} = f - f_0$ is given by:

$$\frac{\partial \tilde{f}}{\partial t} + \dot{\mathbf{R}} \cdot \nabla \tilde{f} + \dot{v}_{\|} \frac{\partial \tilde{f}}{\partial v_{\|}} = -\frac{\langle \mathbf{E} \rangle \times \mathbf{h}}{B^*} \frac{\partial f_0}{\partial \mathbf{R}} - \frac{q_i \langle \mathbf{E} \rangle}{m_i} \cdot \mathbf{h} \frac{\partial f_0}{\partial v_{\|}} - (v_{\|} \frac{\partial f_0}{\partial v_{\|}} + \frac{1}{2} v_{\perp} \frac{\partial f_0}{\partial v_{\perp}}) \langle \mathbf{E} \rangle \cdot \frac{\mathbf{h} \times \nabla \mathbf{B}}{B^{*2}}$$

Where $\langle \mathbf{E} \rangle$ represents the gyro-averaged perturbed electric field, $B^* = B + (m_i v_{\|}/q_i) \mathbf{h} \cdot \nabla \times \mathbf{h}$ and $(\mathbf{R}, v_{\|}, v_{\perp}, \alpha)$ are the guiding center variables. The $\mathbf{E_r} \times \mathbf{B}$ drift velocity $\mathbf{u} = (-\nabla \phi_0 \times \mathbf{B})/\mathbf{B}^2$, with a given $\phi_0(\psi_p)$, modifies the unperturbed guiding center trajectories:

$$\begin{aligned} \dot{\mathbf{R}} = \quad & v_{\|} \mathbf{h} + \mathbf{u} \big[1 - \tfrac{1}{\Omega} \mathbf{h} \cdot \nabla (\mathbf{u} + v_{\|} \mathbf{h}) \big] + \tfrac{1}{\Omega} \mathbf{h} \times \big[v_{\|} \nabla \times (\mathbf{u} + v_{\|} \mathbf{h}) \times \mathbf{h} + \\ & \qquad + \mu \nabla B + \tfrac{1}{2} \nabla u^2 \big] \\ \dot{v}_{\|} = \quad & -\mathbf{h} \cdot \big[\mu \nabla B + \tfrac{1}{2} \nabla u^2 \big] - \mathbf{u} \cdot \big[\mathbf{h} \times \nabla \times (\mathbf{u} + v_{\|} \mathbf{h}) \big] \end{aligned}$$

For small Mach numbers of the $\mathbf{E_r} \times \mathbf{B}$ drift velocity $\mathbf{u}$, terms of order $(u/v_{thi})^2$ and $\epsilon_B (u/v_{thi})$ can be neglected. The model is closed by a quasi-neutrality equation valid up to $k_{\perp} \rho_L \simeq 2$ [3]:

$$(1 - \nabla_{\perp} \tfrac{T_i}{m_i \Omega^2} \nabla_{\perp})(\bar{n}_i - \tilde{n}_e) = \nabla_{\perp} \cdot \big(\tfrac{n_0}{B \Omega} \nabla_{\perp} \phi \big)$$

$$\tilde{n}_e = n_0 (1 - \alpha_b) \tfrac{e\phi}{T_e} + \int_{trapped} B^* \delta(\mathbf{R} + \rho - \mathbf{x}) \tilde{f}_e \, d\alpha \, d\mu \, dv_{\|} \, d\mathbf{R}$$

$$\bar{n}_i = \int \tilde{f}(\mathbf{R}, v_{\|}, \mu) \delta(\mathbf{R} - \mathbf{x} + \rho) d^6 z$$

The code LORB5 is coupled with the MHD equilibrium code CHEASE [4].

3. Results

Equilibrium profiles for the ASDEX UPGRADE discharge 13149 are shown in Figure 1.
The radial electric field has been computed using a force balance equation.

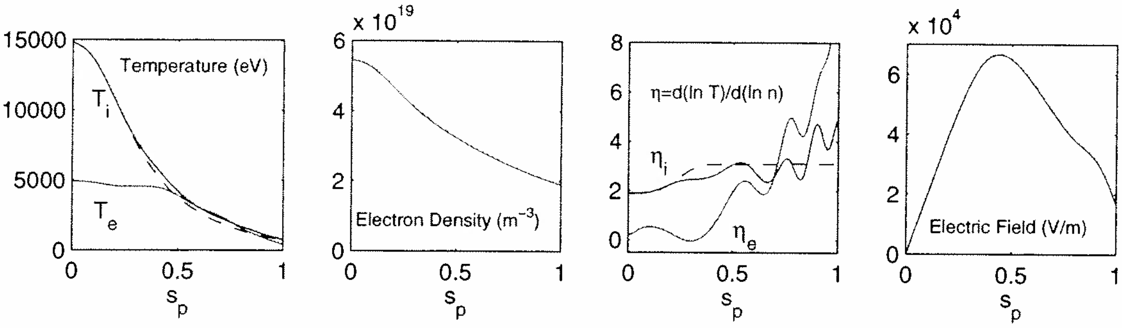

Figure 1. *Interpolated experimental profiles for electrons (red) and ions (blue) as a function of* $s_p = \sqrt{\psi_p/\psi_{p,edge}}$. *Black dashed lines correspond to a flat* η_i *profile.*

In this shot the main contribution to the force balance comes from the $(v_\varphi B_\theta)$ term. Figure 2 shows the complete spectrum of the most unstable modes in the absence of applied radial electric field for fully adiabatic and drift-kinetic trapped electrons. Trapped electron dynamics further destabilize the mode but the frequency is still in the ion diamagnetic direction, therefore the dominant electrostatic mode is an ITG. Moreover, this equilibrium is unstable even when a $\eta_i(s_p) = 0$ profile is used, in this case the instability is driven by trapped electrons and the modes are pure Trapped Electron Modes (TEM). All the ITG modes tend to be localized in the region where the shear is positive and where the η_i profile has a local maximum. In Figure 3 we see that for $n = 40$ there are two modes growing with comparable growth rate, localized around $s_p = 0.55$ and $s_p = 7.3$, corresponding to the first two bumps of the η_i profile. We performed another set of simulations using a flat η_i profile (black dashed lines in Figures 1 and 2). The corresponding ion temperature profile is still inside the experimental error bars. Local bumps on the η_i profile do not affect the global behavior of the system: the growth rate and the mixing length estimate for the diffusion coefficient of the most unstable modes are very close to the previous ones. The radial position of the modes increases linearly with n.

The applied radial electric field has a strong stabilizing effect even with trapped electrons and it is strong enough to completely stabilize ITG modes. Figure 4 shows that for $n = 30$ the ITG mode becomes stable for values of the Mach number lower than the experimental one.

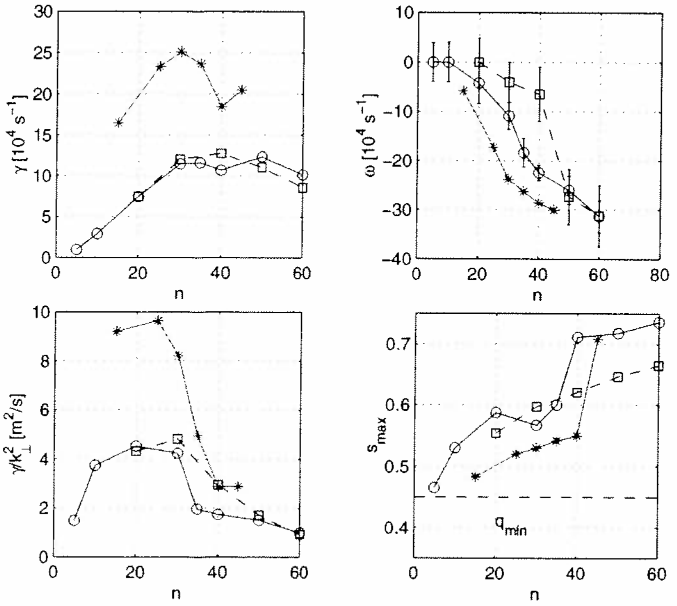

Figure 2. *Growth rates (a), real frequency (b), mixing length estimation of* χ *(c) and radial position (d) for fully adiabatic (blue circles) and trapped (red stars) drift-kinetic electrons. Black squares correspond to flat* η_i *profile, adiabatic electrons.*

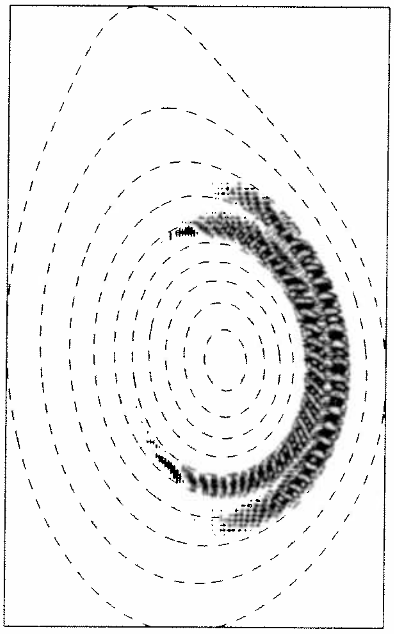

Figure 3. *Poloidal plot of the perturbed electric potential for* $n = 40$, *adiabatic electrons, interpolated* T_i *profile.*

It must be underlined that, linearly, both the local shear and the local value of u, combined with the magnetic shear, contribute to the stabilization [5]. In our simulations we see that a non-zero local value of the $\mathbf{E_r} \times \mathbf{B}$ flow shifts away the maximum of the mode amplitude from the unfavorable ∇B region [6]. This effect is supposed to be less important in the non-linear phase, where the turbulent behavior of the system breaks the ballooning structure of these modes.

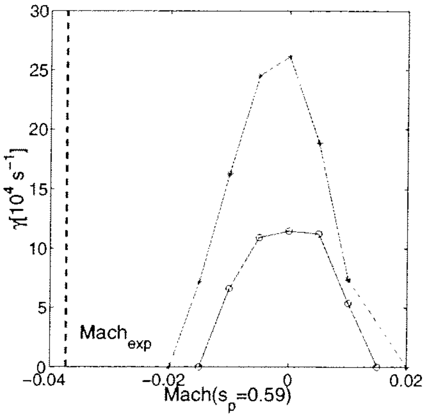

Figure 4. *Mach number scan, $n = 30$, for fully adiabatic (blue circles) and trapped (red stars) electrons.* $Mach(s_p = 0.59)_{exp} = -0.037$.

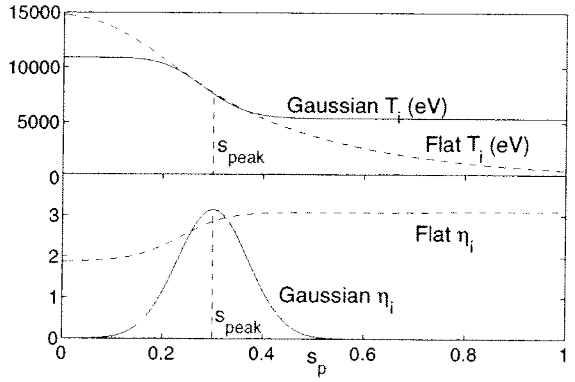

Figure 5. *Gaussian η_i profile centered at $s_{peak} = 0.3$ and corresponding T_i profile,* $\tau(s_{peak}) = \tau(s_{peak})_{exp}$.

In order to study the behavior of the system in the negative shear region, we have produced local ion temperature profiles. The corresponding η_i profile is a Gaussian having an amplitude comparable with the maximum value of the flat η_i profile, $\eta_i(s_{peak}) \simeq 3.2$. The Gaussian width has been chosen larger thn the average radial extension of the mode $n = 30$, flat η_i profile. An example of a Gaussian centered in $s_p = s_{peak} = 0.3$ is given in Figure 5. By displacing the center of the Gaussian along the minor radius we get informations about the local stability of the system. Results for fully adiabatic electrons are summarized in Figure 6, black squares. When the Gaussians are centered in the positive shear region we find modes that have growth rates very close to the global ones. In the negative shear region this magnetic configuration allows for unstable modes but they are much less unstable.

In the negative shear region the ratio $\tau(s_p) = T_e(s_p)/T_i(s_p)$ becomes small while it stays close to unity outside q_{min}. It is well known that small values of τ have a strong stabilizing effect on ITG modes. Another set of simulations has been performed by setting for each Gaussian profile $\tau(s_{peak}) = 1$ (Figure 6, red circles).

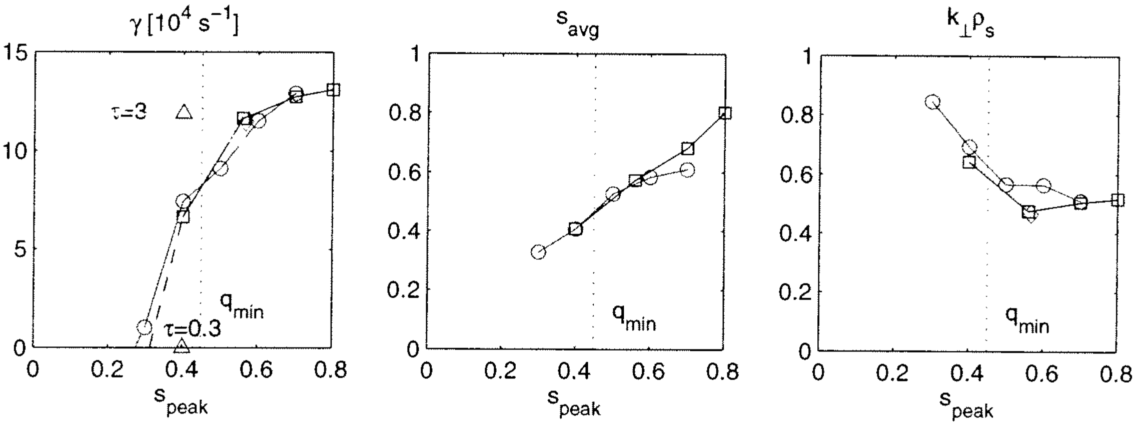

Figure 6. *Growth rate (a), radial position (b) and $k_\perp \rho_s$ (c) of the most unstable modes as a function of s_{peak} for $\tau(s_{peak}) = \tau(s_{peak})_{exp}$ (black squares) and $\tau(s_{peak}) = 1$ (red rircles). Green diamonds, flat η_i profile. Blue triangles, Gaussian profile, $s_{peak} = 0.4$, $\tau(0.4) = 0.3$ and $\tau(0.4) = 3$.*

The experimental value of τ contributes to the stabilization, but it is not strong enough to justify the observed behavior inside q_{min}. The effect of τ can be seen in Figure 6 (blue triangles): $\tau(s_{peak}) = \tau(0) \simeq 0.3$ completely stabilize the ITG mode for $s_{peak} = 0.4$, while the growth rate doubles with $\tau(s_{peak}) = 3$.

The reversed shear configuration itself plays a role in the stabilization. We have produced a new set of equilibria with different q profiles by changing the current profile and keeping the plasma shape and the total current ($I_P \simeq 1MA$) constant (Figure 7). These q profiles are equivalent for $s_p > 0.5$, therefore the results obtained with global profiles are essentially the same. When local T_i profiles, with $\tau(s_{peak}) = 1$, are used (Figure 8) the growth rates obtained with flat or monotonic safety factor profiles show the usual weak linear dependence in the aspect ratio and unstable modes are found down to $s_p \simeq 0.2$. Therefore these two magnetic configurations are much more unstable, for $s_p < q_{min} \simeq 0.45$, than the reverse shear experimental equilibrium. Those modes tend to become slab-like and to have a narrow radial extension and their contribution to the transport could be weak. Trapped electron dynamics can further destabilize these modes. Therefore a similar local analysis will be performed using local T_e profiles and including trapped electrons in the simulation.

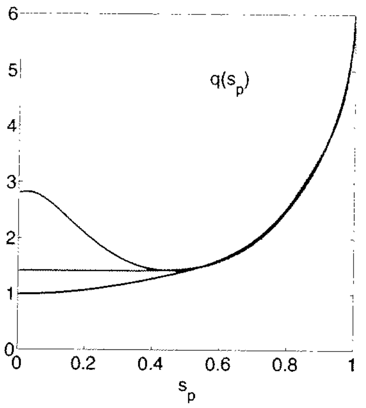

Figure 7. Experimental q profile (blue), flat (red) and monotonic (black) q profiles, constant total current ($I_P \simeq 1MA$)

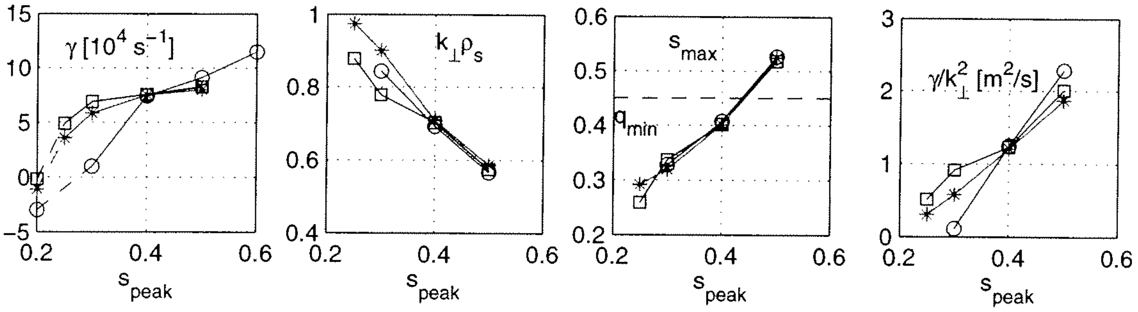

Figure 8. *Growth rate (a), $k_\perp \rho_s$ (b), radial position (c) and mixing length estimation of χ (d), $\tau(s_{peak}) = 1$. for flat (red stars), monotonic (black squares) and reversed (blue circles) q profiles.*

4. Conclusions

The ASDEX Upgrade discharge 13149 is linearly stable when the equilibrium radial electric field is taken into account. Without electric field, the global mode spectrum shows that the most unstable modes are ITG modes, localized in the positive shear region. Unstable modes can be found inside q_{min}, when local η_i profiles are used, albeit with smaller growth rates . In addition to the $\mathbf{E_r} \times \mathbf{B}$ flow, we conclude that at least two other physical mechanisms contribute to stabilize these modes: the reverse shear profile and, to a lesser degree, the local value of τ.

This work was partly supported by the Swiss National Science Foundation. Simulations were performed on the parallel servers SGI Origin 3800 and SWISS-T1 of the Ecole Polytechnique Fédérale de Lausanne.

References

[1] K.H. Burrell, Phys. Plasmas **3**, 4658 (1996)

[2] T.S. Hahm, Phys. Plasmas **3**, 4658 (1996)

[3] A. Bottino *et al.*, Theory of Fusion Plasmas, Int. Workshop, Varenna, 2000, 327

[4] H. Luetjens, A. Bondeson and O. Sauter, Comput. Phys. Commun. **97**, 219 (1996)

[5] L. Villard, A. Bottino and O. Sauter, Phys. Plasmas **9**, (to appear in June 2002)

[6] M. Maccio, J. Vaclavik and L. Villard, Phys. Plasmas **8**, 895 (2001)

Comparisons between Semi-Lagrangian Drift-Kinetic Code and PIC Code Simulations for ITG Studies

M. Brunetti, V. Grandgirard[1], S. Allfrey, A. Bottino, P. Bertrand[2],
P. Ghendrih[1], O. Sauter, J. Vaclavik, L. Villard

CRPP, Association Euratom-Confédération Suisse, EPFL,
1015 Lausanne, Switzerland
[1]*DRFC, Association Euratom-CEA, CEA Cadarache,*
13108 St Paul-lez-Durance, France
[2]*LPMIA, Université Henri Poincaré-Nancy 1, BP 239,*
54506 Vandoeuvre-les-Nancy, France

1 Introduction

In this paper we focus on micro-instabilities destabilized by spatial inhomogeneities, particularly those driven by ion temperature gradients (ITG), which are commonly considered leading candidates to explain the anomalous transport in magnetically confined fusion plasmas. Nonlinear gyrokinetic simulations play an important role in understanding the physics of these micro-instabilities [1]. We present results obtained with a recently developed semi-Lagrangian (SL) code both in the linear and the non-linear regime of the ITG instability, and we compare these results with those obtained with Particle in Cell (PIC) codes which solve the same equations [2, 3].

2 Semi-Lagrangian code

In the SL code, a uniform magnetic field $\vec{B} = B\hat{z}$ in a periodic cylindrical plasma is considered, electrons are assumed adiabatic and finite Larmor radius effects are neglected. Thus, the characteristics of the ions are the guiding-centre (GC) trajectories

$$\vec{v}_{GC} = \frac{\vec{E} \times \vec{B}}{B^2}, \qquad \frac{dz}{dt} = v_{\|}, \qquad \dot{v}_{\|} = \frac{q}{m_i} E_z \tag{1}$$

$\vec{E}$ being the electric field, $q = Ze$ and m_i the ion charge and mass, respectively. The ion distribution function $f(r, \theta, z, v_{\|}, t)$ obeys

$$\frac{\partial f}{\partial t} + \vec{v}_{GC} \cdot \vec{\nabla}_{\perp} f + v_{\|} \frac{\partial f}{\partial z} + \dot{v}_{\|} \frac{\partial f}{\partial v_{\|}} = 0 \tag{2}$$

The system of equations is closed by invoking quasi-neutrality

$$-\vec{\nabla}_{\perp} \cdot \left[\frac{n_0(r)}{B\Omega_{ci}} \vec{\nabla}_{\perp} \Phi \right] + \frac{e n_0(r)}{T_e(r)} (\Phi - < \Phi >) = n_i - n_0 \tag{3}$$

where the first term on the left hand side is the polarization term, $\Phi(r, \theta, z, t)$ is the electric potential, $\vec{E} = -\vec{\nabla}\Phi$, $< . >$ represents the average on the magnetic field lines,

$n_i(r,\theta,z,t)$ is the ion density, $n_0(r)$ is the equilibrium density, $T_e(r)$ is the electron temperature profile and $\Omega_{ci} = qB/m_i$. The integration of the Vlasov equation, Eq. (2), is performed using a time-splitting method and the fact that f is constant along the characteristics of the particles [4, 5]. The Poisson equation, Eq. (3), is solved using a finite element method. The plasma is initialized by exciting a superposition of ITG modes (m,n) with random phases and amplitudes, $f(r,\theta,z,v_\parallel,0) = f_M[1+h(v)g(r)\sum_{mn}\epsilon_{mn}\cos(2\pi nz/L_z + m\theta + \alpha_{mn})]$, where $f_M(r,v_\parallel) = \left(n_0/\sqrt{2\pi T_i/m_i}\right)\,\exp(-m_i v_\parallel^2/2T_i)$, L_z is the cylinder length, and h and g are fourth order polynomials with Dirichlet boundary conditions. The results presented here correspond to simulations with a $(128 \times 64 \times 32 \times 64)$ discretization and $dt = 1$.

3 Linear regime

In order to compare the results of the SL code with analytical values, we neglect the polarization term in Eq. (3) and we consider a flat density profile, $n_0 =$ constant. Moreover, we set the cylinder length to $L_z/\rho_s = 628$ (where $\rho_s = \sqrt{k_B T_{e0}\, m_i}/eB$), the radius to $L_r/\rho_s = 10$ and the electron temperature profile to a constant. The ion temperature profile is such that $d\ln T_i/dr = -\kappa_T \cosh^{-2}[(r - r^*)/\Delta r_T]$ (with $\kappa_T = 4$, $\Delta r_T/\rho_s = 0.1$ and $r^* = 0.5\ L_r$) and $T_i(r^*) = T_{i0} = T_{e0}$. In the limit in which the ITG frequency ω is such that $\omega_{Ti} \gg \omega \gg k_z v_{thi0}$ (where $\omega_{Ti} = (k_\theta/qB)\ dT_i/dr$ is the diamagnetic drift frequency related to the ion temperature gradient and $v_{thi0} = \sqrt{k_B T_{i0}/m_i}$), an unstable mode exists whose growth rate can be analytically estimated and is given by $\gamma = \sqrt{3}\ |k_z^2\ v_{thi0}^2\ \omega_{Ti}|^{1/3}/2$. In Fig. 1 (left), the computed and the analytical values of the growth rate are shown for ITG modes with $n = 4$, $m = 10, ..., 20$. A very good agreement

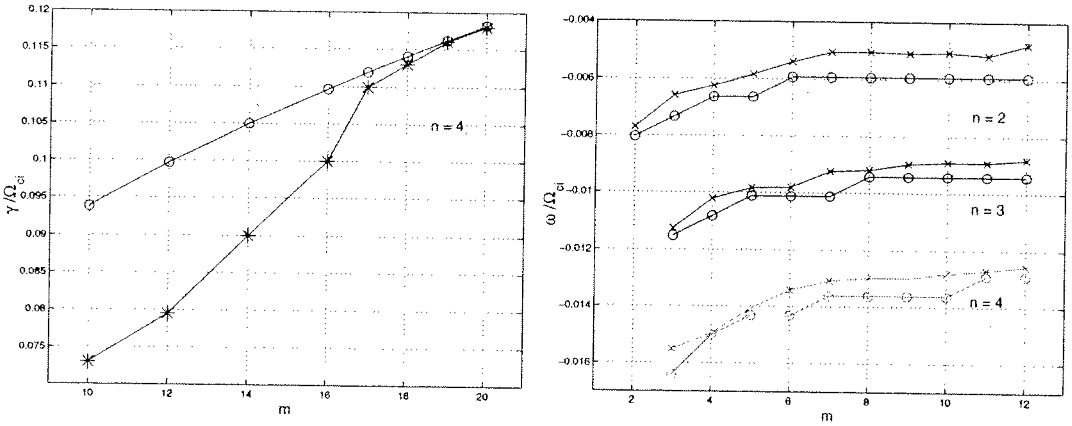

Figure 1: (left) ITG growth rates: numerical (∗) and analytical (o) values; (right) ITG frequencies: values obtained with the SL code (×) and with LORB5 (o).

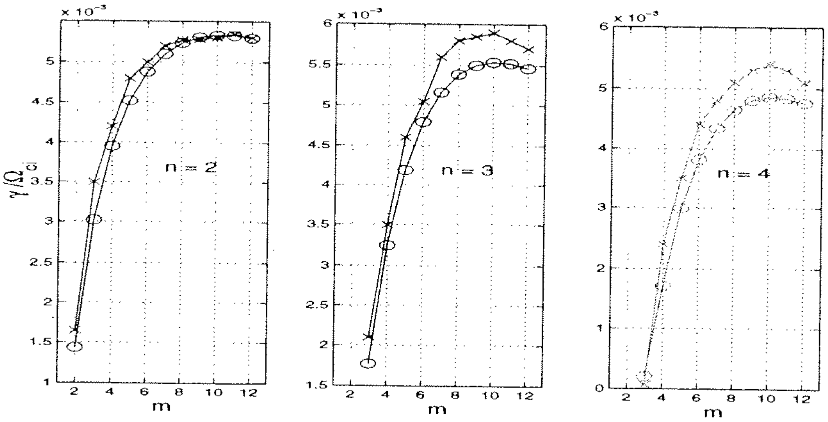

Figure 2: ITG growth rates: values obtained with the SL code (×) and with LORB5 (o).

is reached when the corresponding ITG frequency satisfies the condition in which the analytical formula holds, $\omega \gg k_z v_{thi0} = 0.04\ \Omega_{ci}$ (in the present case for $m > 16$).

When the polarization term is included in Eq. (3), the ITG frequencies and growth rates obtained with the SL code are compared with those obtained with the code LORB5. For the comparisons with the PIC codes we use the following configuration: $L_r/\rho_s = 14.5$, $L_z/\rho_s = 1508$, $\kappa_n = 0.8$, $\Delta r_n/\rho_s = 0.2$, and the other parameters set as before. The electric potential Φ is Fourier filtered in the periodic coordinates, as is done in the PIC codes (the filter retains modes up to $|m| = 16$ and $|n| = 8$). The results are plotted in Fig. 1 (right) and Fig. 2, and show a good agreement between the codes.

4 Non-linear regime

In the non-linear regime, the saturation of the ITG instability occurs. We compare the results obtained with the PIC code ORB5 using 33 million tracers (PIC 33) and 67 million tracers (PIC 67) with those obtained with the SL code. In performing this

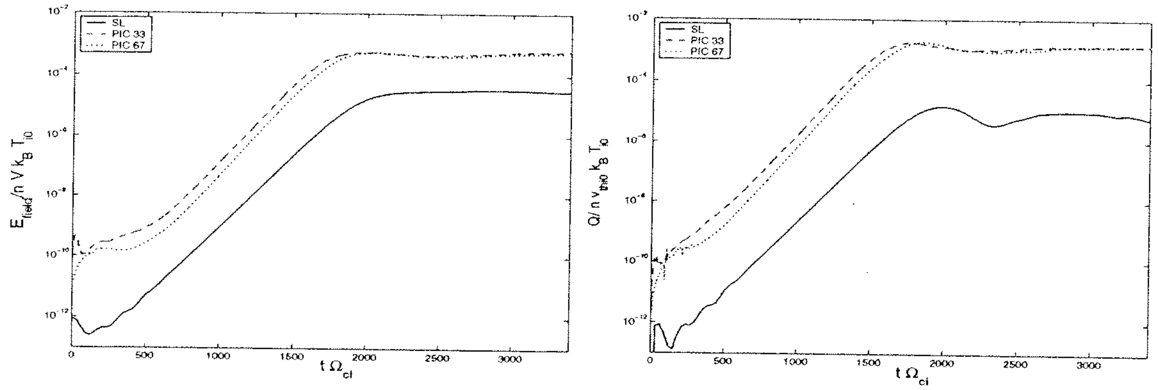

Figure 3: Comparison between the SL code (solid blue), ORB5 with 33 million tracers (dashed red) and ORB5 with 67 million tracers (dotted black): (left) time evolution of the field energy and (right) of the heat flux.

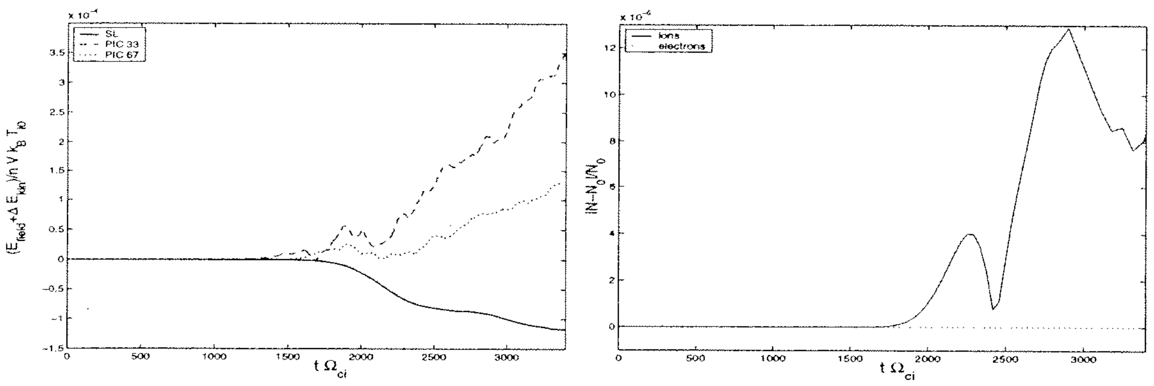

Figure 4: (left) Comparison between the SL code (solid blue), ORB5 with 33 million tracers (dashed red) and ORB5 with 67 million tracers (dotted black): time evolution of the total energy; (right) SL code: time evolution of the relative error in the number of particles.

comparison, we do not include modes with $n = 0$. In Fig. 3 we show the time evolution of the field energy (left) and of the heat flux (right). Even if the overall behavior of these quantities obtained with the two codes is very similar, the level of saturation attained is different (i.e., a factor 100 in the flux). This is an issue that we plan to investigate better in the future. The conservation of the total energy (see Fig. 4, left), which is an important property to verify the quality of a numerical simulation, is equally good in PIC 67 and SL. The latter conserves the number of particles N with a good accuracy (see Fig. 4, right), the relative error in N being of the order of 10^{-5} at the end of the simulation.

5 Conclusions and further work

A SL code has been developed which is able to describe the non-linear phase of the ITG modes instability conserving the total energy of the system to a good accuracy comparable to that attained with the PIC code ORB5. Further investigations are necessary to understand the different level of saturation observed in the heat flux with the two codes.

References

[1] F. Jenko and W. Dorland, *Plasma Phys. Control. Fusion* **43**, A141 (2001) .

[2] A. Bottino et al., *Th. Fusion plasmas* (Proc. Int. Workshop, Varenna, 2000), Ed. Compositori, Bologna, 2001.

[3] T.M. Tran et al., *Th. Fusion Plasmas* (Proc. Int. Workshop, Varenna, 1998), Ed. Compositori, Bologna, 1999.

[4] C.Z. Chen and G. Knorr, *Journal of Comput. Phys.* **22**, 330 (1976) .

[5] E. Sonnendrücker et al., *Journal of Comput. Phys.* **149**, 201 (1999).

Unfolding the Dynamics of Suprathermal Electrons: Experimental and Numerical Tools on the TCV Tokamak

S. Coda, S. Alberti, P. Blanchard, T.P. Goodman, M.A. Henderson, P. Nikkola,
Y. Peysson[a], O. Sauter

Centre de Recherches en Physique des Plasmas
Association EURATOM-Confédération Suisse
Ecole Polytechnique Fédérale de Lausanne, CH-1015 Lausanne, Switzerland

[a]*Département de Recherches sur la Fusion Contrôlée, Association EURATOM-CEA,*
CEA/Cadarache, 13108 Saint Paul-lez-Durance Cédex, France

1. Introduction

Non-equilibrium systems are common in nature, and it is therefore not surprising that electron velocity distribution functions in plasmas often depart from the equilibrium Maxwellian state. Accretion disks around neutron stars, solar flares, coronal mass ejections and interplanetary shocks are familiar examples of space plasma settings in which significant suprathermal electron populations are found. The principal means by which we observe and study these electrons, and indeed we know they exist at all, are the radiation fields they emit upon being accelerated either by a magnetic field (cyclotron emission) or by Coulomb collisions, mainly with ions (bremsstrahlung). By studying the properties of the radiation, we seek to understand the fundamental processes that govern the suprathermal distributions: acceleration, momentum and energy transfer to slower particles, spatial diffusion. Additionally, owing to the complexity of these processes, computer modelling is an indispensable additional tool.

One process that can create and sustain a suprathermal electron population in laboratory plasmas is heating with rf waves. In particular, current drive by lower hybrid waves or electron cyclotron waves (ECCD) operates specifically on electrons travelling at substantially suprathermal velocities. Theory has succeeded in explaining many aspects of current drive, but discrepancies remain in its localisation and efficiency. The importance of current drive for current profile manipulation and instability control in a next-step fusion device motivates steady interest in these wave-particle interaction processes and in the properties of the corresponding non-Maxwellian distributions.

2. Tools on TCV

The TCV tokamak (R=0.88 cm, a=0.25 cm, I_p<1 MA, B_T<1.54 T) is equipped with a 4.5 MW EC heating system. ECCD efficiency in TCV has been generally underestimated by linear theory (by factors ranging from 1.2 to 3) and overestimated by Fokker-Planck quasilinear theory, which predicted strong nonlinear enhancement by the unequalled EC power densities achieved in TCV.

Our main diagnostic tools are a hard X-ray (HXR) pinhole camera (on loan from Tore Supra) and a high field side electron cyclotron emission (ECE) system. HXR bremsstrahlung detection is effected by a linear array of CdTe detectors with an intrinsic resolution of ~7 keV [1], which view the plasma vertically along 14 chords that span the outboard half of the cross section with a radial resolution of ~2 cm on the midplane. Eight energy channels, with adjustable thresholds within the 10-200 keV range, are available for each chord.

The second harmonic X-mode ECE radiometer [2] comprises 24 channels in the 78-114 GHz range, each with a bandwidth of 750 MHz, and observes the plasma along one of two possible horizontal viewlines on the high field side. A third, low field side viewline is also available. The EC radiation observed on the high field side is dominated by relativistically downshifted emission by the higher energy electrons.

Modelling is performed with the CQL3D code, which solves the Fokker-Planck equation in two velocity and one spatial dimensions [3]. The equation includes a quasilinear EC wave damping term, a relativistic collision operator and a model for radial diffusion, with an optional linear dependence on the parallel velocity and a particle-conserving advection term.

3. Dynamical observations

It is observed that suprathermal populations are generated when the EC toroidal injection angle ϕ is nonzero, as required for ECCD, whereas in pure heating mode the distribution remains essentially Maxwellian [4]. Figure 1 shows the effect of sweeping ϕ during a plasma discharge (n_{e0}=2.5x10^{19} m^{-3}, κ=1.6) on two out of three launchers: while the bulk temperature and the lower energy HXR signal remain constant, the high energy HXR emission and the ECE radiative temperature increase rapidly with ϕ.

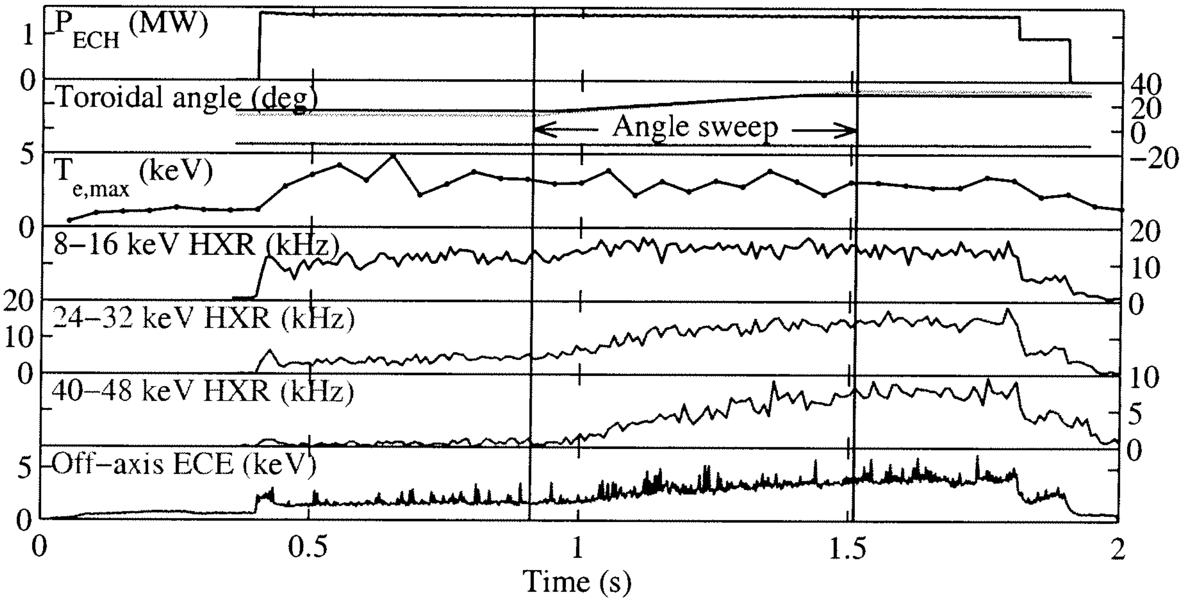

Fig. 1 Sweep of the EC toroidal injection angle on two out of three launchers: the traces shown are the total EC power, the toroidal angles of the three launchers, the peak electron temperature, three energy channels of the HXR signal on a central chord and an off-axis ECE signal.

The suprathermal dynamics will be dominated by the shortest relaxation time in the system. A fundamental question is whether this is the collisional slowing-down time (τ_{sd}) or a transport time stemming from an anomalous cross-field diffusivity D (τ_D~a^2/D). If τ_{sd} is the relevant time scale, the effect of diffusion will be to broaden the fast electron profile by Δw~$(D\tau_{sd})^{1/2}$; as an example, a diffusivity of the order of the bulk thermal diffusivity, D~3 m^2/s, would broaden a 120 keV population profile in these plasmas by 11 cm, i.e. one-half the minor radius. It must be noted, however, that D has been generally estimated to be between

0.3 and 1.0 m^2/s for the suprathermals sustained by lower hybrid current drive, with the exception of JET (where D~6-10 m^2/s) [5].

To study the dynamical evolution at switch-on and switch-off, we have applied square-wave modulation to the EC power and used coherent averaging on the HXR signals to enhance the photon statistics. Photon statistics also rule out a perturbative study, dictating high power levels (2.35 MW) which strongly modulate the target plasma conditions. This causes a major difficulty, as the bulk energy confinement time is of the same order as the slowing-down time for electrons travelling at 5 to 8 times the thermal velocity. Indeed, the bulk temperature rise and fall occur over the same time scales as the HXR and ECE signals. Obviously, keeping the relevant time scales separated will be difficult in any high power current drive studies.

Here, we focus on the time evolution of the HXR *spectrum*. If $\tau_{sd} << \tau_D$, the spectra must be determined by local properties, with no effective communication over distant regions in space. In particular, since heating is applied to different velocity classes in different spatial regions, because of the Doppler shift needed to match the resonance condition locally, the spectral shape should generally vary in space as well. However, in the relaxed state we invariably find that the spectral shape is essentially constant in space, even well outside the theoretical deposition region (albeit at much lower amplitude) [6]; this is most naturally interpreted as an equilibration resulting from radial diffusion, but could also indicate an anomalous deposition profile in both physical and velocity space.

Stronger evidence for the role of diffusion is provided by the time evolution reconstructed by coherent averaging. As shown in Fig. 2(a) for a case with central co-ECCD ($\phi=29^o$), immediately after switch-on the on-axis and far off-axis spectra are very different, the former being larger at low energy and vice versa. As time goes on, the spectral shapes become similar. Figure 2(b) generalises this observation by depicting the profile of the photon "temperature" (from a linear fit to the logarithmic spectra) on the line-integrated signal as a function of the normalised radius: the temperature is initially larger off-axis but evolves over about 10 ms to the familiar constant profile. This effect points clearly to a spatial equilibration: the initially higher off-axis energies are consistent with the larger resonant velocities in that region, while the final relaxed state is everywhere close to the initial temperature on-axis, where most of the power is depos-

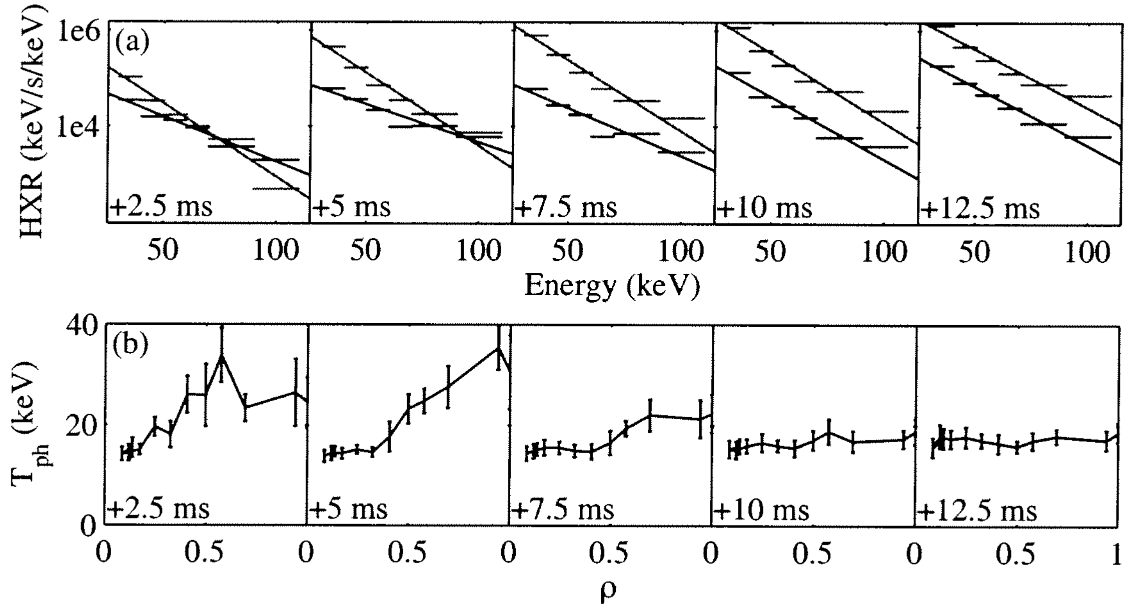

Fig. 2 (a) HXR emissivity as a function of energy in 5 snapshots after the ECCD switch-on (t=0), for a central (red) and an off-axis (blue, ρ~0.6) chord; (b) spatial profiles of the photon temperature for the same snapshots (ρ here indicates the minimum normalised radius for each chord, i.e. the point of tangency to the flux surface).

ited. From the characteristic times observed in these shots, we can set an approximate lower bound D>1.5 m^2s.

4. Fokker-Planck modelling

The discrepancies mentioned at the outset between theory and experiment on the ECCD efficiency have been resolved by including a diffusion coefficient in the Fokker-Planck code. With D~3 m^2/s, the experimentally measured EC-driven current can generally be reproduced [7].

The CQL3D code can also calculate the HXR emission for direct comparison with the experimental data. Without diffusion, not only is the predicted current much too large, the predicted HXR signal is also far narrower spatially than the measured one. Much better agreement is obtained with D=3 m^2/s, as shown in Fig. 3 for a discharge with 0.45 MW central co-ECCD ($\phi=16^o$). The absolute amplitude in the centre and the energy dependence are well reproduced, although the spatial profiles are not in complete agreement.

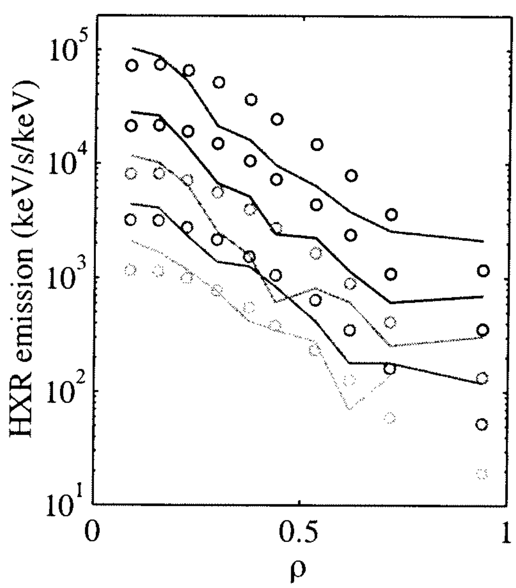

Fig. 3 (a) Predicted (lines) and measured (circles) HXR emission as a function of chordal spatial location for 5 energy channels of 8 keV width in the 16-56 keV range (descending amplitude for increasing energy).

A considerable body of evidence is thus now behind the conclusion that radial transport plays a fundamental role in suprathermal electron dynamics in TCV and in the physics of ECCD. In the future, we plan to extend these studies to a broader parameter range and to exploit the tools described in this paper in a more integrated way, particularly through a calculation of the ECE signals coupled to the Fokker-Planck code.

Acknowledgments

The loan of the HXR camera and associated electronics by the CEA is gratefully acknowledged. Thanks are due to the TCV team for the operation of the tokamak and of the auxiliary heating systems. This work was supported in part by the Swiss National Science Foundation.

References

[1] Y. Peysson, S. Coda and F. Imbeaux, Nucl. Instrum. and Methods in Phys. Res. A **458** (2001) 269; Y. Peysson and F. Imbeaux, Rev. Sci. Instrum. **380** (1999) 3987.
[2] P. Blanchard et al., this conference.
[3] R.W. Harvey and M.G.McCoy, in Proc. IAEA TCM/Advances in Simulation and Modeling in Thermonuclear Plasmas, Montreal (1992)
[4] S. Coda et al., Proc. 26th EPS Conf. on Controlled Fusion and Plasma Physics (Maastricht 1999), Europhys. Conf. Abstr. **23J** (1999) 1097.
[5] Y. Peysson, Plasma Phys. Control. Fusion **35** (1993) B253.
[6] S. Coda et al., Proc. 28th EPS Conf. on Controlled Fusion and Plasma Physics (Madeira 2001), Europhys. Conf. Abstr. **25A** (2001) 301.
[7] R.W. Harvey, O. Sauter, R. Prater, and P. Nikkola, Phys. Rev. Lett. **88** (2002) 205001.

Helium Discharge Operation in TCV

I. Condrea, R.A. Pitts, B.P. Duval, S.M. Ahmed, A. Zabolotsky, M. Wischmeier,
A. Karpushov, J. Horacek, Y.R. Martin, J. Mlynar
Centre de Recherches en Physique des Plasmas, Association EURATOM- Confédération Suisse, Ecole Polytechnique Fédérale de Lausanne, 1015 Lausanne, Switzerland

Introduction

There is presently considerable interest in the behaviour and physics occurring in helium discharges compared with deuterium operation. Many of the differences can be ascribed to the changes in impurity production resulting from He operation, where plasma-wall chemistry is virtually absent and atomic physics cross-sections differ markedly. In TCV, an all graphite machine, carbon is the dominant plasma impurity and the use of He is a particularly useful tool for investigating C production processes. Similar discharges in He and D have been performed with the aim of examining the impurity behaviour, the influence on the density limits, detachment and the L-H transition.

Operational conditions and diagnostics

To obtain He discharges on TCV, a standard deuterium prefill was required, followed by He gas fuelling. In this study, ohmically heated configurations, single null lower (SNL) configurations were performed, both with I_p = 340 kA, discharge duration ~ 1s (flattop), typical electron densities of $7 \times 10^{19} m^{-3}$. The ion ∇xB drift direction was away from the X-point for the SNL configuration.

Visible spectroscopic diagnostics with one horizontal and two vertical views (see Fig. 1) combined with one vertical view of UV spectroscopy (SPRED) and soft-X ray cameras are used to observe the plasma impurities behaviour (C II -V, He I- II, D_α). In addition a neutral particle analyser (NPA) and a standard foil bolometer allow us to evaluate the neutral D flux and the total radiated power. For the profiles in the SOL plasma, target Langmuir probes were used.

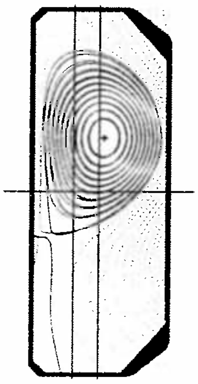

Fig. 1. Equilibria for two divertor configurations in D plasma: SDL (red) and LDL (blue) Also shown the two vertical views for visible spectroscopy (2, 3), SPRED (3) and horizontal view (4).

D-He and He-D changeover

Changeover from D to He was rapid, with He/(He+D) ratios already ~ 60% at the end of the first discharge with more than 80% after ~ 6 identical discharges (see Fig. 2). The He/(He+D) ratios are calculated using the HeI line at 728 nm and the D_α at 652 nm, corrected for the S/ XB assuming an edge temperature of 20 eV. The plasma D neutral flux observed with the NPA decreases to very low values within 0.25 s into the discharge showing that the walls have effectively pumped the D prefill. All carbon lines have lower intensity in He plasmas compared with equivalent D discharges, with Z_{eff} approaching 2 at the highest densities. Figure 3 shows the signal from SX, UV and visible spectros-

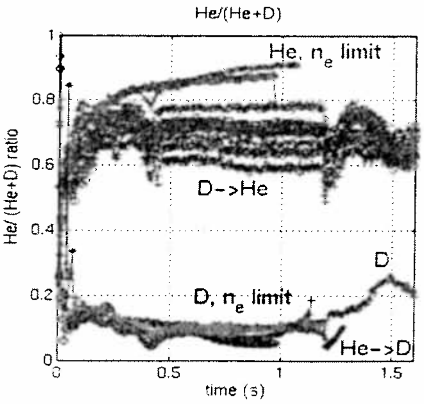

Fig. 2. Evolution of the He/(He+D) ratio during similar He and D shots.

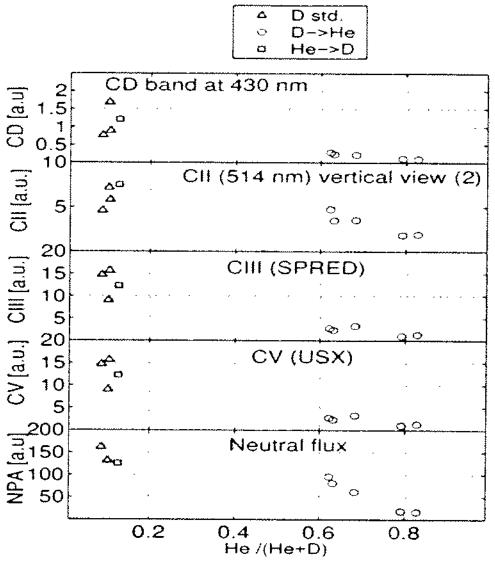

Fig. 3 CD band, carbon emission and neutrals behavior during the D-He changeover.

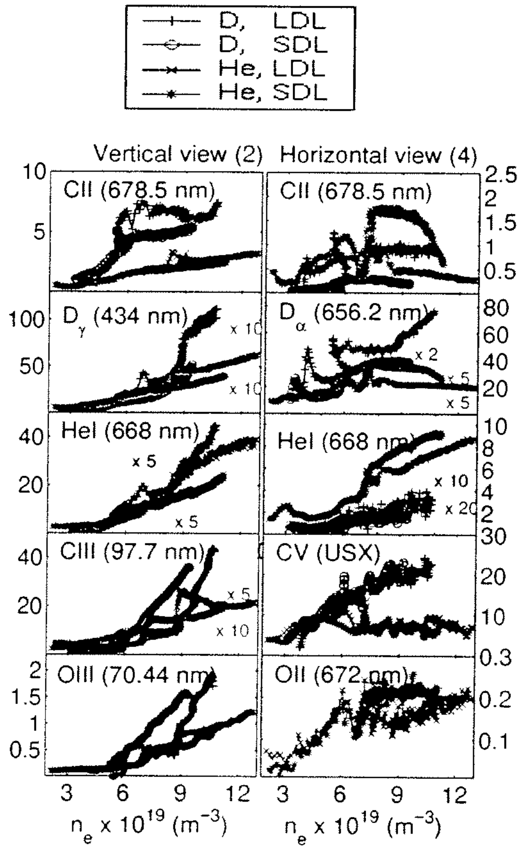

Fig. 4. Impurity dependence on electron density for both vertical and horizontal view. The CV dependence was inserted in the same graph to facilitate the comparison. Values are in [a.u].

copy. The CII radiation, emitted at the plasma edge, is seen to decrease only by a factor ~ 2 while CIII- CV intensities show a stronger decrease (~ 4).

The backward He->D changeover was characterised by similar, or even higher, D neutral flux. The emission intensity of molecular bands of CD fell to low levels for all the He discharges and immediately returned to pre-He levels in the first return discharge.

Impurity behaviour

A set of four discharges ending in density limits were performed in D and He with two different divertor configurations, in order to compare the impurity production and behaviour and determine the density limit of He plasmas in TCV. One configuration has the last closed flux surface (LCFS) at ~ 2.5 cm from the inner wall and a small divertor leg (SDL) whereas the other has the LCFS at ~ 4.5 cm with a long divertor leg (LDL) connecting the bottom wall. The equilibria for the two configurations are shown in Fig. 1. The CII radiation, (see Fig. 4), is localised at the plasma edge with the vertical chord viewing the region of the outer divertor leg and the horizontal chord viewing the region of the inner wall. For the divertor view, there is ~ 2x more carbon in D than in He with a slight intensity increase with n_e for both D and He. This would be the expected behaviour if chemical sputtering is the predominant production mechanism. For the inner wall view, CII shows a strong decrease with n_e (direct physical sputtering) and higher values in He SDL configuration than LDL one. The CV radiation, which is more characteristic of the plasma bulk, again increases with n_e in D but does not change with n_e in He, for both configurations.

Oxygen has similar behaviour in D and He for both configurations and its content does not decrease by more than ~ 2x when passing from D to He. The presence of O could play a role in the production of C as the sputtering yield of O on C, $Y_{O\text{-}C}$ is ~ 10x higher than all the other sputtering yields ($Y_{D\text{-}C}$,$Y_{C\text{-}C}$) for these ion energies and could add to the chemical sputtering of D even in He plasmas. This could explain the higher values for the C levels than observed in other machines. The data show that chemical sputtering is dominating the D plasmas while He physical sputtering together with D (and O) chemical sputtering could be the C production mechanism in He plasmas.

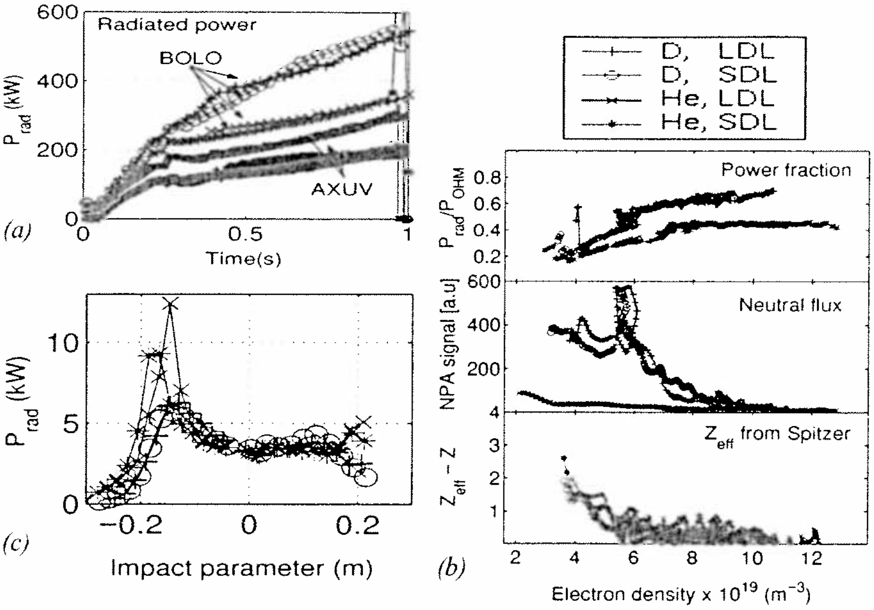

Fig. 5. All graphs are for two shots with D and two in He with SDL and LDL divertor configurations. (a) Temporal evolution of the radiated power measured with bolometry (BOLO) and from XUV radiation (AXUV); (b) Power fraction given by the ratio P_{rad}/P_{in}, neutral flux measured by NPA and Z_{eff} - Z in function of the line averaged electron density; (c) Line integrated radiated power profiles from XUV vs. the impact parameter.

The bolometers measure higher total power in D than He by a factor of 1.5 [see Fig. 5 (a)]. The measured radiation power from the AXUV bolometers, which are not sensitive to the neutral flux, is higher in He, due to higher neutral content in D. The power fraction slightly increases with n_e in D and remains almost constant in He [see Fig. 5 (b)]. The peak emissivity is ~ 2 - 3x higher at the edge and larger in He compared to D [Fig. 5(c)]. This, combined with the spectroscopic results, indicates that He becomes the main radiator for TCV in He plasmas. The electron density and temperature profiles are very similar with 15% higher electron temperature in the He plasmas. The Z_{eff} - Z values from Spitzer calculation [see Fig. 5 (b)] are similar for both D and He plasmas approaching zero at the density limit. This is difficult to understand, since the Z_{eff} depends on $P_{in}*Te^{3/2}$, so the lower input power in He (about 12%) and the 15% increase of the temperature cancel out. Intuitively, with bulk carbon reduced and almost no CX D outflux (from NPA) in He discharges, the plasma purity should be very high. Better Z_{eff} measurements are required to conclude on this point.

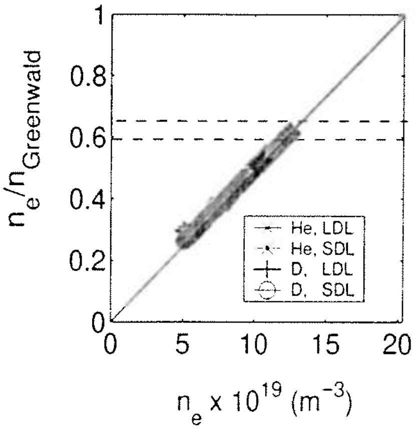

Fig. 6. Electron density normalised to the Greenwald limit (2.03 x10^{20} m^{-3} for TCV with Ip = 340 kA and a = 0.25 m) vs. density. The dashed lines represent the range of density limits obtained in TCV in D plasmas.

Density limit and H mode

The ohmic density limit in TCV diverted He discharges obtained to date is only ~15% higher than that for a similar D discharge. The density limit on TCV is known to be lower than Greenwald limit, although the reasons for this are not understood. Figure 6 shows the dependence of the normalised density to the Greenwald limit against the density. One can see that the higher density limit obtained in the diverted He discharges is in the range of other TCV shots at ~ 65% of the Greenwald limit.

First attempts of obtaining an ohmic H-mode (see Fig. 7) in He indicate that the L-H transition power in pure He is significantly higher than in D. Inverted ∇xB configuration, most favourable for H mode in D in TCV, a plasma current up to 450 kA with elongations varying from 1.6 to 1.75 were performed to locate the conditions for a possible H mode transition. In D, at a lower current than for the He H-mode attempts, with the same plasma configuration and similar values for the power crossing the separatrix, the L-H transition started very early in the discharge followed by an ELM-free phase and concluding with sporadic ELMs and disruption, [Figure 7]. This implies an input power limit exceeding 0.8 MW. In TCV, since ECRH is not efficient at these densities, higher power is not available. This result, which could be very important for the He initiation phase in ITER, is also observed in JET where the power threshold for He H modes is found to be 50% higher than in D H modes, contradicting the theory of the scaling of the power threshold with the mass.

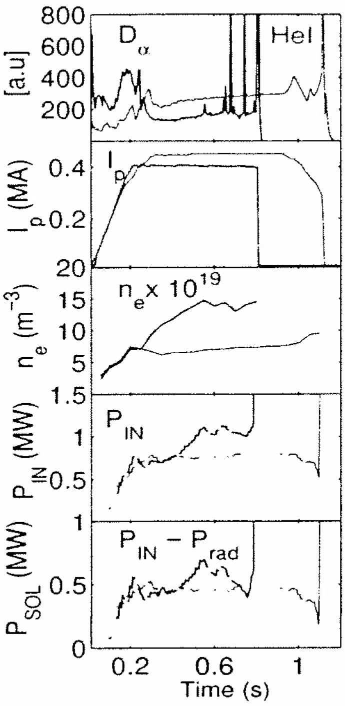

Fig. 7. Comparison between different plasma parameters in two similar shots in He (red line) and D (blue line). Temporal evolution of D_α, HeI, plasma current (I_p), averaged electron density (n_e), input power (P_{IN}) and power at the separatrix.

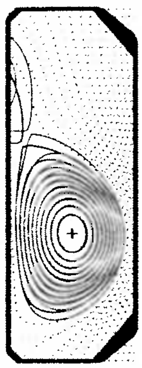

Fig. 8 Two equilibria for He (red line- # 22672) and D (blue line- #22680) with inverted configuration at 0.5 s

Conclusions

He plasmas with ratios of He/(He + D) higher than 90% at high electron density were obtained in TCV using D prefill. Carbon is reduced to lower values than in D and is replaced by He as the main radiator in these discharges. The core C emission dependence on electron density (increasing with n_e for D and constant with n_e in He) shows that C is basically produced by chemical sputtering in D plasmas. The role of O in the C production must be clarified and comparisons with code simulations performed. The limited number of chords observing the divertor region does not allow us to conclude on the location of the source itself.

The L-H transition power in He is significantly higher than in D, an important conclusion that affects the considerations on the low activation phase in ITER. The density limit in TCV diverted He plasmas attempted thus far appears only to be ~15% higher than that in similar D, This is almost certainly linked to the divertor function and the distribution of edge radiation in TCV. Although not presented in this paper, divertor detachment in He is very different to that observed in D (as in JET). There is no observed rollover of target ion fluxes and both the inner and outer targets remain attached at the highest densities achieved. In similar D plasmas, the TCV outer target detaches easily at low density with the inner target following near the density limit.

3D Equilibrium Averaged Description and Consistency Check

W.A. Cooper[1],J. Nührenberg[2], V.V. Drozdov[3], A.A. Ivanov[3], A.A. Martynov[3],
S.Yu. Medvedev[3], Yu.Yu. Poshekhonov[3], M.Yu. Isaev[4], M.I. Mikhailov[4]

[1]*CRPP, Association Euratom-Confédération Suisse, EPFL, Lausanne, Switzerland*
[2]*Max-Planck-Institut für Plasmaphysik, Teilinstitut Greifswald, Germany*
[3]*Keldysh Institute, Russian Academy of Sciences, Moscow, Russia*
[4]*Institute of Nuclear Fusion, RRC "Kurchatov Institute", Moscow, Russia*

1 Background Modelling of 3D equilibrium plasma configurations is a challenging task. The existence of magnetic islands and stochastic magnetic field regions makes a direct [1, 2] modelling time consuming, not very robust and flexible, and hardly useful for systematic equilibrium optimization and stability analysis. More tractable conventional model for 3D MHD equilibrium and stability studies is based on the nested magnetic surface approximation as in standard 3D equilibrium code VMEC [3]. However the code convergence is sensitive to the choice of harmonic set for flux surface representation and significantly deteriorates with increasing resolution.

For equilibrium and stability studies based on the averaging methods a lot of numerical codes have been developed and good agreement for both equilibrium and stability in planar-axis stellarators was obtained [4].

The approach to 2D description of MHD equilibrium and stability proposed in [5] is more general. The key idea is to introduce Riemannian space $\mathbb{R}^3$, in which reference 3D equilibrium is symmetric. The first step in such interpretation was carried out in [6, 7], where it was shown that for arbitrary 3D equilibrium (with nested magnetic surfaces at least) one can construct some formal 2D metric tensor and obtain 2D Grad-Shafranov type equation. The equation was obtained by averaging exact 3D equation. In fact, it is the exact zero 2D moment of equilibrium equation, like Kruskal-Kulsrud equation is the exact zero 1D moment.

2 Scalar equations for 3D MHD equilibria description By assuming the magnetic surfaces $a(r) = const$ exist the ideal MHD equilibrium problem

$$\mathrm{j} \times \mathrm{B} - \nabla p = 0, \quad \mathrm{j} = \nabla \times \mathrm{B}, \quad \nabla \cdot \mathrm{B} = 0 \tag{1}$$

can be reduced to the field equations

$$\nabla \cdot \mathrm{B} = 0, \quad \mathrm{B} \cdot \nabla a = 0, \quad \nabla \cdot (\mathrm{B} \times \nabla a) = 0 \tag{2}$$

and to the force balance equation

$$|\nabla a|^{-2} (\mathrm{B} \times \nabla a) \cdot \nabla \times \mathrm{B} = dp(a)/da. \tag{3}$$

The following statement is valid ([6, 8] for example): for any a priori given family of nested toroidal surfaces $a(r) = const$ the full set of solutions of (2) can be represented by the linear combinations

$$\mathrm{B} = \Phi' \nabla a \times \nabla \theta_\psi + \Psi' \nabla a \times \nabla \zeta_\psi, \quad \mathrm{B} = J \nabla_a \theta_F + F \nabla_a \zeta_F \tag{4}$$

while each summand satisfies (2).

Here

$$(\cdot)' = d(\cdot)/da, \quad \nabla_a(\cdot) = \mathbf{n} \times \nabla(\cdot) \times \mathbf{n}, \quad \mathbf{n} = \nabla a / |\nabla a|,$$

and the pairs of the coefficients $\Phi(a), \Psi(a)$ and $J(a), F(a)$ are arbitrary and refer to toroidal and external poloidal (helicoidal) fluxes or currents. The pairs of the basis vectors $\nabla a \times \nabla \theta_\psi, \nabla a \times \nabla \zeta_\psi$ and $\nabla_a \theta_F, \nabla_a \zeta_F$ are particular solutions of (2). They are generated by the cyclic functions $\theta_{\psi,F}, \zeta_{\psi,F} \in [0,1) \times [0,1)$, which can be interpreted as poloidal (helicoidal) and toroidal angles, satisfying equations

$$L_\psi \theta_\psi = L_\psi \zeta_\psi = 0, \quad L_\psi = \nabla \cdot |\nabla a|^2 \nabla_a(\cdot), \quad L_F \theta_F = L_F \zeta_F = 0, \quad L_F = \nabla \cdot \nabla_a(\cdot). \tag{5}$$

The relations between the fluxes and currents and basis vectors in (4) can be written as

$$\begin{aligned} J &= -\alpha_{22}\Psi' + \alpha_{23}\Phi', \qquad & \alpha_{22}\nabla_a\theta_F + \alpha_{23}\nabla_a\zeta_F &= -\nabla a \times \nabla_a\zeta_\psi, \\ F &= -\alpha_{23}\Psi' + \alpha_{33}\Phi', \qquad & \alpha_{23}\nabla_a\theta_F + \alpha_{33}\nabla_a\zeta_F &= \nabla a \times \nabla_a\theta_\psi. \end{aligned} \tag{6}$$

with matrix elements $\alpha_{ik}(a) = \mathbf{e}_i^F \cdot \mathbf{e}_k^\psi/\sqrt{g_\psi}$ defined by covariant vectors for coordinate variables (5) depending on the shape of magnetic surface only.

Using other combinations of particular solutions of (2) a mixed representation (in terms of poloidal flux and current) of the magnetic field can be obtained:

$$\mathbf{B} = \nabla\Psi \times \mathbf{b}_3^F + F\mathbf{b}_3^\psi, \tag{7}$$

where, as before, each component satisfies equations (2). The vectors $\mathbf{b}_3^{\psi,F}$ can be written as linear combinations of $(\nabla_a\theta_{\psi,F}, \nabla_a\zeta_{\psi,F})$.

Hence for constructing the specific field B, which provides the plasma MHD equilibrium configuration, it is sufficient to know the shape of magnetic surfaces and the distribution of any pair from fluxes and currents over these surfaces. Substitution of the magnetic field (in any form) into the force-balance equation (3) yields the equation for function $a(\mathbf{r})$ and together with boundary conditions complements (4)-(6) to a close system of equations.

Such a method with B in the form (7) generates three-dimensional analog of the two-dimensional Grad-Shafranov equilibrium equation (see [7]) having one dimensional zero moment – the Kruskal-Kulsrud equation

$$p'V' = J'\Psi' - F'\Phi'.$$

3 2D Grad-Shafranov type equation for 3D plasma equilibrium as the exact zero two-dimensional moment for magnetohydrostatics The following statement was formulated in [6, 7]: for any 3D plasma equilibrium (with nested flux surfaces at least) there exist coordinate system (x^1, x^2, ζ) and corresponding Riemannian space $\mathbb{R}^3$ in which the following conditions are satisfied: i. metric tensor $\hat{g}_{ik}(\mathbf{r})$ is two-dimensional: $\frac{\partial}{\partial\zeta}\hat{g}_{ik} = 0$; ii. poloidal (helicoidal) flux function Ψ is two-dimensional $\Psi = \Psi(x^1, x^2)$ and it is the solution of 2D Grad-Shafranov type equation

$$\hat{\nabla} \cdot \left(\frac{\hat{\nabla}\Psi}{\hat{g}_{33}}\right) + \frac{F}{\hat{g}_{33}}\frac{dF}{d\Psi} - F\hat{\nabla} \cdot \left(\frac{\hat{\mathbf{e}}_3 \times \hat{\mathbf{e}}^3}{\hat{g}_{33}}\right) = -\alpha\frac{dp}{d\Psi}; \tag{8}$$

iii. magnetic field takes the form $\mathbf{B} = (\nabla\Psi \times \mathbf{e}_3 + B_3\mathbf{e}_3)/g_{33}$, with $\mathbf{e}_3 = \partial\mathbf{r}/\partial\zeta$, $< B_3 >_\zeta = F(\Psi)$.

Here $\mathbb{R}^3$ is generated by the metric tensor

$$\hat{g}_{ik} = \sqrt{\hat{g}} < \frac{g_{ik}}{\sqrt{\hat{g}}} >_\zeta, \quad \hat{g} = det\, \hat{g}_{ik} = det^{-2} < \frac{g_{ik}}{\sqrt{g}} >_\zeta, \quad \hat{g}^{ik} = \hat{G}_{ik}/\hat{g}, \tag{9}$$

and

$$\alpha = \alpha(x^1, x^2) = < \sqrt{g} >_\zeta / \sqrt{\hat{g}},$$

$\hat{\nabla}$ is an ∇-operator in $\mathbb{R}^3$. In these formulas $< f >_\zeta = \frac{1}{\zeta_{max}}\int_0^{\zeta_{max}} f(x^1, x^1, \zeta)d\zeta$.

Equation (8) can be obtained by averaging the exact 3D equilibrium equation in any reference coordinate system connected to the natural coordinates (5) by a two-dimensional transformation $x^{1,2} = x^{1,2}(a, \theta_\psi)$, $\zeta = \zeta_\psi - \lambda(a, \theta_\psi)$.

The numerical codes were developed for generation of the Riemannian space metric based on VMEC 3D equilibrium format and for solution of the 2D equation on grid adaptive to magnetic surfaces [9].

4 Consistency check for equilibria with nested flux surfaces The solution of the 2D elliptic equation in the Riemannian space (8) should reproduce the original 3D equilibrium with nested flux surfaces. In particular, it means that in the coordinate system $x^1 = a\cos\theta_\psi, \quad x^2 = a\sin\theta_\psi$ the level lines of the solution $\Psi(x^1, x^2)$ are concentric circles. A deviation from that solution can be estimated by comparing the rotational transform $\iota = -\Psi'/\Phi'$ profile for the 3D configuration and the solution of the averaged equation. Such a consistency check provides more extensive test than the 1D Kruskal-Kulsrud equation balancing the shape of magnetic surfaces against the plasma profiles.

The method was applied to several series of equilibria in conventional stellarators and in the systems with spatial magnetic axes.

The first series was related to the reference LHD configuration [4]. The pressure profile was prescribed in terms of normalized toroidal flux Φ and zero toroidal net current was assumed: $p = p_0(1-\Phi^2)^2, \quad J = 0$. In Fig.1 the rotational transform profiles are compared for a series of equilibria with increasing β. The profiles from the averaged equation match the original profiles with accuracy better than 0.01 for $\beta \lesssim 3\%$ for VMEC resolution with 97 radial nodes equidistributed in toroidal flux and 179 harmonics.

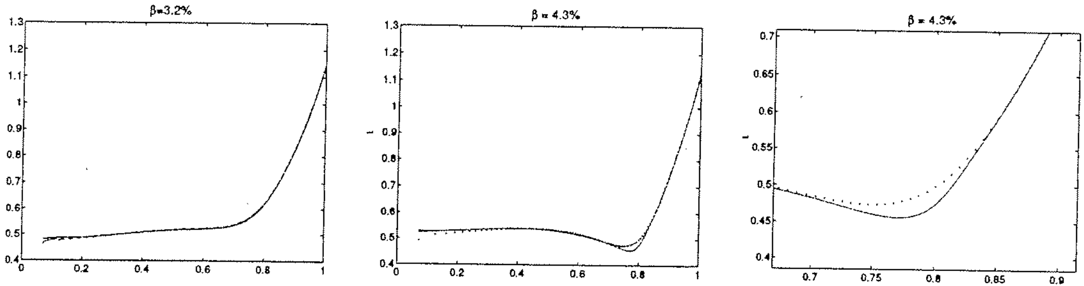

Fig.1 Rotational transform from VMEC solution (dots) and corresponding averaged equation (solid lines) versus square root of normalized toroidal flux. The region of maximal discrepancy for $\beta = 4.3\%$ is zoomed.

However for the equilibrium with $\beta = 4.3\%$ a significant discrepancy (~ 0.05) appeared near the rational surface $\iota = 0.5$ approaching location of the pressure gradient maximum. The discrepancy stays with increased resolution both in VMEC, Riemannian metric generation module to solve elliptic equations (5) and the adaptive grid code to solve the 2D equation.

To check whether it is an indication of magnetic island appearance the pressure profile with another location of the gradient maximum was chosen: $p = p_0(1-\Phi^2)^{10}$. The same effect was reproduced for lower value of $\beta = 1\%$ (Fig.2).

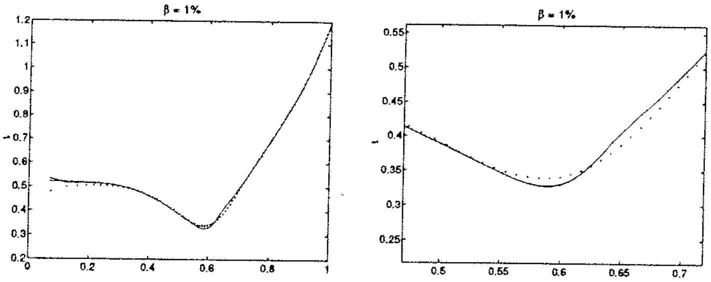

Fig.2 Rotational transform comparison for $\beta = 1\%$ more peaked pressure profile.

Another series is related to the analytic force-free equilibria with $\mathbf{j} = \lambda\mathbf{B}, \quad \lambda = \mathrm{const}$ [10]. Starting from the axisymmetric configuration and applying 3D perturbation generates the series of equilibria including cases with nested flux surfaces, spatial magnetic axis, magnetic islands and stochastic fields. The shape of boundary flux surface was obtained by magnetic field line tracing. The plasma profiles are described by $p = 0, \quad J = \lambda\Phi$. The problem with accuracy in VMEC was encountered: the discrepancy in rotational transform of several percent order was discovered even with radial resolution ~ 200 (Fig.3).

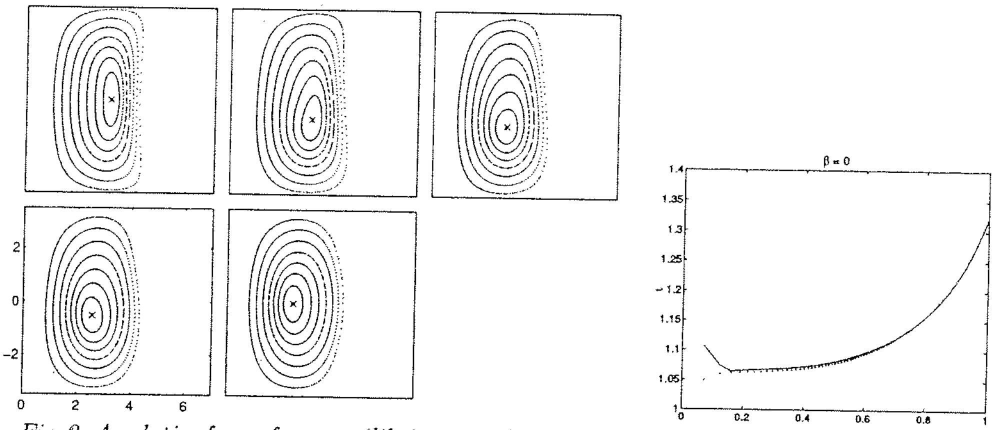

Fig.3 Analytic force-free equilibrium surfaces in different toroidal cross sections (VMEC magnetic axis shown by cross) and rotational transform comparison.

A possible reason for that is a problem with magnetic axis determination. Note that for a configuration with islands the VMEC code also converges to some nested flux surface solution which is not an equilibrium because of uniqueness of the considered force-free configuration. However the same kind of discrepancy in rotational transform profiles was encountered.

5 Discussion A possible use of the averaged description of 3D equilibria is robust and fast computation of approximate equilibria with different β and profiles starting from background 3D vacuum configuration, for example. However the question on the approach applicability range needs to be answered.

An immediate use of the averaged equilibrium description is the consistency check for 3D nested flux surface configurations giving information on numerical equilibrium accuracy and possibly existence of the regular equilibrium problem solution.

Acknowledgements The work is supported in part by the Joint Research Project "Novel Approaches to Improve Confinement in 3-D Plasma Magnetic Systems" INTAS 99-00592.

References

[1] A.Reiman, H.Greenside, *Comput. Phys. Commun.* **43**(1986)157

[2] T.Hayashi, in Proc. of the Joint Varenna-Lausanna International Workshop on theory of fusion plasmas, (1988)11

[3] S.P.Hirshman, W.I. van Rij, P. Merkel, *Comput. Phys. Commun.* **43**(1986)143

[4] Y.Nakamura *et al. J. Comput. Phys.* **128**(1996)43

[5] S.A.Galkin, V.V.Drozdov, A.A.Martynov, Preprint Keldysh Institute of Applied Mathematics, 1991, number 52

[6] L.M.Degtyarev, V.V.Drozdov, Preprint KIAM, 1984, number 32

[7] L.M.Degtyarev, V.V.Drozdov, S.Yu.Medvedev, *Itogi nauki i tekhniki. Ser.: Fizika Plazmy* **6**(1985)81

[8] L.M.Degtyarev, V.V.Drozdov, M.I.Mikhailov, V.D.Shafranov *et al.*, *Fizika Plazmy* **11**(1985)39

[9] S.Yu.Medvedev *et al.*, International Workshop "Innovative Concepts and Theory of Stellarators" Kyiv, Ukraine May 2001. In: Scientific Papers of the Institute for Nuclear research **4**(2001)149

[10] A.A.Martynov, S.Yu.Medvedev, *Plasma Phys. Reports* **28**(2002)259

High elongation in the MAST Spherical Tokamak

G. Cunningham, J.B. Lister*, R. Akers, G. McArdle, J. Qin♦, H. Wilson

EURATOM/UKAEA Fusion Association, Culham Science Centre, Oxon OX14 3DB, U.K.
**Association EURATOM-Confédération suisse, CRPP-EPFL, 1015 Lausanne, Switzerland*
♦ Imperial College, London SW7 2BZ, U.K.

Many conceptual tokamak power plant designs, including the favoured Culham ST reactor, use high elongation as a route to high pressure and bootstrap current. This paper looks at the implications, with regard to vertical position control, when such models are to be tested on a tokamak with fixed coil geometry such as MAST. Several issues emerge, for example: the increasing quadrupole field has the effect of reducing the plasma cross section and edge q, and the bootstrap current is only increased significantly if the internal inductance is low. Also, the vertical stability of the plasma scales in rather unusual ways, for example *reduced* internal inductance leads to *reduced* stability, when the shaping field is constant. The model is compared with MAST experiments where elongation up to 2.5 has already been obtained.

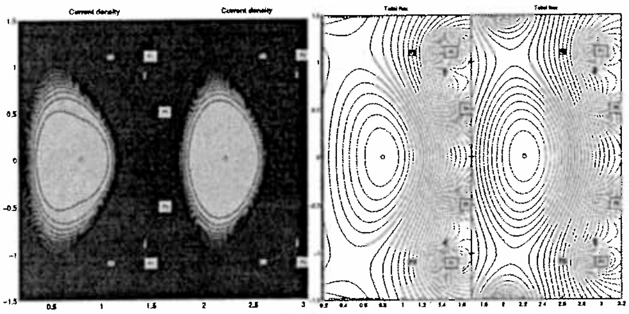

1. Here we see two equilibria, with the same current density profile, calculated at low and high aspect ratio, A=1.44 and 4.56 respectively. The current density and flux plots are superficially similar.

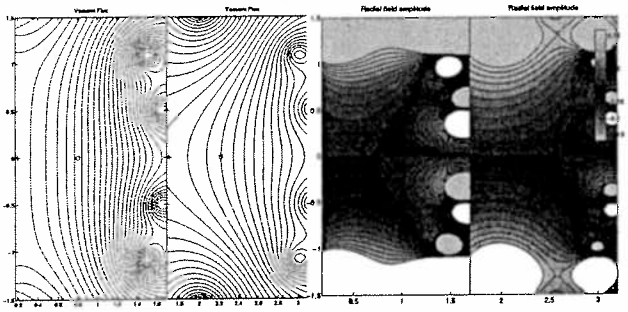

2. However, the vacuum field (left) and its radial component (right), start to show significant differences.

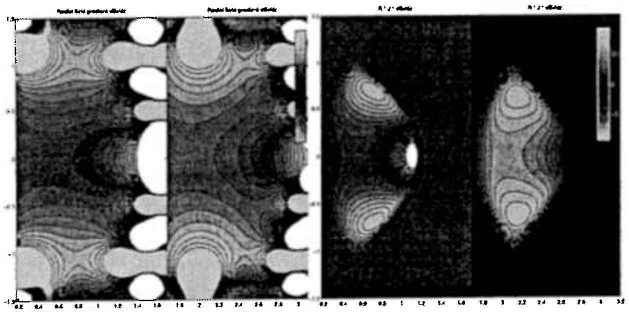

3. As a result, the vertical derivative of the radial field (left) changes sign within the plasma volume, so that when this is crossed with the current density (right) the destabilising force gradient also changes sign within the plasma. In contrast, the large aspect ratio case is more intuitive.

Scaling of the bootstrap current. The bootstrap current is an important issue for steady state tokamak operation. Here we see that the bootstrap current is increased at high elongation, assuming that the same β_N can be achieved, though low l_i is necessary to give a strong effect. Under optimal conditions, a scaling of $I_{boot} \propto 1+\kappa^2$ can be obtained, for fixed β_N, A, I_p/I_{rod}

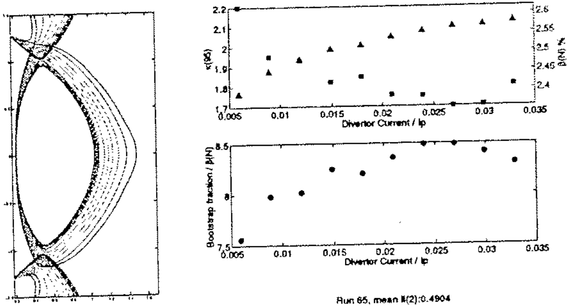

7. On the left is shown the outline of a series of equilibria with the same current density profile but varying divertor current. Although the elongation changes significantly, the changing aspect ratio means that the effect on the bootstrap current is rather weak.

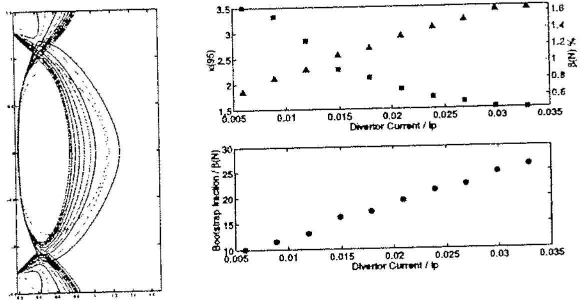

8. In this series of equilibria the l_i is lower, and the divertor current has a greater effect on the elongation. The effect is magnified by the bootstrap current depending more strongly on the elongation, with the result that the bootstrap current scales much more strongly with divertor current.

Scaling of the shape

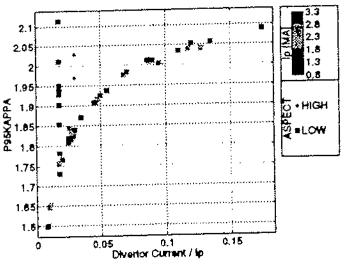

9. As expected, the plasma elongation increases with divertor current, both for the low and high aspect ratio cases.

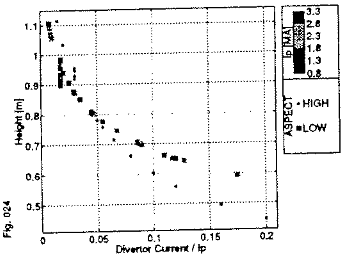

10. However, it is less obvious to see that the plasma height is actually reduced as the divertor current is increased, and this effect is slightly stronger for the high aspect ratio case.

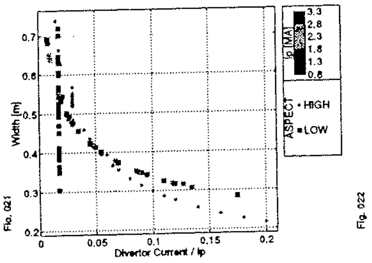

11. The inevitable result is that the plasma width falls rapidly, and the safety factor decreases rapidly, with increasing divertor current. This is in spite of the decrease in major radius and resulting increase in the toroidal field on axis.

Scaling of the vertical stability. The following plots show integral data where each point is calculated from a separate equilibrium. There are two major scans in the database, one at fixed current density profile but varying I_p and divertor current, the other at fixed currents but varying profile (l_i). In this case the destabilising force, which is the sum of the forces shown in figure 3, is compared with the stabilising force, calculated by RZIP[†] using the actual vessel geometry for MAST, for the low aspect ratio case.

[†] *RZIP calculates the dynamic response of the plasma to currents in the equilibrium coils and induced currents in the vessel. It uses a rigid multi-filament representation of the plasma. The vessel-plasma coupling matrix is reduced to an adjustable extent by eigenvector extraction.*

4. As expected, the destabilising force gradient increases rapidly with divertor current. The stabilising force falls initially, probably because the changing shape is moving the plasma away from the poloidal field coils, but then plateaus as most of the stabilisation is coming from the centre column.

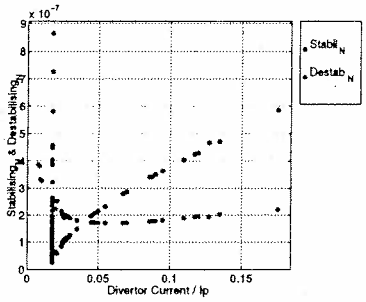

Fig. 204

5. As a result, f_s, the ratio of stabilising to destabilising force gradients, falls strongly with increasing divertor current, if the internal inductance (l_i) is held constant. It is notable that, if l_i is varied at fixed divertor current, then it is the higher l_i plasmas which are most stable, as they have ~~most~~ current near the c~~entre~~ of the machine where the quadrupole field is weak (of course their elongation is lower). This is directly opposite to the case of the conventional aspect ratio tokamak at moderate elongation.

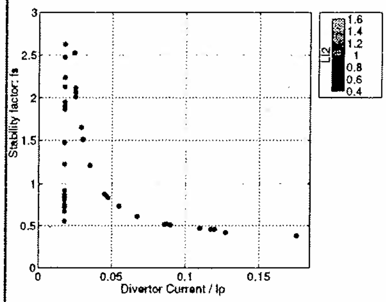

Fig. 203

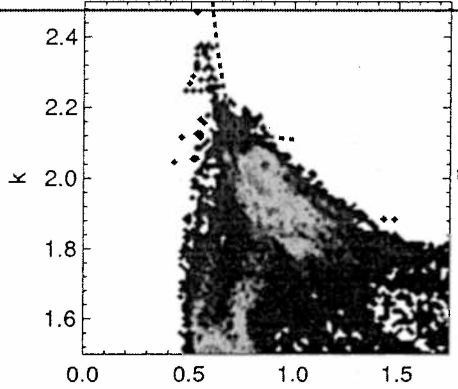

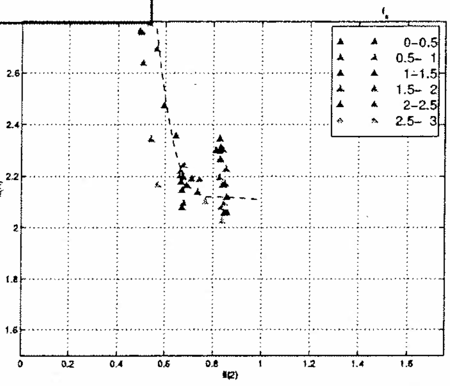

6. These data can be re-plotted as κ *vs.* l_i as a function of the stability index (right). The dashed curve is an 'eyeball fit' to f_s=1.5, which is about the value which the MAST vertical position control system can achieve. If this same curve is over-laid on the distribution of κ *vs.* l_i for actual MAST plasmas (left) it coincides quite well with the high l_i, high κ edge of the distribution. The rather angular shape of this stability curve demonstrates clearly that it is very difficult to achieve high elongation when li is greater than 0.6 or so.

Scaling of the plasma performance

12. As a result of the shape changes described above, the net current carrying capacity, $(a^2+b^2)/R^2$, falls somewhat with increasing divertor current. This is consequence of using a single coil pair to change the elongation.

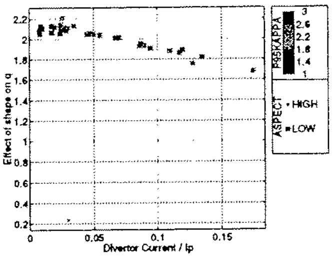

Fig. 023

13. Ideally one would evaluate the maximum attainable β_N from a stability code, but for the present we simply use the Sykes-Troyon scaline for $\beta max \ \alpha \ I_p/aB$, and at first glance βmax appears to be increasing with divertor current. However, q_{95} is falling (colours); if the limit is followed at constant q_{95}, it is seen to fall slowly.

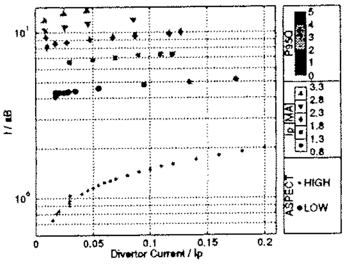

Fig. 025

14. However, with the toroidal field on axis also increasing, the maximum pressure ($P_m = \beta_N.B^2$) is increasing slowly, even at constant q_{95}.

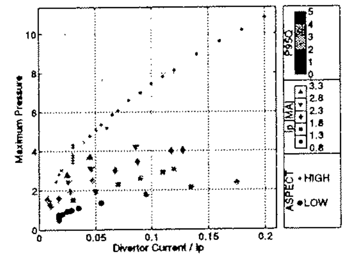

Fig. 026

Conclusion. A very wide range of plasma elongation and current profiles has been been explored on MAST. These show that elongations up to 2.5 can be achieved provided the inductance is kept low. Extensive modelling in the full MAST coil and vessel geometry has now been performed, and this matches the experimental data very well.

As a result of this work it is becoming clear that there are significant differences between the way the way a conceptual tokamak design scales with elongation and the way a the performance of particular ST scales. In the former case the poloidal coils can be positioned at will so that the plasma cross section is maintained. In the latter case, when the coil positions are fixed, increasing the quadrupole field alone reduces the plasma cross section, so that to maintain an acceptable q_{95}, the current also has to be reduced. As a result the Sykes-Troyon limit for β actually falls somewhat as the elongation is increased.

Studies of the relation between the bootstrap current and elongation and inductance have shown how to optimise MAST plasmas to maximise the bootstrap fraction.

Some of the issues which will need to be taken into account in optimising the control system are also becoming apparent, in particular, inhomogeneity in the shaping field is inevitable at low aspect ratio, and causes the plasma stability against vertical displacement to vary strongly across the cross section. There is a similar inhomogeneity in the controlling field. These results will guide the development of the multi-variable digital plasma shape controller and the route to optimum performance of MAST.

Acknowledgements. *This work is funded by the UK Department of Trade and Industry, the EURATOM mobility fund and the Fonds National Suisse de la Recherche Scientifique.*

Active Modification of the ELM Frequency in TCV

A W Degeling, Y R Martin, J B Lister, X Llobet

Centre de Recherches en Physique des Plasmas, Ecole Polytechnique Fédérale de Lausanne,

Association EURATOM-Confédération Suisse, 1015 Lausanne, Switzerland

Introduction. The detrimental effects of ELMs must be ameliorated or controlled if the ELMy H-mode is to be considered a viable scenario for future fusion reactor experiments such as ITER. Since the ELM amplitude is found to scale with the delay between ELMs, a possible approach to this goal could be to control the ELM frequency (f_{elm}), in order to avoid ELMs with large amplitudes. In order to explore how ELMs may be controlled, it is necessary to investigate what types of perturbations affect their dynamics. This paper reports: 1) Observations of intermittent phase locking between ELMs and Sawtooth dynamics on TCV, with entrainment of the ELM frequency to simple integer ratios of the sawtooth frequency (f_{st}); 2) A first attempt on TCV to actively modify the ELM frequency by applying a fast voltage perturbation to the radial field vertical control coils during single null ELMy H-mode discharges.

ELM - Sawtooth Synchronisation. ELM and Sawtooth cycles have periods that are of the same order of magnitude in TCV, which enables the possibility of their dynamics becoming coupled. Evidence of coupling comes in the form of frequency entrainment and phase locking between the two systems. These behaviours are clearly evident from f_{elm} and f_{st} time-series of individual discharges, however a more general result is shown by building a database using all the ELM occurrence times from a large number H-mode discharges (100 were used) and histogramming the ratio of f_{elm} to f_{st}, as shown in Fig. 1a). This figure clearly shows two peaks, centred at 1.0 and 1.7. The peak at 1.0 demonstrates that a large percentage of ELMs are strongly correlated with the sawtooth frequency.

An interesting result is found by plotting the histogram of the time delay between each sawtooth crash (using a centrally viewing soft X-ray chord) and the next ELM Δt_{st-elm}, as shown in Fig. 1b). This figure shows a sharp peak at $\Delta t_{st-elm} = 0$, followed by a minimum at 0.9 ms, and a broad maximum at 2 - 6 ms. There are at least two simple interpretations of this figure: 1) The peak at Δt_{st-}

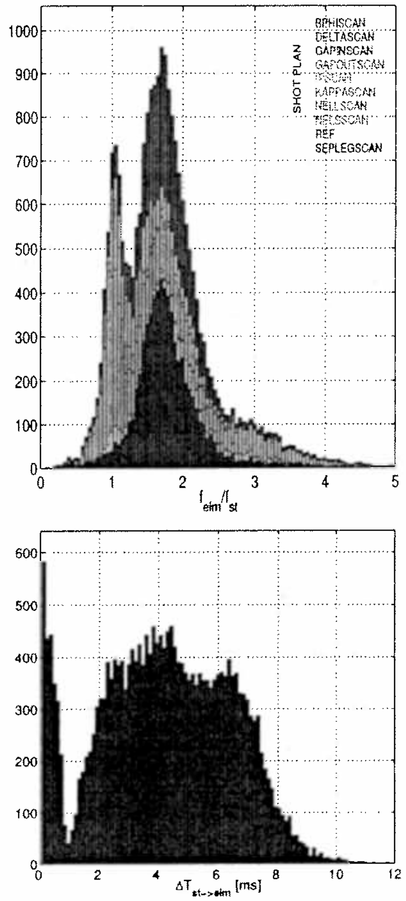

Figure 1: Histogram of f_{elm}/f_{st}, showing discharge categories in which a particular parameter was scanned; Histogram of Δt_{st-elm}

$_{\mathrm{elm}} = 0$ corresponds to ELMs immediately caused by the sawtooth crash (i.e. within 50μs). At these times, if the edge conditions are close to the stability threshold of ELMs, global MHD activity associated with the sawtooth may trigger an ELM; 2) The minimum occurring 0.9ms after the sawtooth crash corresponds to the measured arrival of the sawtooth heat pulse at the edge, which therefore has a stabilising effect on the ELMs, suggesting type III ELMs.

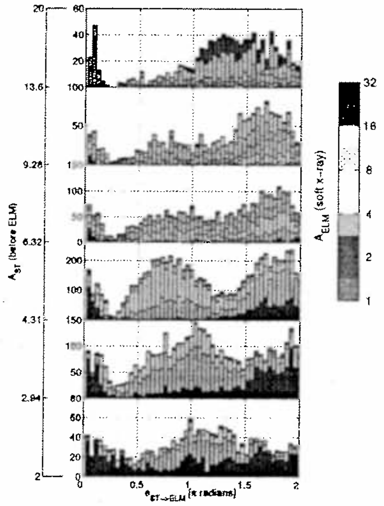

Figure 2: Histograms of the ELM phase in the sawtooth cycle with rows corresponding to increasing heat pulse amplitude [a.u.]

The phase of each ELM in the sawtooth cycle is defined in the database by $\phi = \Delta t_{st\text{-}elm} f_{st}$. Fig. 2 shows a series of histograms of the phase, in which the data has been segregated into rows on the y -axis using the amplitude of the last sawtooth heat pulse that arrived at the edge prior to each ELM (A_{st}, obtained from a soft X-ray chord with $\rho \sim 0.9$). Peaks in the histogram indicate a preferred phase that persists even in different discharges, and clearly indicates coupling. The appearance of a single peak as a function of ϕ corresponds to synchronisation with the fundamental f_{st}, while multiple peaks suggest a harmonic (or sub-harmonic, although this is rare). Fig. 2 shows that as the amplitude of the heat pulse increases, the peaks in the histogram become more apparent, indicating increasing coupling, and also that a transition from two peaks to a single peak occurs. Larger sawtooth crashes are correlated with high κ, and the single peak that forms with high A_{st} is mainly due to a series of discharges in which κ was scanned. This is also indicated in Fig. 1a) by the fact that the peak occurring at 1.0 is mostly comprised of counts from the 'kappascan' category. The histogram colours in Fig. 2 correspond to the size of the decrease in soft X-ray emissivity at the edge ($\rho \sim 0.9$) caused by each ELM, and show that larger amplitude ELMs occur as A_{st} increases. Parameter cuts were made in the database to investigate how the coupling varied with plasma parameters. Fig. 3a) and 3b) show the phase histograms for ELMs preceded by a sawtooth with $A_{st} > 4$ as a function of q_{95} (with $\kappa < 1.9$) and lower triangularity δ_L (with $q_{95} > 2.7$) respectively. The histograms in each case become more peaked as either q_{95} is increased, or δ_L is decreased, which indicates that coupling strengthens with δ_L and weakens with q_{95}.

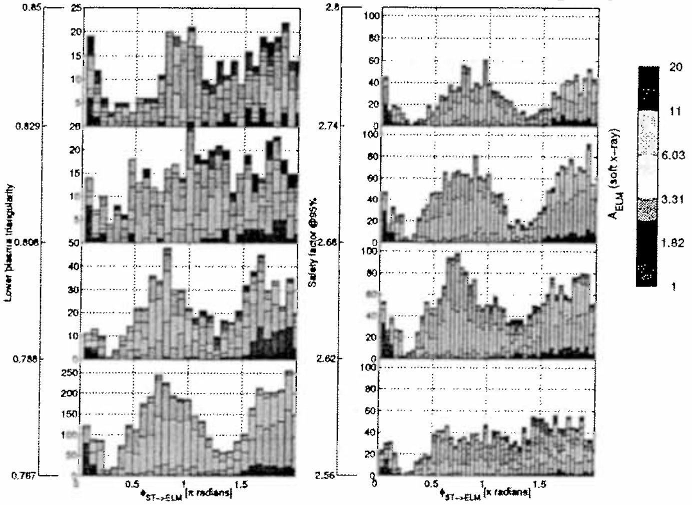

Figure 3: Histogram of ϕ with bins of increasing δ_L; Histogram of ϕ with rows of increasing q_{95}

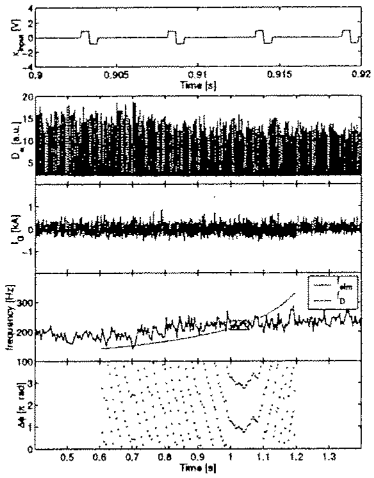

Figure 4: # 20332 Detail of the input signal; D_α time series; G-coil current; f_{elm} (blue), f_D (red) & Δf (green) overwhich f_{elm} is affected by f_D (negligible in this case); ELM phase w.r.t. driver

Active ELM Control Experiments. The fact that the ELMs become synchronised with sawteeth suggests the possibility of actively controlling ELMs with an external driver signal. In this experiment, a fast voltage perturbation is applied to the radial magnetic field coils (G-coils) during single null ELMy H-mode discharges with stationary conditions. The G-coils are located at the top and bottom of TCV within the vacuum vessel and are routinely used for feedback vertical stabilisation. A perturbing signal was added to the vertical stabilisation feedback loop and consisted of a series of square pulses of 1ms duration, with a variable delay between pulses. This produced spike - like pulses in the current to the G-coil (up to 2kA) that resulted in deviations in the plasma vertical position of up to 5 mm. Figures 4 and 5 show two examples in which a constant amplitude pulse train was applied to the G-coil with an increasing driving frequency f_D from 143 to 330 Hz. The top graph in each figure shows a detail of the input signal, and the four following graphs show: the D_α timeseries (showing ELM times), the G-coil current, the timeseries of f_{elm} and f_D, and the phase of the ELMs with respect to the driving signal. The example in Fig. 4a (discharge 20332) shows that the perturbed current in the G-coils is roughly the same magnitude as the control system feedback signal produced by each ELM event, and that no phase synchronisation of frequency tracking occurs. Fig. 5 shows that when the G-coil current perturbation is increased to over 1 kA, the ELM frequency tracks the driving frequency, and the phase maintains a roughly constant value, interspersed with momentary losses in the phase locking. The vertical movement of the plasma caused by the perturbation is measured using magnetic pick-up coils, and gives some insight into how the perturbation might be affecting the ELM dynamics. Fig. 6 shows the results from a series of discharges in which frequency of the pulse train was swept as described above, while the amplitude and polarity of the pulse was varied from discharge to discharge. For each discharge, the range in driving frequency Δf overwhich the ELM phase was clearly affected by the perturbation was estimated and compared with the amplitude of the vertical displacement Δz associated with the perturbation. This figure shows that Δf clearly increases with Δz, that is, the frequency range overwhich ELM dynamics can be affected scales with the applied vertical displacement. We now turn to the question of how these vertical displacements affect the ELM frequency.

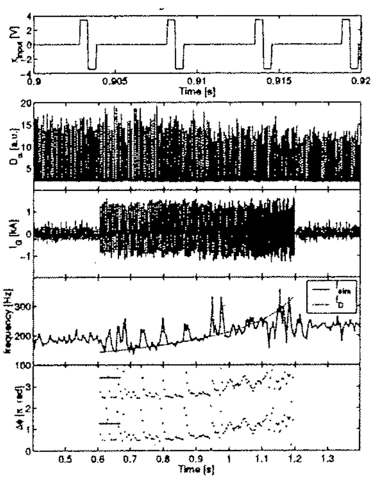

Figure 5: # 20333. Detail of the input signal; D_α time series; G-coil current; f_{elm}, f_D & Δf (green) overwhich f_{elm} is affected by f_D; ELM phase w.r.t. driver

It is generally considered that ELMs occur when a threshold for an MHD instability is exceeded, either in edge current

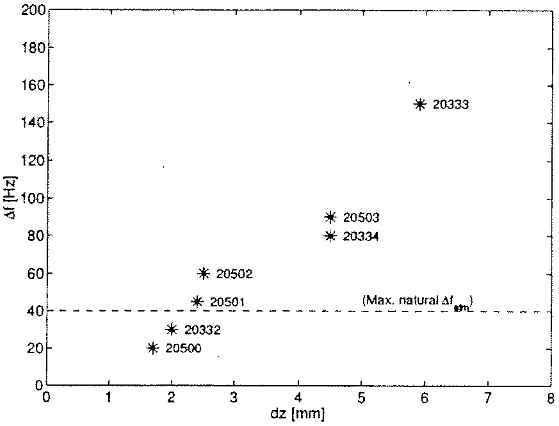

Figure 6: Driver frequency range overwhich ELMs appeared to be affected versus the amplitude of the vertical perturbation. The dashed line indicates the unperturbed f_{elm} fluctuation level. Points below this line indicate discharges in which the perturbation had no detectable effect.

density (e.g. Peeling mode) or pressure gradient (e.g. Ballooning mode).We should therefore consider how the perturbation we apply affects these parameters. If we make the first order approximation that the plasma current displacement is then pressure gradients are not affected by plasma movement. The edge current density is given by $V_{surf} = 2\pi R\eta j_{\phi surf}$, where R and η are the major radius and resistivity, and the surface loop voltage is $V_{surf} = -\frac{d}{dt}\langle\psi_{ext}\rangle = -\langle\frac{\partial\psi_{ext}}{\partial t} + u\cdot\nabla\psi_{ext}\rangle$ and ψ_{ext} is the vacuum poloidal flux. Writing $V_{surf} = V_0(1+\varepsilon(t))$, then to 1st order for vertical displacements $u = \dot{z}$, $V_0 = -\langle\frac{\partial\psi_\Omega}{\partial t}\rangle \approx V_L$ and $\varepsilon = \langle\left(\frac{\partial\psi_G}{\partial t} + \frac{\partial\psi_{VG}}{\partial t} + u\frac{\partial\psi_\Omega}{\partial z}\right)/\frac{\partial\psi_\Omega}{\partial t}\rangle$, where ψ_W is the flux from the ohmic and shaping coils, ψ_G and ψ_{VG} are respectively the flux from the G-coil currents, and their vessel image currents, and <> indicates averaging over the last closed flux surface. The first two terms nearly exactly cancel at the location of the roughly centred plasma, hence $\varepsilon \approx \frac{u}{V_L}\langle\frac{\partial\psi_\Omega}{\partial z}\rangle$. Estimating u from the I_p*z measurement and numerically calculating the integral around the last closed flux surface gives ε ~ 0.1 for discharge 20333. That is, we estimate that the edge current density is being perturbed by about 10% by the externally driven vertical displacements. Such a perturbation might reasonably be expected to affect ELM dynamics.

Conclusions. Observations of the ELM and sawtooth time-series from TCV ohmic H-modes show that the two dynamical systems are frequently synchronised, with the ELM frequency related to the sawtooth frequency by an integer multiple. It was found that sawteeth affect ELMs in two different ways: 1) When the edge conditions are close to the ELM stability threshold, the occurrence of a sawtooth immediately triggers an ELM; 2) A more general coupling that results in a preferential phase for the ELMs in the sawtooth cycle and is dependent on the heat pulse amplitude, plasma shape parameters and q_{95}. A first attempt to actively control the ELM frequency was made by applying an external perturbation to the radial field vertical position control coils inside the vacuum chamber of TCV. It was found that the ELM dynamics became phase locked, and tracked the frequency of the applied signal when the amplitude of the perturbation was sufficiently large - albeit with intermittent breakages in phase lock. Coupling between the driver and the ELMs increased with the vertical displacement caused by the radial field, which strongly suggests that the ELM dynamics are being affected by perturbations in the edge current density.

The authors sincerely thank the TCV Team, without whom these experimental results would be unavailable. This work was partly supported by the Swiss National Science Foundation.

Negative Ions Dynamics and Attachment-induced Ionization Instability in O_2, CF_4 and SF_6 Low-pressure Power Modulated Capacitive RF Plasmas

A. Descoeudres, L. Sansonnens and Ch. Hollenstein

Centre de Recherches en Physique des Plasmas, Ecole Polytechnique Fédérale de Lausanne, CH-1015 Lausanne, Switzerland

Radio-frequency discharges in electronegative gases are widely used in industrial processes, particularly for the manufacturing of semiconductor devices. Oxygen (O_2), sulfur hexafluoride (SF_6) and carbon tetrafluoride (CF_4) are the main electronegative gases employed for such applications. Inductive plasmas are used for most electronic devices fabrication but capacitively coupled plasmas remain the choice in large area applications such as thin film transistors for flat display.

The presence of negative ions changes considerably the physics of the plasma. Especially, several instabilities linked with the electronegativity of the gas can develop: ionization waves, attachment-induced ionization instability and instabilities attributed to the transition between inductive and capacitive modes in inductive discharges. Furthermore, it is experimentally difficult to do mass spectrometry of negative ions during the discharge. They are indeed electrically trapped within the plasma by the plasma sheath. So, modulated discharges are required to measure them during the afterglow.

Our experimental apparatus is a parallel plate capacitively coupled reactor comprising two stainless steel cylindrical electrodes 13 cm in diameter with a 2.5 or 4 cm electrode gap. The typical plasma parameters used are: gas pressure 0.1 – 0.4 mbar, gas flow of 13 sccm SF_6, of 20 sccm CF_4 and of 50 sccm O_2, RF power up to 100 W at 13.56 MHz. A low frequency (50 Hz – 1 kHz) square wave modulation is applied to the high frequency excitation. This modulation permits the measurements of the negative ions during the afterglow and to differentiate between transient and steady-state phenomena.

For the characterization of the plasma, we use a voltage probe connected directly to the RF electrode to measure the peak-to-peak voltage. A Scientific Systems Langmuir probe coupled to a boxcar integrator is used to obtain time resolved current-voltage characteristics. We measure the global emission intensity with a Perkin Elmer C953 photomultiplyer and quartz fiber optics. Finally, we use a Balzers PPM422 mass spectrometer combined with a EG&G Ortec multi channel scaler to obtain time resolved ions flux measurements.

As shown in Fig. 1, the negative ions dynamics are different for the three studied gases.

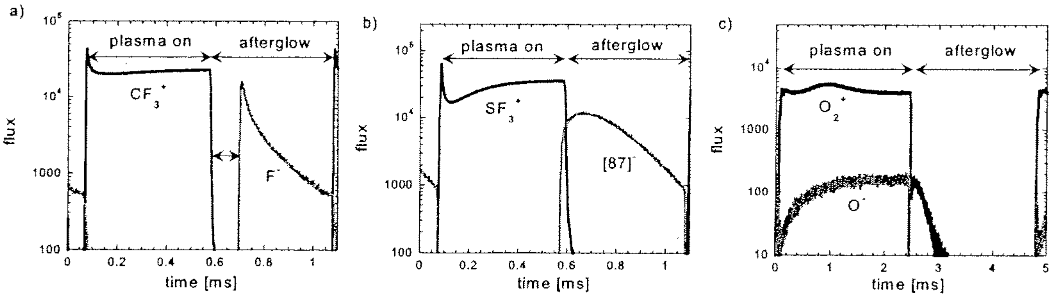

Fig. 1 : Positive and negative ions flux in a) CF_4, b) SF_6 and c) O_2 plasmas

A delay of 0.12 ms is measured before the escape of the negative ions in the CF_4 plasma (Fig. 1a). This corresponds to the collapse time of the sheath. In SF_6, a very short delay is observed (Fig. 1b): the sheath collapses almost instantly. This explains the dependence of the negative ions flux with the modulation frequency in these two plasmas (Fig. 2). The constant delay in CF_4 results in a cutoff frequency (4 kHz). At higher frequencies, the modulation period is shorter than the sheath collapse time, and therefore no negative ions can escape the plasma anymore. Similar results have been found in silane modulated plasmas [1]. In SF_6, the sheath collapse so fast that negative ions can be measured up to 100 kHz. The O_2 plasma, weakly electronegative, behaves completely differently. A small amount of negative ions is measured during the discharge, but no negative ions are observed during the afterglow (Fig. 1c). The attachment and ionization cross sections given in Fig. 3 are useful to understand the origin of the differences observed.

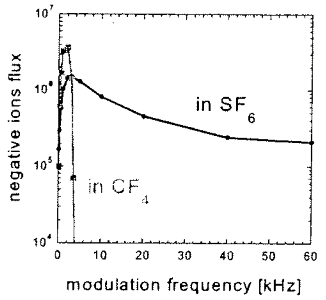

Fig. 2 : Negative ions flux vs modulation frequency

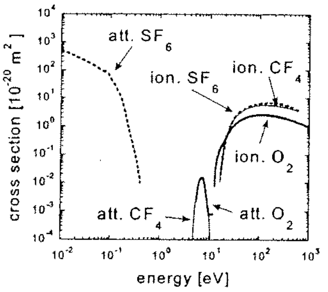

Fig. 3 : Ionization & attachment cross sections

The SF_6 stands out from the two other gases by his very efficient low energy attachment. In the beginning of the afterglow, electrons are rapidly attached to form negative ions. This is the cause of the fast collapse of the sheath. The weak luminosity and the low self bias voltage of this plasma illustrate his strong electronegativity (low electronic density). The negative ions in CF_4 plasma are created by high energy electron attachment, so they can be formed only during the discharge. Therefore in the afterglow the low energy electrons are lost by diffusion and not by attachment. This electrons loss process is slower and the negative ions are still trapped for about 0.1 ms by the remainig sheath. In O_2 discharges, detachment reactions of O^- by $O_2(a^1\Delta_g)$ metastables are very effective. This is the reason why we do not measure negative ions in the afterglow. The negative ions observed during the discharge mut result from indirect formation at the mass spectrometer orifice.

An unstable phenomenon can develop in O_2 and CF_4 discharges under specific conditions of power and pressure: between 185 and 490 V in O_2 (resp. 220 and 550 V in CF_4) at 0.25 mbar, above 0.195 mbar in O_2 (resp. 0.1 mbar in CF_4) at 250 V. This instability behaves globally in the same way in these two plasmas, but SF_6 discharges remain stable under any conditions. The stability of this plasma will be explained further.

Oscillations in the kHz range are detected simultaneously with all our available diagnostics. Fig. 4 shows such oscillations on voltage envelope, positive ions flux, light emission and floating potential in O_2 plasmas.

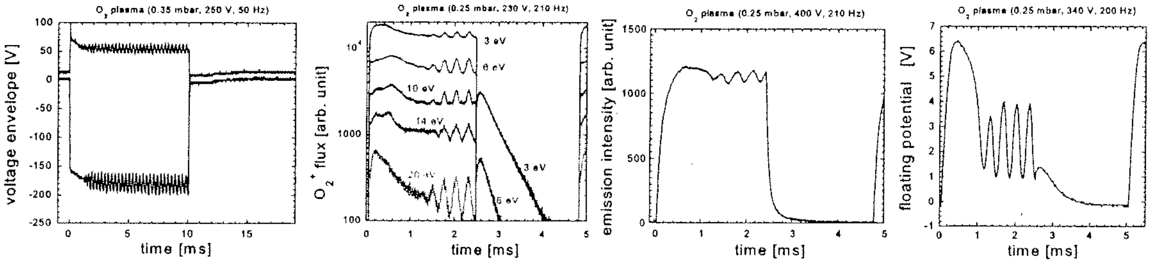

Fig. 4 : Instability observation on voltage envelope, positive ion flux, light emission and floating potential

Discharges in mixtures of electronegative and electropositive gases show directly the link between negative ions and the instability. The amplitude of the oscillations increases with the concentration of the electronegative gas.

These oscillations are due to the attachment-induced ionization instability described in details by Nigham and Wiegand [2]. The instability mechanism can be summarized with Fig. 5. A small initial increase in the electronic density n_e is generally followed by a decrease in the electronic temperature T_e due to the quasi-steady nature of the electron energy response. This diminution of T_e has different consequences according to the nature of the gas. In electropositive plasmas, electrons are created by ionization and lost mainly by diffusion to the walls. Ionization is less effective if T_e is diminished, so the electronic density decreases. This negative feedback stabilizes the perturbation. In electronegative plasmas, electrons can also be lost by attachment, and the efficiency of this process depends on electronic temperature. In certain cases, the attachment can become less effective than ionization if T_e decreases. Consequently, the initial disturbance is reinforced by this positive feedback and the discharge becomes unstable. In this type of instability, n_e and T_e are the physical values that are the source of the oscillations, leading to changes on the other measurable values.

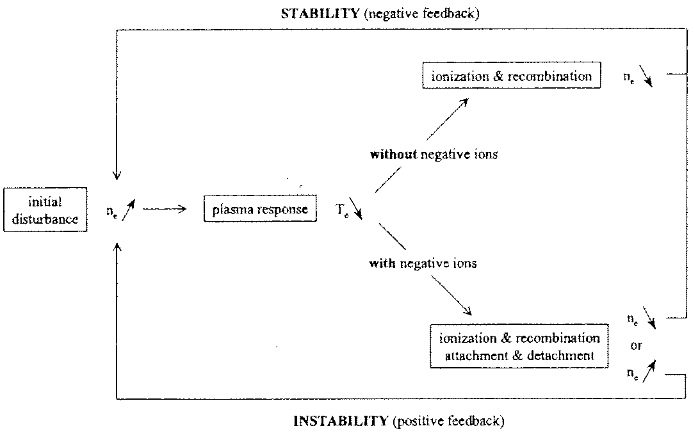

Fig. 5 : Instability mechanism

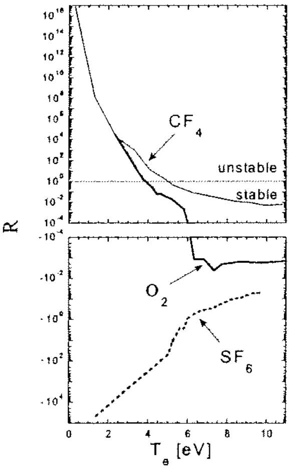

Fig. 6 : Instability criterion

This general description can be specified with a necessary condition for the appearance of the instability, derivated from the conservation equations of electronic and ionic densities [2]. The plasma can be unstable if

$$R = \frac{k_a \hat{k}_a}{k_i \hat{k}_i} > 1$$

where $k_j = \sqrt{\frac{2e}{m_e}} \cdot \int_0^\infty \sigma_j(E) \cdot f(E) \cdot E \cdot dE$ and $\hat{k}_j = \frac{T_e}{k_j} \cdot \frac{\partial k_j}{\partial T_e} \equiv \frac{\partial \ln k_j}{\partial \ln T_e}$

Practically, the criterion is fulfilled if the attachment rate coefficient increases with electronic temperature and if attachment and ionization rate coefficients are of a magnitude at least comparable (electronic density of the same order of magnitude than negative ions density).

Fig. 6 shows calculations of the ratio R for the three gases (f calculated with Bolsig from Kinema Software [3]). The ionization cross sections and therefore the ionization rate coefficients are quite similar for the three gases. But SF_6 differs from O_2 and CF_4 by his attachment cross section. The calculations of R demonstrate that O_2 and CF_4 plasmas can be unstable at low electronic temperature. On the contrary, the SF_6 plasma always remains stable because the attachment rate coefficient decreases with T_e ($R < 0$ at any electronic temperature). The peculiar attachment cross section is the source of the stability of SF_6 discharges.

[1] Howling A A, Sansonnens L, Dorier J-L and Hollenstein C 1994 *J. Appl. Phys.* **75** 1340

[2] Nighan W L and Wiegand W J 1974 *Phys. Rev. A* **10** 922

[3] Pitchford L C, O'Neil S V and Rumble J R 1981 *Phys. Rev A* **23** 294

Global Gyrokinetic Study of Finite β Effects on Linear Microinstabilities

G.L. Falchetto[†] and J. Vaclavik

Centre de Recherches en Physique des Plasmas,
Association Euratom-Confédération Suisse, EPFL, 1015 Lausanne, Switzerland
[†] Present address:*DRFC, Association Euratom-CEA, CEA Cadarache,*
13108 St Paul-lez-Durance, France

1. Introduction

Electromagnetic microinstabilities in tokamak plasmas are studied by means of a linear global eigenvalue numerical code, in the framework of gyrokinetic theory. The behavior of toroidal ITG modes and electromagnetic modes in the presence of finite β, of the Shafranov shift and of trapped particle dynamics is analysed. In particular the present study provides an insight on the properties of the so-called kinetic ballooning mode [1],[2] or shear-Alfvénic Ion Temperature Gradient mode [3], AITG. The threshold for the destabilization of this mode is identified and its radial structure first disclosed, owing to the global formulation.

2.The electromagnetic gyrokinetic global model

A low frequency electromagnetic perturbation is applied to a collisionless plasma, having low - but finite - β (the parallel perturbations of the magnetic field are thus neglected). Ion dynamics is described by the gyrokinetic equation; non adiabatic electrons are taken into account, with passing particles described as drift-kinetic and trapped electrons through the bounce averaged drift-kinetic equation, as in [4]. The system is closed by the quasi-neutrality equation and the parallel component of Ampère's law. The formulation is applied to a large aspect ratio toroidal configuration, with circular shifted magnetic surfaces. The system is solved in Fourier space, taking advantage of a decomposition adapted to the toroidal geometry [5, eq.3], and can be cast into the compact form:

$$\begin{pmatrix} \mathcal{M}_{\phi\phi} & \mathcal{M}_{\phi\mathcal{A}} \\ \mathcal{M}_{\mathcal{A}\phi} & \mathcal{M}_{\mathcal{A}\mathcal{A}} \end{pmatrix} \begin{pmatrix} \hat{\phi} \\ \hat{A}_{\|} \end{pmatrix} = 0 \tag{1}$$

where each of the submatrices is a sum over the contributions from the different particle species. The solution to the electromagnetic gyrokinetic equation is provided by solving for its propagator, which comes down to solve for the trajectories of gyrocenters. As far as one neglects the Shafranov shift, which is implemented to passing particles in a second step, the gyrocenter trajectories are the same as for the electrostatic case, thus the propagator for passing ions stays as in [4], whereas an explicit form for the propagator for passing electrons is derived making use of some approximations.

2.1 Passing Electrons. Passing electrons are considered as quasi-adiabatic, meaning that the non-adiabatic electron contribution to matrix ${\mathcal{M}_{\phi\phi}}^{el.}$ is negligible, furthermore use is made of the drift-kinetic approximation and of the frequency ordering $\omega \sim \omega_{ne} \ll \bar{\omega}_{te}$, ω_{ne} and $\bar{\omega}_{te}$ being the electron diamagnetic frequency and the average electron transit frequency. This ordering allows one to retain the diamagnetic drift only in ${\mathcal{M}_{\mathcal{A}\mathcal{A}}}^{el.}$.

The circulating electron propagator is therefore:

$$\mathcal{P} = \sum_{p=0,\pm 1} J_p\left(k_\perp v_{dz}/\omega_t\right)\, J_{p'}\left(k_\perp v_{dz}/\omega_t\right) \left.\frac{\exp\left[i\,(p-p')(\theta+\bar{\theta})\right]}{i\left(k_{\|}v_{\|} - p\,\omega_t - \omega\right)}\right|_{p'=p-m+m'} \tag{2}$$

Remark that since the electron transit frequency is much higher than the frequencies of the modes under study, one retains just its lower harmonics $p = 0, \pm 1$, though the poloidal coupling effect is preserved. Furthermore, consistently with the frequency ordering, the Bessel functions J_0, $J_{\pm 1}$ are expanded in their small argument, $k_\perp v_{dz}/\omega_{te} \ll 1$.

2.2 The Shafranov shift. The effect of finite β on the equilibrium has been taken into account separately from that due to the sole electromagnetic perturbation. One would like to point out that no use is made of the usual "$s-\alpha$" model. For the considered equilibrium, the Shafranov shift can be derived analytically by solving the Grad-Shafranov equation perturbatively. The radial derivative of the Shafranov shift is evaluated as: $\Delta' = \frac{\mu_0}{2}\, R p'\, {q_s}^2/{B_\varphi}^2$. Hence the magnetic flux and the gyrocenter trajectories are accordingly modified, giving rise to an explicit expression for the electromagnetic gyrokinetic equation which takes into account the Shafranov shift. In practice the implementation is carried out by substituting the modified wavevectors in the propagator.

3. Numerical Results

The simulations have been performed choosing a hydrogen toroidal plasma having the following magnetic geometry: $B_0 = 1.$Tesla, $R = 2.m, a = 0.5m$, a polynomial safety factor profile, $q_s(s) = 1.25 + 0.67s^2 + 2.38s^3 - 0.06s^4$, which satisfies $q_s(s_0) = 2$, while the magnetic shear is $\hat{s}(s_0) = 1$, $s_0 = 0.6$. The density profile and the identical electron and ion temperature profiles have been chosen $N(s)/N_0 = \exp\left[-(a\Delta s_n/L_{n0})\tanh((s-s_0)/\Delta s_n)\right]$; $T(s)/T_0 = \exp\left[-(a\Delta s_T/L_{T0})\tanh((s-s_0)/\Delta s_T)\right]$; with $\Delta s_n = 0.35$, $L_{n0} = 0.4m$, $\Delta s_T = 0.20, L_{T0} = 0.2m, T_0 = 7.5KeV$. The density $N_0 \equiv N(s_0)$ is evaluated from the value of $\beta(s_0) = 2\mu_0 N_0(T_0^e + T_0^i)/B_0^2$. Fixing a toroidal mode number $n = 7$, scans over the parameter β have been carried out, taking into account the only circulating particle dynamics and including the Shafranov shift effect, or adding trapped electrons. Note that, once the temperature T_0 is fixed, a scan over β corresponds to a scan over density.

Results, presented in Fig. 1 show a strong stabilization of toroidal ITG modes with finite β, whereas the frequency does not change much. At approximately half the value of β for which the stabilization of the ITG mode occurs, an electromagnetic mode, AITG, is destabilized. The growth rate of this mode rises rapidly, overcoming the ITG maximal growth rate already at $\beta(s_0) \simeq 1.5\%$, whereas its frequency is initially 6 times larger than the ITG's and decreases significantly with β. The threshold for the destabilization is located at half the critical value for MHD local ballooning stability, $\beta_c^{\mathrm{MHD}}(s_0) = 2.04\%$ as computed with KINX MHD stability code.

The effect of the Shafranov shift on the stability of electromagnetic modes is also depicted in Fig. 1. One can observe that it engenders a very strong stabilization of toroidal ITG modes (diamonds) and it is already effective at very low values of β. The threshold for the stabilization occurs at a value of $\beta \simeq 0.5\%$, corresponding to a factor 10 lower than the value obtained considering only the electromagnetic perturbation. Concerning the AITG modes, for the parameter regime analysed here one observes a complete stabilization. To highlight this effect, results from computations performed including 5% of the Shafranov shift value are also reported in Fig. 1 (dashed line with triangles). It is evident that the growth rate of the AITG mode is halved.

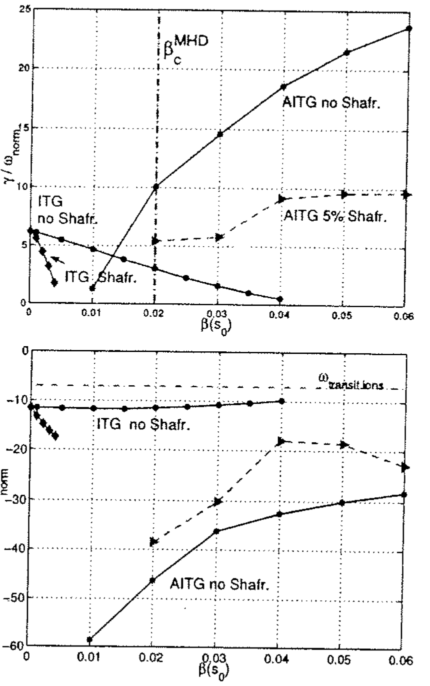

Figure 1: Normalized growth rates (top) and real frequencies (bottom) of ITG and AITG modes (full lines with circles and $*$), ITG modes with the Shafranov shift (diamonds) and AITG modes including 5% Δ' (dashed line). The local MHD ballooning limit β_c^{MHD} is also marked. $\omega_{norm} = \rho_{Li} v_{thi}/a^2 \simeq 3 \cdot 10^4$ Hz.

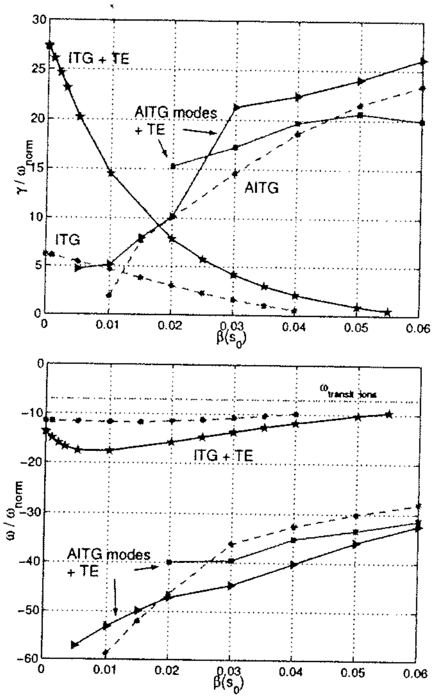

Figure 2: Normalized growth rates (top) and real frequencies (bottom) of ITG and AITG modes coupled to trapped electrons (full lines). The corresponding most unstable modes without trapped electrons are reported in dashed lines, for comparison.

Results from computations performed taking into account trapped electron dynamics have shown that the coupling to trapped electrons leads to a further destabilization of both the toroidal ITG and the AITG mode, as depicted in Fig. 2. In particular one can observe that the coupling to trapped electrons strongly enhances the ITG mode growth rate, which is then rapidly decreasing with increasing β. The complete stabilization of the coupled ITG-trapped electron mode occurs at a value of β slightly higher than for the pure ITG [5]. From Fig. 2 it is also evident that in presence of trapped electrons, a second electromagnetic mode can eventually become dominant for some values of β; the overall effect of the coupling to trapped electrons appears to be a destabilization of the AITG mode.

A typical AITG mode radial structure is shown in Fig. 3. It is evident that the mode envelope is not smooth as for toroidal ITG modes and modulations on small radial scales appear due to high radial wavenumbers produced by electron dynamics. One can also observe that the amplitude of the poloidal components of the electrostatic potential is maximal near the corresponding rational surfaces, for which $k_{\|}(s,m) = 0$, whereas, the poloidal components of the parallel vector potential vanish there. Remark that the mode is not radially localized around the magnetic surface where the temperature gradients are maximum, but around different rational surfaces, generally much inner, depending on the value of β. The mode structure in the poloidal plane is shown in Fig. 4, for an AITG mode at $\beta = 6\%$ and for the same mode coupled to trapped electrons. One can observe that the structure reflects the behavior of the potential poloidal components and the ballooning character of the mode is more pronounced when it is coupled to trapped electrons.

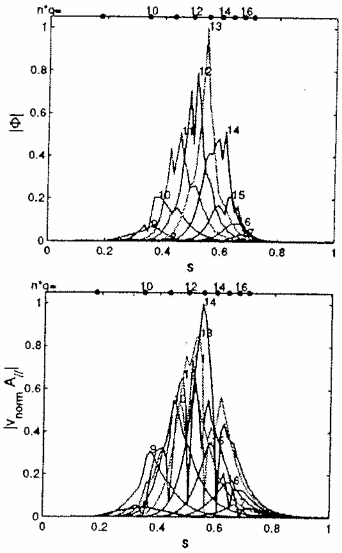

Figure 3: Poloidal mode decomposition in configuration space for the electrostatic potential(top) and parallel vector potential(bottom) of an AITG mode at $\beta = 6\%$. Mode rational surface positions are reported on the top axis.

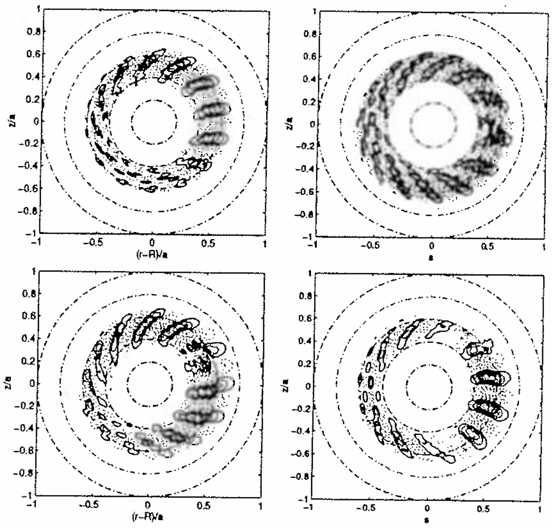

Figure 4: Contours in poloidal plane of the electrostatic potential(top) and parallel vector potential(bottom) for the AITG mode at $\beta = 6\%$ (left) and for the same mode coupled to trapped electrons (right).

Acknowledgements *One of the authors is grateful to L. Villard for stimulating discussions and acknowledges A. Martynov for the KINX computations. This work was partly supported by the Swiss National Science Foundation. The computations have been performed on the Origin 3000 of the EPFL.*

References

[1] W. Tang, J. Connor, and R. J. Hastie, Nuclear Fusion **21**, 1439 (1980).

[2] C. Z. Cheng, Physics of Fluids **25**, 1020 (1982).

[3] J. Dong, L. Chen, and F. Zonca, Nuclear Fusion **39**, 1041 (1999).

[4] S. Brunner, M. Fivaz, T. Tran, and J. Vaclavik, Physics of Plasmas **5**, 3929 (1998).

[5] G. L. Falchetto and J. Vaclavik, in *Theory of Fusion Plasmas, Proc. Int. Workshop, Varenna, August 2000* (Editrice Compositori, Società Italiana di Fisica, Bologna, 2000), p. 321.

ECCD and Bootstrap Current Profiles in Advanced Scenario Plasmas in TCV

T.P. Goodman, R. Behn, S. Coda, I. Condrea, M.A. Henderson, P. Nikkola , O. Sauter

Centre de Recherches en Physique des Plasmas, EPFL
Association EURATOM-Confederation Suisse, CH-1015 Lausanne, Switzerland

Introduction

The electron cyclotron wave (ECW) system is the only auxiliary plasma heating system on TCV: It provides both electron cyclotron heating (ECH) and current drive (ECCD). Starting with an inductively-driven, constant, plasma current, either the loop voltage is set to zero, or better yet, the external inductive electric field is set to zero by a feedback system just after ECCD is started. The ECCD is in the same direction as the existing plasma current (CO-CD). In this way, over the past few years, TCV has demonstrated that *1)* it is possible to drive the entire plasma current for ~2s by ECCD and the accompanying bootstrap current (~10-20%), *2)* when too much power is deposited centrally the plasma is disruptively MHD unstable, *3)* the normalized local current drive efficiency $\eta_T = IR_0n_e/T_e/P$ decreases rapidly as power is deposited at larger normalized radius ρ, consistent with particle trapping[1], and *4)* balancing points 2 and 3 leads to a maximum driven current in TCV of 210kA using all six 82.6GHz (2nd harmonic X-mode: X2), 2s, 0.5MW gyrotrons of the ECW system[2]. In addition, by using two pairs of gyrotrons switched on one pair after the other, a 2.8s fully ECCD driven plasma of slightly more than 100kA has been demonstrated[3]. This has now been extended to 4s. This is the maximum possible pulse length in TCV and is determined by the ECW system.

Here we make a preliminary report on the extension of these results to steady-state fully ECCD driven advanced scenarios with ~80% bootstrap fraction by the use of *off-axis only* ECCD to create negative central shear (reversed shear).

General features of plasmas fully sustained by off-axis ECCD

The full plasma current has been driven non-inductively for the first time in TCV using 0.9MW of *off-axis* ECCD *only* from two of the gyrotrons in the system. None of the millimeter wave power is deposited near the center of the plasma. The presence of fast electrons at the plasma center and across the entire plasma cross-section is evidenced[4] by a hard X-ray camera on loan from CEA-Cadarache. Spatial (radial) diffusion of RF generated supra-thermal electrons away from the deposition region can supply current carrying fast electrons on-axis. As it also reduces the quasi-linear effects of RF diffusion, it can remove the order of magnitude discrepancy between the measured I_{CD} (45kA) and that calculated by the CQL3D Fokker-Planck code when radial diffusion is not included (460kA). (The power densities in TCV are well above those required for strong quasi-linear enhancement of the driven current[5].) Off-axis power deposition produces off-axis temperature and density gradients, favoring generation of bootstrap (BS) current. The addition of the ECCD and BS current profiles is peaked off-axis and the resulting safety factor profile exhibits good confinement[6].

Driven current profiles

In steady state, the total I_{CD} is given by the measured I_p minus the bootstrap current I_{BS}; which is calculated using the electron density and temperature profiles measured each 50ms by Thomson scattering. The externally applied electric field is kept zero by feedback. Internally generated electric fields are assumed to be zero if the plasma configuration is stable but, may play a role during transients. Cold plasma ray-tracing, performed using TORAY-GA, provides input for Fokker-Planck absorption and current drive calculations, using CQL3D. It has been shown recently with this code that radial diffusion play a much more important role in determining the current drive efficiency in TCV than, for example, in DIII-D[7]. The code provides two models for diffusion (and advection), with different parallel velocity dependencies; corresponding, approximately, to electrostatic (constant in $v_{//}$) and electromagnetic ($\sim v_{//}$) anomalous radial diffusion. The radial profile of the diffusion coefficient increases towards the plasma edge in the model. A single fit parameter is then adjusted until the total driven current matches the measured value. (The advection term is adjusted to maintain the measured density profile. It is proportional to the diffusion coefficient). In the region of 6-D phase space where the power is deposited, the diffusion coefficients for both models match within approximately a factor of two (3-6m^2/s). The effect of diffusion is twofold. First, the current drive efficiency predicted for the high power densities of TCV is drastically reduced to values still larger than the linear result, and second, the I_{CD} is spread to the center of the plasma, although no power is directly deposited there. This is seen in figure 1a-d.

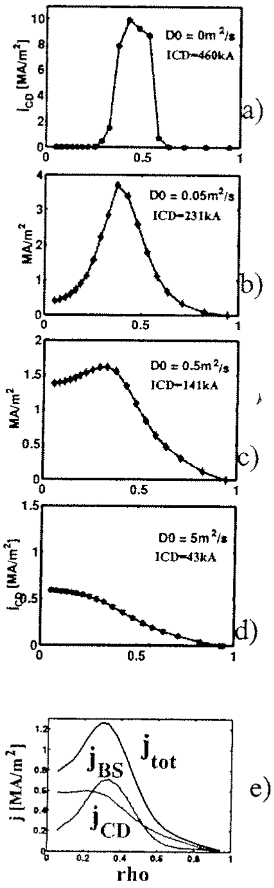

Figure 1 The CQL3D ECCD current profile broadens and the total driven current is reduced as radial diffusion is increased (a-d). The total current density profile (e) is a combination of the lower curve (d) and the bootstrap current calculated from the density and temperature profiles (Fig. 3)

The deposition location of the ECCD plays a crucial role in the evolution of the discharge. It determines the amount of ECCD driven current and the gradients that lead to the bootstrap current generation. The ratio of the two contributions to the total current will vary with the CO-CD deposition location. When far enough off-axis, the total current profile is very flat to slightly hollow as the off-axis peaked j_{BS} is added to the flattened j_{CD} profile. When counter-CD is added to this configuration inside of the CO-CD deposition location, j_{tot} becomes clearly hollow (Fig. 1e). The resulting current profile and the measured pressure profiles are used in CHEASE to reconstruct the q-profile (Fig. 2). The q-profile calculated by the standard TCV reconstruction code LIUQE, using external magnetic data and low order polynomials, is shown for comparison. A clear reversed shear profile is found by CHEASE.

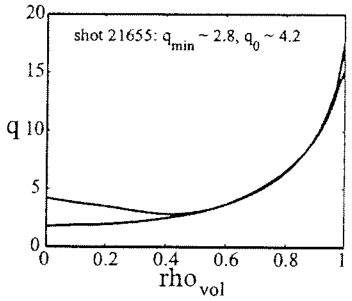

Figure 2. The reversed shear q-profile calculated by CHEASE using the current profiles of figure 1e (red curve) is compared with the "standard" profile found by the LIUQE reconstruction code (blue curve).

eITB creation and driven current

Rebut-Lallia-Watkins (RLW) global energy scaling describes most TCV plasmas well; although, improved central electron confinement (ICEC) has been reported in Ohmic plasmas with off-axis ECH and counter-CD on-axis[8]. In the fully sustained plasmas described in this work, adding additional ECH or, especially, counter-CD in the plasma center demonstrates that an electron internal transport barrier (eITB) exists due to the combination of the off-axis CO-CD and bootstrap current. The electron energy confinement time τ_{Ee} in non-disruptive plasmas exceeds the RLW confinement time τ_{RLW} by up to a factor of 4.5 (i.e $H_{RLW} \equiv \tau_{Ee} / \tau_{RLW} \leq 4.5$). When the central counter-CD is increased beyond a certain point, the pressure profile becomes too strongly peaked, the plasma is MHD unstable, strong mode activity is observed and the good confinement is lost. However, by controlling the amount of central counter-CD, it is possible to stay just below the instability limit.

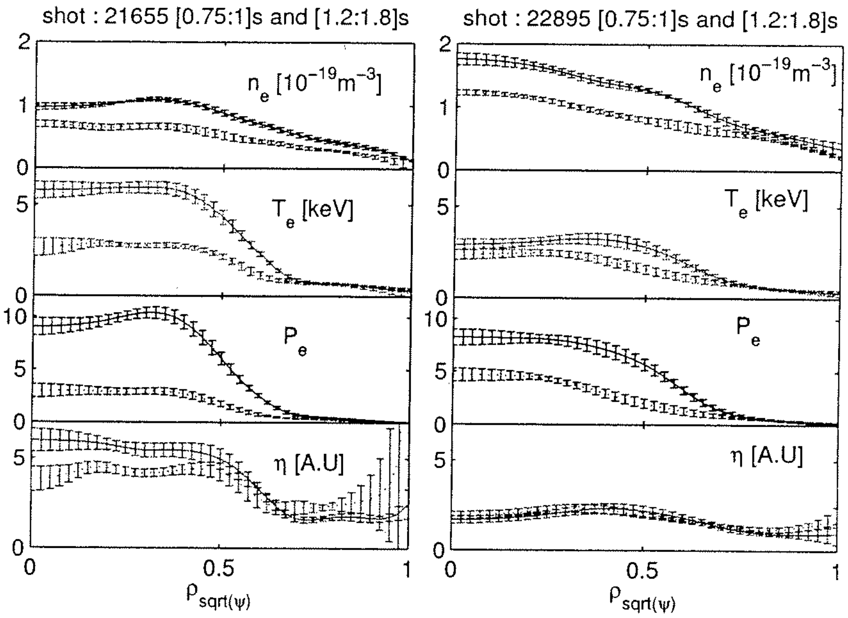

Figure 3. Electron density, temperature, pressure and CD efficiency related Te/ne for 2 high bootstrap fraction shots before and after the addition of central ECH and counter-CD. The off-axis CO-CD power deposition is centered near normalized radius of 0.6. Bootstrap fractions of 50% (21655) and 76% (22895) are calculated for plasma currents of 90kA and 70kA, respectively. The higher density of 22895 reduces the current drive by a factor of 2 prior to the central heating but ultimately increases bootstrap fraction.

The eITB is controlled by the off-axis ECCD deposition location. When additional ECH power is added inside of the barrier, the pressure profile peaks, the BS current increases, the eITB is reinforced and the bootstrap current increases further. It might be expected that the total current would increase accordingly. However, in general in TCV the average density rises as the ECH power is increased. The local ECCD efficiency is proportional to T_e/n_e while the BS current is proportional to the gradients of n_e and T_e. The constant of proportionality for the density is ~2-3 times as large as for the temperature[9]. When T_e/n_e remains constant as ECH is added inside the barrier, the BS current can increase while the ECCD current does not change. In this case, the bootstrap *fraction* will increase with additional ECH power. In the case of counter-ECCD added inside the barrier, the ECCD current can even decrease. Thus, the total plasma current (ECCD + BS) need not increase significantly even when the bootstrap current increases.

The electron density, temperature, pressure and current-drive-efficiency related ($\eta \equiv I_{CD}/P \sim Te/ne$) profiles are shown from top to bottom in Fig. 3. Two shots are shown; 21655 (left) at low density ~0.6 x 10^{19} and 22895 (right) at twice the density. Initially, 0.9MW of off-axis CO-CD sustains the current and the profiles evolve on a current redistribution timescale (few 100ms). Once the current has evolved, 0.45MW of counter-CD is added inside the barrier. In shot 22895, an additional 0.45MW of ECH heating power was added to each phase of the shot to permit higher density operation. The total power was 1.4MW for shot 21655 and 2.3MW for 22895. The lower curves are averages over ~200ms prior to the addition of power inside the barrier and the upper curves are averaged over ~800ms during the central heating phase. The change in profiles occurs during a few tens of milliseconds. The CO-CD is deposited around $\rho \sim 0.5 - 0.6$ in shot 21655 and $\rho \sim 0.6–0.7$ in shot 22895. The current drive efficiency remains nearly constant when the additional power is added, except in the central part of 21655 where the counter-CD occurs.

Conclusions

Plasmas have been fully sustained by off-axis ECCD. The driven current profile is flattened by radial diffusion of the fast electrons. Large bootstrap contributions to the total current profile produce steady state reversed shear profiles exhibiting steady-state eITBs. Bootstrap fractions of up to ~80% are acheived by proper distribution of 2.3MW of power.

References:

---

[1] O. Sauter, *et al.*, Phys. Rev. Lett. **84**; 3322 (2000).

[2] S.Coda, *et al.*, Plasma Phys. Controlled Fusion **42**, B311 (2000).

[3] T.P. Goodman, *et al.*, Proc. of IAEA FEC-2000, Sorrento 2000.

[4] S. Coda, *et al.*, this conference, oral.

[5] R.W. Harvey, *et al.*, Phys. Rev. Lett. **62** (1989) 426.

[6] O. Sauter, *et al.*, this conference, poster.

[7] R.W. Harvey, *et al.*, Phys. Rev. Lett. **88** (2002) 205001.

[8] Z.A.Pietrzyk, et al. PRL Vol. 86 No. 8 (2001) 1530

[9] O.Sauter, *et al.*, Phys. Plasmas **6**, 2834 (1999).

SEMI-LAGRANGIAN DRIFT-KINETIC CODE FOR SLAB-ITG TURBULENCE

V. Grandgirard, M. Brunetti[1], S. Allfrey[1], A. Bottino[1], P. Bertrand[2],
P. Ghendrih, X. Garbet, A. Ghizzo[2], G. Manfredi[1], M.Ottaviani,
Y. Sarazin, O. Sauter[1], J. Vaclavik[1], L. Villard[1]

DRFC, Association Euratom-CEA, CEA Cadarache, 13108 St Paul-lez-Durance, France.
[1] *CRPP, Association Euratom-Confédération Suisse, EPFL, 1015 Lausanne, Switzerland.*
[2] *LPMIA, Université Henri Poincaré-Nancy 1, BP 239, 54506 Vandoeuvre-les-Nancy, France.*

1 Introduction

Understanding and extrapolation of confinement properties remains a key issue for present and future devices. Recent analysis has revealed significant discrepancies between gyrokinetic and fluid calculations. A proper investigation of gyrokinetic turbulence is mandatory to understand turbulent transport in fusion plasmas.
This work deals with non-linear global simulations of instabilities driven by ion temperature gradients (ITG) in an inhomogeneous collisionless plasma confined by a strong uniform magnetic field. Here are presented the first non-linear results obtained with the recently developed Semi-Lagrangian (SL) 4D code.

2 Drift-kinetic model

We consider a collisionless plasma, cylindrical and periodic, which focuses the study to SLAB-ITG modes. The magnetic field is assumed uniform $\vec{B} = B_z\vec{e_z}$ and electrons are considered adiabatics. The Larmor radius effects are neglected so that the ion trajectories are governed by the guiding-center (GC) trajectories, hence :

$$\vec{v_{GC}} = \frac{\vec{E}\times\vec{B}}{B^2} \quad ; \quad \frac{dz}{dt} = v_\parallel \quad ; \quad \dot{v_\parallel} = \frac{q}{m}E_z \tag{1}$$

We assume that there is no fluctuating magnetic field and we use the electrostatic approximation to compute the electric field : $\vec{E} = -\vec{\nabla}\Phi$ where the scalar $\Phi(r,\theta,z,t)$ represents the electric potential. The evolution of the distribution function $f(r,\theta,z,v_\parallel,t)$ is described by the drift-kinetic Vlasov equation :

$$\frac{\partial f}{\partial t} + \vec{v_{GC}}\cdot\vec{\nabla}_\perp f + v_\parallel\frac{\partial f}{\partial z} + \dot{v_\parallel}\frac{\partial f}{\partial v_\parallel} = 0 \qquad \text{with } \vec{\nabla}_\perp = (\frac{\partial .}{\partial r}, \frac{1}{r}\frac{\partial .}{\partial \theta})^t \tag{2}$$

which couples the $\vec{E}\times\vec{B}$ motion across the magnetic field to the motion parallel to the magnetic field. This equation is non-linearly coupled to the quasi-neutrality equation :

$$-\nabla_\perp\cdot\left[\frac{n_0(r)}{B\Omega_0}\nabla_\perp\Phi\right] + \frac{e\,n_0(r)}{T_e(r)}\left(\Phi - \lambda\langle\Phi\rangle\right) = n_i - n_0 \tag{3}$$

where Ω_0 denotes the ion cyclotron frequency ; T_e and n_0 respectively the electron temperature and density profiles. The ion density profile is given by $n_i(r,\theta,z,t) = \int dv_\parallel\, f(r,\theta,z,v_\parallel,t)$ and $\langle\cdot\rangle$ represents the average on the magnetic field lines. The parameter λ is equal to 1 or 0 if the zonal flows are taken into account or not.

3 Linearised dispersion relation

The linearisation of the Vlasov equation (2) and the quasi-neutrality equation (3) is done by splitting f into its Maxwellian equilibrium part and a fluctuating part of first order in the fluctuations. The linear dispersion relation is then :

$$D(\omega) = \left(\kappa(r) + \frac{m^2}{r^2} + \frac{1}{Z_i T_e(r)}\right) T_i(r) + 1 - zZ(z)\{-1 + \frac{\omega^*_{ni}}{\omega} + \frac{\omega^*_{Ti}}{\omega}\left[-\frac{1}{2} + \frac{z}{Z(z)} + z^2\right]\}$$

where Z is the Fried and Conte relation with $z = \frac{\omega}{k_\parallel \sqrt{2T_i}}$ while the diamagnetic drift frequencies are defined by $\omega^*_{Ti} = T_i(r)\frac{d \log T_i(r)}{dr} k_\theta$ and $\omega^*_{ni} = \frac{1}{\eta}\omega^*_{Ti}$ with $\eta = \frac{d \log T_i(r)}{d \log n_0(r)}$. $k_\theta = m/r$ and $k_\parallel = 2\pi n/L_z$ represent the Fourier space vectors, with Lz the cylinder length. The radial electric potential is approximated by $\exp(-g(r))$ where $g(r)$ is chosen such that $\Phi(r)$ is close to the η initial profile. In this case, the function $\kappa(r)$ is $\kappa(r) = -\left[\frac{\partial^2 g(r)}{\partial r^2} + \left(\frac{\partial g(r)}{\partial r}\right)^2 + (\frac{1}{r} + \frac{1}{n_0(r)}\frac{dn_0(r)}{dr})\frac{\partial g(r)}{\partial r}\right]$.

The solutions $\omega/D(\omega) = 0$ are computed using a Nyquist algorithm, with $\omega = \omega_r + i\gamma$ where ω_r correspond to the frequency and γ to the linear growth rate. The dependence of γ according to the mode numbers m and n is shown in figure 1.

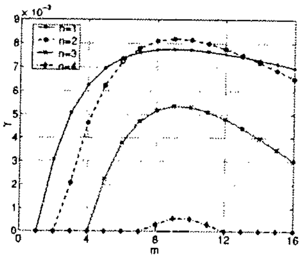

Figure 1: linear growth rate

4 The global Semi-Langrangian code

The non-linear simulations are performed with a recently developed 4D code written in fortran 90 and parallelized with MPI. This code is based on the Semi-Lagrangian method [1]. The purpose of the SL method is to make the best use of the Lagrangian (Particle in Cell code for example) and Eulerian numerical schemes. Therefore to have a good description of the phase space in particular in regions of low density, with an enhanced stability. In this approach, the mesh grid is kept fixed in time in the phase space (Eulerian method) and the Vlasov-equation is integrated along the trajectories (Lagrangian code) using the fact that the distribution function is constant on the trajectories. Cubic spline interpolations are performed to evaluate the new value of the distribution function on the grid points. Indeed, if f is known over the whole fixed grid at the time t, then f at the next time $t + \Delta t$ can be deduced, for each node X_i of the mesh, by $f\left(X_i(t + \Delta t), t + \Delta t\right) = f\left(X(t, X_i, t + \Delta t), t\right)$, where $X(t, X_i, t + \Delta t)$ is the position in the 4D phase space of this point X_i at the previous time t.

The integration along the trajectories is performed with a time-splitting algorithm, which allows one to divided the resolution of the 4D advection equation into the resolution of a succession of 2D and 1D advections. The second order of the global numerical scheme is obtained by conserving a symmetry in the advection and by using a predictor-corrector algorithm in time.

5 Results

The plasma is initialized by exciting a superposition of ITG mode (m, n) with random phase α_{mn} and amplitude ϵ_{mn} such that

$f(r, \theta, z, v_\parallel, 0) = f_M(r, v_\parallel) \times (1 + \sum_{mn} \epsilon_{mn} \cos(\frac{2\pi n}{L_z} z + m\theta + \alpha_{mn}))$ where the Maxwellian function f_M is defined by $f_M(r, v_\|) = (n_0/\sqrt{2\pi T_i/m_i})\exp(-m_i v_\|^2/2T_i)$. In the following, the temperature is normalized to T_{e0}, where T_{e0} is defined such that $T_e(r_0)/T_{e0} = 1$ (with r_0 a reference point). The time is normalized to Ω_0^{-1}, the velocity to the sonic velocity $c_s = \sqrt{\frac{T_{e0}}{m_i}}$ and the electric potential to $\frac{T_{e0}}{q_i}$. We impose a vanishing fluctuating part of the distribution function at the boundaries in the r and $v_\|$ directions. Periodic boundary conditions are used in the θ and z directions. The electron temperature is kept constant while the ion temperature (fig 2.a) and the density profiles (fig 2.b) are chosen such that the $\eta_i = d\log T_i/d\log n_0$ is larger than 2 in a sufficiently large region to generate instabilities (fig 2.c).

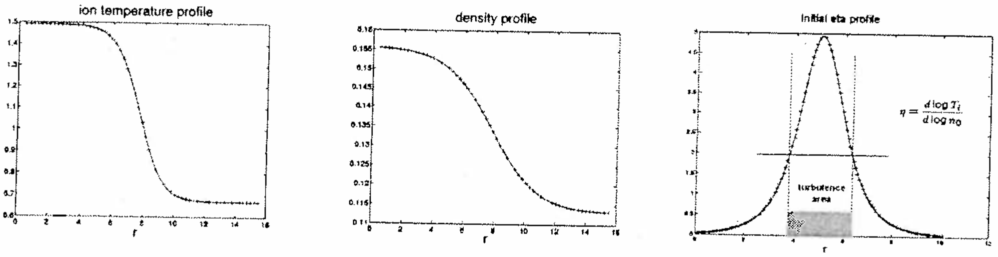

(a) (b) (c)

Figure 2: (a) Ion temperature profile : $T_i(r)$. (b) Density profile : $n_0(r)$. (c) η_i profile.

Role of the zonal flows in the non-linear phase

The SL code is able to simulate the linear and non-linear phase of the SLAB-ITG turbulence. Indeed, we observe an exponential increase in the linear phase (fig. 3), where the linear growth-rate is comparable to the one predicted by the linear study (fig. 1) and the non-linear saturation is well described too. As first non-linear results we present the effect of the zonal flow (case $\lambda = 1$ in (3)) on the turbulent transport. A cross-section of the electric potential shows larger poloidal convection cells in the case $\lambda = 0$. In figures 5.(a) and (b), we see the relaxation of the initial density and ion temperature profiles to the critical threshold values. Besides, comparing the ion temperature profile variation and the flux time evolution, we see the stabilizing effect of the zonal flows.

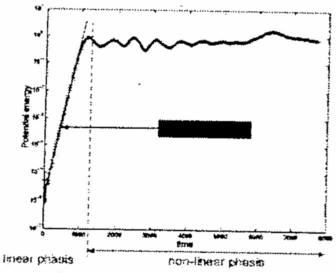

Figure 3: Evolution of Φ^2 : linear phase + non-linear phase

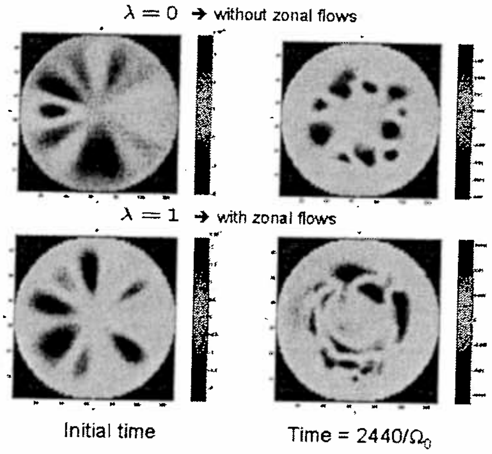

Figure 4: Cross-section of the electric potential in (r, θ), at initial time and time in the saturation phase (t=2440/Ω_0), for both cases $\lambda = 0$ and $\lambda = 1$.

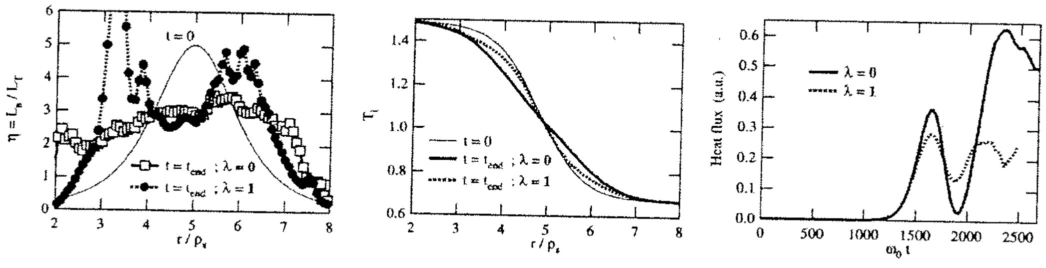

(a) (b) (c)

Figure 5: Comparison without ($\lambda = 0$) and with ($\lambda = 1$) zonal flows for : (a) η profile, (b) ion temperature profile, (c) flux. In (a) and (b) the black lines correspond to the initial state.

Energy and particle conservation

A drawback of the SL method is that the particle conservation is not assured. In our case the number of electrons is constant due to their adiabaticity, but not the number of ions. Nonetheless, the relative error is of the order of 10^{-5} (fig 6.(a)), which is acceptable considering that the order of the interpolation error with cubic splines is of 10^{-6}.In figure 6.(b)), we see that the variation of the kinetic energy $E_{kin} = 1/2 \int (f - f_M) v_\parallel^2 dV \, dv_\parallel$ is balanced by the variation of the potential energy $E_{pot} = 1/2 \int (n_i - n_0) \Phi dV$. However, the total energy $E_{tot} = E_{kin} + E_{pot}$ is not exactly conserved. We still have to understand how this energy conservation can be improved.

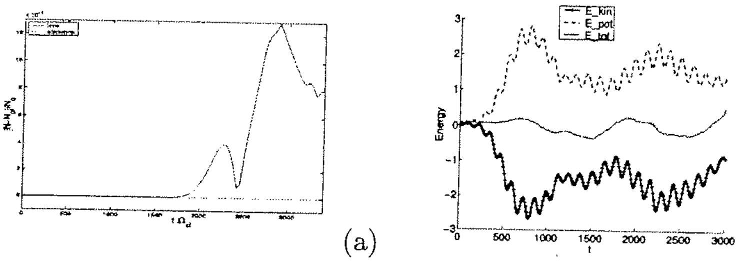

(a) (b)

Figure 6: (a) Relative error of the particle number . (b) Conservation of the total energy

6 Conclusion

A Semi-Lagrangian 4D code has been developed which is able to describe the non-linear phase of the SLAB-ITG turbulence. As first results we have shown the stabilizing effect of the zonal flows. Further investigations are necessary to improve the conservation of the total energy.

References

[1] Sonnendrücker E. et al., 1999 *Journal of Comput. Phys.*, **149**, 201-220.

[2] T.M. Tran et al., 1999 *Proc. Varenna-Lausanne Int. Workshop*, ISPP-18.

[3] Manfredi G et al., 1996 *Phys. Plasmas*, **3** 202.

[4] Depret G. et al., 2000 *Plasma Phys.*, **42** 949.

Critical Behaviour of Fast Particles Induced by NBI in Sawtooth Stability Modelling

J. P. Graves, N. N. Gorelenkov[1], O. Sauter
Centre de Recherches en Physique des Plasmas, Association EURATOM-Confédération Suisse, EPFL, 1015 Lausanne, Switzerland.
[1]*Princeton Plasma Physics Laboratory, Princeton, NJ, 08543, USA.*

The question of extended sawtooth quiescent periods and the relationship to strong kinetic stabilisation is a crucial issue for future large tokamaks. A particularly relevant issue addressed here is the response of neutral beam injected (NBI) ions on internal kink stability. Such a study is of interest for a number of reasons, not least because strongly sheared toroidal plasma rotation of up to 30 kHz has been measured in NBI discharges in JET [1], and correlations between changes in sheared plasma rotation and sawtooth stability have been predicted [2] and observed [3]. Also of interest is the effect of the injection angle, and resulting pitch angle distribution, on fast ion stabilisation. In particular it is seen that fast ion stabilisation of sawteeth in JET NBI plasmas could be dominated by fluid effects rather than kinetic effects. This follows because fluid effects are found to be strongly stabilising where there are large fractions of passing ions, which unlike trapped ions, spend more time in the inner region of good curvature. Such speculations can be made, for the first time, because all contributions significantly affected by anisotropy are evaluated accurately and included in the evaluation of the potential energy δW of the ideal internal kink instability.

The analysis is split into the response of the core plasma 'c' and the hot minority NBI ions 'h' on internal kink stability. The temperature of the core plasma is assumed to be low enough such that thermal ions do not give rise to kinetic effects, and the distribution function of the core plasma is assumed to be isotropic in pitch angle. However, NBI ions are in general anisotropically distributed and are fast enough to give rise to kinetic effects, which in turn are strongly dependent on the plasma rotation driven by NBI. The plasma anisotropy is limited by the empirically justified assumption that the isotropic core pressure is around two thirds of the total pressure. The following analysis therefore seeks to obtain the fast ion response of NBI in a weakly anisotropic plasma which is flowing at sub-sonic speeds.

The equilibrium hot ion pressure tensor can be described [4] by the double adiabatic model: $\underline{\underline{P_h}} = P_{h\perp}\underline{\underline{I}} + (P_{h\|} - P_{h\perp})\hat{e}_{\|}\hat{e}_{\|}$, where $\underline{\underline{I}}$ is the unit dyadic and $\hat{e}_{\|}$ the unit vector parallel to the magnetic field. If the equilibrium is perturbed by a MHD mode with displacement vector $\boldsymbol{\xi}$, a potential energy term $\delta W_{hf} = \frac{1}{2}\int d^3x\,\boldsymbol{\xi}^* \cdot (\nabla \cdot \underline{\underline{\delta P_h}})$ (where f denotes 'fluid') arises as a consequence of a convective perturbation of the fast ion distribution function: $\delta F_h = -\boldsymbol{\xi} \cdot \nabla F_h$. It can be shown that [5]:

$$\delta W_{hf} = -\frac{1}{2}\int d^3x \left[\boldsymbol{\xi} \cdot \nabla \left(P_{h\perp} + P_{h\|}\right) - \left(P_{h\perp} + P_{h\|} + C_h\right) \frac{\boldsymbol{\xi} \cdot \nabla B}{B}\right] \frac{\boldsymbol{\xi}^* \cdot \nabla B}{B}, \tag{1}$$

where $C_h = \pi m_h \int_{-\infty}^{\infty} d\mathcal{E} \int_0^{\infty} d\mu\, (B(\mu B)^2/|v_{\|}|)\partial F_h/\partial \mathcal{E}$ is defined for a hot ion distribution $F_h(r, \mathcal{E}, \mu)$ with mass m_h. Equation 1 quantifies the effect of anisotropy on the internal kink mode. In particular the second term in the square brackets of Eq. 1 was identified by Mikhailoskii [6] as being a possible candidate for an anisotropically driven instability. The first term in Eq. 1 also quantifies the effect of anisotropy, but this time through the poloidal dependence of the pressure components $P_{h\perp}$, $P_{h\|}$.

The leading order contributions to the toroidal plasma rotation arise from a finite pressure gradient of the thermal ions and from an equilibrium radial electric field E. It is appropriate to assume that poloidal flow is strongly damped [7], such that the toroidal rotation of the core plasma is given by $\Omega = \Omega_E + \omega_{*pi}$ with $\Omega_E = qE/B_0 r$ and $\omega_{*pi} = -qP_i'/eZn_iB_0r$, where eZ, n_i and P_i are respectively the charge, density and pressure of thermal ions and $' \equiv d/dr$. The common source of rotation for the different plasma species is that arising from the equilibrium electric field $\Omega_E(r)$. Hence, for NBI scenarios, one can envisage a mechanism whereby the momentum of the injected ions initially rotates the plasma, which in order to satisfy the force balance equation, must establish a radial electric field.

For analysing the hot ion response of 'sawtooth modes' with mode frequency ω, it is usually assumed that $\omega_{*h} \gg \omega$ and $\langle\omega_{mdh}\rangle \gg \omega$, where ω_{*h} and $\langle\omega_{mdh}\rangle$ are respectively the hot ion diamagnetic and bounce averaged magnetic drift frequencies. This is appropriate because, in contrast to 'fishbone modes', which generally satisfy [8] $\omega \sim \langle\omega_{mdh}\rangle$, sawteeth are believed to have mode frequencies of the order of ω_{*pi}. However, when toroidal rotation is present, the mode frequency is Doppler shifted [2]: $\omega \rightarrow \omega - \Omega_E(r_1) = \tilde{\omega}$. The dispersion relation for the internal kink mode can then be written in such a way that strongly subsonic sheared toroidal plasma rotation only appears in the kinetic contribution [2]. The present paper will be concerned with differential rotation $\Delta\Omega_E(r) = \Omega_E(r) - \Omega_E(r_1)$ of variable magnitude up to $\Delta\Omega_E \sim \langle\omega_{mdh}\rangle$, and the following orderings apply: $\langle\omega_{mdh}\rangle \sim \omega_{*h} \gg \tilde{\omega} \sim \omega_{*pi}$. The hot kinetic contribution to the internal kink mode is then:

$$\delta W_{hk} = -2^{5/2}\pi^3 m_h \frac{\xi_0^2}{R_0}\int_0^{r_1} dr\, r B_0 \int_{1/B_{\max}}^{1/B_{\min}} d\alpha\, \frac{I_q^2}{K_b}\int_0^{\infty} d\mathcal{E}\, \mathcal{E}^{5/2}\frac{\partial F_h}{\partial \mathcal{E}}\left[\frac{\omega_{*h} + \Delta\Omega_E}{\langle\omega_{mdh}\rangle + \Delta\Omega_E}\right], \tag{2}$$

where $\alpha = \mu/\mathcal{E}$ is a pitch angle variable, and K_b and I_q are defined for example in Ref. [2]. Assuming that the mode does not lie inside the gap in the Alfvén continuum $0 < \tilde{\omega} < \omega_{*pi}$, the ideal stability criterion is given by $\delta W_T + \delta W_{hf} + \delta W_{hk} > 0$, where δW_{hk} denotes the real part of Eq. (2) and δW_T is the toroidal contribution to stability as described for example by Bussac *et al* [9].

The hot ion distribution function that is appropriate for this study will be invariant to rapid gyromotion and finite orbit widths. Thus it must be expressible in the form $F_h(\mathcal{E}, \mu, r)$. The absolute velocity dependence of the NBI population is approximately described by a simple slowing down distribution $\sim 1/v^3$. However, the velocities of the minority ions will be focused to some extent in the direction of injection. A model distribution function [10] which includes these effects is as follows:

$$F_h(\mathcal{E}, \mu, r) = \frac{c(r)}{\mathcal{E}^{3/2}}\exp[-(\lambda - \lambda_0)^2/\Delta\lambda^2] \tag{3}$$

for $0 \leq \mathcal{E} \leq \mathcal{E}_m$ and $F_h = 0$ for $\mathcal{E} > \mathcal{E}_m$. The pitch angle $\lambda = B_0\mu/\mathcal{E}$ is valid for $0 \leq \lambda \leq 1/(1-\epsilon)$, with $B = B_0(1-\epsilon\cos\theta)$. The coefficient $c(r)$ assumes the role of normalising the distribution function. It is proportional to $P_h(r) \equiv \left(\langle P_{h\perp}\rangle + \langle P_{h\|}\rangle\right)/2$ where angular brackets denote averaging over poloidal orbits (both passing and trapped). The parameter λ_0, which describes the mode (or central) pitch angle is to leading order defined in terms of the angle of injection χ (from perpendicular) as $\lambda_0 \approx \cos^2\chi$. Hence for perpendicular injection ($\chi = 0$) it is clear that $\lambda_0 = 1$, which indicates that the distribution function is peaked in trapped space. For azimuthal injection ($\chi = \pm\pi/2$) the central pitch angle is $\lambda_0 = 0$. The spread of the distribution in pitch angle is governed by the parameter $\Delta\lambda > 0$. For example, on letting $\Delta\lambda \rightarrow 0$, Eq. (3) becomes a delta function (with discontinuity located at λ_0) such as that used by Chen *et al* [8] to model the effects of NBI on fishbones. The other extreme is $\Delta\lambda \gg 1$ which yields an isotropic distribution, independent of λ_0, such as that used in Ref. [11] to analyse the effects of slowing-down alpha particles on the internal kink mode.

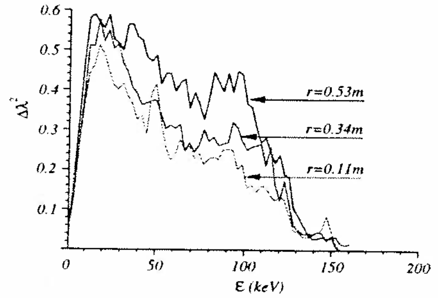

Figure 1: Showing Transp simulations for JET discharge 53595 which yield $\Delta\lambda(\mathcal{E}, r)$ and also λ_0 (not shown here).

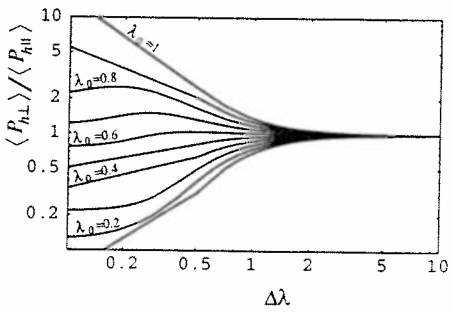

Figure 2: The anisotropy A_h verses $\Delta\lambda$ for different λ_0.

It is possible to parameterise the distribution function of Eq. (3) by employing the Transp code [12] to post-processes the distribution function from experimental data. One can then fit Eq. (3) to the computed distribution function and obtain the parameters λ_0 and $\Delta\lambda$. Figure 1 demonstrates this procedure for JET discharge 53595. In particular, while the central pitch angle is $\lambda_0 \approx 0.5$ for this discharge, the pitch angle width $\Delta\lambda$ exhibits a functional dependence on $\mathcal{E}$ and r. This is to be expected because preference in pitch angle will become less (but still significant) as the minority ions slow down due to collisions. However, for this paper, it is sufficient to employ an effective pitch angle width which is an average value over energy and radius. Hence, for discharge 53595 the effective pitch angle width is approximately $\Delta\lambda = 0.5$, and is in fact close to the actual width within the range $0 < r < r_1 \sim 0.4m$

and $40keV < \mathcal{E} < 80keV$. Evaluating the poloidal averaged second moments of Eq. (3) facilitates the plot of Fig. 2 which shows $A_h = \langle P_{h\perp} \rangle / \langle P_{h\|} \rangle$ versus $\Delta\lambda$ for different λ_0. It can be seen that the isotropic limit $A_h = 1$ is rapidly reached for $\Delta\lambda > 2$ regardless of λ_0, while $A_h \sim 10$ or $\sim 1/10$ can be obtained for sufficiently small pitch angle width ($\Delta\lambda \sim 0.15$) and $\lambda_0 > 0.9$ or $\lambda_0 < 0.2$ respectively. For JET discharge 53595, for which $\Delta\lambda \approx 0.5$ and $\lambda_0 = 0.5$, one finds that $A_h \approx 0.7$.

The stability of the internal kink mode is now determined for various NBI scenarios. The fluid contribution of Eq. (1) is obtained upon substituting the leading order eigenmode (the top hat), and together with the kinetic contribution of Eq. (2) is solved exactly upon assuming the model distribution function of Eq. (3). The following profiles and parameters typical of JET equilibria are employed: $a = 1.25$m, $R_0 = 3$m, $B_0 = 3$T. The safety factor profile is $q = q_0(1 + \lambda_q(r/a)^{2\nu_q})^{1/\nu_q}$ with $q_0 \equiv q(0) = 0.75$, $\lambda_q = 22.62$ and $\nu_q = 1.74$ which gives $r_1/a = 0.36$ and $q_a = 4.6$. The poloidal averaged pressure profile for the hot ions is given by $P_h(r) = P_{h0}[1-(r/a)^2]^2$ with P_{h0} the central pressure. This profile represents well the TRANSP simulations. One can write $P_{h0} = e\, n_{h0} T_{h0}$, where e is the absolute charge of the electron, n_{h0} is the density of hot ions and T_{h0} the corresponding temperature (units of electron volts) for a Maxwellian distribution. Quantities chosen here are $n_{h0} = 0.135 \times 10^{19}/m^3$ and $T_{h0} = 80$ keV. Such a temperature corresponds to that produced by the Octant 4 NBI system in JET. Note that although the anisotropy is varied in the following sections, $P_h(r) = \langle P_{h\perp} + P_{h\|} \rangle /2$ remains unchanged throughout. The injection energy $\mathcal{E}_m$ arrives from the property $m_h \mathcal{E}_m / eT_{h0}(eV) \sim 1$. Hence $m_h \mathcal{E}_m / e = 80$ keV is employed. The charge coefficient Z_h is chosen to be unity, i.e. either hydrogen or deuterium is assumed. The pressure profile of the core plasma enters $\delta W_h = \delta W_{hf} + \delta W_{hk}$ through a parameter of the magnetic precession frequency [13]. The core plasma pressure profile assumed is $P_c = P_{c0}[1 - (r/a)^2]^3$, where $P_{c0} = e(n_{i0}T_{i0} + n_{e0}T_{e0})$, with $n_{i0} = n_{e0} = 4 \times 10^{19}$ and $T_{i0} = T_{e0} = 4.5$ keV. Hence the ratio of the core pressure and hot ion pressure $P_c/P_h = 10/3$ in the centre, which is a typical value for NBI experiments. For this choice of total pressure $P_c + P_h$ and q profile, Bussac's [9] toroidal term is very small ($\delta\hat{W}_T = -0.00066$) such that ideal stability is largely determined by $\delta\hat{W}_h = \delta W_h/(6\pi^2 R_0 \xi_0^2 \epsilon_1^4 B_0^2/\mu_0)$. The toroidal rotation profile which accurately fits the data of Ref. [1] is $\Omega_E(r) = \Omega_{E0}\left[1 - (r/a)^2\right]^{3/2}$. Hence for the parameters chosen, the differential rotation $\Delta\Omega_E(r) = \Omega_E(r) - \Omega_E(r_1)$ at the centre is $\Delta\Omega_E(0) \approx 0.2\,\Omega_{E0}$.

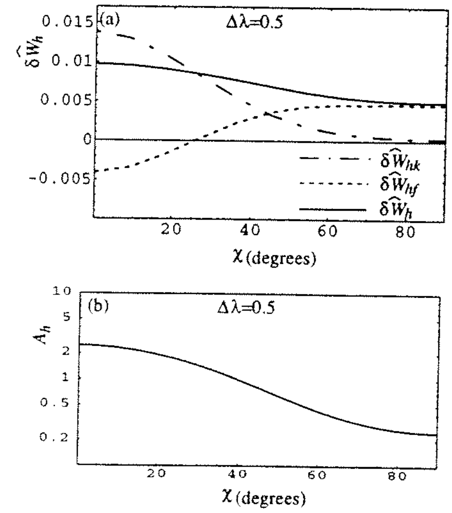

Figure 3: Showing (a) the hot ion response as a function of χ for Δλ=0.5 and zero plasma rotation. (b) Depicts a linear–log plot of the anisotropy A_h.

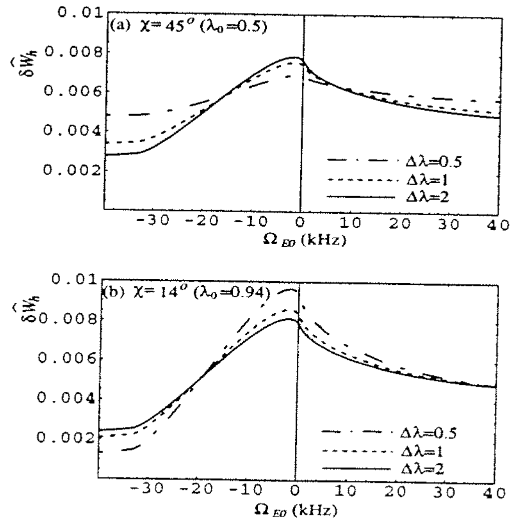

Figure 4: Showing the hot ion response with respect to Ω_{E0} for three differing pitch angle widths. (a) is for χ=45 degrees and (b) is for χ=14 degrees.

Figure 3 (a) plots $\delta\hat{W}_h$, $\delta\hat{W}_{hk}$ and $\delta\hat{W}_{hf}$ as a function of χ for $\Delta\lambda = 0.5$. As expected, $\delta\hat{W}_{hk}$ is largest for perpendicular injection, for which nearly all the ions are trapped, and diminishes as χ approaches zero. Meanwhile, the fluid contribution is destabilising for perpendicular injection since the predominantly trapped ions are located in the region of poor curvature. For tangential injection it can be seen that the influence of passing ions, which spend most time in the region of good curvature, give rise to strong fluid stabilisation of the mode. The net result is that hot ion stability varies only moderately with respect to injection angle or indeed with the corresponding degree of anisotropy A_h, as shown in Fig. 3 (b). It is important to note that the approximate range of the total plasma anisotropy

$A = (P_c + \langle P_{h\perp}\rangle)/(P_c + \langle P_{h\|}\rangle)$ is $0.75 < A < 1.25$ over the full range of χ. For such a small range of anisotropy the effect on the toroidal contribution δW_T of the resulting slightly shaped flux surfaces is ignorable [14]. It is also interesting to compare Fig. 3 with $\delta\hat{W}_h = 0.0056$ which is obtained for the highly simplified analytical model employed in Ref. [15] for slowing down alphas and Ref. [16] for NBI ions. Note that $\delta\hat{W}_h$ in [15] and [16] agree if a correction factor of $2^{-1/2}$ is used in the former.

Finally Fig. 4 shows $\delta\hat{W}_h$ with respect to a realistic range of central toroidal plasma rotation. Figure 4 (a) is for $\chi = 45$ degrees, which corresponds to the injection angle on the Octant 4 NBI system in JET. It is seen that counter-rotation of -30 kHz reduces $\delta\hat{W}_h$ by more than a factor of two if the distribution function is close to isotropic ($\Delta\lambda = 2$). Co-rotation of 30 kHz also reduces $\delta\hat{W}_h$ but not by as much as counter rotation. The sensitive dependence of kink mode stability on plasma rotation weakens for decreasing $\Delta\lambda$ since, as seen in Fig. 3 (a), $\delta\hat{W}_h$ is then increasingly dominated by $\delta\hat{W}_{hf}$; a quantity independent of toroidal rotation. In contrast, for an injection angle of $\chi = 14$ degrees, Fig. 4 (b) shows that toroidal rotation can greatly diminish hot ion stability when $\Delta\lambda$ is small. This is because, for such an injection angle, the number of trapped ions increases for reducing $\Delta\lambda$. Hence, while both co and counter rotation reduces the stabilising kinetic contribution, fluid effects remain strongly destabilising for this case. An injection angle also of $\chi = 14$ degrees was employed in the PDX experiment where co and counter beam injection gave rise to contrasting sawtooth and fishbone characteristics [17].

In conclusion, a semi-analytical approach within the framework of ideal kinetic theory has been employed to model the effects of NBI ions on sawteeth. The analysis complements recent investigations into NBI stabilisation of JET sawtoothing plasmas [10,16]. Investigation of experimentally relevant scenarios have highlighted the importance of plasma rotation and anisotropy, both of which arise as a consequence of the injection of neutral beams. For the distribution function parameterised to model JET NBI discharges, where beam injection is approximately 45 degrees, it is shown that the anisotropic fluid term is more stabilising to the ideal internal kink mode than the kinetic term. The stabilising role of passing ions, often ignored in similar studies, is crucial. This would be even more evident for scenarios where the injection angle approaches azimuthal, which is seen to be a possible effective means of stabilising sawteeth. Both co and counter plasma rotation of realistic amplitude and shear are shown to have an important influence on hot ion stabilisation for NBI populations which have large trapped fractions. Extrapolation to more energetic particles indicates that toroidal rotation is not expected to significantly modify alpha or ICRF minority ion stabilisation of sawteeth, although the kinetic stability of thermal ions is predicted to be strongly modified by plasma rotation in fusion grade plasmas [2]. The analysis employed in the present paper will also assist in determining the effects of anisotropy on ICRF sawtoothing discharges. This would be particularly important for discerning the applicability of employing auxiliary heated ions in JET to predict the effects of isotropic alpha particles in ITER.

It is a pleasure to acknowledge the assistance of Dr. C. Angioni. This work has been supported in part by the Swiss National Science Foundation.

References

[1] D. Testa, C. Giroud, A. Fasoli and K. -D. Zastrow, Phys. Plasmas **9** 243 (2002).
[2] J. P. Graves, R. J. Hastie and K. I. Hopcraft, Plasma Phys. Contol. Fusion **42**, 1049 (2000).
[3] D. J. Campbell, Private Communication.
[4] G. F. Chew, M. L. Goldberger and F. E. Low, Proc. R. Soc. London, **A236**, 112 (1956).
[5] R. O. Dendy, R. J. Hastie, K. G. McClements and T. J. Martin, Phys. Plasmas **2**, 1623 (1995).
[6] A. B. Mikhailovskii, Sov. J. Plasma Phys. **9**, 190 (1983).
[7] J. W. Connor, S. C. Cowley, R. J. Hastie and L. R. Pan, Plasma Phys. and Control Fusion **29**, 919 (1987).
[8] L. Chen, R. B. White and M. N. Rosenbluth, Phys. Rev. Lett. **52**, 1122 (1984).
[9] M. N. Bussac, R. Pellat, D. Edery and J. L. Soulé, Phys. Rev. Lett. **35**, 1638 (1975).
[10] N. N. Gorelenkov, M. F. F. Nave, R. Budny, C. Z. Cheng, *et al*, ECA Vol. **24B** 1553 (2000).
[11] K. G. McClements, R. O. Dendy, C. G. Gimblett, R. J. Hastie and T. J. Martin, Nucl. Fusion **35**, 1761 (1995).
[12] R. Budny, Nucl. Fusion **34**, 1247 (1994).
[13] J. W. Connor, R. J. Hastie and T. J. Martin, Nucl. Fusion **23**, 1702 (1983).
[14] N. A. Madden and R. J. Hastie, Nucl. Fusion **34**, 519 (1994).
[15] F. Porcelli, D. Boucher and M. N. Rosenbluth, Plasma Phys. Controlled Fusion **38**, 2163 (1996).
[16] C. Angioni, A. Pochelon, N. N. Gorelenkov, *et al*, Plasma Phys. Control. Fusion **44**, 205 (2002).
[17] K. McGuire, R. Goldston, M. Bell, M. Bitter and K. Bol, *et al*, Phys. Rev. Lett. **50**, 891 (1983).

Stability at high performance in the MAST Spherical Tokamak

M. J. Hole, L. C. Appel, R. J. Buttery, M. Grayznevich, K. G. McClements, O. Sauter*, A. Martynov* , A. Thyagaraja and the MAST team.

EURATOM/UKAEA Fusion Association, Culham Science Centre, Abingdon, OX14 3DB, UK.
**CRPP , Association EURATOM-Confédération Suisse, EPFL, 1015 Lausanne, Switzerland.*

1.0 Introduction

The MAST Spherical Tokamak (ST) provides one of the first opportunities to examine the stability properties of the ST in power-plant relevant regimes. This is important in assessing the potential of the ST as a possible route to fusion power. It can also provide crucial tests and data for conventional tokamak physics. High performing regimes are now being routinely accessed on MAST, and their stability properties explored. In this paper, we divide our attention into three stability subjects in MAST: ideal MHD stability limits, Neoclassical Teraing Modes (NTM's), and Alfvenic physics.

2.0 Ideal MHD Stability limits

The ideal n=1 kink instability is likely to set the ultimate performance limit to plasmas in the ST, unless a close fitting conducting wall and active feedback system is introduced into the device. Here, ideal n=1 external kink mode stability limits have been investigated in MAST using the finite element code KINX [1], which computes linear ideal MHD growth rates and eigenvectors of axi-symmetric plasmas surrounded by a vacuum layer and a conducting wall. For the stability calculations, three codes were used to compute the equilibrium: EFIT [2], which computed the experimental equilibrium using magnetic and kinetic constraints; CHEASE [3], which computed a higher resolution equilibrium; and CAXE [4], which was used to remap the equilibrium into a KINX input file. To calculate the stability of an EFIT computed equilibrium, CHEASE took the edge as the flux surface at normalized poloidal flux ψ_n=99.5% of the EFIT last closed flux surface. The radial electron pressure profile was taken from Thomson scattering data. Calculations from LOCUST [5] suggest that in MAST, the fast ion pressure profile comprises no more than ~20% of the total pressure. In this work we have assumed that the ion and electron pressure profiles are the same. To calculate the marginal stability boundaries, the pressure p and flux surface averaged current density I^* profiles were remapped by: $p_1(\psi_n)\rightarrow\gamma p_0(\psi_n)$, $I_1^*(\psi_n)\rightarrow I_0^*(\psi_n^{\,t})$, and the pressure multiplier γ raised until the resultant equilibrium was unstable. For each γ, a shooting method was used to adjust the power index t until the on-axis safety factor, $q(0)$=1.1. Together with the constraint of the total plasma current, this ensured an approximately constant q profile.

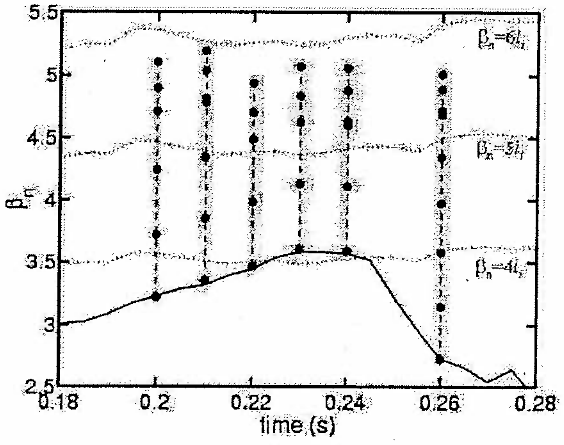

Figure 1: *Time trace of β_n for shot 6271, together with stability trajectory for stable (•,γ=1), (•,γ>1) and unstable (•,γ>1) points.*

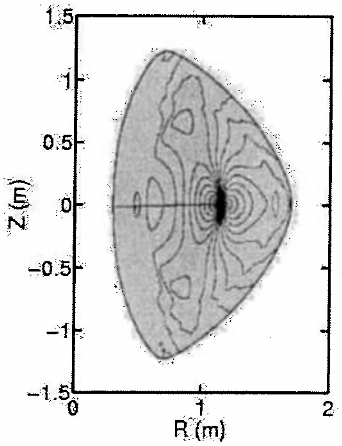

Figure 2: *Normal displacement lines for marginally unstable n=1 external kink mode at 210ms*

Figure 1 is a time trace plotting the normalized beta, β_n for shot 6271. Here, $\beta_n = \beta_t (\%)/I_n$: defined in terms of the toroidal beta, $\beta_t=2\mu_0\langle p\rangle/\langle B_0^2\rangle$, with B_0 the vacuum toroidal magnetic field at the geometric axis and the brackets denoting volume average; and the normalized plasma current $I_n=I_p/(a\ B_0)$, where a is the minor radius. For each point in Fig. 1 the KINX stability computation has been performed, and the point colour coded for stability [γ=1 (magenta), or γ>1 (blue)] or instability (red). The dotted line shows different multiples of the plasma inductance, l_i. By inspection, the stability limit lies around $\beta_n = 5.5 l_i$, approximately 25% above the highest β_n reached in MAST to date. Figure 2 is a plot of the normal mode displacement of the marginally unstable n=1 external kink mode at 210ms. The figure shows that the outboard displacement (yellow) is large with respect to the inboard displacement (blue). Near the geometric centre, the perturbation is predominantly m=1, whilst near the edge the perturbation is predominantly m=2. Numerical convergence tests have been performed, which verify convergence of the eigenvalues to marginal stability and instability at a (r,θ) grid of greater than 150x150 points. Preliminary calculations confirm the mode is stabilized with a conformal wall at ~40% of the minor radius.

Figure 3 is a grey-scaled histogram plot of β_n vs. l_i. of the MAST operating space. Overlaid is the trajectory to instability of the no-wall n=1 external kink mode. The plots show that the present MAST operating space is well below the hard ideal n=1 MHD limit. Finally, Fig. 4 plots the trajectory to instability as a function of pressure peaking factor. The slight decrease in pressure peaking factor (p(0)/<p>) with increasing β_n is a result of increasing Shafranov shift. Overlaid on Fig. 4 are ideal n=1 external kink mode, no wall stability limit calculations by Menard *et. al.* [6] for aspect ratio A=1.5, q(0), and q*/q(0)=1.5,3.0, where q* is the cylindrical kink safety factor [6]. The calculations are in good agreement with the MAST case studied here, with A=1.42 and q*/q(0)=2.55. Finally, the data points are values of β_n vs. pressure peaking factor, calculated by rerunning EFIT with pressure constrained to the TS data.

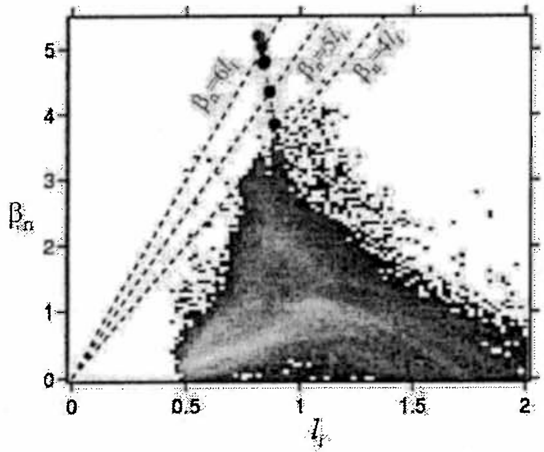

Figure 3. *Histograms of β_n vs. l_i. of the MAST operating space, together with stability trajectory of shot 6271 (see legend of Fig. 1).*

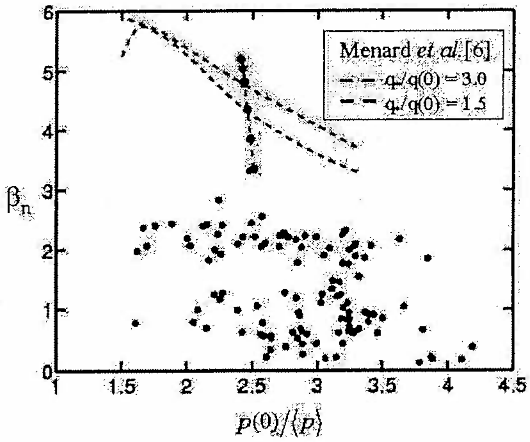

Figure 4: *Stability trajectory of shot 6271 at 210ms (see legend of Fig. 1). Overlaid are no-wall stability limits calculated by Menard et al. [6], and kinetically constrained EFIT MAST data (•).*

3.0 Neoclasssical Tearing Modes

Whilst the ideal n=1 ideal kink instability may set the ultimate performance limit in the ST, the practical limit to performance for many conventional tokamak scenarios is posed by the NTM. Aspect ratio is a key parameter for this mode, entering into the various physics terms governing behaviour in different ways. Thus the ST provides an ideal testing ground for NTM physics models. NTM modes have been identified in the ST on MAST, first reported by Buttery *et al.* [7]. Their behaviour validates the underlying physics models, not only matching the expected trends and effects, but consistent with detailed numerical predictions for key physics parameters. The modelling also highlights the strong role of field curvature effects for the ST, as predicted by Kruger *et al.* [8], with fits from MAST consistent with a 60% stabilisation of the bootstrap drive [9]. As the ratio of bootstrap drive to field curvature effects scales as $\sqrt{\varepsilon}\,\beta_p\,s\,/\,\beta$, where s is the magnetic shear, this indicates a possible new route for avoidance of these instabilities in the ST, via further optimisation of profiles or variation in q. In addition, the ST's naturally high shaping enables operation with higher q(0), thus removing rational surfaces associated with either the seeding physics or the NTM itself.

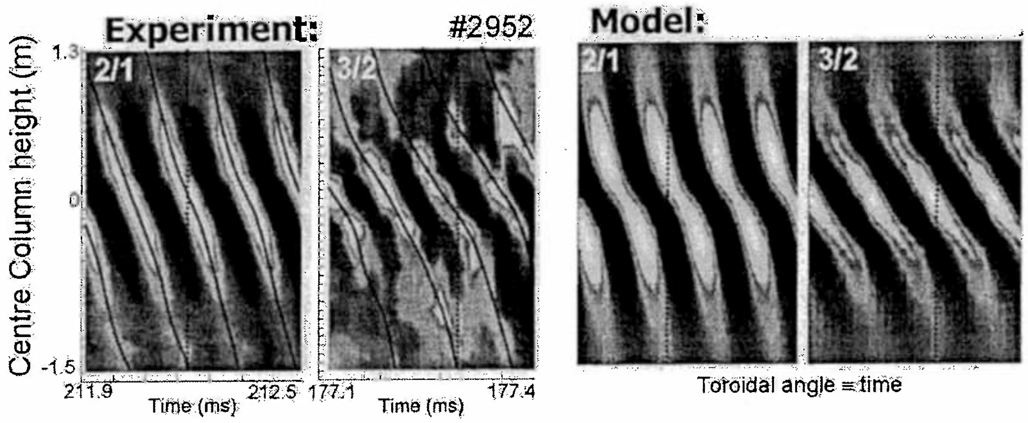

Figure 5: *Observed and predicted mode structure on centre column magnetic array for shot 2952.*

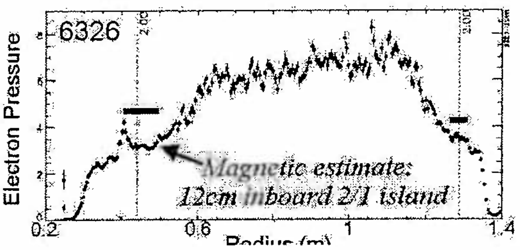

Figure 6: *TS electron pressure for shot 6326.*

In further work, geometry corrections for the previous cylindrical estimates of island size have been obtained by three-dimensional field modelling. Here, the island is represented as a toroidally-sinusoidal sheet current perturbation, matching the measured magnetic amplitude and consistent with the observation of a single dominant harmonic from magnetics. Field lines were followed in full 3D geometry to measure the vacuum solution island sizes, showing 3/2 island sizes, (typically ~4cm) are very similar to the cylindrical approximation, while 2/1 islands (~8cm) are only ~25% lower than the cylindrical estimates. This modelling has also been used to test measurements of poloidal mode numbers, previously deduced from centre column vertical array. The model confirms that the majority of the modes' structures are observed on the inboard size, and correct identification of the modes as shown in Fig. 5. These estimates are now confirmed by new measurements using the 300 point Thomson scattering diagnostics, which shows structures at q=2 of similar scale to the island sizes predicted by magnetically based estimates for a 2/1 tearing mode in shot 6326 , as shown in Fig. 6.

4.0 Alfvénic activity

Discrete activity in the range 80kHz to 450kHz has been observed in neutral beam injection (NBI) heated discharges using both H^+ and D^+ co-injection with beam energies exceeding 35keV. A spectrogram of high-frequency activity for shot 4396 is shown in Fig. 7. At the time of the observed activity: I_p=600kA, B_0=0.4T, A=1.9, triangularity δ=1.5 and $v_{\|}/v_A \cong 1.7$ ($v_{\|}$ is the beam velocity and v_A is the Alfvén velocity at the magnetic axis). Discrete activity is observed from around 15ms after the start of the1MW H^+ NBI and continues until just after an internal reconnection occurring at 151ms. The high frequency activity occurs in two frequency ranges consistent with TAE activity $f_{TAE}=v_A/4\pi Rq \cong 175$kHz, and with EAE activity

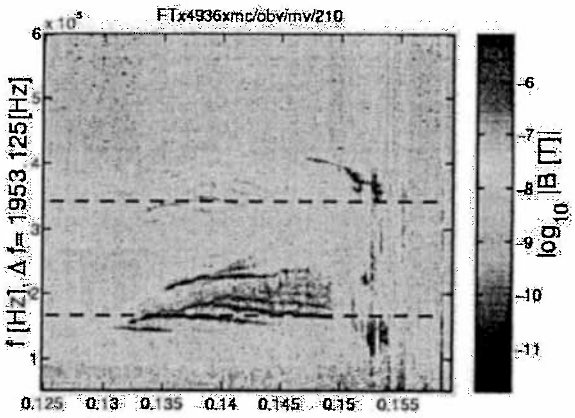

Figure 7: *Spectrogram of an outboard mirnov coil for shot 4936 during NB-heating. Discrete modes occur first in the TAE gap (~170kHz) and from 147ms in the EAE gap (~350kHz).*

$f_{TAE}=v_A/2\pi Rq \cong 350$kHz, where R is the radius of the magnetic axis, and q taken to be one. Continuous Alfvén spectra, computed using CSCAS [10], indicate TAE and EAE gaps for low-n modes (n<5). Calculations using the non-linear hybrid MHD guiding centre code HAGIS [11] predict the most unstable toroidal modes are in the range n=4 to n=6. Figure 8 shows an n=3 EAE eigenfunction computed by the ideal MHD code MISHKA-1 [12]. The stronger toroidal coupling in a spherical tokamak results in more than 2 dominant poloidal harmonics.

High frequency Alfvénic activity has also been observed in ohmic plasmas. The activity is generally at a very low ampltiude with mode number n=0, consistent with the excitation of n=0 global Alfvén eigenmodes and low poloidal mode number [13]. Simulations using the 2-fluid turbulence code CUTIE[14] suggest the high frequency is correlated with long-timescale MHD events such as IREs or ELMs. There is no observed effect of these modes on plasma performance but they may be useful as a diagnostic.

5.0 Conclusions

We have investigated three stability subjects in MAST. Ideal MHD calculations have shown that there is scope for at least a rise of 25% in normalized beta, β_n, in MAST before reaching the hard, n=1 external kink mode limit. In future, time resolved TS data and higher NBI beam power will provide scope to further probe beta limits in MAST. Secondly, we have reviewed recent progress in NTM physics, and suggested routes to stabilziation in the ST. In this work, we have modelled the measured magnetic amplitudes with toroidally sinusoidal sheet perturbation, predicting island sizes similar to cylindrical estimates. Similar island sizes have been seen in profiles from 300 point TS scattering diagnostics. Thirdly, we have reported on high frequency Alfvénic activity in Ohmic plasmas, at low amplitude with n=0, consistent with excitation of GAE modes. Finally, we presented evidence of beam-driven EAE activity in MAST. Measured frequencies agree with computed locations of the EAE gap in the Alfven continuum. Drive calculations suggest the most unstable EAE modes are in the range n=4 to n=6. Computations of an n=3 EAE eigenfunction show the presence of more than 2 dominant poloidal harmonics.

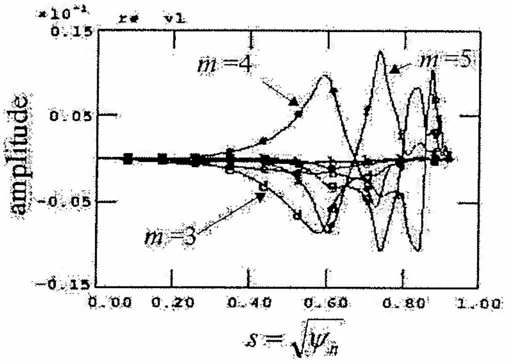

Figure 8: *An EAE eigenfunction with n=3 computed using MISHKA-1[12].*

This work was jointly funded by the U.K. Department of Trade and Industry and EURATOM. O. S. is supported in part by the Swiss National Science Foundation. Special thanks to Dr. S. Medvedev, Keldysh Ins. of Applied Math.for assistance with the stability calculations.

[1] L. Degtyarev *et al.* Comp. Phys. Com.. **103**, (1997).
[2] L. Lao *et al.* Nuc. Fus. **30** pp 1035, (1982).
[3] H. Lutjens *et al.* Comput Phys Commun **97**, 219, (1996).
[4] S. Medvedev *et al.* 20th EPS, (1993).
[5] R. J. Akers *et. al.* Nuc. Fus. **42**, pp122-135, (2002).
[6] J. E. Menard *et al.* Nuclear Fusion, **37**(5), (1997).
[7] R. J. Buttery et al., Contr. Fus. Plas. Phys. **25A** pp. 597, (2001)
[8] S. E. Kruger *et. al.*, Phys. Plas. **5**, 455, (1998).
[9] R. J. Buttery *et al.*, Phys. Rev. Lett. **88**, 125001 (2002).
[10] S. Poedts, E. Schwarz, Journ Comp Phys, 105, 165 (1993).
[11] L. C. Appel *et al*, 7th IAEA, Göteborg (2001).
[12] A. B. Mikhailovskii *et al.*, Plas. Phys. Rep, 23, 844 (1997).
[13] K. G. McClements *et al.*, submitted to Nuclear Fusion (2002).
[14] A. Thyagaraja, Plas. Phys. and Cont. Fusion, 42,B255 (2000).

Relaxation of the DNBI Deposited Particles in the TCV Plasmas

A.N.Karpushov, P.Bosshard, B.P.Duval, J.Mlynar

Centre de Recherches en Physique des Plasmas,
Association EURATOM – Confédération Suisse, EPFL, 1015 Lausanne, Switzerland

ABSTRACT.

The paper presents results of a high-energy fast ion population relaxation in the TCV. The fast hydrogen ions are created by diagnostic neutral beam (DNB) deposition in plasma. In the NPA measurements the increase of the neutral particle flux was correlated with DNB current. By taking that the observed flux increase to be the result of charge-exchange (CX) of the DNB deposited particles on the plasma neutrals, the NPA can be used to observe the DNB deposited ion energy distribution. The measurements of CX spectrum were performed for a range of plasma parameters with a modulated diagnostic neutral beam, the characteristics of DNB deposited ion population are sensitive to the plasma parameters (electron temperature, electron and neutral density profiles).

1. EXPERIMENT LAYOUT.

The neutral particle analyser [1,2] on TCV views the plasma centre along a vertical chord (Fig.1). It consists of 5 energy channels with electrostatic discrimination. The NPA voltage sweeps the energy channels to measures neutral particle energies in the range of (0.6→8 keV).

The DNBI on TCV has a maximum extraction voltage (E_0) of 52 kV [3] with an effective beam current of up to 3 A. The beam is usually pulsed with a 12→150 ms duty period and was installed on the TCV Tokamak for CXRS ion temperature measurements [4]. The TCV beam consists of ~50% of the neutrals with full energy (E_0), ~27% of $E_0/2$, ~18% of $E_0/3$ and ~5% of ~$E_0/18$ (beam current fractions). The ~80 kW injected power is small compared to the TCV ohmic power (250 kW – 1 MW). The beam has a divergence of 0.7^0 and a gaussian cross section (~7 cm diameter). The beam is injected horizontally at an angle to the machine center of 11.25^0. The toroidal angle between DNB and NPA TCV sections is 67.5^0.

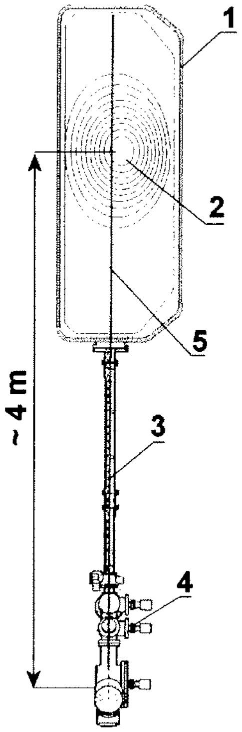

Fig1: NPA layout, 1-TCV vacuum chamber, 2-plasma, 3-NPA duct, 4-NPA, 5-view line.

2. NPA ION TEMPERATURE MEASUREMENT.

In the standard regime of NPA measurements (Fig.2), the high energy tail of CX atoms entering the analyzer was observed to increase during DNB injection (Fig.3). For a Maxwellian ion energy distribution, the ion temperature T_i is proportional to the logarithm of the “charge exchange spectrum” ($F_{dc}(E)$) slope: $\frac{E}{T_i}+\frac{3}{2}\ln(T_i)\sim-\ln\left(\frac{J(E)}{\sigma_{cx}(E)\cdot E}\right)=-\ln(F_{dc})$ [5], where $J(E)$ is the energy spectrum of neutrals entering the NPA collimating system. Putting $F_{dc}(E)$ in on a semi-log plot one should obtain a straight line whose slope reflects the ion temperature. In most situations the plasma does not have a unique ion temperature and the attenuation from neutral creation to the NPA is not negligible. The mean free path with respect to the sum of CX and impact ionisation increases with increasing the neutral energy. The result is that the “CX spectrum” measured by this “passive” technique is not linear on a semi-log plot. The low energy tail of the “CX spectrum” is dominated by the cold edge regions ($\sigma_{abs}\cdot n_e\cdot a_{pl}>>1$). For moderate plasma conditions in a Tokamak, $n_e\cdot a_{pl}/T_i\sim10^{19}m^{-2}keV^{-1}$ [6] the core ion temperature can be measured by fitting the CX-spectrum with a simple exponential in the energy range of ~ 3 to 10 T_i. In general, the small decrease of $T_i(0)$ that results from the contributions to the CX flux from regions outside the plasma centre is partially compensated by the increasing of $T_i(0)$ associated with increased attenuation of low energy neutrals escaping from the plasma. $F_{dc}(E)$ fitted by the straight line in on a semi-log plot ($3T_i<E<10T_i$) for DNB “OFF-phase” gives an ion temperature with a statistical error 1-5%.

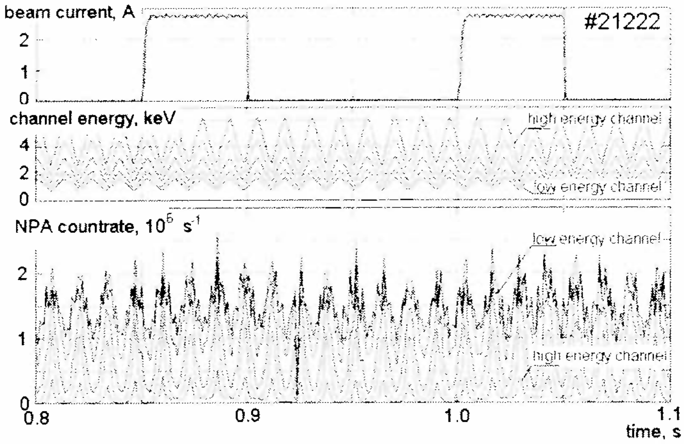

Fig.2 Modulation of the DNBI current, NPA analyzing voltage and counter traces from NPA channels.

It was proposed that the increase of high energy CX flux to NPA is the result of charge–exchange of the DNB deposited particles whose energy distribution function is ~$1/E$. For the DNB “ON-phase” the “CX-spectrum” was well fitted by the sum of a Maxwellian and $1/E$ ion energy distribution. With this assumption it was found that the measured “NPA ion temperature”

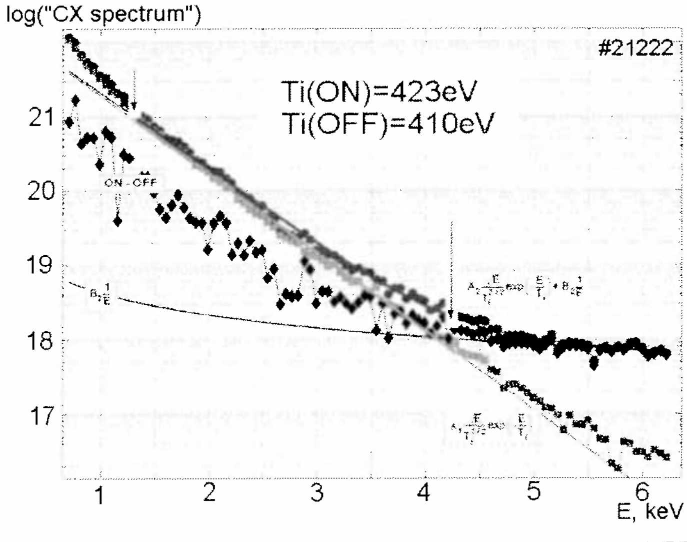

Fig.3: The NPA “CX spectrum” for ON (red) and OFF (green) DNBI phases with ion spectrum fitting.

increases during DNBI pulses (Fig.3) by 2-10%.

3. NPA MEASUREMENT WITHOUT ENERGY SWEEP.

To examine the effect of DNB deposition, a series of experiments was performed, in which the NPA was operated with fixed analysis energies (Fig.4). The increase of the NPA signals was correlated with DNBI modulation and for all energy channels. To improve the statistics the time frames of NPA traces during the current flat top of plasma discharge (few DNBI pulses) were summed, shown in Fig.5. The measured time shift between the increased CX flux from the plasma and DNBI modulation ranged from 2→40 ms. The delay and decay times (Fig.6) of the CX fluxes are a few ms. A 0-space-dimensional numerical model was constructed to describe the relaxation of the DNB deposited particles in collisions with plasma ions and electrons at a fixed, and realistic, temperatures (Fig.6). It is based on a solution of kinetic equation for energy distribution function [7].

The time characteristics of NPA counting strongly depend on the plasma density (1→8×10^{19} m^{-3}) and electron temperature (0.3→1.5 keV). The fast ion relaxation (52→2 keV) is dominated by the electron drag. The time shift between increasing of CX flux and DNB injection is found to be proportional to the ion energy loss time $\tau_{ie}^{E} \sim T_e^{3/2}/n_e$. The dependence of "time shift" between 5th (6.24 keV) NPA channel counter trace and beam current on the parameter $T_e^{3/2}/n_e$ is shown in Fig.7.

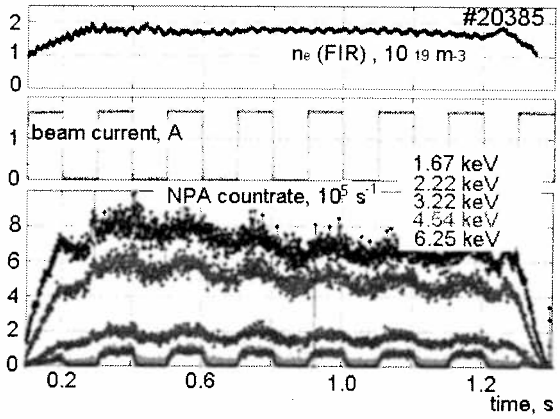

Fig.4: Variation of the NPA counting during modulated DNB injection.

4. CONCLUSIONS.

Comparison with experimental results allow us to conclude that :

- Increase of the high energy tail of CX neutral flux during DNB injection can indeed be explained by CX of fast hydrogen ion population produced as a result DNB deposition in plasma.
- The relaxation of fast ions is determined by their Coulomb collisions with electrons and plasma deuterium and impurity ions.
- For TCV ohmic shots 70-90% of the DNB absorbed power goes to the electrons so

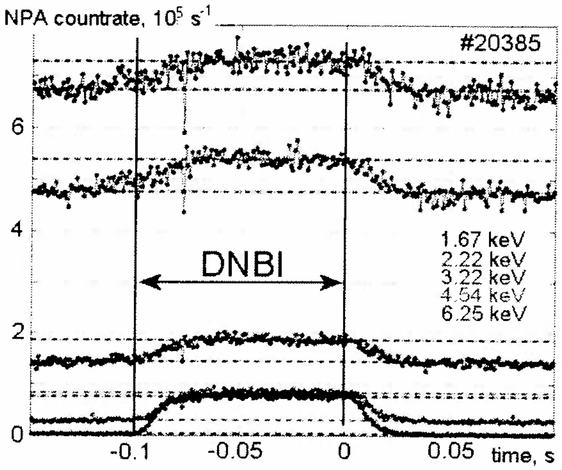

Fig.5: NPA countrate increasing during DNB injection.

the plasma ion power from the DNB is only 5-15% of that from the plasma electrons.

- The energy transfer from the DNBI deposited ions to plasma ions increases the NPA ion temperature by only 2-10%.
- The "time shift" between DNB current and increasing of high-energy tail of CX neutral flux from plasma depends on the plasma parameters and is proportional to $\tau_{ie}^{E} \sim T_e^{3/2}/n_e$.

REFERENCES

[1] V.V.Afrosimov et al., *Sov. Phys. - Tech. Phys.* **20**(1), (1975) 33

[2] A. de Chambrier, *These* No.712 (1987) de l'Ecole Polytechnique Federale de Lausanne (Suisse).

[3] J.Mlynar et al., *Diagnostic Neutral Beam injector at the TCV Tokamak*, CRPP report LRP 710/01, (2001)

[4] P.Bosshard et al., *28th EPS Conf. on Contr. Fusion and Plasma Phys., Madera, Portugal*, **ECA 25A**, (2001) 365

[5] V.V. Afrosimov and A.I. Kislyakov, *International School of Plasma Physics, Varenna, Italy,* (1982) 289-310

[6] R.J. Goldston, *International School of Plasma Physics, Varenna, Italy,* (1982) 263-287

[7] A.Karpushov et al., *27th Conf. On Contr. Fusion and Plasma Phys. Budapest,* **ECA 24B**, (2000) 920

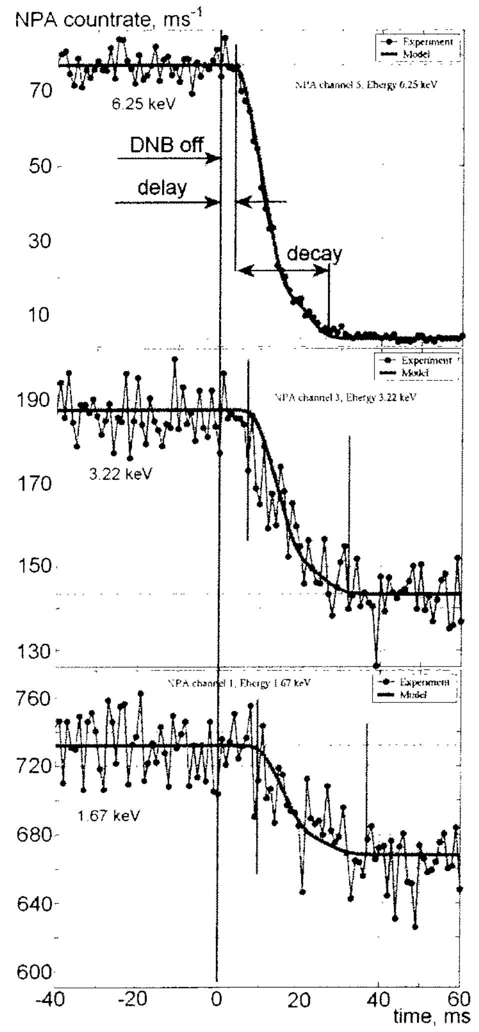

Fig.6: Comparison of NPA counting traces and modelling for signal decreasing after DNBI switching off.

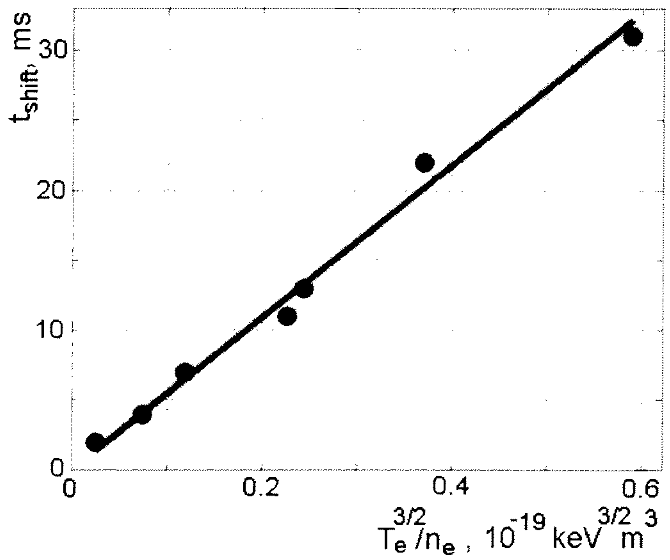

Fig.7: "Time shift" between 5th (6.24 keV) NPA channel counter trace and beam current vs. $T_e^{3/2}/n_e$ parameter.

Pulse Height Analysis X-ray spectroscopy in the tokamak TCV

T.I.Madeira, P.Amorim[1], B.P.Duval[2], C.A.F.Varandas

Associação EURATOM-IST, Centro de Fusão Nuclear,
Av. Rovisco Pais, P-1049-001Lisboa,Portugal

[1]Departamento de Física da Faculdade de Ciências da Universidade de Lisboa
e Centro de Física Atómica da Universidade de Lisboa

[2]Association EURATOM-CRPP, Centre de Recherches en Physique des Plasmas,
Lausanne, Suisse

Introduction

A PHA system has been successfully installed on TCV and used to measure the X-ray emission from a variety of plasma configurations. The preamplifier output from a Canberra model GUL0055P diode was shaped and pile-up inspected by a Canberra model 2024 gated integrator. The amplitude of the resulting pulse was recorded by an INCAA model TRCH CAMAC module with 12 bit signal amplitude resolution, 1 Msamples of on-board memory and a 1 μs cycle time. An Interface Amplifier and Time Generator, (IATG)[1] module, was integrated into the TCV timing system such that every 1-50 ms (user defined) a time tag was recorded into the acquisition memory, permitting the post-reconstruction of the arrival time of groups of events. The diode is fully depleted, (active area of 50 mm^2, active thickness 5 mm), by applying a bias voltage of 1000 V. The electric field thus generated inside is uniform and perpendicular to the detection surface, collecting charge from the whole detector volume. This large detection volume makes the diode sensitive to a wide range of x-ray energies ranging from a few eV to hundreds of keV and increases the probability that an incoming photon will loose all its energy in the diode. Since, in TCV, runaway electrons and hard X-rays[2] often present, the detector spends time processing unwanted pulses. Even though the electronics for signal processing and data acquisition have been optimised to improve the data throughput to match the high flux 2 s time duration of a TCV plasma pulse, the system is limited by pulse processing speed capability. The diode was mechanically coupled, via a high vacuum flight line ($<10^{-7}$ mbar), to TCV, and included the possibility of externally changing the viewing aperture and in line beryllium filters thickness. For calibration purposes, an ^{55}Fe radio-active source could be positioned in front of the diode. Four collimators of 0.3, 0.6, 1.0 and 1.15 mm diameter at the end of the flight tube limited the detector's étendue to the plasma to avoid saturation. The diode cryostat forced a horizontal mounting on TCV and the variety of plasma equilibrium that can be created in TCV made this geometry problematic as the plasma core is not always centred in the vessel so the diode is not always facing some plasma section. A centred configuration is not favoured on TCV since it does not benefit from the passive vertical position wall stabilisation.

The electron temperature deduced from PHA agrees better with the filtered diode and Thomson scattering system diagnostics, when the count rate did not exceed ~30 kHz. The values obtained were comparable to the Thomson measurement and 10 % higher than the filtered diodes, but all measurements agreed to within the error bars [3]. Line radiation was rarely observed.

The NEW PHA concept

An improved system must provide a higher count rate, to improve the diagnostic's time resolution and be vertically mountable on TCV. To meet the need for high throughput, mandatory in Tokamaks of short pulse duration and high-energy fluxes, the original detector was replaced by a Roentec XFlash Silicon Drifted Detector 1000B[4]. This detector consists of a very thin (~ 300 μm) fully depleted silicon wafer, making it only sensitive in the soft X-ray range and transparent to higher X-ray energies. An electric field, with a strong component parallel to the surface, drives signal electrons towards a small integrated collecting anode. The electric field is generated by a number of increasingly reverse biased field strips covering only one surface of the device. The radiation entrance side is a non-structured p+ junction, giving a homogeneous sensitivity over the whole detector's sensitive area (~5 mm^2). The extremely small value of the anode capacitance, which is almost independent of the active area, allows higher energy resolutions (FWHM<175 eV at 5.9 keV) even with short shaping times (<0.5 μs) compared to conventional photodiodes and Si(Li) detectors, making it suitable for high count rate applications (~1 MHz). These detectors also feature an integrated thermally stabilised thermoelectric cooler, which can operate the diode down to −10 °C. The power supplies for the cooler and the diode can be located far from the diode itself. To complement this system, a commercial Digital X-ray Processor (DXP) CAMAC unit, optimised for X-ray detector analysis, was installed. This unit has four integrated basic sections: a front-end Analogue Signal Conditioning; an ADC digitising at 40 MHz; a digital Filter, Peak detector, Pileup Inspector (FiPPI) to numerically filter the digitised signal stream generate triggers following an x-ray event; and a Digital Signal Processing (DSP) Unit for pulse height analysis, data corrections, surveillance of the other system sections (ASC and FiPPI) and communication with a host processor.

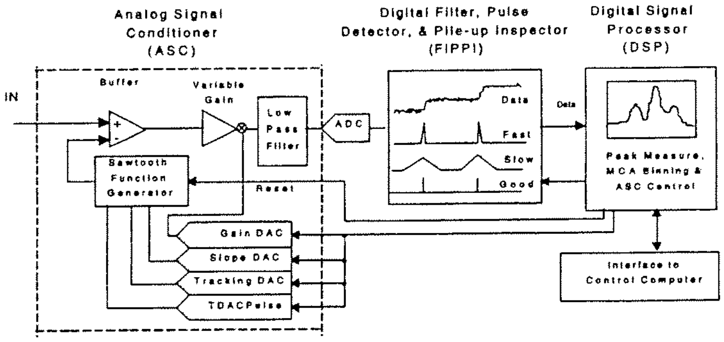

Fig.1: Block Diagram of the DXP channel architecture, showing the major functional sections

At present, data analysis is performed "off line" but only due to restrictions in the available software. Since basic data analysis of the PHA X-ray data, both for continuum and line radiation measurements, is straightforward, the final goal is to provide real-time data analysis with a temperature and impurity content monitor that can be used for machine feedback. A 4 DSP VME based card [5], is being programmed for fast data acquisition and simultaneous real-time data treatment with a view to providing very long pulse diagnostics for a machine such as ITER. The current goal is to obtain spectra with sufficient statistics every 10 ms, fit the data in real-time to evaluate the quality of the measurement and adjust remotely controllable X-ray PHA filters and apertures and finally provide the PHA data to the TCV control system. A separate DSP system could provide higher quality spectra with a reduced time resolution.

Experimental Performance

The best energy resolution for the combination Germanium detector with the traditional analogue signal treatment was 202 eV, for the 5.9 keV x-rays at a rate of 30 kHz. Above this limit, the spectral lines are still observed but the resolution is increasingly degraded until 50 kHz where the spectrum is useless. Trials with the SDD plus the analogue pulse conditioning showed that it was possible to improve the system energy resolution to ~180 eV and the throughput by a factor of 1.5, but pileup events are still fatal above 50 kHz, as the analogue modules saturate. With the CAMAC DSP unit, the energy resolution and the throughput were considerably improved for both detectors.

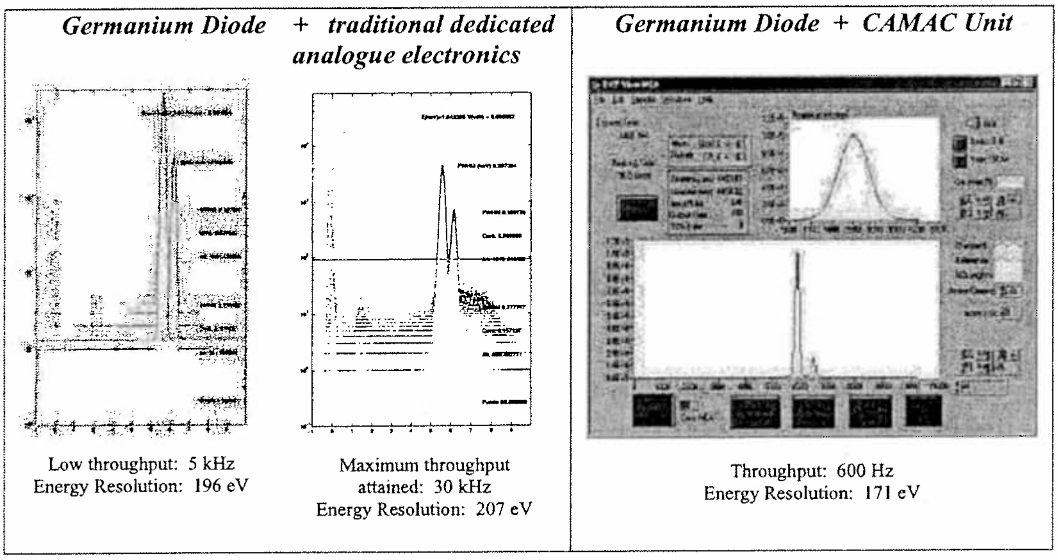

Germanium Diode + traditional dedicated analogue electronics

Germanium Diode + CAMAC Unit

Low throughput: 5 kHz
Energy Resolution: 196 eV

Maximum throughput attained: 30 kHz
Energy Resolution: 207 eV

Throughput: 600 Hz
Energy Resolution: 171 eV

Fig 2.1: Results obtained with an ^{55}Fe radioactive source

SDD + traditional dedicated analogue electronics

SDD + CAMAC Unit

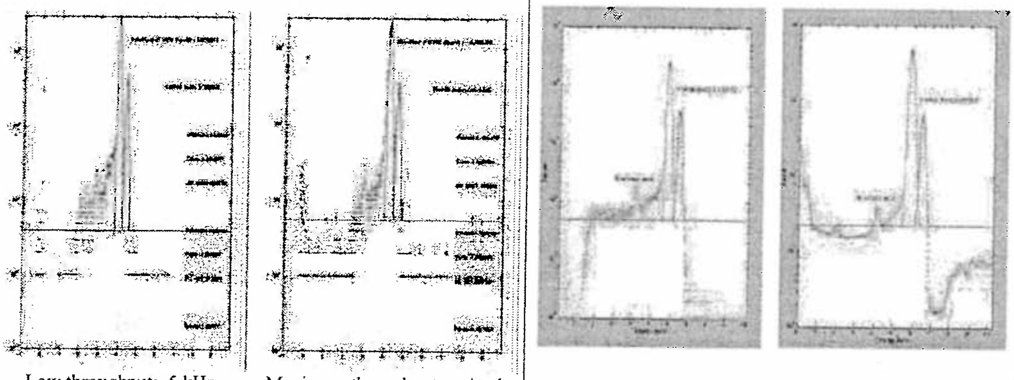

Low throughput: 5 kHz
Energy Resolution: 181 eV

Maximum throughput attained: 50 kHz
Energy Resolution: 214 eV

Low throughput: 3.7 kHz
Energy Resolution: 175 eV

Throughput: 110 kHz
Energy Resolution: 255 eV

Fig 2.2: Results obtained with an ^{55}Fe radioactive source

Conclusions

The results obtained show that a "modernised" PHA system with an electronically cooled diode and state of the art DSP signal treatment can result in greatly improved performance over traditional analogue components. The simplicity of the data analysis, the high quantum efficiency and the very low étendue required to a high intensity source, like a Tokamak plasma, could make this diagnostic very suitable for routine observation and control of a burning plasma.

Aknowledgements

This work has been carried out in the frame of the Contract of Association between the European Atomic Energy Community and Instituto Superior Técnico and has also received financial support from Fundação para a Ciência e a Tecnologia (FCT).

References

[1] J. Sousa et al., The interface amplifier and timing generator unit for control of operation of an off-line time-resolved X-ray spectrometer, Fusion Eng Des 48 (2000) 47-55

[2] Y. Peysson et al., Hard X-ray CdTe tomography of tokamak fusion plasmas, Nucl Instr Meth A 458 (2001) 269-274

[3] B.P Duval et al., High Count Rate Pulse Height Analysis Spectroscopy on the TCV tokamak, LRP 553/96 CRPP, Lausanne (1996)

[4] P.Lechner et al., Silicon drift detectors for high resolution room temperature x-ray spectroscopy, Nucl Instr Meth A 377 (1996) 346-351

[5] A.P.Rodrigues et al., A high performance real-time plasma control and event detection DSP based VME system, Fusion Eng Des (in press)

Interpretation of Plasma Dynamic Response to Additional Heating Power in ASDEX Upgrade and TCV

A. Manini, J.-M. Moret, F. Ryter[1], A. Sushkov[2] and the ASDEX Upgrade Team

Centre de Recherches en Physique des Plasmas
Association EURATOM-Confédération Suisse, EPFL, 1015 Lausanne, Switzerland
[1] *Max-Planck-Institut für Plasmaphysik, EURATOM-IPP, Garching, Germany*
[2] *Russian Research Centre Kurchatov Institute, 123182 Moscow, Russian Federation*

Introduction

The study of the plasma dynamic response to additional heating power is very important for power deposition localisation and for perturbative transport investigations. Most of the time, data analysis based on Fourier transformation of the space-temporal signals is used to derive amplitude and phase profiles. This technique, though, is not capable of fully separating the contribution to the signals coming from the sawteeth and from the applied perturbation due to the strong phase locking between the two signals, leading to potentially misleading results. Hence, in order to treat the problem correctly, signal processing techniques that respect the spatially distributed character of the measurements are needed.

Signal processing technique

A method based on a system identification using the singular value decomposition (SVD [1]) has been developed and is presented in this paper. In order to illustrate the method in a clear way, a simple example is used. To simplify, let us consider a purely diffusive particle transport model, cylindrical geometry and separable source terms. With these assumptions, the continuity equation becomes

$$\frac{\partial}{\partial t}y_r(t) = \sum_{r'} L_{rr'}y_{r'}(t) + \sum_{m} S_{rm}u_m(t), \tag{1}$$

where L is the linearised transport operator, S_{rm} the separable source term, u_m the temporal inputs related to each spatial source term and y_r are the observables. It is now convenient to perform a base transformation in which L is diagonal, projecting equation (1) on the eigenvectors of L. In this base, the source terms can be expressed as linear combinations of the eigenvectors and the observables y can be expressed as

$$y_{rk} = \sum_{lm} T_{rlm}h_{mlk}, \tag{2}$$

where T_{rlm} contains the amplitude associated to each eigenvector and h_{mlk} describes the time evolution of each source term component induced by each temporal input. Figure 1

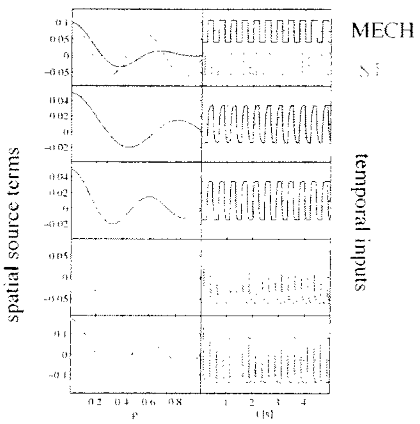

Figure 1. *Spatial source terms T and temporal inputs h for the simple model* ($v_{ST} \sim 1.8\, v_{MECH}$).

shows the example treated here in which modulated ECH (MECH) and sawteeth excite two common eigenvectors with different amplitudes. Each excitation signal is characterised by a specific time constant related to the rise/decay time of the temporal input signal. Using (2), a simulated spatio-temporal set of signals is built. The goal of the signal processing method is, starting from the observables y, to be able to determine the source terms T. The first step consists in performing a SVD decomposition of y. The SVD decomposes the spatio-temporal signals into a unique set of orthonormal spatial and temporal eigenvectors, i.e.

$$y_{sk} = \sum_{q} V_{sq} D_q U_{qk} . \tag{3}$$

V is the orthonormal matrix containing the spatial eigenvectors, called topos, U the temporal eigenvectors, called chronos, and D is a diagonal matrix containing the singular values. Figure 2 shows the result of the application of the SVD to the model. Two conclusions can be drawn: the SVD is not capable of fully separating MECH and sawteeth components, but it is capable of isolating the subspace in which the two dynamics evolve, i.e. the subspace spanned by the two excited eigenvectors, as seen by the two dominant singular values. The next step consists in decomposing the chronos U so that

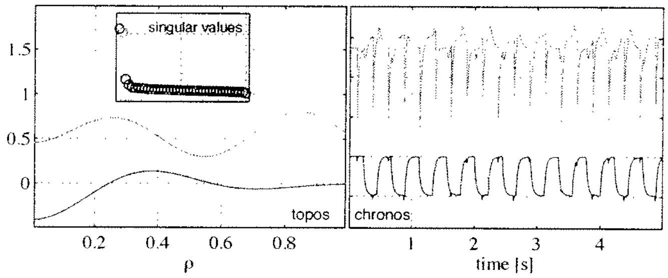

Figure 2. *First two topos and chronos resulting from SVD of the model signals, together with their singular values.*

$$y_{sk} = \sum_{q} V_{sq} D_q U_{qk} = \sum_{lmq} V_{sq} D_q P_{qlm} h_{mlk} . \tag{4}$$

h is determined from a nonlinear minimisation problem, in which the minimisation variables are the above defined time constants, and the SVD chronos are the fitted signals. On the other hand, determining the elements of P_{qlm} is a linear regression problem. Finally, the reconstructed spatial source terms can be calculated from

$$T_{sml} = \sum_{q} V_{sq} D_q P_{qlm} . \qquad (5)$$

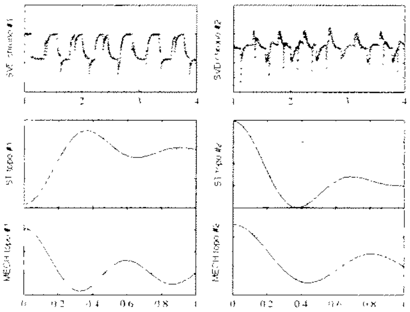

Figure 3. *Top: fit (red) of SVD chronos (blue). Bottom: MECH and sawteeth reconstructed source terms.*

Figure 3 shows the results for the used model: the procedure allows to simultaneously reconstruct each source term.

Experimental results

The above described procedure, called SI-SVD, has been applied to several MECH experiments. Let us first consider ECE measurements of an ASDEX Upgrade discharge in which the MECH was aiming on-axis. Figure 4 shows the calculated power density deposition profile calculated using (5), as well as amplitude and phase profiles after Fourier analysis at the first MECH harmonic of the raw and the treated signals, together with the profiles at the main sawtooth frequency. The power deposition location well corresponds to the expectations, while the treated amplitude and phase profiles clearly show the improvement in the quality of the results. A further advantage of using this method is related to the possibility of analysing the treated signals also at higher MECH harmonics, leading to narrower amplitude and phase profiles, hence to a better determination of the deposition. Another interesting, and for TCV important and necessary, result is related to the analysis of MECH discharges using soft X-ray (SXR) diagnostics. Figure 5 shows the results of a off-axis ASDEX Upgrade experiment. It is clearly visible that the power deposition location is well determined, hence it is possible to use SXR diagnostics for this purpose. To obtain useful

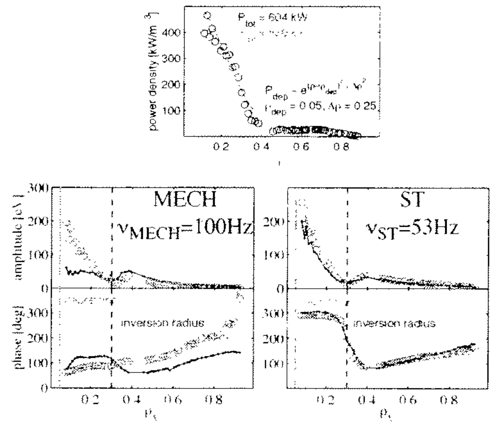

Figure 4. *Top: power density profile (in red a fit using a Gaussian curve). Bottom: amplitude and phase profiles of a on-axis ASDEX Upgrade MECH discharge (black:: untreated; red: SI-SVD treated signals).*

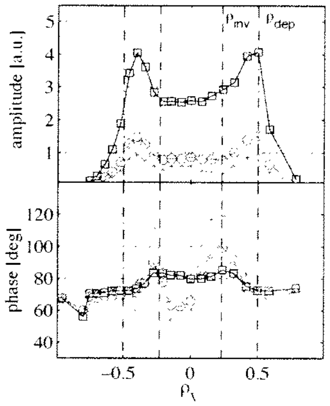

Figure 5. *Amplitude and phase profiles of SXR treated signals at first three odd harmonics (blue: first; red: third; magenta: fifth).*

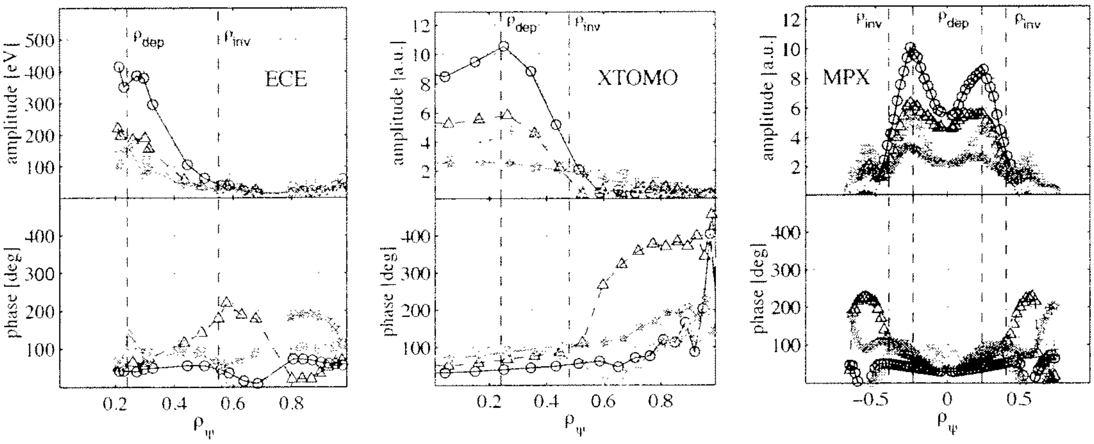

Figure 6. *Frequency scan comparison for the treated signals using different diagnostics. Modulation frequencies: 75 (black circles), 162 (blue triangles), 240 (magenta squares), 335 (red stars) and 718 Hz (green hexagons).*

information on the phase, though, a tomographic inversion of the signals is needed. Taking in consideration these remarks, we can now focus on the analysis and interpretation of TCV MECH experiments using different diagnostics, in particular the ECE [2], soft X-ray tomography (XTOMO) and multiwire proportional X-ray detector (MPX [3]). Figure 6 shows the results of a discharge in which a MECH frequency scan was performed on-axis. It is clearly visible that the profiles are fully coherent between different diagnostics, hence the power deposition location can be determined using also SXR diagnostics. If studies such as transport investigations must be performed, dedicated experiments and deeper signal processing must be accomplished (tomographic inversion, density variations).

In conclusion, the SI-SVD procedure allows to simultaneously reconstruct MECH and sawteeth spatial source terms. Its application to ECH experiments in ASDEX Upgrade and TCV has pointed out in particular, with the parallel analysis and interpretation of different diagnostics data, the possibility of determining the power deposition location using also SXR diagnostics.

Acknowledgements

This work was partly supported by the Swiss National Science Foundation.

Bibliography

[1] T. Dudok de Wit *et al*, *Phys. Plasmas* **1** (1994) p. 3288

[2] P. Blanchard *et al*, this conference, poster P-2.074

[3] A. Sushkov *et al*, this conference, poster P-4.118

Shape Effects on the Stability Limit of the Ideal Internal Kink Mode

An. Martynov, O. Sauter

Centre de Recherches en Physique des Plasmas

Association Euratom - Confédération Suisse, EPFL 1015 Lausanne, Switzerland

The internal ideal kink mode is one of the possible triggers of sawtooth oscillations [1] and it is important to know the stability of the internal ideal kink to be able to predict the behavior of sawteeth. In this work we have studied the behavior of the stability limit on the poloidal beta inside q=1 surface ("beta Bussac") in TCV-like equilibria, varying plasma shape and current profile using numerical MHD codes.

Analytic formulae for internal kink mode

There are several theoretical works giving analytical approximations of dependence of the ideal internal kink growth rate on different plasma parameters [3, 4, 5]. The summary of several of them is given in [1]. The theoretical analysis gives formulae for the normalized variation of the potential energy of perturbation $\delta\hat{W}$ and the growth rate of instability can then be obtained as $\gamma = \delta\hat{W}/\tau_A$ where $\tau_A = 3^{1/2}R/\upsilon_A$ is the Alfven time, R is the major radius and υ_A the Alfven speed. The main parameter which determines the marginal stability limit of the ideal internal kink mode is the "beta Bussac"$\beta_{bu} = 8\pi / B_{pl}^2\,(<p>_1 - p(r_1))$, where B_{pl} is the averaged poloidal magnetic field on the q=1 surface, $<p>_1$ is the volume averaged total pressure inside q=1 surface and $p(r_1)$ is the total pressure on q=1 surface. The mode becomes unstable, when β_{bu} is larger than some value which we will call β_{bu}^{crit}. According to the analytical theory [1], the value of β_{bu}^{crit} is close to

$$\beta^{crit} = 0.3(1\text{-}5/3(r_1\, k_1^{1/2}/(ab)^{1/2}), \qquad (1)$$

where κ_1 is the elongation on q=1 surface, $(ab)^{1/2}$ is the average plasma minor radius.

Parameter range and methods of calculations

TCV (Tokamak à Configuration Variable) is a tokamak, designed especially to explore various plasma configurations. The basic feature of TCV is the unique flexibility, allowing creation of plasmas in a very wide range of shape parameters: elongation up to 2.8 and triangularity between -0.7 and +0.9. The flexible system of EC heating and current drive allows the creation of various current profiles. Both shape and current profiles in TCV plasmas are beyond the range of parameters, for which the analytic expressions for ideal internal kink are obtained.

The ideal MHD code KINX [6] was used for the numerical analysis of the stability of shaped plasmas with various current profiles. The important feature of this finite element code is that the domain decomposition into several subdomains with nested flux surfaces allows the analysis of a broad range of tokamak plasma configurations, including very elongated and triangular plasmas, plasmas with separatrix, doublets etc. This code is an adequate tool for such an analysis.

For a given TCV-like equilibrium produced by the code CHEASE [7] the value of β_{bu}^{crit} is calculated by convergence studies with the code KINX. Thus we ensure that at β_{bu}^{crit} the growth rate of the ideal internal kink mode converges to zero or to a small value.

The scans on plasma elongation ($1.0 \leq \kappa_{edge} \leq 2.8$) and triangularity ($-1.0 \leq \delta_{edge} \leq 1.0$) were performed for the TCV aspect ratio $A \approx 3.6$. In most calculations a quadratic parabolic current profile was used (and in one case a cubic parabolic profile).

Results of calculations and analysis

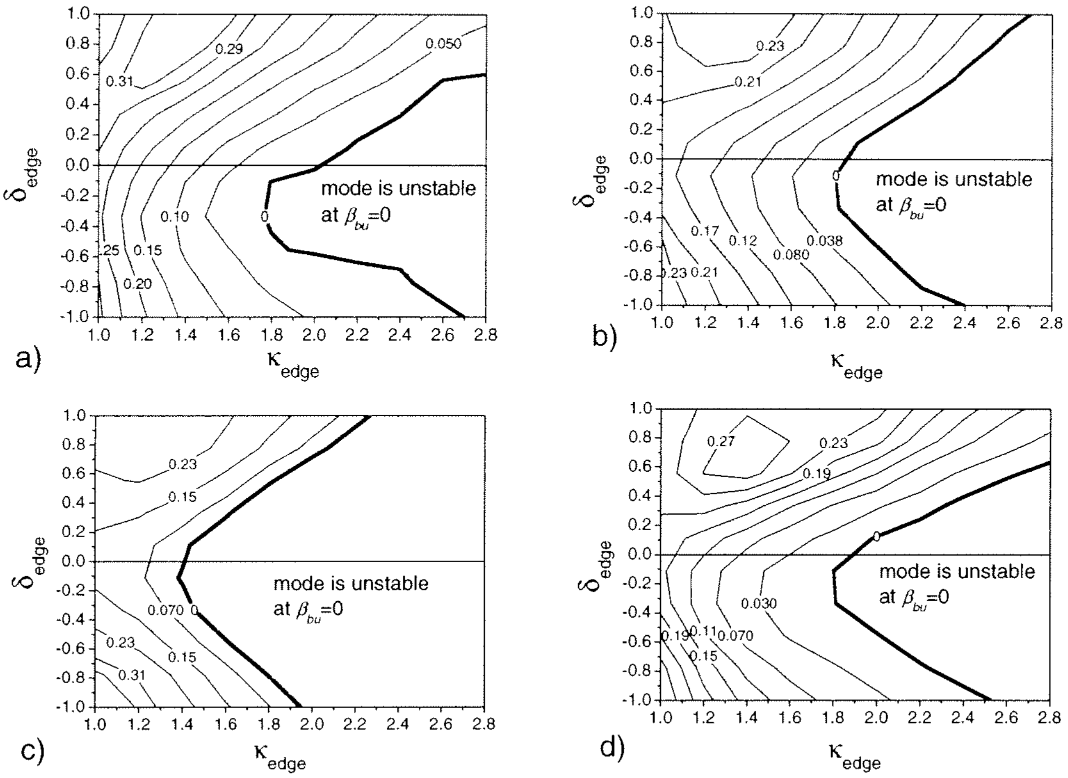

Figure 1. β_{bu}^{crit}: *a)* $\rho_{q=1}=0.25$ *and quadratic current profile b)* $\rho_{q=1}=0.5$ *and quadratic current profile c)* $\rho_{q=1}=0.7$ *and quadratic current profile d)* $\rho_{q=1}=0.5$ *and cubic current profile*

In the geometry scans presented here the current profile and radius of $q=1$ surface $\rho_{q=1}$ were kept fixed. In this case the profile of q inside $q=1$ surface remains almost unchanged (variation of q on axis is less than 10%) in the whole range of geometry variations.

The general character of the stabilization by an increase in triangularity is the same for different equilibria. There is a pronounced effect of elongation which leads to the destabilization of the mode at zero β_{bu}. From Figure 2 we can see that the stability limit is obtained at almost constant elongation on the $q=1$ surface in case of quadratic type profiles:

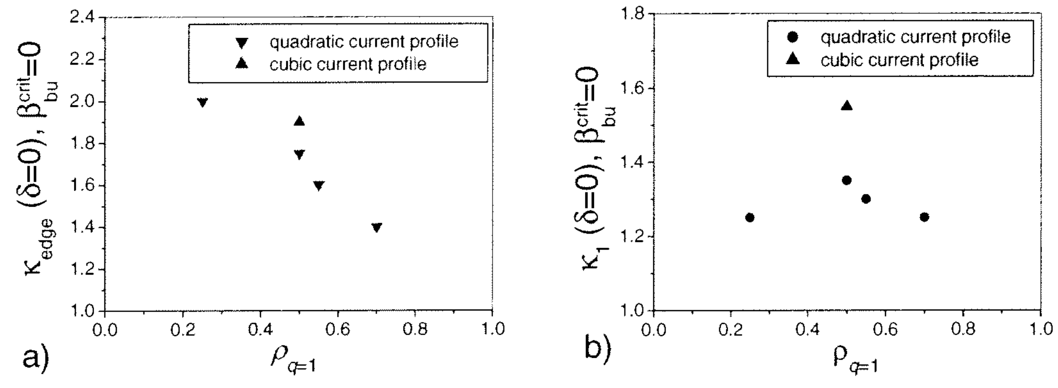

Figure 2. Dependence of a) elongation on the edge and b) elongation on q=1 surface at which the mode is destabilized at zero pressure on radius of q=1 surface

The triangularity has a stabilizing effect, which manifest itself as an increase of β_{bu}^{crit} at the same elongation with an increase of the triangularity, both positive and negative. The destabilization of the mode at low elongation and high positive triangularity is a peculiarity, which, although interesting for further studies, does not represent an interest from the point of view of experiment. The general dependence of β_{bu}^{crit} on triangularity at constant elongation and at constant $r_{q=1}$ corresponds approximately to the behavior of the volume inside $q=1$ surface. The stabilization by negative triangularity is less efficient than by positive triangularity.

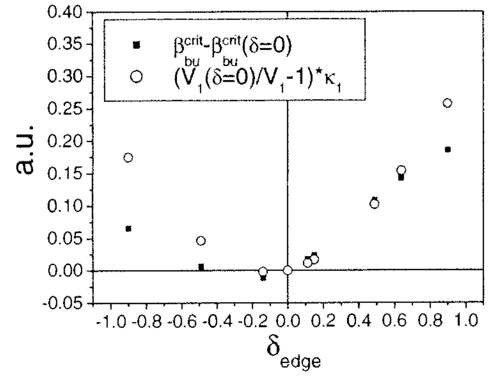

Figure 3. Increase of β_{bu}^{crit} on triangularity compared with behavior of volume inside $q=1$ surface (quadratic current profile, $\rho_{q=1}=0.5$, $\kappa_{edge}=1.6$)

The aspect ratio has a strong impact on the growth rate of the internal ideal kink [1] ($\gamma \propto \varepsilon_1^2$), but according to equation (1) it should not affect substantially the value of β_{bu}^{crit}. Our calculations confirm this:

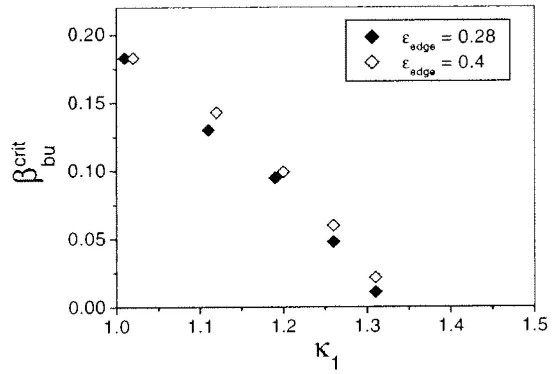

Figure 4. Dependence of β_{bu}^{crit} on elongation on $q=1$ surface at different aspect ratios. Quadratic current profile, $\rho_{q=1}=0.5$

Scalings of calculated dependences

The stabilization of the ideal internal kink mode by positive triangularity is known and it was shown experimentally on TCV [1]. The stabilization by the negative triangularity which appears in numerical calculations [8] has not been demonstrated in TCV experiments and it is an interesting direction for the new experiments. Therefore we have tried to find the description of this effect on basic of the plasma parameters and to simplify the prediction of the mode stability in TCV plasmas. Let us first consider the effect of elongation at zero triangularity. The equation (1) does not describe the results obtained (see Fig.5), so another scaling for quadratic type profiles is proposed :

$$\beta_{bu}^{crit}(\delta=0) = 0.33\,(1.3 - \kappa_1) \,/\, (r_1\, k_1^{1/2} \,/\, (ab)^{1/2})^{2/3} \qquad (2)$$

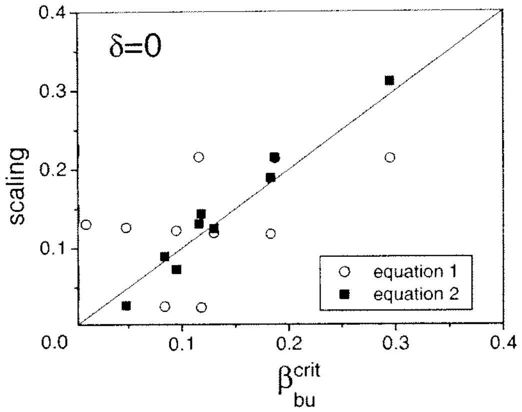

Figure 5. Scaling for β_{bu}^{crit} *at zero triangularity for quadratic current profile.*

By adding the term describing the stabilization by triangularity (Fig.3) and depending only on the edge triangularity (Figure 6a, compare with Figure 3), we can obtain a general scaling for cases with different elongations and triangularities for quadratic current profile

$$\beta_{bu}^{crit} = 0.33\,(1.3 - \kappa_1)\,/\,(r_1\, k_1^{1/2} / (ab)^{1/2})^{2/3} + 0.0111\,(\delta_{edge} + 4)\,(\delta_{edge} + 0.4)^2 \qquad (3)$$

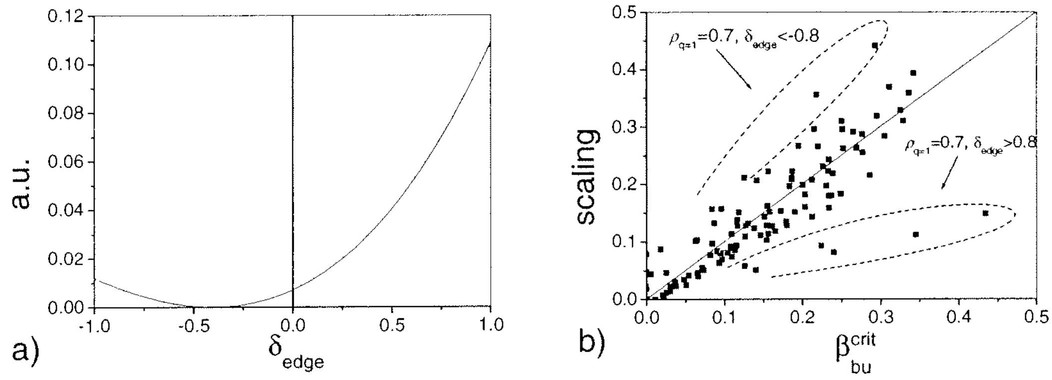

Figure 6. a) Additional term, describing the stabilization by triangularity. b) Scaling (Eq. 3) for parabolic current profile, $1.0 \le \kappa_{edge} \le 2.8$, $-1.0 \le \delta_{edge} \le 1.0$, $A=3.6$

The scaling (Eq. 3) describes satisfactorily the effects of elongation and triangularity for the quadratic current profile, with exception of cases with high $\rho_{q=1}$ and high triangularity, which can hardly be obtained experimentally. This scaling will be used for prediction of sawteeth behavior in TCV experiments.

This work was partly supported by the Swiss National Science Foundation.

References

1 *F. Porcelli et al, Plasma Phys. Control. Fusion* ***38*** *(1996) 2163-2186*
2 *Reimerdes H et al, Plasma Phys. Control. Fusion* ***42*** *(2000) 629-639*
3 *Bussac M N et al, 1975 Phys. Rev. Lett.* ***35*** *1638*
4 *Lutjens H, Bondeson A and Vlad G, Nucl. Fusion* ***32*** *(1992) 1625*
5 *Wahlberg C, 1998 Phys. Plasmas* ***5*** *1387*
6 *Degtyarev L et al, 1997 Comput. Phys. Commun.* ***103*** *10*
7 *H. Lutjens, A. Bondeson, O. Sauter, LPR 545/96*
8 *An. Martynov, O.Sauter ISSP-19 « Piero Caldirola » Theory of Fusion Plasmas (2000) 387*

Neo-Classical Tearing Mode Control through Sawtooth Destabilisation in JET

M.L. Mayoral[1], E. Westerhof[2], O. Sauter[3], B. Alper[1], R.J. Buttery[1], M. De Baar[2],
T.C. Hender[1], D.F. Howell[1], M.J. Mantsinen[4], A. Müeck[5], M.F.F. Nave[6]
and contributors to EFDA JET workprogramme*

1) Euratom-UKAEA Fusion Association, Culham Science Centre, Abingdon, OX14 3DB, UK
2) FOM-Rijnhuizen, Ass. EURATOM-FOM, TEC, PO Box 1207, 3430 BE Nieuwegein, NL
3) CRPP, Assoc. EURATOM-Confederation Suisse, EPFL, 1015 Lausanne, Switzerland
4) Helsinki Univ. of Tech., Ass. Euratom-Tekes, P.O.Box 2200, FIN-02015 HUT, Finland
5) Max-Planck-Institut,, IPP-EURATOM Ass., D-85748 Garching, Germany
6) Centro de Fusao Nuclear, Instituto Superior Tecnico, P-1049-001 Lisboa, Portugal
** See appendix of the paper by J.Pamela "Overview of recent JET results" Proceedings of the 18th IAEA conference on Fusion Energy, Sorrento 2000*

1. Introduction

Neo-classical tearing modes (NTMs) leads to significant reductions of energy and particle confinement and their control is a critical issue for tokamaks performance improvement. Above a certain threshold of the normalised plasma pressure β_N, m=3/n=2 NTMs are metastable and a finite seed island is required to trigger the modes. This seed island is generally generated by perturbations associated with a central sawtooth activity. A strategy was recently developed at the Joint European Torus (JET) to control the NTM seed island by modifying the sawtooth activity [1,2]. Ion Cyclotron Current Drive (ICCD), with waves tuned to the 2nd harmonic Hydrogen (H) cyclotron resonance frequency, is used to create shorter period and smaller amplitude sawteeth which are expected to induce smaller seed islands, thus increasing the plasma pressure at which an NTM is triggered. In a first series of experiments, summarised in section 2, it is shown that the plasma pressure threshold at the 3/2 NTM onset, ($\beta_{N,onset}$), indeed increases when ICCD is applied with a proper resonance localisation for sawtooth destabilisation but that a number of effects can limit this scenario. Experiments to improve the ICCD efficiency have also been performed and are reported in Section 3. The conclusions and prospects to develop this NTM control scheme are presented in Section 4.

2. Increased NTM threshold from ICCD sawtooth destabilisation

On JET, at high magnetic field NTMs cannot generally be destabilised with Neutral Beam Injection (NBI) only. Working at low magnetic fields B_0 between 1.2 and 1.6T and Ion Cyclotron Resonance Frequency (ICRF) waves at 42MHz (2nd harmonic H cyclotron resonance frequency) allows the capability the 'β_N increase at the NTM onset by sawtooth control' scheme, to be tested.

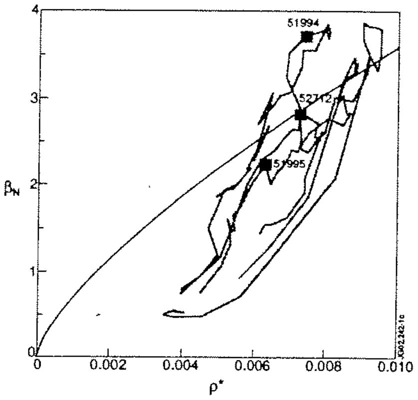

Figure 1: *β_N evolution versus $\rho*$ for discharges 51994 (with ICCD), 51995 and 52712 (NBI-only). The black curve gives the onset scaling with NBI-only.*

With NBI-only, the β_N threshold at the 3/2 NTM onset scales with the normalised ion gyroradius as $\beta_{N,onset} \propto \rho*^{0.7}$ [3]. This is not a sharp limit; the randomness of the necessary seeding perturbation causes the mode onset to spread somewhat with respect to the scaling. In Fig. 1, evolution of three discharges with B_0=1.2T is compared in terms of β_N and $\rho*$. Times of NTM onsets are indicated by squares. In 51994, about 5MW of ICCD is applied for sawtooth destabilisation. The resonance R_{2ndH} is positioned at 2.55m on the high field side (HFS) just outside the q=1 surface. In these discharges the NBI is ramped to slowly increase β_N in order to identify the NTM threshold. In 51995 and 51994 the NBI power waveforms are identical while in 52712, the NBI is identical to the total power in 51994. Whereas in both NBI-only discharges a 3/2 NTM is triggered close to the β_N from the threshold scaling, the pressure in the discharge with ICCD for sawtooth destabilisation considerably exceeds the threshold scaling before a 3/2 NTM is triggered. Table 1 lists a set of discharges in which B_0 is varied to probe the effect of varying resonance position near the q=1 surface. The $\beta_{N,onset}$ values for these discharges (incl. 51994) are given in Fig. 2 as a function of $\rho*$. For NBI-only discharges (red squares), $\beta_{N,onset}$ is close to the scaling. The discharges with added ICRF waves can be divided in three categories. In the first one, ICCD do not lead to sawteeth destabilisation. NTMs are triggered close or below to the usual threshold (pink triangles). In the discharge 52087, the resonance was most likely too far off-axis to have an effect. The second group (black square), represented by the discharge 52054 has only central ICRF and is well below the threshold scaling. The energetic ions produced lead to sawtooth stabilisation via an increase in the central fast ion pressure. In the third group (blue squares), sawteeth are destabilised by the ICCD and $\beta_{N,onset}$ increase relatively to the threshold scaling. Moreover, one can see in Fig. 3 that as the pressure increases the resonance position R_{2ndH} shifts to a smaller major radius and sawtooth destabilisation is possibly lost when the resonance crosses q = 1. This might explain why for some

N° Shot	B_0 (T)	R_{2nd} (m)	τ_{st} (ms)	t_{NTM} (s)	β_N
52077	1.29	2.78	214	24.90	2.55
52054	1.38	3.02	300	24.66	1.55
52079	1.47	3.21	307	25.50	2.35
52080	1.50	3.29	272	27.60	3.35
52082	1.53	3.34	253	28.10	3.45
52083	1.56	3.42	180	28.10	3.60
52087	1.61	3.55	231	26.37	2.65
52084	1.56	-	297	25.50	3.0
52703	1.56	-	315	27.37	3.35

Table 1: *2^{nd} harmonic H resonance radius, sawtooth period ~ 23.5 s, time and β_N at the 3/2 NTM. For discharge 52084 t_{NTM} refers to a 2/1 NTM onset.*

discharges ICCD had no net effect on the pressure threshold and why the improvement is limited in other discharges. Another limitation comes from the loss of the ICRF power (dashed parts of the curves in Fig. 3) due to the poor coupling during ELMs.

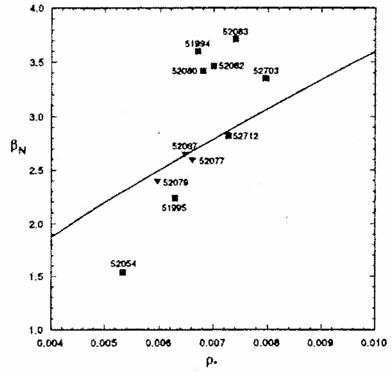

Figure 2: *β_N at mode onset versus $\rho*$ for table1 discharges. The black curve gives the onset scaling for NBI-only discharges.*

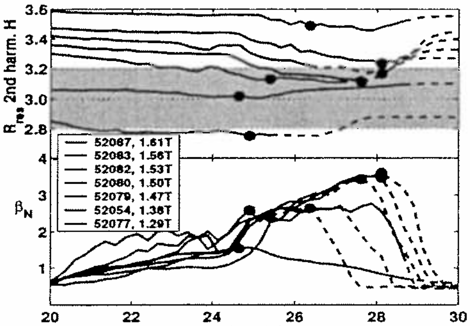

Figure 3: *Time evolution of 2^{nd} harmonic H resonance position and β_N for discharges in table1. The dots indicate the NTM onset, the dashed parts of the curve when P_{ICRF}<1MW and the shaded area the region inside R_{inv}. Reprinted from Ref. [1].*

3. Improvement of sawteeth control by ICCD

Experiments were recently performed to optimise the ICCD effect on sawteeth by changing the H concentration, the ICRF power, the wave phasing and the resonance position R_{2ndH}. Fig. 4 illustrates HFS experiments performed with B_0 ramps between 1.45 and 1.65T, 10% of H-minority and 4MW of ICRF. Optimal conditions for sawtooth destabilisation are found with R_{2ndH} on R_{inv} and –90° phasing. Indeed, due to the local modification of the q profile by the passing ions current [4], sawteeth with very small amplitude and indistinct crashes are obtained around t=23s. As R_{2ndH} goes toward the plasma centre, the fast ions pressure leads to longer period and larger amplitude sawteeth. In agreement with past experiments using central 1st harmonic H resonance, the pinch effect consequences [5] are also observed with a

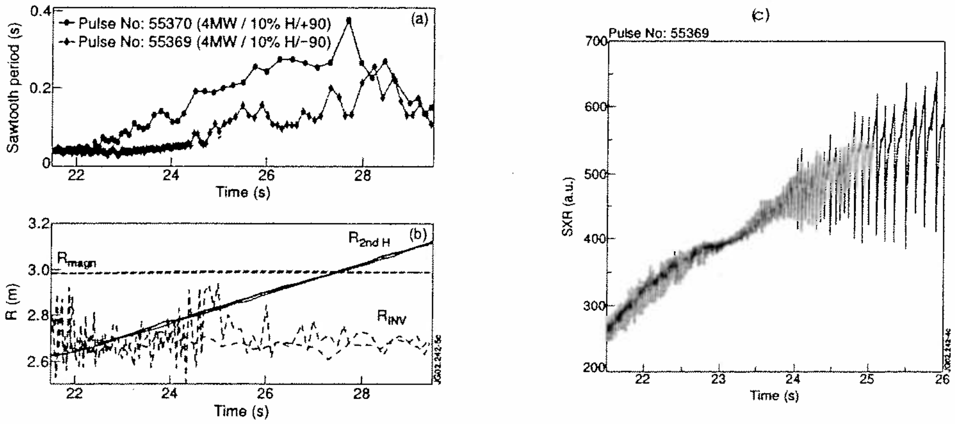

Figure 4: *Time evolution of (a) the sawtooth period; (b) the sawtooth inversion radius R_{INV}, the 2^{nd} harmonic H resonance R_{2ndH} and the magnetic axis radius R_{magn}, for discharges 55370, 55369; (c) Soft X-Ray emission (central channel) for the discharge 55369.*

2^{nd} harmonic scenario and lead to shorter period with –90° phasing compared to +90° phasing. Experiments with R_{2ndH} low field side (LFS) and B_0 ramps between 1.9 and 1.55T are shown in Fig. 6. Because of their finite orbit width, the fast trapped ions give rive to a "diamagnetic" type current [6] and leads to the changes in the sawtooth period observed as R_{2ndH} goes towards R_{inv}, with an minima in the period slightly inside R_{inv}. It has to be noted that in agreement with past numerical studies [6,7] this current is similar with +90° and –90° phasing. Moreover, increase in the sawtooth period (t~23s) obtained in shot 55367 with R_{2ndH} outside R_{inv} could be explained by a current profile modification in the presence of more energetic fast particles [7].

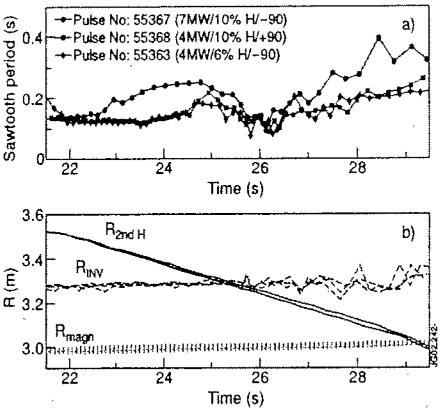

Figure 6: Time evolution of (a) the sawtooth period; (b) the sawtooth inversion radius R_{INV}, 2^{nd} harmonic H resonance R_{2ndH} and magnetic axis radius R_{magn} for discharges 55367, 55368, 55363. In discharges 55367, 7MW of ICRH power is applied.

4. Summary and prospects

A new strategy to control the NTMs onset was developed in recent experiments on JET. It was shown that by carefully positioning the 2^{nd} harmonic H resonance relative to the inversion radius, the sawtooth activity could be controlled and the plasma pressure at the NTM onset significantly increased. The ICCD production with a 2^{nd} harmonic H scenario was systematically studied in order to obtain a reliable and reproducible sawtooth control scenario with the resonance layer either low field side or high field side. In both cases the resonance position appears as a critical factor. In the next experiments, compensation of the resonance drift, as the plasma pressure increases will be performed. Preliminary tests have shown that the required changes of around 0.003T/s are technically feasible. Finally, a new trip management system, currently installed on the JET ICRF plant, is excepted to increase the averaged coupled power during ELMs and thus the ICCD performance.

References

[1] O. Sauter, *et al.*, Phys. Rev. Letters **88** (2002) 105001
[2] E. Westerhof, *et al.*, submitted for publication in Nucl. Fusion (2002)
[3] R.J. Buttery, *et al.*, submitted for publication in Nucl. Fusion (2002)
[4] V.P. Bathnagar, *et al.*, Nucl. Fusion **34** (1995) 1579
[5] L.-G. Eriksson, *et al.*, Phys. Rev. Lett. **81(6)** (1998) 1231
[6] M. J. Mantsinen, *et al.*, accepted for publication, Plasma Phys. Contr. Fusion (June 02)
[7] J. Carlsson, *et al.*, Phys. Plasmas **5** (1998) 2885

This work was performed under EFDA and partly funded by UK Department of Trade and Industry, Nederlanse Organisatie voor Wetenschappelijk Onderzoek, Swiss National Science Foundation and Euratom.

Edge Kink/Ballooning Mode Stability in Tokamaks with a Separatrix

S.Yu.Medvedev[1], Y.Martin[2], O.Sauter[2], L.Villard[2], D.Mossessian[3]

[1]*Keldysh Institute, Russian Academy of Sciences, Moscow, Russia*
[2]*CRPP, Association Euratom-Confédération Suisse, EPFL, Lausanne, Switzerland*
[3]*Massachusetts Institute of Technology, Cambridge, Massachusetts, USA*

1 Kink/ballooning modes High-n ideal modes are possible candidates to trigger the edge localized modes (ELM) instability [1]. The presence of a magnetic field separatrix at the plasma boundary leads to the stabilization of ideal localized peeling modes which require the presence of a rational magnetic surface just outside the plasma surface. However the external kink modes coupled to the ballooning modes set stability limits for the pressure gradient and current density pedestals at the plasma boundary.

The differences between limiter and separatrix geometries relevant to the peeling mode stability analysis were listed in [2]: because the safety factor goes to infinity at the separatrix, there are rational surfaces inside the plasma for any mode number. Moreover, there is a non negligible variation of q across the mode width. The question on the localized peeling mode criterion [3, 4] applicability to the ideal divertor plasma still needs to be answered. Plasma outside the separatrix and possible transition of the peeling mode into resistive tearing mode should be also taken into account.

The edge kink/ballooning mode [2] is a more robust pressure-driven instability which can set the stability limit lower than the $n = \infty$ ballooning modes due to coupling with external modes. It decouples from the peeling mode in a limiter plasma when the first rational surface in vacuum is far from the plasma edge so that the corresponding value of $m - nq \sim 1$ at the plasma boundary. Taking into account the separatrix naturally decouples peeling and ballooning modes and gives kink/ballooning mode stability limits which do not depend on small variations of the safety factor.

2 The KINX code modifications The recent version of the KINX stability code [5] was upgraded to compute high-n mode stability. It uses a new variant of ballooning factor extraction [6] applicable to equilibria with separatrix. The ballooning factor extraction significantly enhances the eigenvalue convergence in case of high toroidal wave numbers especially for large q variations. Another useful option is setting a plasma displacement to zero inside a prescribed magnetic surface and solving only for displacements in the rest of plasma. It provides a possibility to increase the radial resolution near the plasma edge.

The maximal grid dimensions in radial and poloidal directions for the stability calculations were 384 × 384. It allows us to treat mode numbers up to $n \approx 60$ thanks to grid packing near the boundary and the X-point.

3 Edge mode stability with separatrix The KINX code was applied to the computations of the kink/ballooning mode stability of the equilibria related to the Alcator C-Mod and TCV tokamaks.

The first series of the Alcator C-Mod equilibria is described in [7], where the KINX results are compared to the ELITE code [8] for plasma limited by the $\psi = 0.99\psi_{sx}$ magnetic surface. Concerning the results with separatrix, it should be mentioned that the original equilibrium with vanishing current density at the boundary is stable against modes $n = 1 - 60$ and is marginally $n = \infty$ ballooning stable near the boundary. The profiles cut at $\psi = 0.99\psi_{sx}$ were used to recompute the equilibrium and produce current density and pressure gradient pedestals at the separatrix (Fig.1).

In the table below the KINX growth rates normalized to Alfvén frequency are compared for the cases with and without separatrix with the same profiles.

n	$\psi = 0.99\psi_{sx}$	with separatrix
20	0.006	stable
30	0.056	0.024
40	0.093	0.076

The values of growth rates are not sensitive to small variations of the safety factor despite the fact that the peeling mode stability criterion was not satisfied anywhere in the plasma. In Fig.2 the structure of the $n = 30$ mode is presented with and without separatrix at the boundary.

For a preliminary assessment of the TCV edge mode stability the following procedure was proposed. The reconstructed equilibrium pressure profile was replaced with a profile from Fig.1 scaled to get the same value of β at fixed plasma current. The corresponding bootstrap current (not taking collisionality into account) was added to the reconstructed profile of $< \mathrm{jB} > / < \mathrm{B}\nabla\phi >$. For the TCV shots #8856 at $t = 0.3s$ and #11410 at $t = 0.5s$ it gives the profiles presented in Fig.3. The equilibrium corresponding to the shot #8856 is unstable against the modes $n > 10$ even without pedestal at the separatrix. Raising the beta value to $\beta_N \sim 2$ in the series with scaled pressure profile drives the $n = 5$ mode unstable.

The equilibrium corresponding to shot #11410 is stable for profiles without pedestal at the separatrix, as was the case for Alcator C-Mod equilibria. However the range of unstable toroidal wave numbers is shifted to lower $n \gtrsim 10$ for the profiles cut at $\psi = 0.99\psi_{sx}$.

The dependence of the edge mode stability on the pedestal height was studied. The pedestals were produced by cutting the original profiles at $\psi = 0.99\psi_{sx}$ and $\psi = 0.98\psi_{sx}$ and recomputing the equilibria with separatrix at the boundary. In the tables below the growth rates are given for equilibria with different pedestals at the separatrix for the TCV cases (#8856 left and #11410 right).

n	at 0.98	at 0.99	no pedestal
10	stable	0.054	marginal
20	0.057	0.178	0.106
30	0.132	0.249	0.170
40	0.187	0.285	0.192

n	at 0.98	at 0.99	no pedestal
10	stable	marginal	stable
20	stable	0.096	stable
30	0.051	0.141	stable
40	0.088	0.161	stable

For the highest values of current density and pressure gradient at the separatrix corresponding to profiles cut at $\psi = 0.98\psi_{sx}$ the modes are more stable than for the lower pedestal. Possible reasons for that are an edge pressure gradient in the second stability region and a decreased pedestal width.

In the Fig.4 the mode structures for the two TCV cases are presented.

4 Discussion Ideal edge mode stability was computed for equilibria with separatrix at the boundary. In the absence of peeling modes kink/ballooning modes can set β_N limits below the $n = \infty$ ballooning and low-n external kink mode limits depending on the toroidal wave number, current and pressure gradient pedestal. Current density pedestal at the separatrix significantly affects the edge mode stability through coupling of external kink and ballooning modes.

Despite a large current density pedestal a shift of unstable kink/ballooning mode range in toroidal wave number to higher values was discovered when the pressure gradient near the edge is in the ballooning second stability region. Besides the second stability access such stabilization may be also connected with decreasing pedestal width.

Acknowledgements The CRPP authors are supported in part by the Swiss National Science Foundation.

References

[1] P.B.Snyder *et al.*, *Phys. Plasmas* 9(2002)2037
[2] J.W.Connor *et al.*, *Phys. Plasmas* 5(1998)2687
[3] D.Lortz, *Nucl. Fusion* 15(1975)49
[4] J.A.Wesson, *Nucl. Fusion* 18(1978)97
[5] L.Degtyarev *et al.*, *Comput. Phys. Comm.* **103**(1997)10
[6] R.Gruber *et al.*, *Comput. Phys. Commun.* 24(1981)363
[7] D.A.Mossessian *et al.*, *Plasma Phys. Control. Fusion* 44(2002) 423
[8] H.R.Wilson *et al.*, *Phys. Plasmas* 9(2002) 1277

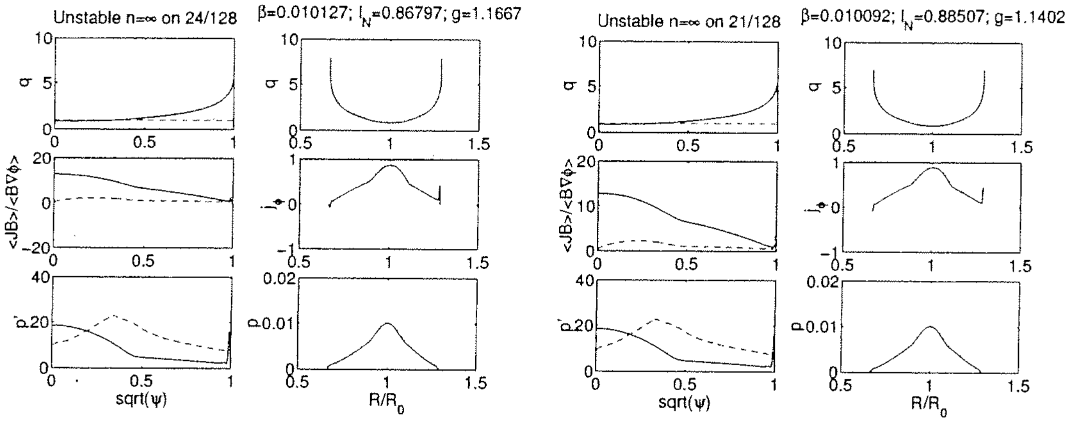

Fig.1 Profiles of the Alcator C-Mod equilibrium: original (left) and cut at $\psi = 0.99\psi_{sx}$ *(right). Both equilibria have separatrix at the boundary. The collisionless bootstrap current and marginal ballooning stable pressure gradient are shown by dashed lines*

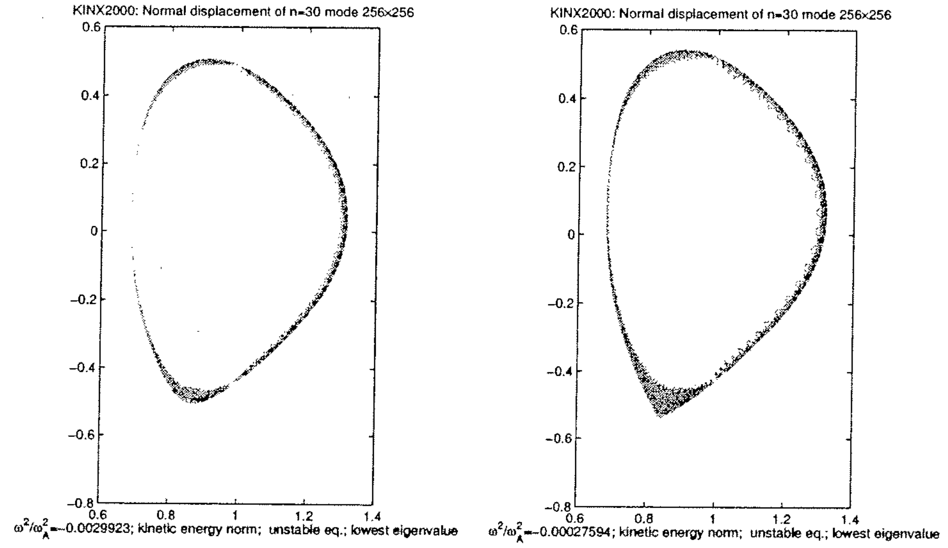

Fig.2 Level lines of normal displacement for the Alcator C-Mod equilibria with (right) and without (left) separatrix. Toroidal wave number $n = 30$

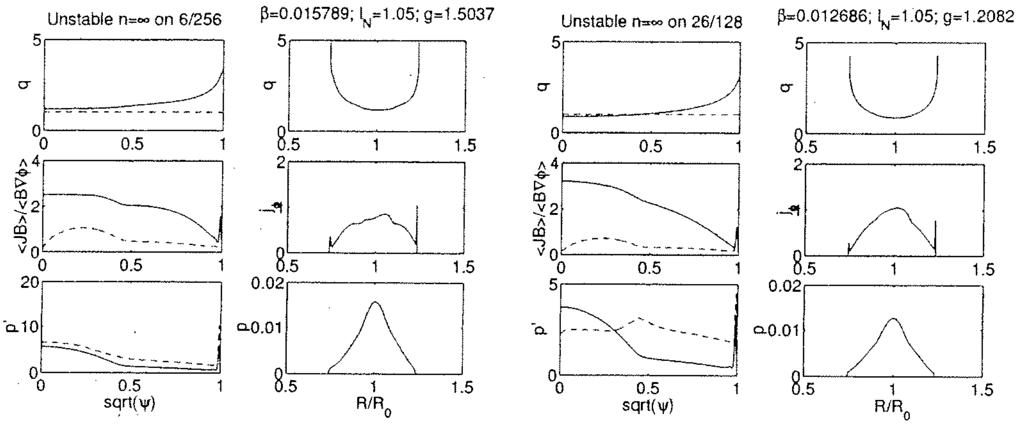

Fig.3 Profiles of the TCV equilibria with pedestal: #8856 (left) and #11410 (right)

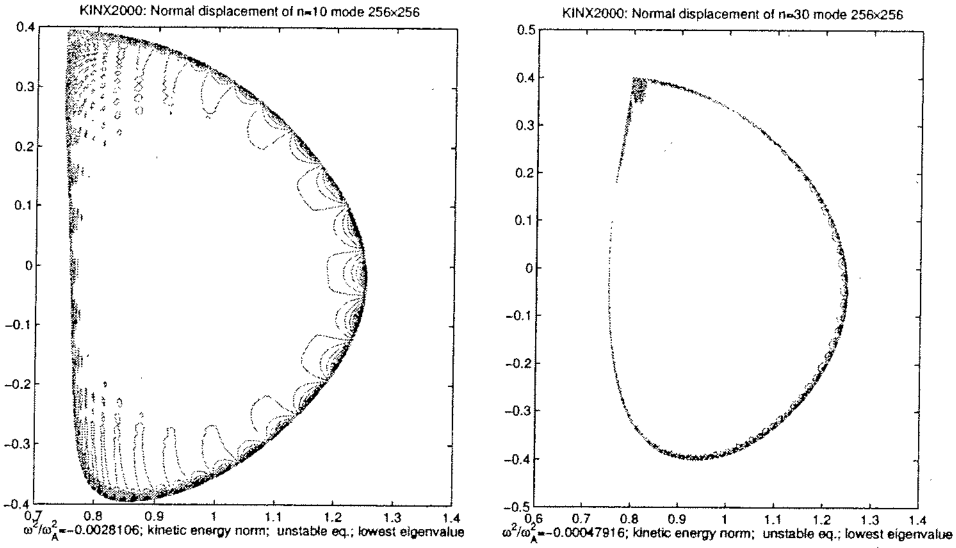

Fig.4 Level lines of normal displacement for the TCV #8856 equilibrium with pedestal at 0.99, $n = 10$ *(left) and for the TCV #11410 equilibrium with pedestal at* 0.98, $n = 30$ *(right)*

Sawtooth Tailoring Experiments with ECRH in ASDEX Upgrade

A.Mück[1], T.P.Goodman[2], H.R.Koslowski[3], F.Ryter[1], E.Westerhof[4], H.Zohm[1],
ASDEX Upgrade Team[1]

[1]*Max-Planck-Institut für Plasmaphysik, EURATOM Assoziation, D-85748 Garching*
[2]*CRPP EPFL, Association Euratom, CH-1015 Lausanne*
[3]*Forschungszentrum Jülich, Institut für Plasmaphysik, D-52425 Jülich*
[4]*FOM-Rijnhuizen, EURATOM-FOM, TEC, PO Box 1207, 3430 BE Nieuwegein, NL*

1. Introduction:

A tokamak plasma is unstable against the sawtooth instability when the safety factor q drops below unity. In a sawtooth, a slow rise in plasma temperature is followed by a rapid crash, triggered by a (1,1) kink mode. In the crash phase, the hot plasma center is thrown out into colder outer plasma regions. This process can be used to remove helium ash or impurities from the plasma center.

The control of the sawtooth instability is of great relevance for future reactor-grade devices such as ITER. It is expected that the α-particles created in D-T fusion processes lead to sawtooth stabilization. Long sawtooth free periods might lead to so-called monster sawteeth which could trigger a Neoclassical Tearing Mode (NTM) [1].

The goal of this work is to investigate how to control the sawtooth instability.

2. Experiments:

In ASDEX Upgrade, to influence sawteeth in neutral beam injection (NBI) heated plasmas, local electron cyclotron current drive (ECCD) or electron cyclotron resonance heating (ECRH) is used. The sawtooth period and amplitude can be changed by relatively small amounts of ECRH/ECCD. The ECRH deposition was swept by magnetic field ramps. All following discharges except the one in figure 1 are H-mode plasmas with 0.8 MA plasma current, 5 MW NBI power, densities about $6 \cdot 10^{19}$ m^{-3}, and about 0.9 MW of ECRH power, provided by two gyrotrons. The cold resonance for 2nd harmonic X-mode lies at $B = 2.5$ T in the plasma center. By magnetic field variations from about -2.05 T to -2.65 T, the ECRH deposition was moved from $\rho_{pol} \approx 0.6$ on the high field side out to $\rho_{pol} \approx 0.3$ on the low field side.

The influence of different NBI sources on the sawtooth behaviour seems to be dependent on the NBI beam trace geometry. In the discharge in figure 1, the different beam sources were used separately for about 1 s each. There was a plasma current of 0.8 MA, 2.5 MW NBI power, densities about $3 \cdot 10^{19}$ m^{-3} and a -2.0 T magnetic field. The beams NBI 6 and 7 are the most tangential beams with more deposition outside of the plasma center than the other beams. There the highest stabilization was seen (no Soft X-Ray (SXR) signal available). NBI 2 and 3 deposit closer and more perpendicular to the center and seem to show less stabilization. The beams 5,8 and 1,4 are the least tangential ones and have even more central deposition. There the sawteeth seem to be least stabilized. In future, this will be further investigated.

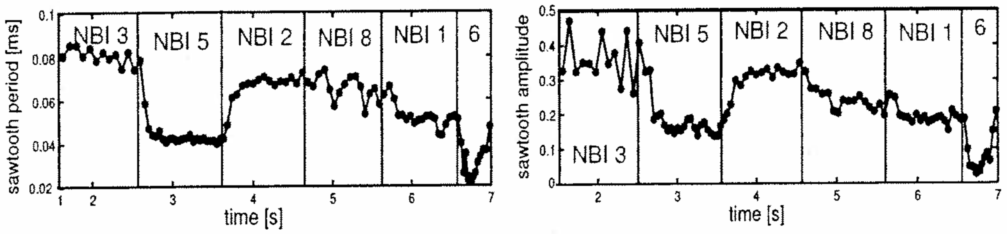

Figure 1: Influence of different NBI sources on sawtooth behaviour

To obtain an ECRH deposition profile in the *heating case* comparable to the following co-/ctr-ECCD experiments, one gyrotron was driving co-ECCD, the second one ctr-ECCD with a toroidal angle of ±15 degrees. The net current is expected to add up to zero. In all figures, the jump at $\rho_{pol} \approx -0.25$ is due to different NBI sources. In the sawtooth period graphs, negative values for ρ_{pol} are chosen to distinguish between high field side (HFS) and low field side (LFS), $\rho_{pol} > 0$. By using the ray tracing code TORBEAM, the ρ_{pol} values for the varied B field were simulated. The amplitude is still drawn over B field. The small dots in all figures are reference points without ECRH.

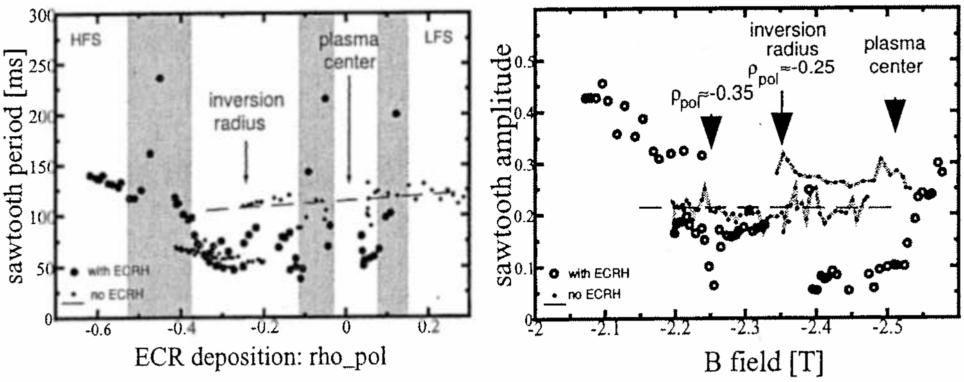

Figure 2: Sawtooth period variation by magnetic field scan with ECRH

In Porcelli's model [2], the kink mode is destabilized if its growth rate $\gamma > c_r \omega_{*i}$ with c_r a constant of order unity and ω_{*i} the diamagnetic frequency. This equation can be rewritten as a triggering condition for sawteeth: $s_1 > s_{1,crit}$. s_1 is the shear at the $q = 1$ surface and $s_{1,crit}$ the critical shear, calculated from different plasma parameters.

Generally by using ECRH in addition to the NBI heating, higher values of power density are created which lead to larger pressure gradients. Larger pressure gradients cause an increase in the critical shear [2]. This increase in the critical shear leads to stabilization of sawteeth (increase in sawtooth period) with NBI. In NBI heated plasmas, as well, fast particle effects have to be taken into account. In figure 2 at $\rho_{pol} \approx -0.45$, a strong increase in the sawtooth period is observed in the shaded area. Slightly inside this peak at $\rho_{pol} \approx -0.35$ a very narrow minimum in sawtooth amplitude appears. In the center, there is a broad minimum in sawtooth amplitude. Close to $\rho_{pol} \approx \pm 0.1$, a second, very narrow peak in sawtooth period is observed. To make sure that this peak is not a side effect of the overlay of co- and counter-ECCD, a narrow region was scanned with pure heating. The raw (SXR) data is shown in figure 3.

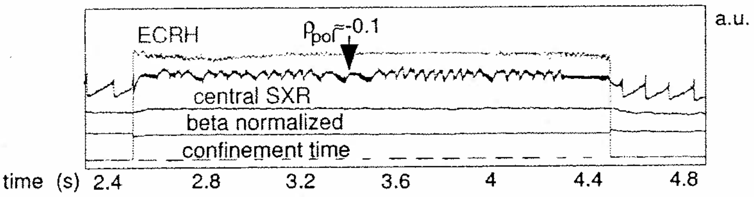

Figure 3: SXR time trace of B field scan with pure ECRH around $\rho_{pol} \approx -0.1$, NBI beams 3,7

Even in the pure heating case, a change in the sawtooth behaviour is observed at $\rho_{pol} \approx -0.1$. Possibly the ECRH was deposited in a magnetic island, but further investigation is needed.

In the *co-ECCD case*, two gyrotrons were used with a toroidal angle of -15 degrees. Close to $\rho_{pol} \approx -0.4$ in the shaded area in figure 4, an even bigger maximum in sawtooth period than for heating is observed. Complete stabilization was achieved at fixed magnetic field with ECRH deposition at $\rho_{pol} = -0.42$ and a total driven current of $I_{ECCD} = 23.9$ kA. A strong (1,1) mode was observed. Probably, the (1,1) mode was strongly destabilized that sawtooth activity was prevented by the mode itself.

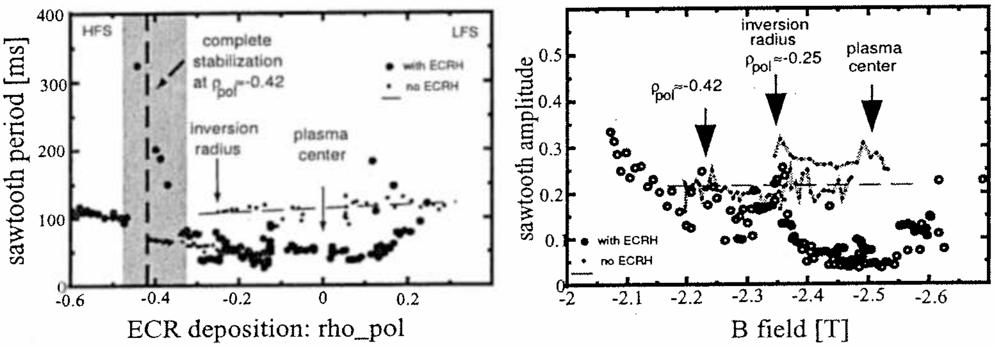

Figure 4: Sawtooth period variation by magnetic field scan with co-ECCD

Inside the sawtooth inversion radius, the sawteeth were destabilized. In this area, the amplitude is much less than in the reference case without ECRH. In a scan around $\rho_{pol} \approx -0.1$ like in the heating case, no change in the sawtooth period was observed. The amplitude remained low.

For *counter-ECCD*, two gyrotrons were used with a toridal angle of +15 degrees.

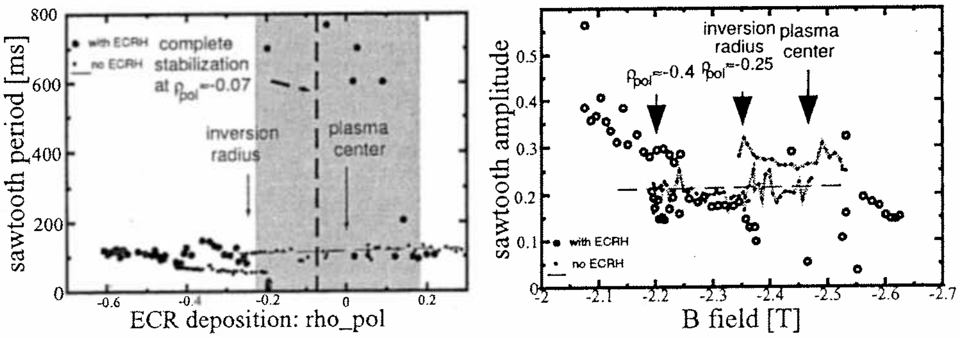

Figure 5: Sawtooth period variation by magnetic field scan with ctr-ECCD

At $\rho_{pol} \approx -0.4$ in figure 5, the maximum observed in the heating case completely vanished. For counter-ECCD with deposition slightly outside the $q = 1$ surface, the current gradient and with it q' likely increases. This has a destabilizing effect on the sawteeth. For deposition inside the sawtooth inversion radius, a broad maximum in sawtooth periode and minimum in amplitude was found in the shaded area. For deposition slightly inside the $q = 1$ surface, the current gradient and with it q' might decrease. This has a stabilizing effect on the sawteeth. With constant magnetic field, complete stabilization was achieved at $\rho_{pol} \approx -0.01$ and with a total driven current of $I_{ECCD} = -22.4$ kA and a strong (1,1) mode. To investigate the behaviour of the sawtooth period, amplitude and how much power is needed for stabilization, in figure 6 an ECRH power ramp was performed.

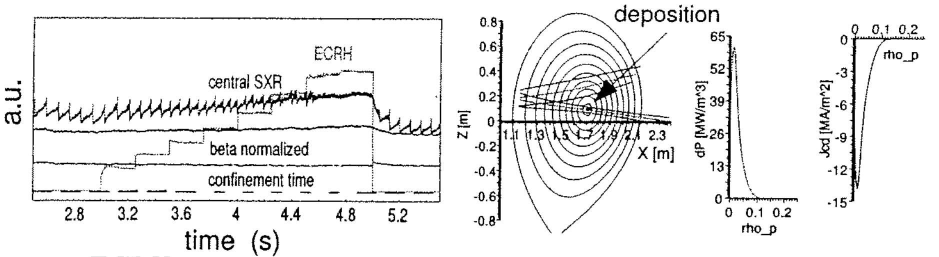

Figure 6: ECRH power ramp up with ctr-ECCD at $\rho_{pol} \approx +0.01$, NBI beams 3,7

With 0.7 MW heating power (same ctr-ECCD scenario than before), the sawteeth could be completely stabilized. The sawtooth period remained about constant, but the amplitude constantly decreased.

Summary:

Magnetic field scans were performed with additional ECRH or co-/ctr-ECCD. In the heating case, sawtooth stabilization was observed at about $\rho_{pol} \approx -0.4$ on the HFS. At $\rho_{pol} \approx -0.1$, a second peak in sawtooth period was found. With co-ECCD, the peak in the sawtooth period increased. Inside the sawtooth inversion radius, the sawteeth were destabilized. As expected, the co-ECCD behaviour inverted for the ctr-ECCD case pointing towards significant current drive. The peak at $\rho_{pol} \approx -0.4$ diminished, even disappeared. Inside the sawtooth inversion radius, a broad maxiumum in sawtooth period was observed. For central deposition, an ECRH power ramp up showed that with increasing power the sawtooth amplitude decreased to zero with constant period.

Generally, around the plasma center, a broad minimum in sawtooth amplitude is observed for heating, co- and counter-ECCD.

In the future, experiments will be performed using more NBI power to investigate the onset of NTMs by varying sawtooth behaviour. Additionally, a look at the influence of different NBI sources on the sawtooth behaviour and theoretical modelling of the sawtooth instability is planned.

References

[1] E. Westerhof et al., Nuclear Fusion, Vol. 41, No. 13

[2] Porcelli et al., Plasma Phys. Control. Fusion **38** (1996) 2163-2186

Study of ideal external mode in LHD

Y. Narushima, K.Y. Watanabe, S. Sakakibara, N. Nakajima, K. Nishimura,
H. Yamada, K. Yamazaki and LHD experimental group
National Institute for Fusion Science, 322-6 Oroshi-cho, Toki, Gifu 509-5292, Japan
W.A. Cooper[1]
1) *Centre de Recherches en Physique des Plasmas,*
Association Euratom / Confederartion Suisse, EPFL, 1015 Lausanne, Switzerland

1. Introduction

Serious MHD instabilities leading to the degradation of the energy confinement time and the termination of the discharge have not been observed in experiment on the Large Helical Device (LHD) [1]. It is worthwhile to investigate the characteristics of the MHD activities in the LHD plasma theoretically and experimentally. In this paper, we focus on the external mode (particularly m/n=1/1 mode). The low-n ideal MHD analysis is performed for n=1 mode family on the LHD plasma using the three-dimensional stability code **TERPSICHORE** [2].

2. Characteristics of ideal MHD stabilities of LHD plasma at peripheral region

The analyzed plasma has the magnetic axis at R_{ax}=3.6m and no plasma current I_p=0. The plasma pressure p is expressed as $p=p_0(1-\rho^2)^k$. Here, p_0, ρ, and k are the central plasma pressure, normalized minor radius in flux coordinate, and the parameter of the profile with the range of 0.2 to 1.0, respectively. The equilibrium is solved by VMEC code [3] under the condition of the free boundary. Figure 1 shows low-n ideal MHD mode unstable region in <β> - dβ/dρ diagram for n=1 mode family. The all symbols mean the destabilized points with respect to the low-n interchange mode calculated by **TERPSICHORE** under the free boundary condition. The black, green and red lines

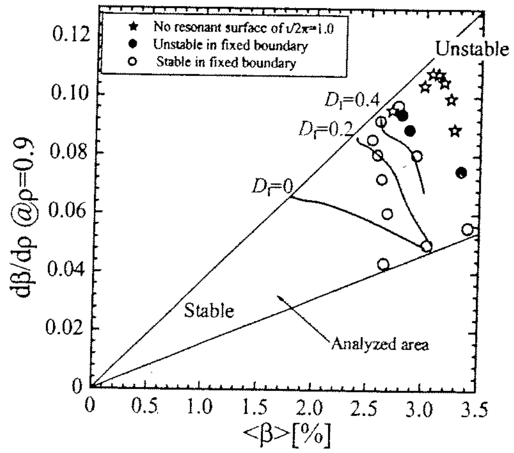

Fig. 1 Relation between the beta and the pressure gradient at ρ=0.9.

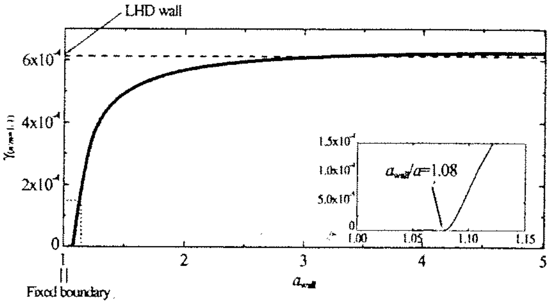

Fig. 3 Wall effect on external mode.

eigenvalue on $a_{\rm wall}$ (the ratio of the averaged radius of the wall and the plasma boundary) with the range from 1.0 (fixed boundary) to 5.0. The growth rate is almost constant at $a_{\rm wall}$>2.0, that is, the results are almost same as a free boundary condition. The eigenvalue decreases steeply with $a_{\rm wall}$ below $a_{\rm wall}$<1.5, and finally, the external mode can be stabilized with $a_{\rm wall}$ <1.08. We also adopt a wall shape that is similar to the real LHD vacuum vessel shape. In this case, the eigenvalue is equal to the case of $a_{\rm wall}$=3.0, which means the real LHD wall is equivalent to the case of $a_{\rm wall}$=3.0 with regard to the m/n=1/1 mode so that the real LHD wall represents a nearly free boundary condition for ideal MHD stabilities.

4. The domain where external mode appears

We focus on the effect of the profile of the rotational transform, especially the value at edge $\iota_{(1)}/2\pi$. Here, we also assume p=$p_0(1-\rho^2)^{0.5}(1-\rho^8)$. To obtain the equilibrium in various $\iota_{(1)}/2\pi$, the position of the plasma boundary is changed in the calculation with VMEC. One way to produce such plasma configuration experimentally is usage of a limiter [5]. The low-n unstable region under the free boundary condition is shown in Fig.4. The points of open and closed symbol mean low-n stable and unstable, respectively. In the unstable symbols, the closed circles mean the largest amplitude of ξ_s for m/n=2/1 modes and closed stars for 1/1 mode. The red solid and dashed lines indicates the contours of Mercier parameter with $D_{\rm I}$=0, 0.2, for $\iota/2\pi$=0.5 resonant mode, respectively, and blue solid line indicates the contour of $D_{\rm I}$=0 for $\iota/2\pi$=1.0 resonant mode. The contour of $D_{\rm I}$=0.2 for $\iota/2\pi$=1.0 does not exist in this equilibrium region. The red symbols mean low-n unstable even in the fixed boundary condition and the modes are destabilized in the Mercier unstable region with $D_{\rm I}$(@$\iota/2\pi$=0.5)>0.2 regardless of the value of $\iota_{(1)}/2\pi$. These mode structure shows the internal mode and the main component is m/n=2/1 mode (Fig4.(a)). Under the fixed boundary condition, there does not

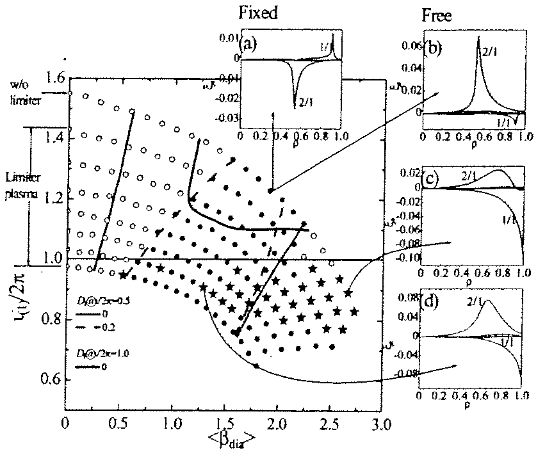

Fig.4 The unstable domain with respect to low-n mode.(n=1 mode family).

mean the contours of Mercier parameter [4] with D_I=0, 0.2, and 0.4, for $\iota/2\pi$=1.0 resonant mode respectively. In the case of the fixed boundary condition, the points of the closed circle remain unstable, and the amplitude of the radial component of the displacement vector (ξ_s) at plasma boundary is zero ($\xi_{s(1)}$=0). This structure is defined as "internal mode" henceforth. In this case, the qualitative correlation between the D_I and low-n mode is found. On the other hand, under the free boundary condition, the domain of low-n unstable region expands wider in comparison with the fixed boundary condition. In typical LHD plasma with low-β, the $\iota/2\pi$=1.0 and 0.5 resonance surfaces are inside plasma. However, $\iota/2\pi$=1.0 surface disappears under high-β. The equilibrium shown by stars do not have the resonant surface of $\iota/2\pi$=1.0. In this situation, the displacement vector at ρ=1.0 has the meaningful value and this mode structure is defined as "external mode" henceforth. The ξ_s profile of an external mode has a structure with a dominant m/n=1/1 contribution, as described in section 3.

3. Detail of mode structure and wall effect against the external mode

Figure2 shows an example of the mode structure of the external mode whose dominant mode is m/n=1/1. The pressure profile is assumed as $p=p_0(1-\rho^2)^{0.5}(1-\rho^8)$ and β=2.73%. This profile does not have the surface current originate from the pressure gradient at ρ=1.0. The rotational transform at plasma boundary ($\iota_{(1)}/2\pi$) is below 1.0 (Fig.2 (d)). As shown in Fig.2 (a), the components of m/n=2/1 and 1/1 mode appear together. The amplitude of ξ_s of the m/n=1/1 mode is maximum at ρ=1.0, where it locally indicates the tendency toward stability (D_I<0, dW>0, Fig.2(b)(c)). On the other hand, m/n=2/1 mode shows the off-resonant mode and its peak position is ρ=0.7. The potential energy at that position is positive that means the stability by m/n=2/1 mode.

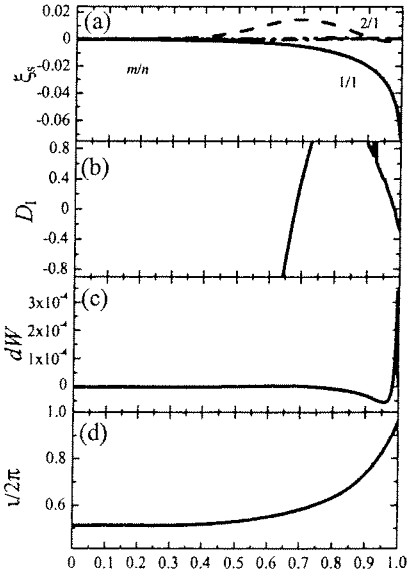

Fig. 2 The profile of (a)ξ_s, (b)D_I (c)dW, and (d)$\iota/2\pi$.

The external mode is stabilized under the fixed boundary condition. **TERPSICHORE** is able to calculate the stability with various wall shapes. To examine the wall effect against the mode, the analysis of stability is carried out with the various walls whose shapes are similar figures of the plasma boundary. Figure 3 shows the wall effect on the external mode as the dependence of the exist the mode structure in which the m/n=1/1 appears independently. Under the free boundary conditions, the low-n unstable area is expanded to Mercier stable and $\iota_{(1)}/2\pi>1.0$ region more widely than the case under the fixed boundary condition. In case of $\iota_{(1)}/2\pi>1.0$, the low-n unstable area stays in Mercier unstable region and the mode structure is similar to an internal mode (Fig.4 (b)). In case of $\iota_{(1)}/2\pi<1.0$, on the other hand, the unstable region exists even in Mercier stable region and the mode structure clearly shows the characteristics of an external mode (Fig.4 (c)). In this case, the amplitude of m/n =1/1 becomes larger than that of m/n=2/1. At the region with Mercier unstable and $\iota_{(1)}/2\pi<1.0$, the mode structure has the comparable amplitude of ξ_s of m/n =2/1 and 1/1 (Fig.4 (d)). These show that the structure of an external mode, which has the meaningful m/n =1/1 mode, appears in the region of $\iota_{(1)}/2\pi<1.0$ regardless of the value of D_I under the free boundary condition.

4.Conclusion

The low-n analysis for n=1 mode family is performed on the LHD plasma. The analysis with **TERPSICHORE** predicted that the external mode with m/n=1/1 would be unstable in the high beta region. The external mode structure, which has the m/n=1/1 mode, appears under the free boundary and $\iota_{(1)}/2\pi<1.0$. The perfectly conducting wall of $a_{\mathrm{wall}}<1.08$ stabilizes the external mode. The real LHD wall is equivalent to the $a_{\mathrm{wall}}=3.0$, which is almost free boundary condition. The region where external mode appears lies under the condition of the free boundary and $\iota_{(1)}/2\pi<1.0$, even in Mercier stable and/or low-β region. If the condition with no rational surface of $\iota/2\pi=1.0$ inside the plasma can be produced, the external mode could be studied experimentally.

References

[1] S. Sakakibara, H. Yamada, K.Y. Watanabe, Y. Narushima et al., *Plasma Phys. Control. Fusion* **44** No 5A (2002) A217

[2] W. A. Cooper, *Plasma Phys. Control. Fusion* **34**, (1992) 1011

[3] S. P. Hirshman, W. I. Van Rij, and P. Merkel, *Comput. Rhys. Commun.* **43**, (1986) 143

[4] J. L. Johnson, J. M. Greene, *Plasma Phys.*, **9**, (1996) 611

[5] K. Nishimura, K. Ida, K. Kawahata, and K. Kozo et al., *Journal of Plasma and Fusion Research SERIES*, **4**, (2001) 106

Phase Contrast Imaging of Mode-Converted Ion Cyclotron Waves in the Alcator C-Mod tokamak

E. Nelson-Melby[†], M. Porkolab, A. Mazurenko, Y. Lin, P.T. Bonoli, and S.J. Wukitch

Plasma Science and Fusion Center, Massachusetts Institute of Technology, Cambridge, Massachusetts

Introduction

The Alcator C-Mod tokamak uses electromagnetic waves in the ion cyclotron range of frequencies (ICRF) for auxiliary plasma heating. When there is more than one ion species present in the plasma, an ion-ion hybrid resonance layer can exist. If the long wavelength fast wave (FW) launched from the low-field side encounters this resonance, it can mode-convert into a short wavelength wave which can subsequently heat electrons. This type of situation has been studied experimentally [1–3] and theoretically [4–7]. The short wavelength wave excited in the hot core of the plasma in this manner has usually been identified as an ion Bernstein wave (IBW). However, very recently it was realized that the dominant mode conversion process for the FW in Alcator C-Mod (and in any hot tokamak with significant plasma current) is into an electromagnetic ion cyclotron wave (ICW) as predicted by Perkins in 1977 [8]. This wave propagates to the low-field side along a magnetic flux surface, and damps by electron Landau damping before reaching the cyclotron resonance layer.

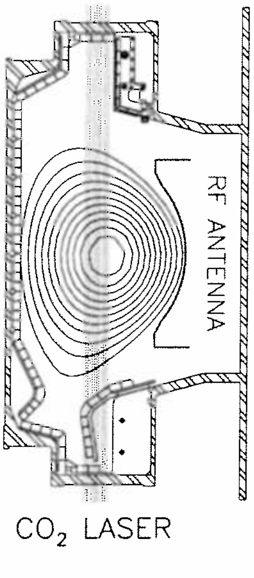

Figure 1: The Alcator C-Mod tokamak, with PCI laser path shown.

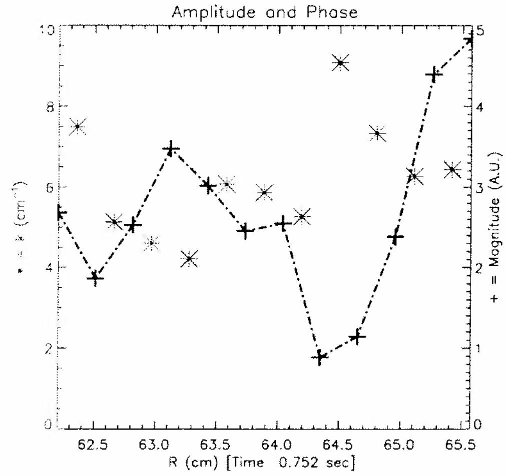

Figure 2: Amplitude (+) and Phase (*) (represented by an effective k number) for the Fourier-transformed PCI signal.

Experimental Observations

Phase Contrast Imaging (PCI) [9], combined with an optical heterodyne technique [10], has been used to detect electron density fluctuations at the launched RF frequency of 80 MHz. Figure 1 is a cross-section of the Alcator C-Mod tokamak (major radius 67 cm, minor radius

22 cm) showing the path of the PCI laser through the plasma, and the position of the RF antenna. Line integrated signal levels as small as 1×10^{15} m^{-2} (with a steady-state electron density of $2 - 4 \times 10^{20}$ m^{-3}) can be distinguished from the background noise. Figure 2 shows measurements near the core of the plasma during a discharge with a mode conversion layer present in the plasma. The plasma consisted of H, D and ^{3}He in a background toroidal field of 5.8 Tesla and plasma current of 800 kA. The plasma density was 2×10^{20} m^{-3} and the temperature was 1.2 keV. The spatial structure shows peaks and troughs in amplitude across the PCI laser beam, with 1-2 cm separating the peaks. From the phase of adjacent PCI channels, and assuming a plane wave with a single wavevector passing from one channel to the next, an effective wavenumber k can also be deduced. This is shown in Fig. 2 by the asterisks (*). Note the major radial wavenumbers are all positive, indicating that the phase velocity of this wave is towards the antenna. The magnitude of the wavenumbers thus measured are between those of the FW and typically expected IBW wavenumbers. This is consistent with ICW wavenumbers [8].

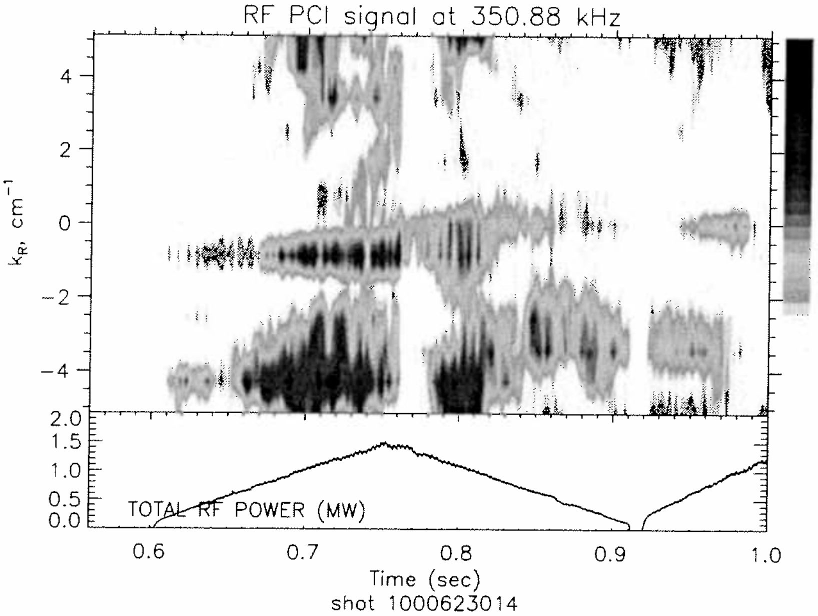

Figure 3: Simultaneous observation of FW and ICW in the k spectrum.

Figure 3 shows the wavenumber spectrum and RF power as a function of time for a plasma discharge where both the FW and mode-converted ICW were observed in the same view. The FW appears at $k \simeq -1$ cm^{-1}. The ICW appears as the larger spread of wavenumbers around -4 cm^{-1}. For this measurement, the laser beam was expanded to a greater width than that used for Fig. 2, thus the large positive wavenumbers usually observed are aliased and appear mostly as negative wavenumbers of approximately -4 cm^{-1}. After detailed analysis of the ion species concentrations [11], it was determined that in all these experiments, the ion-ion hybrid layer was several centimeters to the high-field side of the PCI viewing range. Thus the PCI is detecting the FW travelling away from the antenna (negative k number), and also the ICW travelling back towards the antenna and away from the mode-conversion region (positive k number). Thus the ICW phase and group velocities are in the same direction. This is contrary to what would be expected for an IBW, which is a backward wave. An IBW travelling away from the mode-conversion region towards the antenna would have a negative phase velocity (negative k number).

Numerical Modelling of the Electromagnetic Ion Cyclotron Wave

The full-wave ICRF code TORIC [5] was used to simulate the expected electron density fluctuation pattern in the plasma. The parallel electric field component $E_{||}$ was found to contribute most to the electron density fluctuation, and the ICW was particularly strong in $E_{||}$. An IBW did appear in some simulations to the high-field side of the mode conversion layer, but with much smaller amplitude than the ICW.

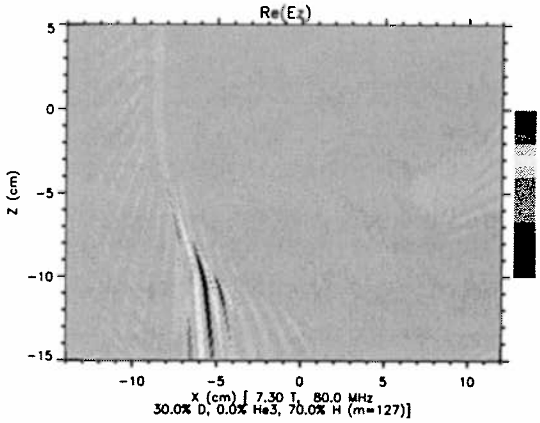

Figure 4: $E_{||}$ for $I_p = 400$ kA

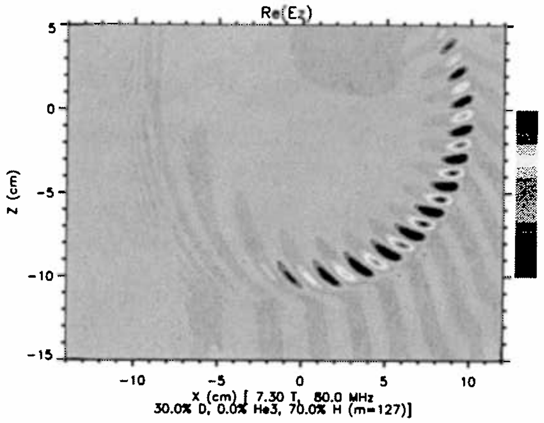

Figure 5: $E_{||}$ for $I_p = 1600$ kA

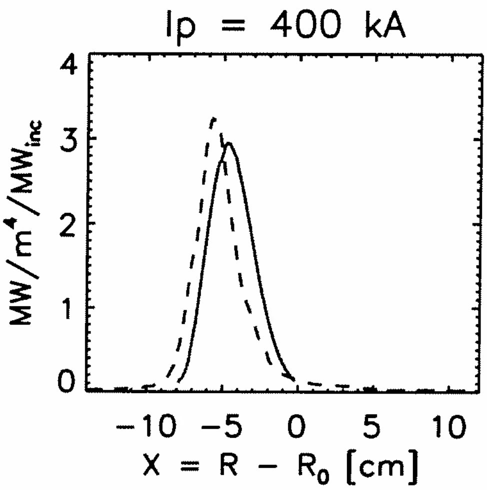

Figure 6: Power deposition profile for I_p 400 kA (MW/m^3 per m per MW incident).

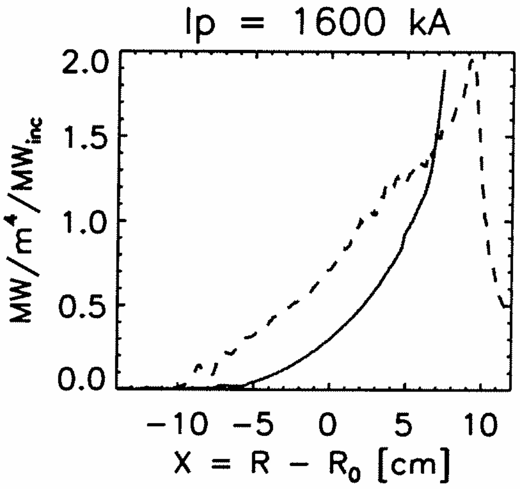

Figure 7: Power deposition profile for I_p 1600 kA (MW/m^3 per m per MW incident).

Figures 4 and 5 are the results of TORIC simulations of D-H plasmas (30% deuterium, 70%

hydrogen, 7.3 Tesla, 2.4×10^{20} m^{-3}, 1.5 keV) where the electromagnetic ICW also appears to the low-field side of the ion-ion hybrid layer. The real part of the parallel electric field near the center of the plasma is shown for toroidal mode number 10 (TORIC solves for the RF electric field by decomposing into toroidal and poloidal mode numbers — Figs. 4 and 5 are the results of combining 127 poloidal mode numbers). Note that the ICW propagates much farther at higher current (the amplitude is also larger). Perkins noted that the mode-converted ICW required the presence of a poloidal magnetic field. This has been verified by simulations with very low plasma current, in which there was hardly any ICW excited. Figures 6 and 7 show the power deposition profiles for the ICW. The dashed lines are those predicted from TORIC (power damped to electrons), and the solid lines are from integrating the imaginary part of the perpendicular wavenumber as obtained from solving the full electromagnetic hot plasma dispersion relation for fixed frequency, but with complex $k_\perp$ and $k_\parallel$, the two being related by the (approximate) relation

$$k_\parallel = \frac{n_\phi}{R}\frac{B_\phi}{B} + k_\perp \frac{B_\theta}{B}, \tag{1}$$

where B_ϕ is the toroidal and B_θ the poloidal magnetic field components (B is the total magnetic field), R is the major radius, and n_ϕ is the toroidal mode number.

Conclusions

The mode conversion of fast waves into electromagnetic ion cyclotron waves in multiple ion species plasmas predicted by Perkins 25 years ago has been observed and identified for the first time by the PCI diagnostic in the Alcator C-Mod tokamak. The strong magnetic shear off the midplane in tokamak geometry is responsible for this mode conversion, instead of conversion into the IBW. The full-wave ICRF code TORIC has been used to study these waves and the predicted electron density fluctuation pattern, and compares favorably with the PCI measurements. This FW to ICW mode conversion process should also play a role in future D-T plasmas with near equal mixtures of deuterium and tritium, if ICRF waves are used as an auxiliary heating source. These results indicate that localized electron heating along a flux surface should be possible, which could lead to current drive and improved confinement.

Work Supported by D.o.E. Coop. Agreement DE-FC02-99ER54512.

†Present address: CRPP-EPFL / PPB013, CH-1015 Lausanne, Switzerland

References

[1] J. Jacquinot, B. D. McVey, and J. E. Scharer, Phys. Rev. Lett. **39**, 88 (1977).
[2] T. Group, A. Truc, and D. Gresillon, Nucl. Fusion **22**, 1577 (1982).
[3] P. Lee et al., Phys. Rev. Lett. **49**, 205 (1982).
[4] C. N. Lashmore-Davies, V. Fuchs, A. K. Ram, and A. Bers, Phys. Plasmas **4**, 2031 (1997).
[5] M. Brambilla, Plasma Phys. Contr. Fusion **41**, 1 (1999).
[6] E. F. Jaeger et al., Phys. Plasmas **8**, 1573 (2001).
[7] A. Jaun, T. Hellsten, and S. C. Chiu, Nucl. Fusion **38**, 153 (1998).
[8] F. W. Perkins, Nucl. Fusion **17**, 1197 (1977).
[9] H. Weisen, Rev. Sci. Instrum. **59**, 1544 (1988).
[10] A. Mazurenko, PhD thesis, Massachusetts Institute of Technology, 2001.
[11] E. Nelson-Melby, PhD thesis, Massachusetts Institute of Technology, 2001.

Optimisation of the Current Profile with far off-axis ECH Power Deposition in high Elongation TCV Plasmas

A. Pochelon, Y. Camenen, F. Hofmann, S. Alberti, C. Angioni, T.P. Goodman,
M.A. Henderson, P. Nikkola, L. Porte, O. Sauter, A. Scarabosio

Centre de Recherche en Physique des Plasmas
Association EURATOM-Confédération Suisse
Ecole Polytechnique Fédérale de Lausanne
1015 Lausanne, Switzerland

Introduction: Plasma shaping is a means to improve tokamak performance. In order to test the β-limit predicted by ideal MHD for highly elongated plasmas, one has to achieve discharges at a normalised plasma current $I_N=I_p/aB\sim2MA/mT$. Highly elongated discharges are, however, vertically unstable and can only be stabilised by providing sufficient current density close to the plasma edge. In ohmic discharges, this is achieved operating at a low safety factor q_{edge}. In TCV, ohmic plasmas with an elongation $2.2<\kappa<2.8$ have been stabilised at high $I_N\sim2.8$-3.5MA/mT [1]. In order to extend the range of equilibria to lower I_N, where ohmic discharges are no longer stable, current profile broadening by a non-ohmic method is required. Far off-axis 2nd harmonic X-mode ECH (X2) has been applied in TCV [2,3] allowing the creation of highly elongated discharges ($\kappa\sim2.48$) at low current and high safety factor ($I_N\sim1.05$MA/mT, $q_{edge}\sim10$). Increasing the current towards $I_N\sim2$ requires more X2 power to broaden the current profile, stressing the needs of optimising the efficiency of this method. This paper presents parametric dependencies of far off-axis ECH current profile broadening and initial tests of 3rd harmonic central heating to increase the plasma β.

ECH system: TCV is capable of delivering 4.5MW ECH power for 2s pulse length: 3MW at the 2nd harmonic and 1.5MW at the 3rd harmonic (X3). The X2 system is composed of six 500kW gyrotrons at 82.7GHz with six independent low field side (LFS) launchers (four upper lateral and two equatorial), steerable during the discharge. The X3 system is composed of three 500kW gyrotrons at 118GHz with one independent top launcher, also steerable during the discharge. The cut-off density of X2 and X3 waves is respectively 4.25 and 11.5 $10^{19}m^{-3}$.

ECH high elongation experiments: Typical time traces are shown in **Fig. 1**. Just before ECH turn on in the ohmic phase, the target plasma has an intermediate elongation ($\kappa\sim1.75$) and the pre-programmed quadrupole and hexapole fields are then kept constant throughout the ohmic and the EC heated phase. X2 power is deposited far off-axis ($\rho_{dep}=(V_{dep}/V_{max})^{1/2}>0.5$), using upper lateral launchers because their shorter beam path reduces refraction effects at high density. The local EC power deposition leads to a local increase of the temperature, which modifies the resistivity profile. The inductive current profile is consequently broadened and the plasma elongation κ increases. The κ ramp-up duration gives the order of magnitude of the current diffusion time.

Current profile analysis: Since the quadrupole and hexapole fields are kept constant during the discharge, a *plasma elongation* increase is necessarily due to a broadening of the current profile. The modification of the current profile is essentially due to the modification of the resistivity profile (ECCD and bootstrap current represent ~8% of the total plasma current), so that the *temperature profile* is also an indicator of the current profile in the asymptotic limit. The *internal inductance* l_i is computed by the equilibrium reconstruction code LIUQE using magnetic measurements [4]. It decreases when the elongation increases or when the current profile is broadened. For instance, if κ is increased from 1.75 to 2.4 without any change of the current profile, l_i decreases by 8%. To separate the direct plasma shape influence, we can define a normalised inductance $l_i^* \sim l_i\ (l^2/4\pi S)$, where S is the plasma cross section area, and l a parameter depending on the plasma cross section perimeter and on the poloidal magnetic field [5]. The proportionality constant is chosen to have $l_i^*=l_i$ at the beginning of the EC heating for a standard shot. We define Δl_i^* as the difference between l_i^* at the start of EC heating and the asymptotic value during the plateau period. The ECH deposition location and the plasma first-pass power absorption are computed with the ray tracing code TORAY-GA [6]. The experimental results are compared to the fixed boundary transport code PRETOR based on the RLW model [7,8].

Deposition location and power dependence: The standard parameters are I_p~300kA, n_{eo}~2.5 $10^{19}m^{-3}$ (to avoid strong refraction), P_{EC}~1MW, ρ_{dep}~0.7, fixed launchers with the same ρ_{dep} ($\Delta\rho=0$), no toroidal angle ($\varphi=0$). The explored parameter range is $0<P_{EC}<1.8$MW and $0.1<\rho_{dep}<0.8$ [5].

The influence of the deposition location on the current profile is shown in **Fig. 2**. The optimal EC power deposition location for broadening the current profile appears to be a rather narrow region, $0.55<\rho_{dep}<0.7$, both from experiment and transport simulation. With a deposition inside ρ~0.55, the current profile broadening effect is reduced and becomes even inverted for $\rho_{dep}<0.4$ (current profile peaking for the experiment and the PRETOR simulation). On the other hand, for $\rho_{dep}>0.75$, the deposited EC power is not well confined and the action on the current profile is reduced. The values of the internal inductance computed by LIUQE and the one computed by PRETOR are slightly different, which can be explained by the choice of the current profile functional in the LIUQE reconstruction, optimised for ohmic profiles.

The effect of the EC power launched is shown in **Fig 3**. More than 90% of the power launched is absorbed at the first pass. The current profile broadening effect increases first steeply with the total absorbed power before saturating above P_{abs}~0.45MW. The saturation is very pronounced on the total internal inductance variation Δl_i^* and is partly explained by the ρ_{dep} asymptotic value: for $P_{abs}>0.45$MW, the asymptotic ρ_{dep} reaches the low value of ρ_{dep}~0.51, where the scheme looses in efficiency, according to the result of **Fig. 2**. The saturation is less pronounced but still visible on the initial $-l_i^*$ ramp rate (not shown here) or for the PRETOR simulation, which are both obtained at constant, optimal ρ_{dep}.

The saturation with power found at constant ρ_{dep} both on the initial l_i^* ramp rate and in the PRETOR simulations suggests a non-linear increase thermal diffusivity χ_e with absorbed power. The χ_e profiles corresponding to the data of **Fig. 3** are shown in **Fig. 4**. χ_e is shown to increase with power just outside the deposition radius, corresponding to a global electron confinement time τ_{Ee} decrease of 6.5 to 3.5ms.

Overdense operation: In the search of optimising the efficiency of off-axis deposition to increase plasma elongation, operating at high density has been found to allow the highest elongations with the lowest X2 power for a given plasma current. The increase of elongation with density at constant injected power is shown in **Fig. 5a**. It has been regularly observed in the ohmic elongation experiments in TCV that l_i decreases with density. This is further observed with off-axis ECH and can be infered from the electron temperature profile: in

Fig. 5b, the $T_e^{3/2}$ profile is shown to be flattened on axis at high density, which results in a broadening of the current profile.

With off-axis heating at low current, 300kA, sawteeth are lost during the elongation ramp-up when q_o moves above unity, without noticeable mode activity. At high density, a burst of internal modes occurs at the q_o~1 crossing. At higher density, this mode activity persists during the full discharge. The mode activity is analysed with the help of the 64 channel multiwire proportional soft X-ray diagnostic [9], and reveals an m=1, 2, 3 mode structure inside the inversion radius, **Fig. 6**. The very flat spectrum measured, where the m=2 and 3 mode amplitude are respectively 70% and 20% of the m=1 amplitude, is a typical signature of a flat current profile [10].

Initial experiments with central X3 deposition: The use of far off-axis X2 ECH in high density discharges has allowed increasing substantially the range of elongated equilibria at intermediate currents, as shown in **Fig. 7**. High density equilibria, that are overdense in the core, provide interesting target plasmas for X3 heating. An example of an initial experiment of X3 central power deposition [11] is shown in **Fig. 8**. The plasma has an elongation of 2.36 and is centrally overdense to X2. The Thomson electron temperature is increased by 1keV with 0.5MW of X3 heating, reaching β_T~1%. The drop in κ and the increase in l_i is partly due to the central heating, which peaks the current profile on a typical current diffusion time scale, making the mode activity of Fig. 6 dissappear in some 20ms.

Conclusions: With the help of far off-axis X2 power deposition used to broaden the current profile and to elongate the plasma, high elongation centrally overdense discharges at intermediate I_N have been created to study their confinement properties with X3 central heating.

This work was partially supported by the Swiss National Science Foundation.

References

[1] F. Hofmann, et al., Phys. Rev. Lett. **81**, (1998) 2918.
[2] A. Pochelon, et al., Nucl. Fusion **41** (2001) 1663.
[3] F. Hofmann, et al., Plasma Physics and Controlled Fusion, **43** (2001) A161.
[4] F. Hofmann, et al., EPS Conf. on Plasma Phys. and Contt. Fus., Vol. **19**, Part II (1995) 100.
[5] Y. Camenen et al., Proc. of EC-12, Aix-en-Provence, France, May 2002.
[6] K. Matsuda, IEEE Trans. Plasma Sci. **17** (1989) 6.
[7] D. Boucher et al., IAEA TCM Adv. in Simul. & Model. Thermonucl. Plasmas, Montreal (1993)142.
[8] C. Angioni, et al., Theory of Fus. Plasmas, Varenna 2000, ISSP-19 (Ed. Comp, Bologna, 2001) 73.
[9] A. Sushkov et al., this conference, P4.118.
[10] P-A. Duperrex et al., Nucl. Fusion **32** (1992) 1161.
[11] S. Alberti et al., this conference, P2.073.

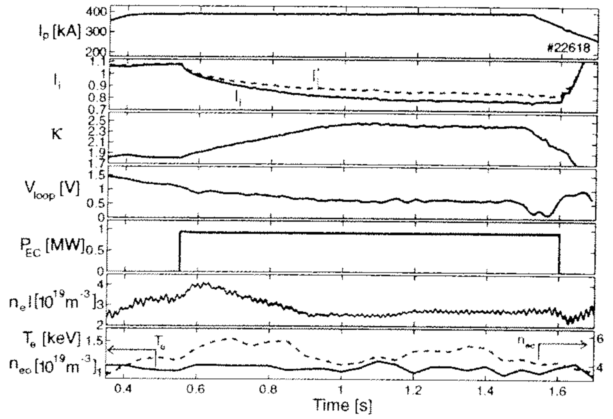

Fig. 1 Decrease of l_i and increase of κ with far off-axis ECH applied in the current plateau.

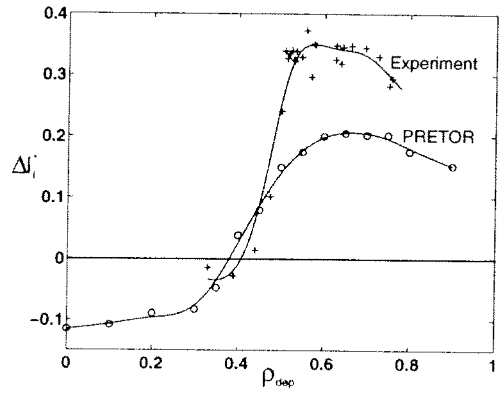

Fig. 2 Current profile change for different radial deposition location ρ_{dep}. I_p=300kA, P_{EC}=1MW.

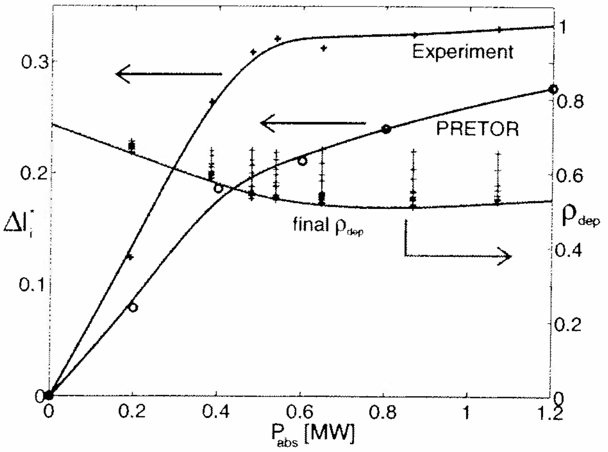

Fig. 3 Current profile change for different absorbed power, from experiment and from PRETOR. $\rho_{dep}=0.7$, $I_p=300kA$, $n_{eo}\sim2.5\ 10^{19}m^{-3}$.

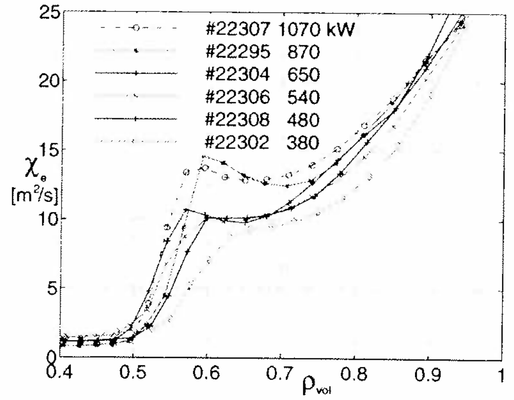

Fig. 4 Current diffusivity χ_e *for the power scan of fig. 3.*

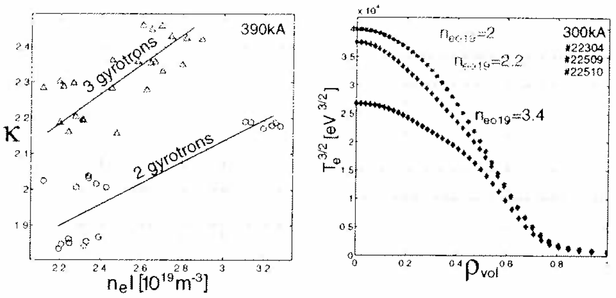

Fig. 5a, b High density operation:
a) κ improves with density at constant EC power, b) the resistivity deduced current profile is flattened and therefore broadened with density.

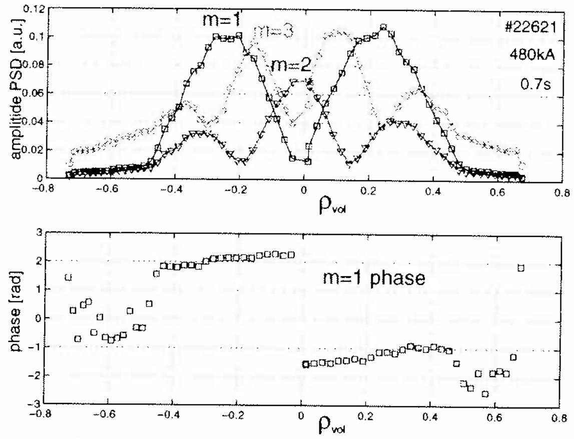

Fig. 6 m=1,2,3 mode activity inside inversion radius $\rho_{inv}=0.4$, from the 64 channel soft X-ray multiwire proportional chamber diagnostic.

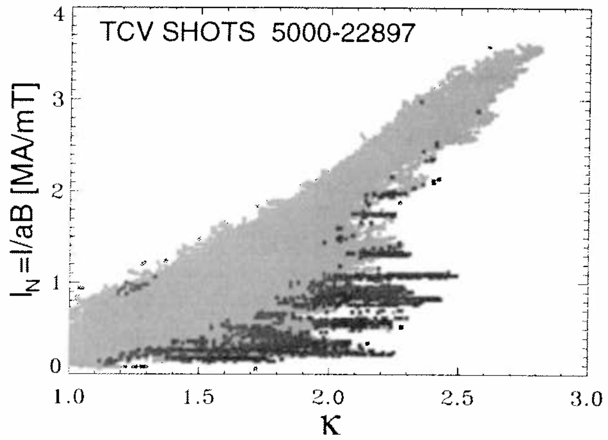

Fig. 7 Range of TCV operation in TCV: Ohmic discharges (green) and ECH (red). Off-axis ECH allowed reaching κ=2.48 at low I_N.

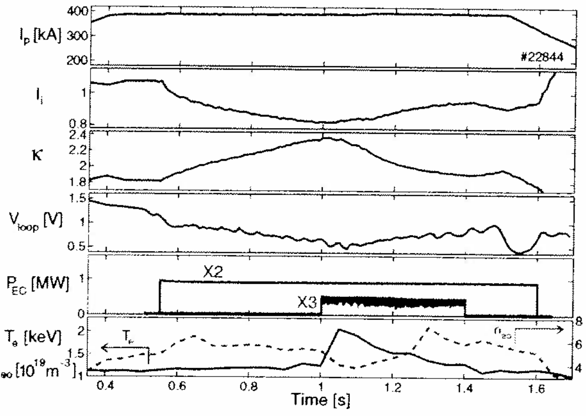

Fig. 8 X3 central heating (0.5MW) on a high density high elongation off-axis heated prepared target.

A Low–Frequency Electromagnetic Wave Propagation Code in 2D and 3D

P.Popovich, W.A.Cooper, L.Villard

Centre de Recherches en Physique des Plasmas,
Association EURATOM - Confédération Suisse, EPFL, 1015 Lausanne, Switzerland

The studies of the 3D plasma perturbations in the low-frequency domain (ICRF and shear Alfvén waves, both continuum part of the spectrum and discrete eigenmodes) have received considerable interest lately because of their potential importance for plasma heating, stability and current drive in stellarators [1, 2]. While analytical analysis of low-frequency global oscillations of plasma is still possible for relatively simple geometries, numerical solutions are required for a realistic fully 3D stellarator geometry with inhomogeneous plasma. We are developing a code LEMan for modeling low-frequency electromagnetic wave propagation in inhomogeneous 3D plasmas of a finite spatial extent, including the effects of absorption of the incident wave, reflection from the walls, etc. This requires the solution of the full wave equation. The equation is formulated in terms of the vector and scalar electromagnetic potentials $(\vec{A}, \phi)$:

$$\left\{ \begin{array}{rcl} \nabla^2 \vec{A} + k_0^2 \hat{\epsilon} \cdot \vec{A} + i k_0 \hat{\epsilon} \cdot \nabla \phi & = & -\dfrac{4\pi}{c} \vec{j}_{ext} \\ \nabla \cdot (\hat{\epsilon} \cdot \nabla \phi) - i k_0 \nabla \cdot (\hat{\epsilon} \cdot \vec{A}) & = & -4\pi \rho_{ext} \end{array} \right. \tag{1}$$

This choice of the formulation guarantees that, applying standard finite elements, the solution is free from the numerical pollution [3]. The underlying equilibrium is obtained numerically with the ideal MHD VMEC code [4], presuming a nested toroidal flux geometry. This equilibrium is then treated in the TERPSICHORE code [5]. TERPSICHORE recalculates all the equilibrium quantities (metric elements, magnetic field components) in the Boozer magnetic coordinate frame [6]. The wave equation (1) is formulated as a variational principle best suited for discretization with finite elements:

$$\left\{ \begin{array}{l} \int\limits_{\Omega} dV \left[-(\nabla \times \vec{F}) \cdot (\nabla \times \vec{A}) - (\nabla \cdot \vec{F})(\nabla \cdot \vec{A}) + k_0^2 \vec{F} \cdot (\hat{\epsilon} \cdot \vec{A}) + i k_0 \vec{F} \cdot (\hat{\epsilon} \cdot \nabla \phi) \right] \\ \qquad\qquad + \int\limits_{\delta\Omega} \vec{dS} \cdot \left[\vec{F} \times \nabla \times \vec{A} + \vec{F} (\nabla \cdot \vec{A}) \right] = -\dfrac{4\pi}{c} \int\limits_{\Omega} dV \vec{F} \cdot \vec{j}_{ext} \\ \int\limits_{\Omega} dV \left[\nabla G \cdot (\hat{\epsilon} \cdot \nabla \phi) - i k_0 \nabla G \cdot (\hat{\epsilon} \cdot \vec{A}) \right] + \int\limits_{\delta\Omega} \vec{dS} \cdot \left[i k_0 G \, \hat{\epsilon} \cdot \vec{A} - G \, \hat{\epsilon} \cdot \nabla \phi \right] \\ \qquad\qquad = -4\pi \int\limits_{\Omega} dV G \rho_{ext}, \end{array} \right.$$

where $(\vec{F}, G)$ are test functions, $k_0 = \omega / c$.

The integration over the whole volume of plasma and vacuum (pseudosurfaces) is implied. This approach simplifies the implementation of the vacuum region — numerically, the only difference between vacuum and plasma is the dielectric tensor $\hat{\epsilon}$. For the plasma-wave interaction description, the classical cold plasma model has been implemented. This model includes the effects of finite electron mass, thus the parallel component of the electric field. This allows for the modeling of the mode-conversion effects. The vector potential is written as a sum of a normal, binormal and parallel components, that, along with the scalar potential, are the actual unknowns of the equation. Such a choice of the unknowns largely simplifies the boundary conditions, that otherwise could have been very complicated in a realistic 3D stellarator configuration. Plasma perturbations are excited with an external antenna. The antenna is modeled numerically by specifying the volume density of external sources of current $\vec{j}_{ext}$ and charge ρ_{ext} in the vacuum or inside the plasma. Fourier decomposition in toroidal and poloidal angles is then applied, combined with finite elements in the radial direction. This approach may prove to be particularly efficient for the case of Alfvén waves, because the condition of the Alfvén resonance and mode conversion is satisfied on the magnetic surfaces [7] (at least in axisymmetric configurations), and the number of the Fourier modes needed to describe the solution in this case may be relatively small. Linear finite elements are sufficient for the discretisation of the cold plasma dielectric tensor because it does not include any differential operators. But linear elements may still be a cause of bad convergence near the magnetic axis. The analytical investigation of the equation has shown that certain Fourier components of the potentials have diverging derivatives on the axis. This deteriorates the convergence of the scheme, because integrals in the variational form containing these derivatives diverge logarithmically. This has partly been avoided by replacing the first finite element with a modified one that corresponds to the asymptotics of the solution. This method has considerably improved the convergence. For example, the proper eigenfrequencies of vacuum cavity oscillations that converged linearly with the standard linear finite elements have close to quadratic convergence with the new modified elements.

The full wave equation with a given antenna excitation entirely defines the solution, which in our case is the set of perturbed vector and scalar potentials. All the other quantities such as EM fields and power fluxes are calculated from the potentials. These diagnostics can also be used for the self-consistency verification of the solution, namely to evaluate the energy conservation. The total power absorbed in the plasma between the magnetic axis and the magnetic flux surface labeled s should be equal to the inward power flux through this surface plus the power coupled in the antenna inside this surface:

$$P_{plasma}(s) = iS_{flux}(s) + P_{ant}(s)$$

The real part of this relation corresponds to the reactive power, and the imaginary part is the resistive power. The classical cold plasma dielectric tensor does not include resistivity, but we modeled it by introducing a small imaginary part in the frequency. A convergence study in a low aspect ratio ($R/a = 5$) 2D geometry has shown linear dependence of the maximum discrepancy in the powers (in the local power balance) on the mesh step. The global power balance has been much easier to satisfy in all the cases analysed.

An important test of the code in the geometry allowing an analytical solution has been an analysis of the oscillation spectrum of a cold plasma cylindrical plasma column. Different modes have been studied — global eigenmodes of the Alfvén wave, local Alfvén resonances (continuum), fast magnetosonic waves for several poloidal mode numbers. The structure of the modes obtained with the global code in the large aspect ratio limit agrees with the analytical solution, which is known for constant plasma density profile in the limit of zero electron mass and low frequency [8]. There is no analytical solution in the general case of arbitrary density profile with poloidal magnetic field, but the positions of resonant Alfvén surfaces can still be calculated, and they are in a good agreement with the LEMan code results.

A more complicated configuration has been used to test the code in the 2D geometry. A comparison of modes structure in a realistic tokamak configuration between the LEMan code and the LION code [9] has been made. The positions of the local Alfvén resonances are in a good agreement with the LION calculations, forming a gap in frequencies near the $q = 1.5$ surface, which is a very characteristic toroidal effect. The gap (fig 1.) is formed near the crossing of two cylindrical branches of the Alfvén continuum ($n = 1$, $m = -1, -2$) because the symmetry is broken in the poloidal direction, and different poloidal modes couple.

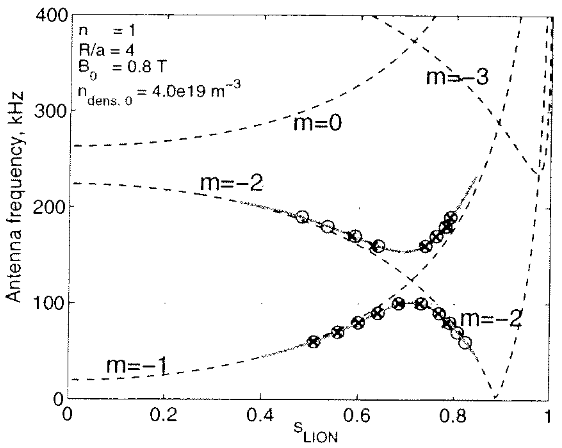

Figure 1. *The structure of the Alfvén continuum near the gap. Dotted lines — cylindrical modes, solid lines — approx. positions of the modes in toroidal geometry, circles — LION code calculations, crosses — LEMan results.*

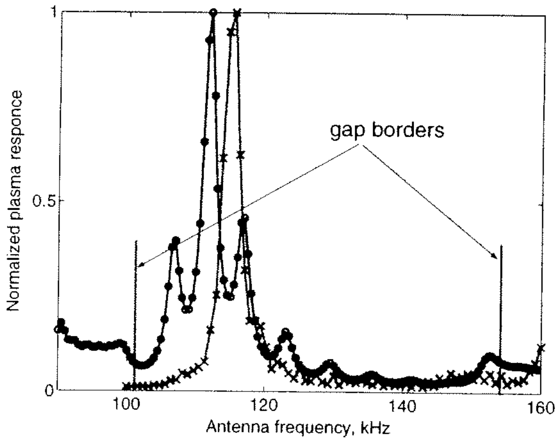

Figure 2. *Frequency scan in the gap region. Circles — LION code, crosses — LEMan results.*

The corresponding wavefields show similar behaviour in both codes, apart from the expected effects due to the difference in physical models (different dielectric tensors). The LION code uses an approximation of zero electron mass, hence the parallel component of the electric field vanishes and the fields become singular on the resonant surface (at zero resistivity). An inclusion of the finite electron mass in the tensor results in the appearance of short wavelength oscillations propagating from the Alfvén resonance — the mode conversion effect. A frequency scan in the region of the gap reveals the presence of a discrete mode. Both the LEMan code and LION show a peak in plasma response (total power coupled in the antenna) within less than 3% difference in frequency (fig. 2). The peak corresponds to the toroidicity induced Alfvén eigenmode (TAE). The discrepancy in frequency can be explained by slight difference in the equilibrium, produced by different codes (VMEC and CHEASE). This is a strong test of the toroidal structure of the new code, because the presence of the gap and the TAE are purely toroidal effects. A comparison of Alfvén resonant surface positions between LION and LEMan has been also made for a series of Soloviev equilibria. Using analytical equilibria allows us to avoid the numerical imprecisions of the equilibrium code. All these tests have shown a good one-to-one correspondence between the results.

Many Alfvén modes already exist in tokamak geometry. However, the "zoo" of the possible modes becomes much more diverse in the fully three dimensional configurations [10]. In 3D, the symmetry is broken both in poloidal and toroidal directions, so not only poloidal, but also toroidal modes can be coupled. Even with a relatively simple cold plasma dielectric model the structure of the wavefields in a realistic stellarator configuration is very hard to analyse because of the coupling between different poloidal and toroidal modes. In order to test the 3D structure of the code, at the same time keeping the spectrum of modes relatively simple, we have taken a mirror-like two period configuration with large aspect ratio ($R/a = 10^2$).

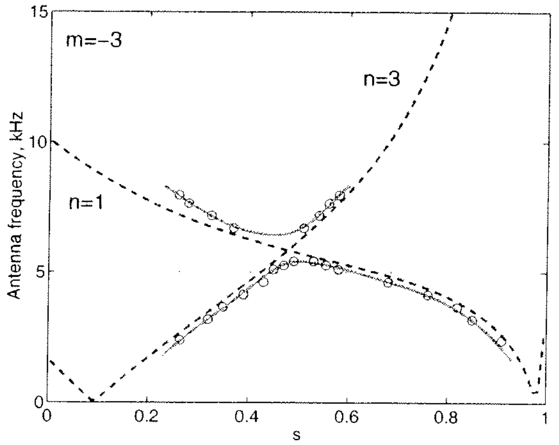

Figure 3. *The structure of the Alfvén continuum near the mirror-induced gap. Dotted lines — cylindrical modes, solid lines — approx. positions of the modes in the mirror geometry.*

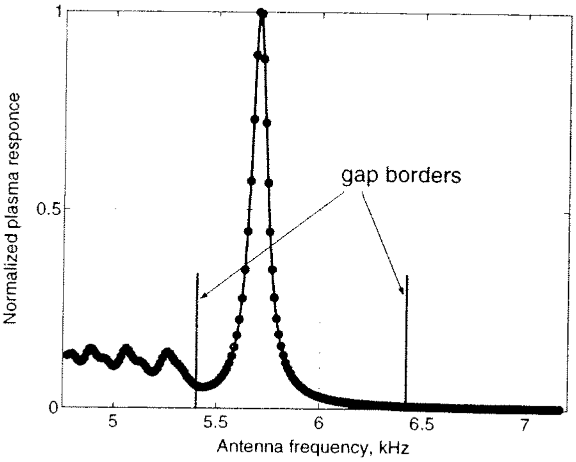

Figure 4. *Frequency scan in the gap region.*

Because of the periodicity, only modes with $n - n' = kN$ are coupled, where N is the number of periods and k — any integer. Analogously to the toroidal coupling in tokamak, the mirror-induced coupling of modes with different n results in the formation of a gap near the crossing of the cylindrical branches of the Alfvén continuum (fig 3). The plasma response as a function of antenna frequency has a peak inside the gap that can be explained by a presence of a mirror-induced Alfvén eigenmode (MAE) (fig 4).

References

[1] E. F. Jaeger, L. A. Berry, E. D'Azevedo, D. B. Batchelor, M. D. Carter, and K. F. White, Phys. of Plasma 9(5) (2002) 1873

[2] V.Vdovin, T.Watari, A.Fukuyama, Proc. ICPP 96 (Nagoya 1996),1070; NIFS-469 L.

[3] A. Jaun, K. Appert, J. Vaclavik, L. Villard, Comp. Phys. Comm. 92, 153 (1995)

[4] S.P. Hirshman, U. Schwenn and J. Nührenberg, J. Comput. Phys. 87, 396 (1989)

[5] D.V. Anderson, W.A. Cooper, R. Gruber, S. Merazzi and U. Schwenn, The International Journal of Supercomputer Applications 4, 34 (1990)

[6] A. Boozer, Phys. Fluids 23(5), 904 (1980)

[7] E. Tennfors, Plasma Phys. Contr. Fus. 28 (1986) 1483

[8] K. Appert, J. Vaclavik, L. Villard, Phys. Fluids 27 (2), 1984

[9] L. Villard, K. Appert, R. Gruber, J. Vaclavik, Comput. Phys. Reports 4 (1986) 95

[10] Ya. I. Kolesnichenko, V. V. Lutsenko Phys. of Plasmas 8(2), 491 (2001)

DINA simulations of TCV Electron Cyclotron Current Drive and Heating

D. Raju[1], V. N. Dokouka[2], J-Y. Favez[3], R. R. Khayrutdinov[2],
J. B. Lister[3] and V. E. Lukash[4]

[1]*Institute for Plasma Research, Bhat, Gandhinagar-382 428, Gujarat, India*
[2]*TRINITI, Troitsk, Russia*
[3]*Centre de Recherches en Physique des Plasmas, Association EURATOM-Confédération Suisse, EPFL, 1015 Lausanne, Switzerland.*
[4]*RRC Kurchatov Institute, Moscow, Russia*

1 Introduction

A complete knowledge of the operational behaviour of a tokamak discharge requires a reliable numerical simulation. A great effort has already been dedicated on several tokamaks to benchmarking the 1.5D axisymmetric, time-dependent tokamak plasma simulation code, DINA. Ohmically heated TCV plasma discharges have been validated by the DINA code and this validation exercises encouraged us to extend the simulation to a full discharge evolution of shaped TCV plasmas with electron cyclotron current drive and heating. DINA has been implemented in the user-friendly MATLAB and transparent environment for rapid execution of full discharge simulations. Simulation results are presented in this paper for discharges with fully non-inductive current drive, intense additional heating and a mixture of the two. Discharges with off-axis current drive and with substantial bootstrap current are also being simulated and preliminary results are presented here.

2 Description of SIMULINK model

Increased reliance on detailed models of the operational behaviour of a tokamak discharge requires a positive validation of the reliablity of any numerical code. To simulate a full plasma discharge evolution also requires correct simulation of the diagnostics, the feedback control and the power supplies.

The Tokamak á Configuration Variable (TCV) [1] is specially designed to explore the operational benefits of shaped plasmas over a wide range of plasma shapes. Consequently, in order to provide shaping flexibility, all the polidal shaping coils and Ohmic coils are controlled independently. To simulate the full shaped plasma evolution, we have implimented a user-friendly MATLAB SIMULINK model of the Hybrid Analogue-Digital TCV plasma control system [2] which performs a matrix multiplication onto the measured signals in order to create an estimator which is compared with 24 analogue reference signals. The resulting feedback error vector is integrated, differentiated and amplified to produce 3 signals per element, a total of 72 signals. These signals are then multiplied by a matrix to obtain 24 correction signals. The correction vector along with a vector consisting of the 18 PF coil currents is multiplied by a matrix to get 20 voltage signals which are added to a pre-programmed feedforward time-varying vector. The

SIMULINK control model of the full system was scrupulously tested on various TCV plasma discharges as well as on plasmaless pulses. The measured signals are fed to the inputs and the simulation is performed for the whole discharge duration. The simulated control system outputs of the model are then checked against the experiments. These open loop tests satisfied us prior to connecting any linear or nonlinear model in closed loop.

The DINA code [3] uses an inverse variable technique [4] to find the coordinates of the equilibrium magnetic surfaces and permits the flux coordinates to be determined very quickly and accurately. This code solves the circuit equations for the PF coil currents, vacuum vessel and passive structure eddy currents self-consistently with the evolving plasma equilibrium. Many additional features like Neutral beam and RF heating, pellet injection, runaway electrons, halo current models, current drive and bootstrap currents, α-particles heating and modules for breakdown and null field formations are available inside the code. Two sets of Ohmically heated TCV plasma discharges have been validated by DINA code in previous work on TCV [5, 6]. Firstly, the experimental response of limited and diverted plasmas to low amplitude PF voltage pulses, applied to all coils, were compared with DINA simulations. In a second exercise, the "free-fall" Vertical Displacement Events (VDEs) produced by disabling the vertical position feedback were simulated during the very large vertical movement possible in the highly elongated TCV vacuum vessel. These two validation exercises increased our confidence in the ability of DINA to simulate a full TCV discharge evolution, including the free-boundary evolution of the plasma shape itself.

DINA has now been implemented in MATLAB as a "MEX S-function" which provides a powerful mechanism for augmenting and extending SIMULINK's capability. This S-function block is connected to the TCV control block to make a closed loop (Fig. 1). Many additional inputs for this S-function block can be specified as MATLAB variables. At each fixed integration time step, this coupled system is advanced and the time evolution is progressively simulated.

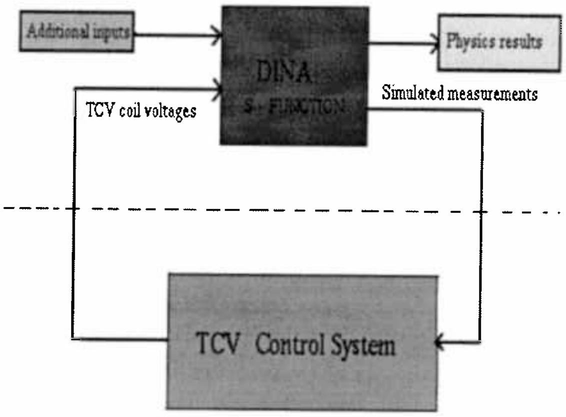

Figure 1: TCV-DINA model in SIMULINK

The first simulation will inevitably disagree. The coil voltage to plasma current transformer transfer function is a lossy integrator. Any inexactitude in the plasma inductance leads to an offset in the primary current. Any inexactitude in the plasma resistance leads to a roughly linear divergence between simulated and experimental primary transformer currents. Trying to tweak a time-dependent plasma resistance, either ad hoc or by tweaking the plasma transport is time-wasting and pointless, since it teaches us nothing. In [5] we detrended the PF currents, with justification. In the full pulse DINA simulations we have chosen a pragmatic approach. A low gain feedback loop is added to the DINA simulations allowing the divergences of the primary OH1, OH2 currents to be corrected by adjusting a linear plasma resistance multiplier, a "Z_{eff} modifier", onto neoclassical resistivity. This feedback has to be turned off as soon as the Electron Cyclotron Current Drive (ECCD) comes in.

A second obvious difficulty stems from the positive temperature dependence of current drive efficiency. This will also lead to diverging solutions in the simulation. Several other factors such as transport coefficients, width and location of heat deposition, location of an internal transport barrier, density profile must be adjusted properly to obtain a simulation reasonably close to the experiment. What is "reasonable" depends on the question which the simulation is trying to answer.

3 Discussion

We present one of the typical simulations of TCV discharge # 19692 which is an ECH assisted discharge with far off-axis deposition. During this experiment the vacuum shaping field is preprogrammed and the plasma current centroid is controlled by feedback (R,Z). This allows the plasma shape to evolve as the current profile is modified by the EC heating power, in which case the plasma boundary shape is a strong function of the evolving current profile. The results are shown in Fig. 2, in which we superimpose two simulation results. In the first one, the electron heat conductivity (T-11 scaling) is multiplied by two (red line) and in the second one, it is multiplied by one (green line). We see a significant improvement in the matching of the evolution of the plasma elongation.

There are some other sources of disagreement possible in the DINA simulations. Differences between DINA and LIUQE results for plasma parameters can be due to the different set of equilibrium parametrisation used by these codes. In the case of the LIUQE equilibrium reconstruction code, reconstruction of the plasma evolution is done by means of a set parameterised functions for plasma current and pressure profiles and a fitting algorithm calculates the most suitable plasma parameters. However in DINA, the simulation starts with a set of initial conditions and then the plasma profiles evolve in a totally free manner.

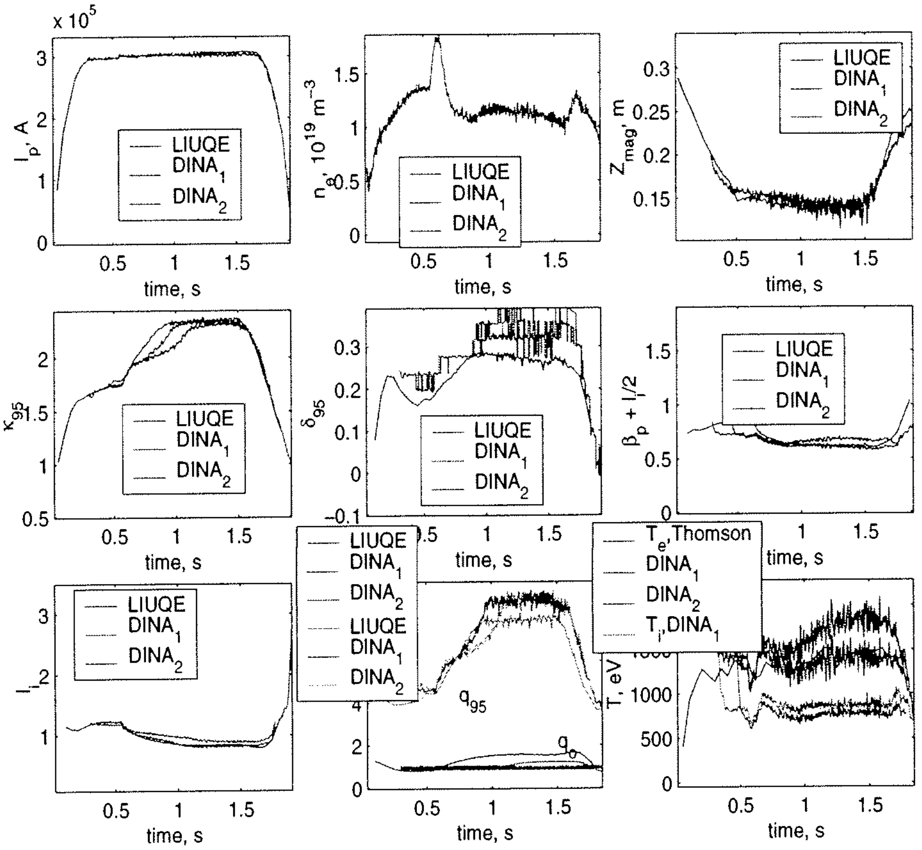

Figure 2: Results of ECH assisted TCV discharge # 19692 with two different simulations with electron heat conductivity multiplied by two (red line) and multiplied by one (green line).

Acknowledgements:

This work was partly supported by the Fonds National Suisse de la Recherche Scientifique.

References

[1] F. Hofmann, et al., Plasma Physics and Controlled Fusion, 36 (1994) B 277.

[2] J. B. Lister, et al., Fusion Technology, 32 (1997) 321.

[3] Khayrutdinov R.R., and Lukash V.E., J. Comp. Physics, 109 (1993) 193

[4] S. C. Jardin, N. Pomphery and J. DeLucia, J. Comp. Physics, 66 (1986) 481

[5] R.R. Khayrutdinov, J.B. Lister, V.E. Lukash, J.P. Wainwright, 43 (2001) 321.

[6] J- Y. Favez, R. R. Khayrutdinov, J. B. Lister and V. E. Lukash, Plasma Physics and Controlled Fusion, 44 (2002) 171.

Electron ITB In Fully Non-Inductive Reverse Shear Scenarios

O.Sauter, R. Behn, S. Coda, I. Condrea, T.P. Goodman, M.A. Henderson, P. Nikkola

Centre de Recherches en Physique des Plasmas
Association EURATOM-Confédération Suisse, EPFL, 1015 Lausanne, Switzerland

Introduction

In the last few years the powerful electron cyclotron heating (ECH) system on the tokamak à configuration variable (TCV) has been used to modify the current density and pressure profiles in order to obtain improved performances. The performance of a tokamak scenario can be improved in many different aspects. Some of these are the energy confinement time, the plasma density, the prospective for steady-state and therefore the bootstrap current fraction, the neutron rate, the ion temperature, the ratio Te/Ti or the degree of control of the current and pressure profiles. As only electrons are heated with auxiliary power on TCV, we are not considering properties related to the ion temperature, except that we can have very high T_e/T_i ratio. In previous experiments, improved confinement has been obtained with the addition of counter-current drive (cntr-CD) in the center. First due to sawteeth suppression [1] and then with discharges pre-heated with off-axis ECH deposition in order to be able to create flat and reverse shear in the center even with a large ohmic current contribution [2]. This latter scenario, leading to improved core electron confinement (ICEC), could be sustained in a quasi-stationary state and led to very high central electron temperature (T_e~10-15keV) and peaked pressure profiles. In this way high confinement, up to $H_{RLW}=\tau_{Ee}/\tau_{RLW}\sim3.5$, has been obtained at relatively high plasma current and density (Note taht in this paper we shall normalise the confinement time to the RLW scaling [3] as it usually predicts well confinement properties of dominantly electron heated discharges). These scenarios, however, are inherently non steady-state, similarly to the fast I_p ramp-up in conventional advanced scenarios, as they rely on a strong ohmic current contribution.

On the other hand, using the flexible EC system on TCV in order to spread the electron heating and current drive profiles, we have been able to sustain the full plasma current non-inductively, up to 210kA, for the whole gyrotron pulse length, 2s [4, 5]. It has even been shown that the discharge could be sustained twice as long by stacking the gyrotron pulses back to back, albeit at half power and plasma current [4]. In this way we have gained a lot of experience in long-pulse discharges, with a specific feedback loop to set $I_{ohmic}=0$, and on the ways to control the pressure and current profiles in order to avoid MHD modes in particular. As the characteristic current redistribution time, τ_{crt}, is typically of the order of 0.15-0.2s in TCV and the confinement time with strong electron heating of about 2ms, at densities around $10^{19}m^{-3}$, we have sustained discharges fully non-inductively for up to 2000 τ_{Ee} and 20 τ_{crt}.

In this paper we present first results on combining these two approaches in order to develop advanced scenarios with electron internal transport barrier (eITB) and truly steady-state regimes, that is with no residual ohmic current which could compensate transient loss of current drive efficiency for example.

The existence of an eITB in fully sustained scenarios

The typical experimental set-up is the following: starting from a stationary low current ohmic plasma, two or more gyrotrons are applied in co-CD off-axis to sustain the total plasma current without leading to peaked current profiles. The confinement improves and the bootstrap current builds up leading to non-monotonic current profiles. The analysis of the driven and bootstrap current in these scenarios and of the formation of a non-monotonic q profile is described in details in Ref. [6]. After 0.6-0.8s, an additional gyrotron is applied in the plasma core in order to probe, demonstrate and evaluate the eITB and the improved confinement in the core. Such a case is shown in Figs. 1 and 2, #21654, in which 2 gyrotrons (0.9MW) of type A, Fig. 1a, are coupled to the plasma at 0.4s and one additional ECH beam on-axis (type B) is applied at 1.2s. The plasma current decreases after 0.4s, Fig. 1b, since the ohmic current is turned off with a specific feedback which keeps a constant current in the ohmic transformer after 0.42s. As the off-axis current drive efficiency is smaller than in the core, the total plasma current evolves towards about 60-80kA depending primarily on the plasma density. At 1.2s the central temperature and H_{RLW} increase rapidly, on the energy confinement timescale, up to H_{RLW}~3.5 (Fig. 3, 21654, blue). Note that, at 1.2s, τ_{Ee} stays constant even though P_{EC} is increased by 50%, which demonstrates that the plasma core indeed has improved core confinement properties. As the n_e and T_e profiles evolve rapidly, it means that the eITB is already formed, as can be seen from the T_e profile (0.8-1.05s) in Fig. 2b, and the additional central heating simply enhances it.

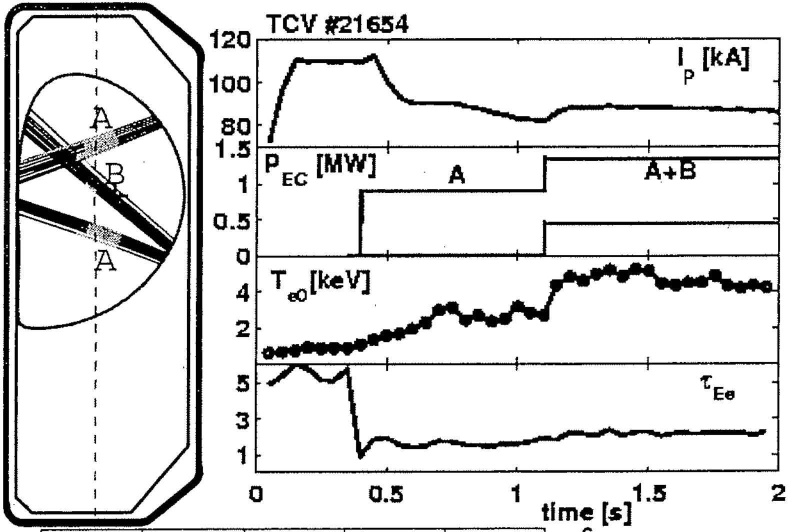

Fig. 1 (left): Two off-axis co-CD (A), then one on-axis ECH (B). Ohmic transformer constant from 0.42s. Note that τ_{Ee} stays constant albeit a 50% increase in input power.

Fig. 2 (bottom): Profiles before and after central heating. The eITB is evidenced with the additional ECH, but exists also before.

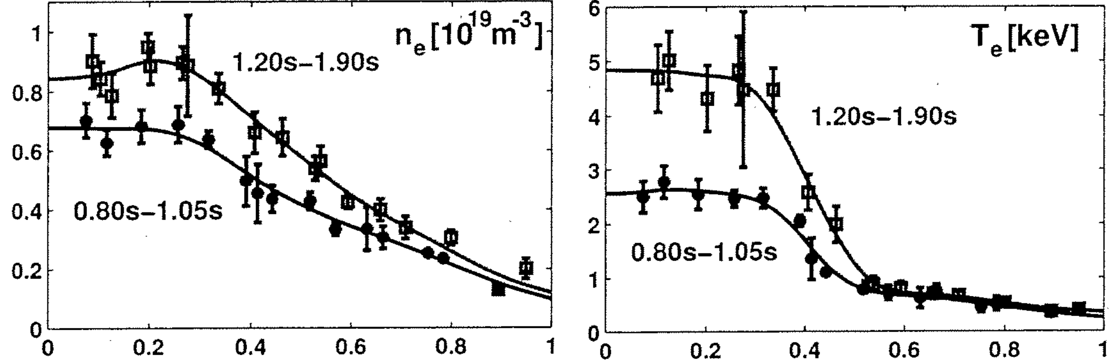

The EC power is applied on a stationary ohmic plasma, at 0.4s, as no I_p ramp is used to form the eITB. Therefore the barrier and the improved confinement region form at some point in time, or gradually, when the current profile evolves from a peaked (ohmic) to a non-monotonic shape. In order to test if there is a sharp bifurcation, for example at the moment when the q profile becomes reversed, we compare #21654 with the discharge #21649 in which the central beam is applied from the beginning at 0.4s. We see in Fig. 3 that the confinement starts at H_{RLW}~2.3, which corresponds to standard confinement with central heating and peaked current profile [4], and evolves slowly to the steady-state value, on the current redistribution timescale. Therefore it is indeed the change in current profile which is responsible for the improvement in the core confinement. As there is no momentum input and T_i is small, about 200eV, no effects of rotation shear are expected and the eITB can be formed solely thanks to the modification of the q profile.
In order to test this result further, we have added a small oblique angle to the central EC beam in order to have cntr-CD. Already with a toroidal angle of only φ=–5°, the performance is significantly increased (#21655, Fig. 3) up to H_{RLW}~4.5 and T_{e0}~6keV. With φ=-15° the confinement is even better and it leads to overly peaked profiles, which are MHD unstable, leading to a disruption 20ms after the last Thomson data point. Note that as the discharge is fully sustained by the EC beams and the bootstrap current, we can control both the current and pressure profiles. Therefore it is easy to stay just below the ideal MHD limit and sustain an advanced scenario with a strong and wide electron ITB in steady-state without any MHD activity.

Co- versus Cntr-CD in the center

The direct relation between the confinement properties and fine tuning of the q profile has been further tested by comparing two discharges with identical beam aimings, except the central beam has opposite φ angle (+4.2° and –4.2°). That is we compare a small cntr-CD with the equivalent small co-CD in the center and therefore the same doppler shift and deposition profile. The results are shown in Fig. 4. The core temperature and H_{RLW} are higher for the case with cntr-CD in the center (#21892) than for the case with co-CD (#21893). However this latter case still has improved confinement (H_{RLW}~2.8>2) and a clear eITB. Note also that the H_{RLW} factor obtained with central ECH (φ=0) lies in between these two cases, confirming the continuous confinement improvement observed in discharge #21649 when the current profile evolves from peaked to non-monotonic. Detailed analyses are underway to determine the q profile for these cases and see if both have reverse shear, as expected due to the significant bootstrap current contribution [6].

We have also studied the effect of aiming more or less off-axis with the co-CD beams. In this way less or more current is driven and the value of q_{min} in particular can be controlled [6]. We have obtained eITBs and improved confinement for very different scenarios, except when the current is too peaked. However detailed analyses are required to quantify the range of q_{min} values spanned during these experiments. In some cases, MHD modes appear and the barrier does not form.

High bootstrap fraction and eITB position

Using almost all the X2 power available, up to 5 gyrotrons (2.3MW), we have started to optimise the discharge #21655 to increase the bootstrap fraction. We have added one ECH beam in the core and one ECH off-axis, to avoid too peaked profiles. In addition we have considerably increased the density, privileging bootstrap current over ECCD. In this way we have obtained a steady-state scenario with $I_{BS}/I_p \sim 80\%$ and very good confinement properties, $H_{RLW} \sim 3.5$, fully sustained for $1000\tau_{Ee}$ and $8\tau_{crt}$ (Fig. 5). The barrier is so sharp we cannot resolve it fully with a 3-5cm resolution. Moreover we see that the barrier position does not move even though the reverse shear is due to the barrier itself, through the local maximum in the pressure gradient. Thus there is no problem of alignment between the bootstrap current and the improved confinement region. This is in fact not astonishing from the above results which show that the electron core confinement is controlled essentially by the q profile.

This work is supported in part by the Swiss National Science Foundation

[1] Z. A. Pietrzyk, *et al.*, Phys. Plasmas **7**, 2909 (2000).
[2] Z. A. Pietrzyk, *et al.*, Phys. Rev. Lett. **86**, 1530 (2001)
[3] P. H. Rebut et al, Proc. 12th IAEA conf., Nice 1988, IAEA, Vienna, 1989, Vol. 12, p.191
[4] O. Sauter et al, Phys. Rev. Lett. **84**, 3322 (2000)
[5] S. Coda et al, Plasma Phys. Controlled Fusion **42**, B311 (2000).
[6] T. P. Goodman et al, this conference, poster

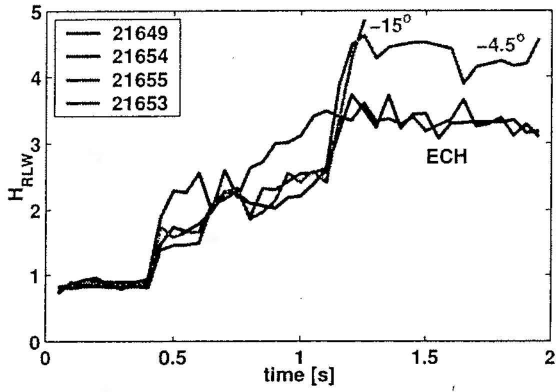

Fig. 3: Confinement factor time evolution with different angles for central beam and timings

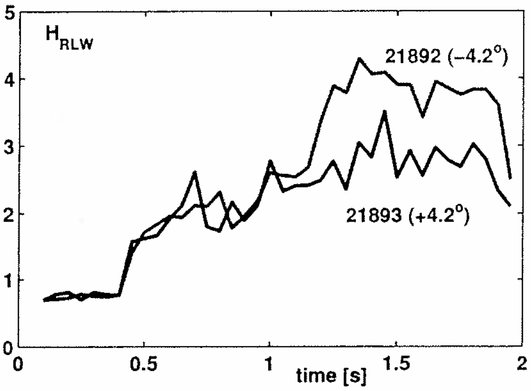

Fig. 4: Significant improvement with small central cntr-CD vs co-CD

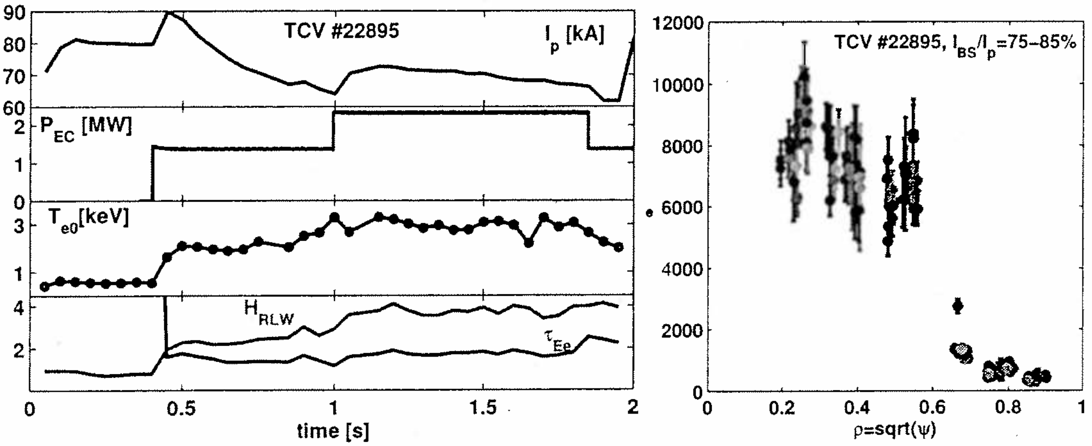

Fig. 5: Steady-state fully sustained eITB scenario with about 80% bootstrap current. The barrier position does not evolve during 1.2-1.8s, as seen from p_e profiles.

MHD Instabilities during Current Ramp Up as a Function of Plasma Shape in the TCV Tokamak

A. Scarabosio, A. Pochelon, Y. Martin

Centre de Recherches en Physique des Plasmas, Ecole Polytechnique Fédéral de Lausanne
Association EURATOM-Confédération Suisse, Lausanne, Switzerland.

The beneficial effect of plasma shaping during the initial current ramp up of L-mode ohmic discharges was noticed and regularly used early in TCV (*Tokamak à Configuration Variable)* operation as a way to reduce or suppress MHD activity or disruptions [1]. The details of the phenomena are studied in this paper.

The typical evolution of a disruptive discharge is shown in fig.1. The safety factor values q_{edge} and q_{95} are decreasing during the current rise while the plasma shape (κ =1.3, δ =0.2) is kept constant. An MHD mode of dominant toroidal number n=1 starts at t = 0.351 s, typically when the q=3 rational surface is entering the edge region of the last 5% of the flux as seen in fig.2. The mode rotates in the electron diamagnetic drift direction with a frequency of about 7 kHz. During this initial stage, the dominant poloidal number m is 3, therefore the instability is located on the q=3 rational flux surface at the plasma edge. When the mode has reached high amplitude, at 0.388 s, the dominant poloidal number m changes to 2. Figure 3 illustrates this transition that suggests a destabilizing interaction between the external kink mode [2] and a mode localized on q=2. The frequency and the amplitude of the mode are modulated by the sawtooth crashes visible in the central soft x-ray signal at the bottom of fig.1, probably caused by a magnetic coupling with the sawteeth precursor. At 0.372 s, the amplitude begins to grow linearly while the frequency slows down. This is due to the interaction of the mode with the resistive metallic walls [3] that drags the magnetic island created by the instability.

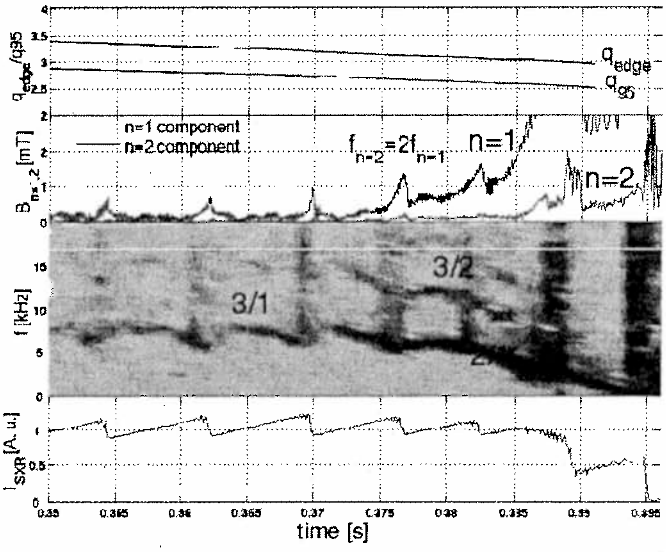

Fig.1. *Summary of the shot 21400*

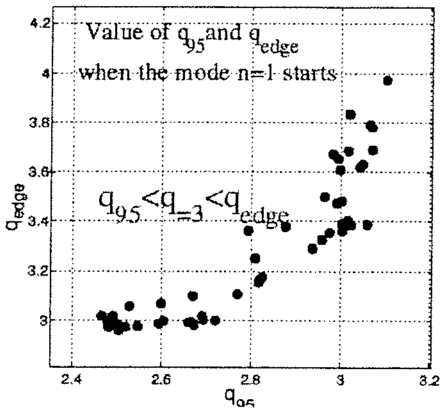

Fig. 2. *Value of q_{edge} and q_{95} at the triggering of the n=1 mode*

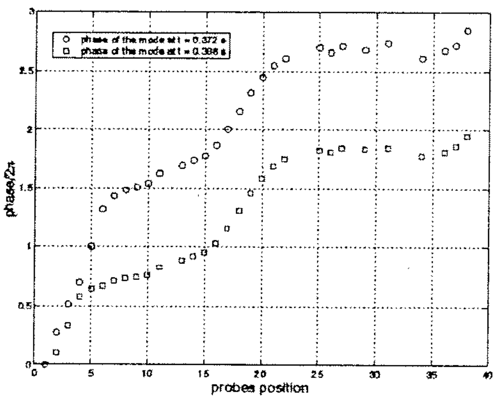

Fig. 3. *Phase variation of the magnetic signal from the Mirnov coils along a full turn of the poloidal direction at t=0.372 and t=0.388 s.*

At 0.374 s an m/n=3/2 mode is triggered with $f_{n=2} = 2f_{n=1}$ indicating coupling between the different resonant surfaces. The triggering of this mode can be explained by the nonlinear modification of the current profile due to the presence of the 2/1 and 1/1 islands [4].

The coherent poloidal magnetic structure is extracted from the Mirnov coils using the Singular Value Decomposition method. It has been compared with a model for the reconstruction of magnetic islands [5] before the disruption at 0.388 s. Figure 4 shows a good agreement between the experiment and the model using two islands on the q=2 and q=1.5 rational surfaces identifying therefore the instabilities as the tearing modes. It should be noted that no good agreement with the island model could be found for the dominant 3/1 mode probably due to the distortion from the external kink. Using the cylindrical approximation in [6] the estimated maximum island sizes reached before the disruption are of 7 and 5 cm for the 2/1 and 3/2 mode respectively. Although these values are unrealistic, considering that the resonant surfaces are only 3-4 cm apart, they point to the possibility of strong interactions between the islands or the vacuum vessel leading to the disruption. The presence of a central MHD mode can be inferred from the Fourier analysis of the line integrated soft x-ray

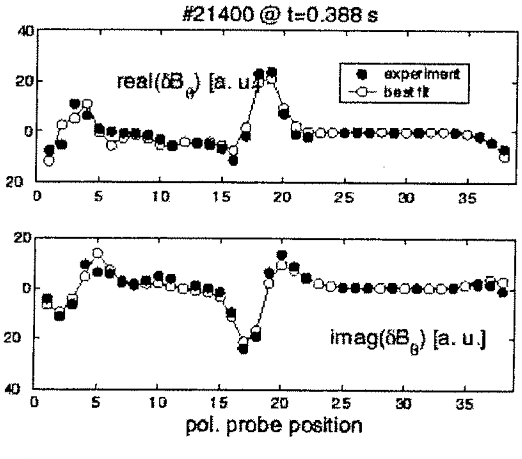

Fig.4. *Comparison of the poloidal mode structure from SVD analysis and the island model*

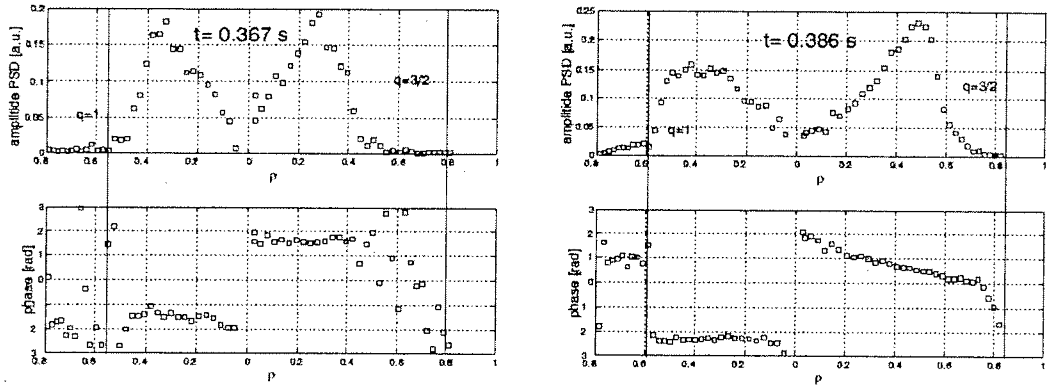

Fig. 5. *Left: amplitude and phase of the sawteeth precursor from SXR at t=0.367 s. Right: amplitude and phase of the central mode at t=0.386 s.*

emissivity shown in fig. 5, during the sawteeth precursor activity at t = 0.367 s and later at t = 0.386 s when the mode becomes continuous. Clearly the high and low field side oscillations are in opposite phase revealing a dominant m=1 poloidal mode number while the amplitude has two peaks inside the q=1 surface. The mode structure at 0.386 s, although similar to the sawtooth precursors is modified by the presence of the outer modes. It is interesting to note that the frequency of the oscillation always matches, inside the error bars, the frequency of the edge magnetic signal, as can be seen in fig. 6, suggesting a strong interaction between the 2/1, 3/2 and 1/1 islands that all rotate at the same speed.

Figure 7 schematizes the influence of shape on the MHD stability dividing the $\kappa - \delta$ space in disruptive and non-disruptive regions together with the mode numbers of the dominant instability. We firstly note the absence of disruptions for $\kappa > 1.4$, $\delta < -0.4$ and $\delta > 0.2$. A detailed analysis of the database reveals that for these ranges of parameters the 3/2 mode was never triggered and there was no continuous transition between the 3/1 and the 2/1 mode. The 2/1 mode which can be detected in very few shots, is rotating at low saturated amplitude with a different frequency or simply it is not present simultaneously with the 3/1 mode. Figure 8 summarizes cylindrical tearing stability index (Δ') calculations performed for several shots in the database using the experimental profiles. It shows the 2/1 tearing mode to be marginally stable for this scenario but no clear shape dependence of the Δ' is visible, leaving the shape stabilization unexplained. On the

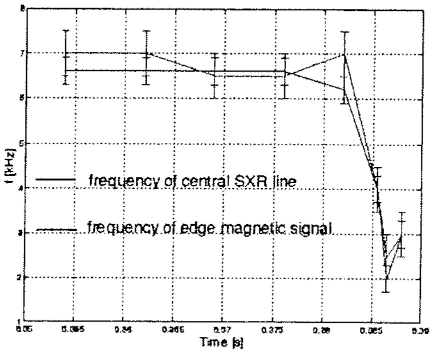

Fig 6. *Frequency of the edge magnetic (red) and central SXR (blue) perturbation*

other hand the current rise could lead to high edge current gradients generated by skin effect leading to unstable profiles. Although in these experiments the rate of the current rise is too low, 500-800 kA/s, for producing any appreciable effect on the current profile. This hypothesis has been confirmed using the transport code PRETOR [7] to simulate this non-stationary condition. These calculations point out the difficulties of explaining the evolution of this instability only in terms of current profile. Besides the data analysis shows the mode coupling between the tearing modes and the external kink to be a key element of the dynamic.

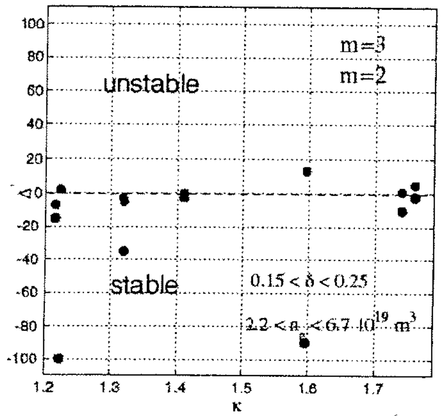

Fig. 8. *Cylindrical stability index* Δ' *for 2/1 (blue) and 3/1 (red) for different* κ

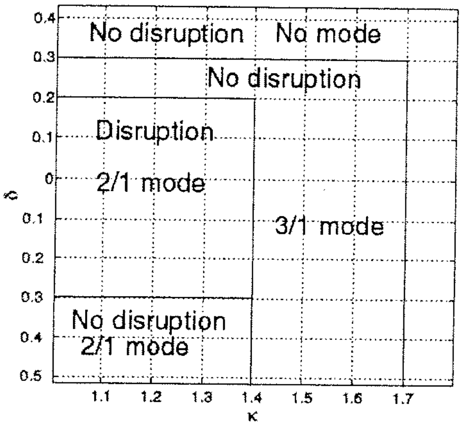

Fig. 7. *Disruption events in* $\kappa - \delta$ *plane and main mode*

This experimental conclusion is supported by the theoretical analysis presented in [8]. In this work the stability of the so called "fully reconnected" solution of the tearing dispersion relation is studied with a Δ' shooting code solving ideal MHD equations. Toroidal and shape coupling are retained within the code. When using circular cross section a strong destabilizing effect of the 2/1 tearing is clearly seen while q_{edge} approaches the value of 3 due to the toroidal coupling with the 3/1 external kink. If the plasma shaping parameters, κ or δ, are taken into account, other rational surfaces are coupled resulting in a complete stabilization of the mode even for modest κ or δ values, consistently with the observations presented here.

This work was partially supported by the Swiss National Science Foundation

Reference

[1] Y. R. Martin, Workshop on MHD and NTM's, March 15-16, 1999, Lausanne, Switzerland.
[2] Freidberg, Magnetohydrodynamics, MIT Press, Cambridge, Massachusetts,1989.
[3] M. F. F. Nave, J. A. Wesson, Nuclear Fusion, Vol 30, No. 12, 1990.
[4] B. V. Wadell et al., Physical Rev. Letter, Vol. 41, No. 21, 1978.
[5] H. Reimerdes,VI^{e} Congres, "Plasmas" de la SPF, 7-9 April 1999, Orleans, France.
[6] G. Bateman, MHD instabilities. MIT Press, Cambridge, Massachusetts,1978
[7] C. Angioni et al., Theory of Fusion Plasmas, Varenna, 2000, (ed. compositori, Bologna)
[8] R. Fitzpatrick, R. J. Hastie, T. J. Martin, Nuclear Fusion, Vol. 33, No. 10, 1993.

Investigation of Impurity Transport in TCV

E. Scavino, J. S. Bakos[1], B. P. Duval, H. Weisen

Centre de Recherches en Physique des Plasmas
Association EURATOM - Confédération Suisse, EPFL, 1015 Lausanne, Switzerland
[1] KFKI Research Institute for Particle and Nuclear Physics
Budapest, Hungary

1. Summary

The effect of plasma parameters on impurity transport has been systematically investigated by laser ablation of Si trace impurities into a wide range of TCV discharges. The presence of these impurities leads to a strong increase of soft X-ray emission, whose intensity shows a characteristic pulse-like shape following ablation, with rise times in the range of 6-8ms, reflecting the penetration time, followed by a longer, exponential decay phase, which is taken as a measure of the impurity lifetime in the plasma.

The experimental study of the lifetime of the impurities in ohmic L-mode plasmas has been carried out with scans of the triangularity, elongation, plasma current, line averaged electron density and toroidal magnetic field.

The parameters δ, I_P and n_e have little effect on the impurity lifetime, while B_T and κ show a marked and surprising effect as higher values lead to shorter lifetimes.

The 1-D code STRAHL[1-2] has been used to simulate the X-ray emission from the impurities. The simulations show that the impurity edge diffusivity is strongly influenced by discharge conditions, correlating inversely with residence time, while the central transport is dominated by sawtooth activity rather than diffusive transport. The pinch velocity is found to be positive, (towards the plasma edge), and fairly independent of the plasma conditions.

2. Signals from X-ray diagnostics

The array of 200 soft X-ray photodiodes[3] is used as the main diagnostics in order to track the impurity concentration and emissivity inside the plasma. Following ablation, a fast increase of the emissivity from the plasma is recorded, showing a characteristic pulse-like shape adding to the background. As the photodiodes are masked by thin Beryllium filters, the spectral sensitivity is negligible below 1keV, thus obliterating the UV emission from many low ionisation states of the impurity. In the case of Silicon, the photodiodes record only the soft X-ray line emissions from H-like and He-like ions, in addition to part of the bremsstrahlung and recombination radiation. The results of a simulation with STRAHL are shown in Fig. 1. The total *detected* X-ray power as well as its components are plotted in the case of a steady state flat profile of impurities, assuming corona equilibrium.

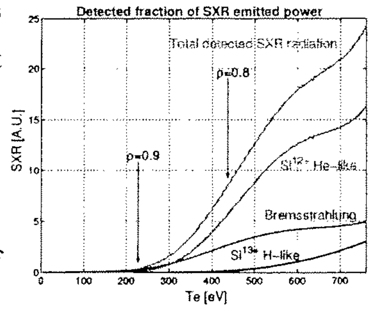

Fig.1. Detected soft X-ray emissivity vs electronic temperature in shot #19785. There is ***almost no contribution from plasma edge.***

3. Experimental results

The experimental study of the impurity behaviour and of their confinement time has been carried on with scans of the triangularity (δ = -0.16 to +0.65), elongation (κ = 1.6 to 2.3, with constant profile of q_{eng} and hence same sawtooth radii [4]), line averaged electron density ($n_e = 1.9*10^{19}m^{-3}$ to $6.5*10^{19}m^{-3}$), plasma current (I_P = 160KA to 520kA), and toroidal magnetic field (B_T = 0.9T to 1.5T). Targets were limited, ohmically heated plasmas in L-mode.

The different line-integrated signals along the soft X-ray system viewchords show many common features like the exponential decay time, which is taken as the confinement time -or "lifetime"- of the impurities, and a residual asymptotic signal due to a low level of recycling the TCV walls. For a wide range of many parameters, the impurity lifetime is found to be almost constant at a value of around 25ms. In particular, this is observed in the electron density scan (at least for limiter plasmas, Fig. 2a), in the plasma current scan for I_P > 250KA (Fig. 2b) and in the triangularity scan for $\delta > 0.16$ (Fig. 2c). For Ip or delta below the values indicated, the impurity lifetimes show a marked increase.

All these discharges were performed at the nominal toroidal magnetic field B_T = 1.5T and at κ = 1.6. A reduction of the magnetic field intensity produces an increase of the lifetime to almost the double, around 48ms, being all other parameters constant. This surprising effect, which seems to contradict the role of the magnetic field in the confinement of charged particles, is evident in Fig. 3a.

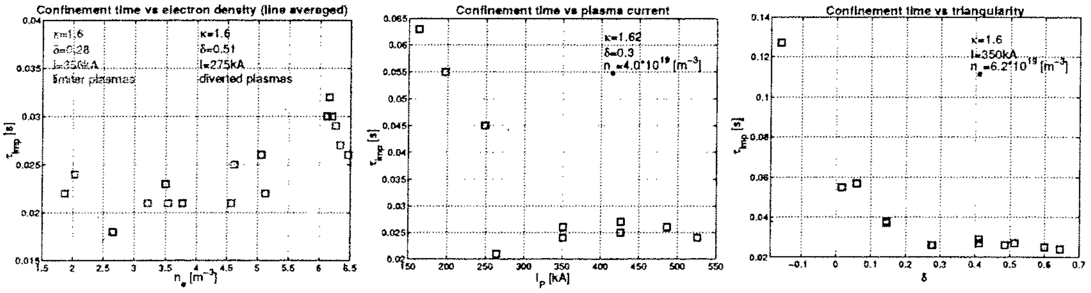

Fig. 2. (a) The electron density scan (line averaged) shows a slight difference in limiter and diverted plasmas. The lifetime is little sensitive to density, except for higher values ($n_e > 6*10^{19}m^{-3}$). (b,c) Values of the lifetime are flat up to marked thresholds in plasma current and triangularity.

The elongation scan was performed as well at B_T = 0.9T (Fig.3b). In agreement with the magnetic field scan, for low elongations the impurity lifetimes lie around 48ms, and are reduced to 20ms for increasing κ values at about 2.3. This behaviour is observed not only on the absolute value of the lifetime, but also in comparison with the electron energy confinement time, which in this scan is roughly constant. This factor-of-three decrease of the ratio τ_{imp}/τ_{Ee} is attractive for advanced, elongated tokamak reactor designs.

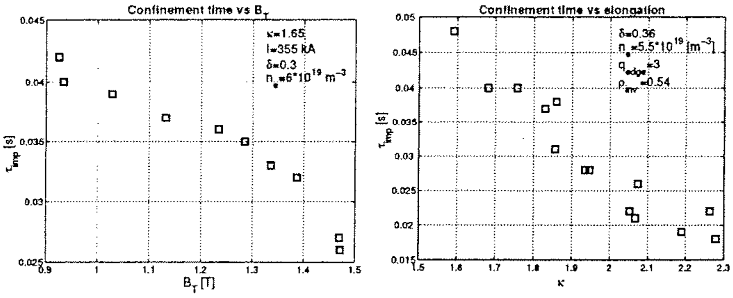

Fig. 3. (a) Non intuitive behaviour from the scan of the toroidal magnetic field. (b) The elongation scan has been performed at B_T = 0.9T and constant sawtooth inversion radius at ρ_{pol}=0.54.

4. Transport simulations

The 1-D simulation code STRAHL is used to calculate the time evolution of the impurity concentration after ablation and the corresponding X-ray signals as they would be measured by the photodiodes. Given the real plasma profiles of density and temperature as inputs, it is possible to evaluate the effects of different values of the transport parameters (diffusivity and pinch velocity profiles) as well as of the role of sawteeth in the transport of the impurities. It has been found that the lifetime, i.e. the exponential decay of the peaked signals, is determined mainly by the values of diffusivity and pinch velocity in the confinement region outside the inversion radius, while the central parameters and the sawteeth play negligible effects. The D and v profiles are marginally important provided the central and edge values are the same. In Fig. 4 some scans of D_0, D_{edge} and v_{edge} are shown, referring to shot #19785 in the triangularity scan. In order to reproduce the correct values of τ_{imp} and of the signal fwhm (the black rectangle in Fig.4, with an approximation of 2%), the bestfitting values - D_{edge}= 0.3 m^2/s and v_{edge}= +4.3m/s - are identified with an approximation of no more than 10%, beyond which it is not possible to find bestfitting (D,v) couples. The scan of D_0 in Fig.4 shows that it is not possible to determine the central diffusivity this way. It is a remarkable fact that the value of the edge pinch ve-

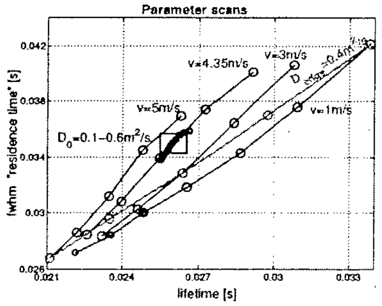

Fig. 4. Scans of the diffusivity and pinch velocity profiles in shot #19785. D_0 varies between 0.1m^2/s and 0.6m^2/s marginally affecting τ. The edge velocity is necessarily around 4m/s.

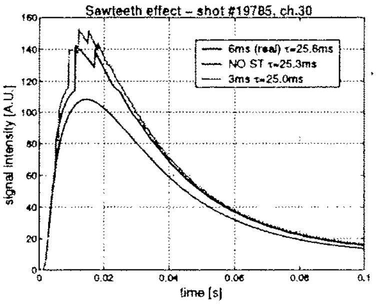

Fig. 5. Sawteeth frequency scan in simulation of shot #19785 affects the influx phase and the peak intensity of the signals.

locity is found to be positive, i.e. directed outward, and fairly independent of plasma conditions, at least in all situations in which τ lies around the plateau at 25ms. Anyway the reproduction of shot #19782 (δ=0.05, τ=57ms), which is almost identical in size to plasma #19785 (δ=0.27, τ=26ms), shows similar values for D_{edge}, which is still around 0.35m^2/s, while v_{edge} changes towards low negative (inward) values.

Fig. 5 shows how the removal and the change of sawteeth frequency affect the simulated signals. The effect on the impurity lifetimes is less than 10%, while they influence significantly the influx phase. Sawteeth act as a rapid transport device towards the plasma centre in the first phase after the ablated impurities arrive at the plasma edge, as their radial profile is still hollow. As a consequence, sawteeth transiently increase the inward flux and the concentration of impurities in the centre of the plasma, with respect to plasmas without sawteeth.

The determination of the central diffusivity D_0 can be attempted by reproducing the correct global risetime of the signal, for example from 20% to 80% of its peak value. Another possibility is the reproduction of the correct increase of the signal between two consecutive sawteeth during the influx phase. Both values are very sensitive to the duration of the source and to the delay of the first sawtooth following the start of the impurity influx. The spread of the particle source in time, which lasts about 4-5ms, makes the incertitude on the central diffusivity quite important. Anyway, the correct risetime of the chord viewing the centre of the plasmas seems to be approached with fairly high values of the central diffusivity D_0.

Acknowledgements

This work was partly supported by the Swiss National Science Foundation.

References

[1] K. Behringer, JET Report No. JET-R(87) 08, 1987

[2] R. Dux, IPP Garching, STRAHL User Manual, private communication (2000)

[3] I.Furno, PhD Thesis, Ecole Polytechnique Féderale de Lausanne, Switzerland (2001)

[4] H.Weisen et al, *Nucl. Fusion* **42** (2002) 136

Measurements of Helicon Wave Propagation and Ar II Emission*

J. Scharer,[1] B. White,[1] S. Tysk,[1] K. Akhtar,[1] A. Degeling,[2] G. Borg[3] and R. Boswell[3]
[1]University of Wisconsin, Madison, USA 53706, [2]Ecole Polytechnique Fédérale de Lausanne, Switzerland 1015, [3]Australian National University, Canberra, Australia 0200

Abstract

Wave magnetic field, optical and Langmuir probe measurements are carried out to examine fast and thermal electron contributions to plasma ionization in helicon plasma sources. Comparison of double half-turn and a double half-turn helix experiments are carried out. Spatio-temporal measurements of 443 nm peak emission show that the emission is modulated at the source frequency. The peak count phase of the modulation propagates along the plasma at a comparable speed as the local helicon wave phase velocity. Computer modeling is carried out to examine wave field effects on electron acceleration and ionization contributions arising from non-Maxwellian fast electrons.

I. Introduction

The central question in the physics of helicon sources is the cause of their highly efficient ionization and strong wave damping, which is not well explained by either collisional or Landau damping processes. A particular matter at issue is the existence, in some operating regimes, of a population of fast electrons comprising a non-Maxwellian component of the electron distribution, and the significance of its role in helicon ionization processes. In this paper we report on experiments performed on the WOMBAT[1,2] 20 cm diameter helicon experimental facility in which argon plasmas were created by means of a double half-turn antenna with densities in the range 10^{11}-$1\text{x}10^{12}/\text{cm}^3$. We also report on the 10 cm diameter UW helicon plasma wave facility that is excited by a double half turn helix. The optical measurements are of the Ar II line at 443 nm. The 443 nm emission upper state is 35 eV above the ground state.[1] Thus, electrons of fairly high energy are required to populate these states, and emission at 443 nm is indicative of their presence. The objective of this paper is to show that substantial non-Maxwellian contributions to the source ionization for this regime can exist. Experimental measurements of the wave B_z magnetic field components are compared with those predicted by the AntenaII[3] full wave boundary code for helicon modeling. The code also determines the wave electric fields consistent with the helicon wave hot plasma dielectric tensor. The corresponding wave E_z field produced by the code is incorporated in a non-linear one-dimensional code that illustrates the evolution of a non-

Maxwellian electron distribution and enhanced Argon ionization above what a Maxwellian distribution would produce under these experimental conditions.

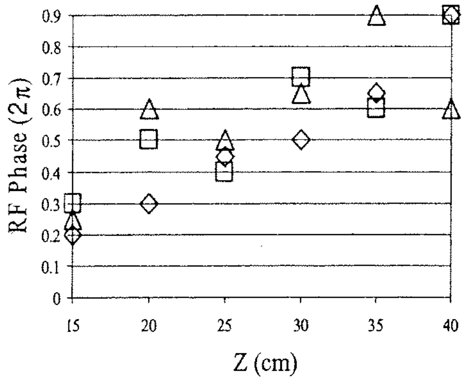

Figure 1: Optical Emission Peak

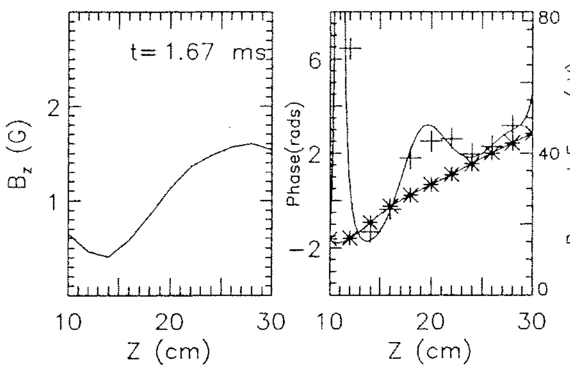

Figure 2: Wave Magnetic Field and Phase Resonant Electron Energy

Figure 1 shows the variation of the peak in the 443 nm emission relative to a reference rf phase vs. optical probe position for three runs of data taken for the above plasma density and wave phase velocity. A single emission peak is observed during a radiofrequency period, which indicates that it is caused by a traveling wave interaction and it is has a 25% modulation. The range of local electron resonant energies corresponding to the peak emission phase velocity corresponds to electron energies of 30-52 eV. This corresponds well to the local wave phase velocity over this range obtained from the B_z probe indicating that traveling wave-particle interactions play a significant role in fast electron creation for ionizing processes in the helicon source for this case.

II. Analysis of the wave field phase velocity and correlation with optical emission

We first analyze the measured wave magnetic field (B_z) local phase velocity and compare it to the observed velocity of the peak Ar II emission. An analysis of the local wave phase velocity and resonant electron energy, $E=mv_\phi^2/2$, was carried out for this case at t=1.67 ms from the start of the pulse where the density is constant as shown in Fig. 2.

The average B_z wave phase velocity for the traveling wave portion of the curve is 3.2×10^6 m/s corresponding to an average resonant electron energy of 29 eV over the range from z=12-30 cm. The corresponding local differential resonant electron energies indicated by crosses over the same range are from 18-46 eV. The stars indicate the local wave phase and the smooth curve connecting the crosses serves as a guide to the eye for this data. The electron resonant energies in this range are quite sufficient to excite the upper state for the 443 nm emission either from the ionic ground state or from the neutral state. The wave continues as a traveling wave until about z=35 cm where it changes to a standing wave character. This can be due to the substantial axial density gradient in this region as well as a decrease by 10% in the static magnetic field over this range.

Computer simulations of the wave-plasma interaction for the axial component of the wave electric field corresponding to the measured wave axial magnetic field phase were carried out. They show that enhanced ionization compared to a 3 eV Maxwellian occurs due to the wave field interaction with the electrons with a local maximum ionization rate close to where the measured density peaks at 13 cm downstream from the antenna. An increase in the distribution function for electrons in the energy range (20-45 eV) comparable to the wave phase resonant velocities and energies corresponding to the peak Ar II emission speed is predicted. This implies that a substantial contribution to ionization due to non-Maxwellian electrons under these helicon source conditions exists.

III. Current UW helicon plasma source research.

The University of Wisconsin helicon plasma facility uses a twisted double helix antenna and a 10 cm diameter Pyrex chamber. The length of the chamber is 1.6 meters. A broadband amplifier and a capacitive match box are used to couple up to 1 kW of 13.56 MHz RF power to argon plasma. Diagnostic tools include Langmuir, magnetic field and optical probes. Figure 3 shows an interesting phenomenon that occurs at the transition from the inductive mode to the helicon mode. The density is initially high and then decays as time

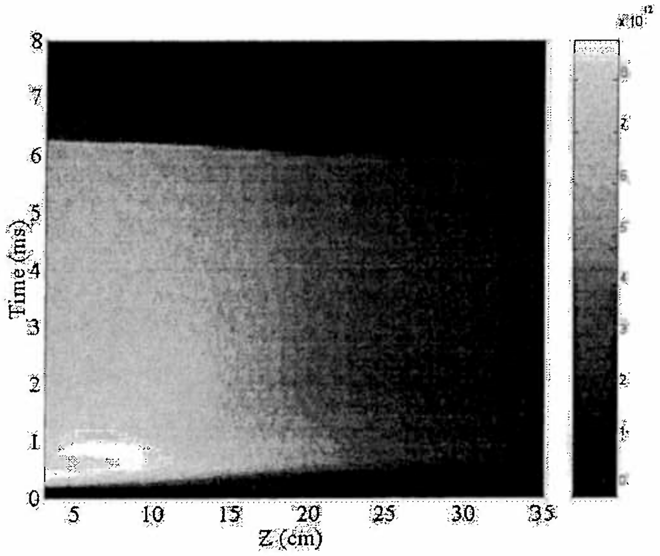

Figure 3: Density (cm^{-3}) assuming an electron temperature of 3 eV verses time during the pulse and axial position for the transition from inductive mode to helicon mode (800 Watts, 200 Gauss).

goes on. This is in contrast to the other cases where the density gradually increases with time. Figures 4 and 5 show magnetic field probe results for the transition mode and the helicon mode. The transition mode has more of a traveling wave character (due to the near linear phase variation) while the helicon mode shows more of a standing wave character.

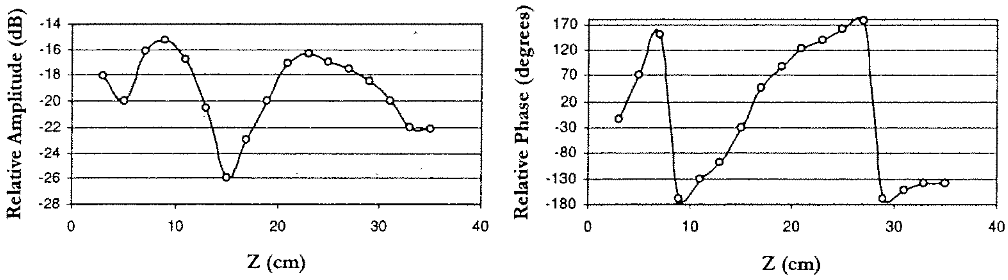

Figure 4: B_z relative amplitude and phase verses axial position for the transition mode (700 Watts, 200 Gauss).

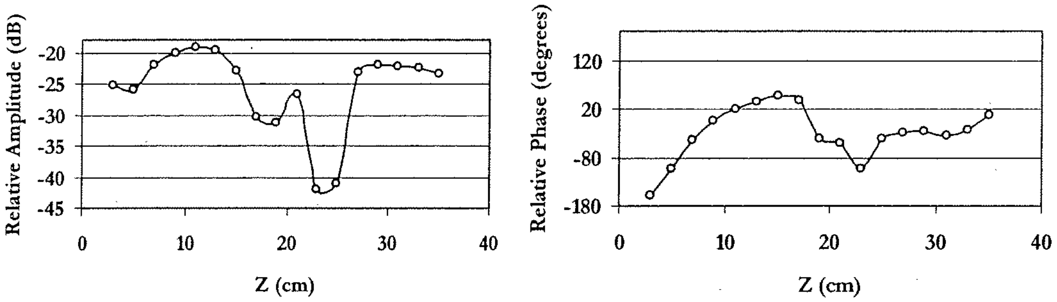

Figure 5: B_z relative amplitude and phase verses axial position for the blue (helicon) mode (800 Watts, 1000 Gauss).

Photon Binning results for the 443 nm emission are being carried out. Care is being taken to use cable with high isolation (>90 dB) so that modulation is not created by noise. Also the Labview software that does the correlating is carefully being checked to reproduce both random and correlated test signals. A new oscilloscope with a fast sampling rate (4 GS/s) has been acquired and is being incorporated into the system.

Acknowledgements

*Research supported by NSF Grant ECS-9905948 and AFOSR Grant F49620-00-1-0191. J. Scharer also thanks the Australian National University for their generous support while there.

References

1. J. Scharer, A. Degeling, G. Borg and R. Boswell, "Measurements of helicon wave propagation and Ar II emission, to be published in Physics of Plasmas, 34 pages (2002).
2. A. Ellingboe, R. Boswell, J. Booth, and N. Sadeghi, Physics of Plasmas, **2**, 1807 (1995).
3. X. Guo, J. E. Scharer, Y. Mouzouris, and L. Louis, Physics of Plasmas, **6** (8), 3400, (1999).

Quasi-Isodynamical Configurations without Transitional Particle Orbits

A.A.Subbotin [1], W.A.Cooper [2], M.Yu.Isaev [1], M.I.Mikhailov [1], J.Nührenberg [3],
M.F.Heyn[4], V.N.Kalyuzhnyj[5], S.V.Kasilov[5], W.Kernbichler[4], V.V.Nemov[5],
M.A.Samitov [6], V.D.Shafranov [1], R.Zille[3]

[1] *Russian Research Centre "Kurchatov Institute", Moscow, Russia*
[2] *Centre de Recherches en Physique des Plasmas, Association Euratom-Confédération Suisse, Ecole Polytechnique Fédérale de Lausanne, Switzerland*
[3] *Max-Planck-Institut für Plasmaphysik, IPP-EURATOM Association, Germany*
[4] *Institut für Theoretische Physik, Technische Universität Graz, Graz, Austria*
[5] *Institute of Plasma Physics, National Science Center "Kharkov Institute of Physics and Technology", Kharkov, Ukraine*
[6] *Moscow State Engineering and Physics Institute, Moscow, Russia*

Abstract

The possibility for collisionless confinement of all reflected particles in a stellarator with poloidal direction of the contours of B on the magnetic surfaces is investigated computationally. As a result, a configuration is found with $<\beta>\approx 5\%$ in which all reflected particles started at the inner half of the plasma have very long collisionless confinement time.

It is also shown that the requirement of good particle confinement is well compatible with the Mercier and resistive local-mode stability conditions.

Introduction

The investigations of the possibilities to improve the particle confinement have shown that approaching quasisymmetry leads to this goal for configurations with helical [1] and axial [2] directions of the contours of B on the magnetic surfaces. For the third possible direction of the contours of B on the magnetic surfaces, the poloidal one, the corresponding condition of quasisymmetry can not be satisfied in closed magnetic systems, in particular not in the linear approximation with respect to the distance from the magnetic axis. As was shown during the W7-X optimization (see, e.g. Ref. [3]) and more rigorously formulated in Ref. [4], the improvement of collisionless particle confinement in such systems can be achieved by optimization of the contours of the second adiabatic invariant $\mathcal{J} = \int v_{\|} dl$ to be constant on magnetic surfaces, *for deeply to moderately deeply trapped particles.* In Ref. [4] this condition was named quasi-isodynamicity. As was shown in Ref. [4], it can be fulfilled in configurations far from quasisymmetry. The barely reflected particles in those configurations are confined for a long time but eventually lost due to collisionless stochastic diffusion.

The possibility to fulfill the condition of quasi-isodynamicity for all reflected particles was studied analytically in Ref. [5]; the poloidal direction of the contours of B was considered in near-axis approximation. The main conclusion was that the condition $\mathcal{J} = \mathcal{J}(s)$ can not be fulfilled exactly for all reflected particles, but can be satisfied with any prescribed accuracy. In Ref. [6] the helical direction of the contours of B was considered for a model field strength; the method used can be applied to systems with poloidal direction of the contours of B, too.

In the present paper the possibility to collisionlessly confine all reflected particles for a long time is investigated numerically for the system with poloidal direction of the contours of B. Results are presented for a configuration with aspect ratio $A \approx 12$, six periods and finite plasma pressure, $<\beta>\approx 5\%$.

The choice of penalty functions

The optimization procedure was performed with the VMEC code [7] for the equilibrium computation and the JMC code [8] for obtaining the spectrum of B in magnetic coordinates. The orbit integration code in magnetic coordinates [9] was used as a diagnostic to check the quality of the optimized configuration.

To find a configuration with poloidally closed contours of B the condition of pseudosymmetry [10] as it was formulated in Ref. [11] was used for constructing the penalty function. This condition itself is not sufficient for good particle confinement [12], thus, in addition the requirement for the contours of $\mathcal{J}$ started at some prescribed magnetic surface to be closed inside the plasma column for all values of B_{ref}, i.e for all reflected particles, was imposed. In the last stage of the optimization the requirements of Mercier and resistive local-mode stability were imposed, in addition. The results of the optimization were checked by direct calculation of the α-particles loss for a power plant-size configuration. In addition, the transport and stability properties of the optimized configuration were investigated with a suite of field line following codes [13,14].

Results of the optimization

A 3D view of the optimized configuration is shown in Fig. 1. The color here indicates the value of the magnetic field strength. The characteristic feature of this configuration is the nearly straight magnetic axis in the regions of the field strength extremes (two regions in one period). The contours of $\mathcal{J}$ are shown in Fig. 2 for increasing values of B_{ref}, $B_{\text{ref}} = B_{min} + i(B_{max} - B_{min})/7$, $i = 1...6$, in polar-coordinate representation $\sqrt{s}, \theta$ with s the flux label. The top left contours are near the minimal value of B_{ref} and the bottom right ones near the maximal one. The red color corresponds to maximal value of $\mathcal{J}$ showing the max-$\mathcal{J}$ property of this configuration. It is seen that – for all values of B_{ref} – contours of $\mathcal{J}$ started from inner half of the plasma column are closed inside the plasma. The direct check of α-particle confinement shows that using $\mathcal{J}$-optimization is adequate to reach the collisionless confinement goal. Fig. 3 shows the history of particles lost during a time of flight of 10 sec for particles started from 2/3 of minor plasma radius. There is no loss of particles started at 1/2 and smaller plasma radii.

Fig. 4 shows the radial dependence of the largest Fourier coefficients of the magnetic field strength. It is seen that the bumpy component here is larger than in the quasi-isodynamic configuration described in Ref. [4].

The results of Mercier and resistive local-mode stability in the optimized configuration calculated by the JMC code are shown in Fig. 5 for $<\beta>= 5\%$.

The optimized configuration was investigated by field line following codes, too (see, e.g. Ref. [13,14]). These calculations have confirmed the Mercier stability of the configuration. In addition, the Pfirsch-Schlüter factor (the ratio $< j_{\|}^2 > / < j_{\perp}^2 >$) was calculated. It was shown that this factor is approximately 0.13-0.15, showing the significant reduction of the secondary current. Fig. 6 shows the radial dependence of the effective ripple determining the level of transport in the $1/\nu$ regime. It is worth to emphasize that in the optimization procedure only the requirement of the closedness of $\mathcal{J}$ contours was imposed. The further minimization of the effective ripple is possible, as it was seen during the optimization.

Conclusions

It is shown that using $\mathcal{J}$-optimization together with optimization toward pseudosymmetry (i.e using information about the magnetic field strength only, without direct calculation of particle drift motion) permits to find configurations with good collisionless particle confinement. It is also shown, that these criteria for confinement improvement are well compatible with the conditions of Mercier and resistive mode stability.

Acknowledgments

This work was supported by INTAS Grant No 99-00592, by the Russian-Germany agreements WTZ-V RUS-563-98 and WTZ-RUS-01/581, by the Russian Federal program on support of leading scientific schools, Grant No 00-15-96526, by the Russian Fund for Basic Research, Grant No 00-02-17105, by the Fonds National Suisse de la Recherche Scientifique and Euratom, by the Association EURATOM-OEAW and by the Austrian Academy of Sciences.

References

[1] Nührenberg J. and Zille R., Phys. Lett. A **129** (1988) 113.
[2] Nührenberg J., Lotz W., Gori S., Theory of Fusion Plasmas (Varenna 1994), Editrice Compositori, Bologna (1994) 3.
[3] Lotz W., Nührenberg J., Schwab C., in Plasma Physics and Controlled Nuclear Fusion Research 1990 (Proc. 13th Int. Conf., Washington 1990) IAEA, Vol. 2, IAEA, Vienna (1991) 603.
[4] Gori S., Lotz W., Nührenberg J., Theory of Fusion Plasmas (International School of Plasma Physics), Bologna: SIF (1996) 335.
[5] Shafranov V.D. Plasma Phys. Control. Fusion **43**, (2001) A1.
[6] Cary J.R., Shasharina S.G., Phys. Rev. Letters **78** (1997) 674.
[7] Hirshman S.P. and Betancourt O., J. of Comput. Physics **96** (1991) 99.
[8] Nührenberg J., Zille R., Theory of Fusion Plasmas (Varenna 1987), Editrice Compositori, Bologna (1988) 3.
[9] Fowler R.H., Rome J.A., Lyon J.F., Phys. Fluids **28** (1985) 338.
[10] Mikhailov M.I., Cooper W.A., Isaev M.Yu., Shafranov V.D., Skovoroda A.A., Subbotin A.A., Theory of Fusion Plasmas (International School of Plasma Physics), Bologna: SIF (1998) 185.
[11] Skovoroda A.A., Plasma Physics Reports **24** (1998) 989.
[12] Mikhailov M.I., Isaev M.Yu., Nührenberg J. et. al., 28th EPS Conf. on Controlled Fusion and Plasma Physics, Funchal, Portugal, ECA Vol. **25A** (2001) 757 (http://epsppd.epfl.ch/Madeira/html/authors/nav/AutS08fr.html).
[13] Nemov V.V., Kasilov S.V., Kernbichler W., Heyn M.F., Phys. Plasmas **6** (1999) 4622.
[14] Nemov V.V., Plasma Physics Reports **23** (1997) 683.

Fig. 1. Boundary magnetic surface of the optimized configuration also showing the magnetic topography. The colors define the range of the magnetic field strength (red – maximum, blue – minimum.

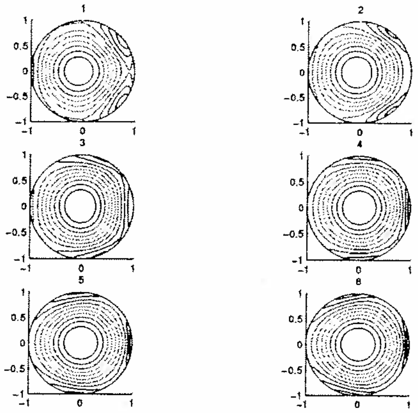

Fig. 2. $\mathcal{J}$ contours for increasing values of B_{ref} in polar-coordinate representation $\sqrt{s}, \theta$ with s being the flux label.

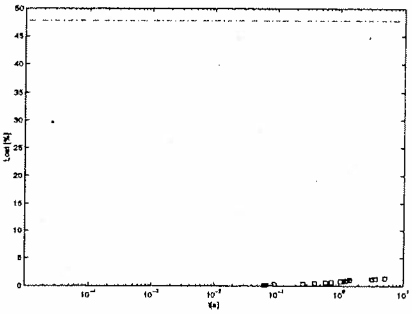

Fig. 3. Collisionless α-particle confinement in the optimized configuration as a function of the time of flight. One thousand particles are started at $s_{start} = 0.44$ (2/3 of the plasma radius); the dashed line shows the fraction of the reflected particles.

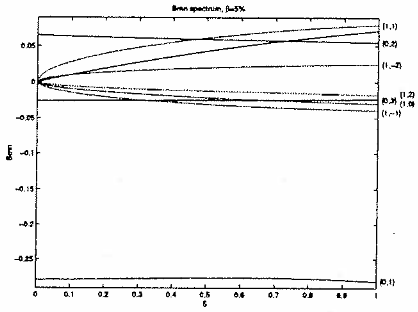

Fig. 4. Radial dependencies of few largest Fourier coefficients $B_{m,n}$ for optimized configuration. $B_{0,0}$ is shown by black line and is plotted in the form $B_{0,0}(s) - B_{0,0}(0)$, with $B_{0,0}(0) = 1$.

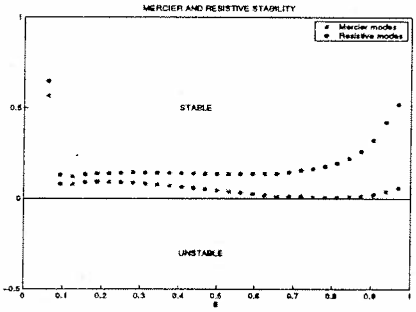

Fig. 5. Mercier and resistive modes stability along the radial coordinate.

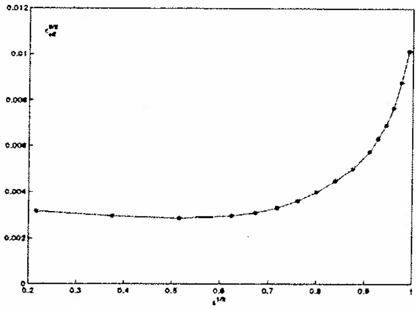

Fig. 6. Radial dependence of the "effective ripples" for optimized configuration.

TCV High Resolution X-ray Imaging Diagnostic

A. Sushkov [1,2], Y. Camenen[1], S. Coda[1], I. Klimanov[1], A. Pochelon[1], H. Weisen[1]

[1]*Centre de Recherches en Physique des Plasmas*
Association EURATOM-Confédération Suisse
EPFL, 1015 Lausanne, Switzerland
[2]*Russian Research Centre Kurchatov Institute,*
123182 Moscow, Russia

INTRODUCTION

A Multiwire Proportional X-ray (MPX) detector was used on the Tokamak a Configuration Variable (TCV) in a high spatial resolution X-ray imaging diagnostic. This vertically viewing 64 channel X-ray system has been designed to complement the existing TCV soft X-ray tomography system consisting of ten 20-channel pinhole cameras (spatial resolution ~ 3 cm) [1] by enhancing the spatial resolution of X-ray emissivity measurements. The objectives are the observation of magnetohydrodynamic (MHD) activity and transport barriers phenomena and an improved the determination of the Electron Cyclotron Heating (ECH) deposition profile. The diagnostic measures the plasma emission in the 3-30 keV range with a radial resolution of about 5 mm and a frequency bandwidth of a 50 kHz. This paper outlines the design of the system and also presents some initial results, which demonstrate the diagnostic potential.

THE DIAGNOSTIC DESIGN

The diagnostic consists of a vertically mounted helium-filled cylindrical camera with a rectangular aperture (Fig.1). The dimensions of the aperture are 2x40 mm^2. The camera is equipped with a planar MPX detector consisting of 64 non-separated channels. Each channel has a sensitive area of 2x40 mm^2. The spatial resolution of the diagnostic at the vessel mid-plane is about 5 mm. The camera is separated from the vacuum vessel by a first beryllium window of thickness 250 μm. The MPX detector has a second beryllium window of thickness 100 μm. Thus the diagnostic views the plasma through two beryllium foils totalling 350 μm thickness. An additional aluminium foil of thickness 308 μm was used in some of the experiments to observe a higher energy electron population, as discussed in the article.

The MPX detector is a modified version of a multiwire proportional chamber developed for the T-10 tokamak X-ray monochromator [2]. The construction of the MPX detector is similar to that of multiwire proportional counters [3] commonly used in charged particle physics. 64 parallel anode wires situated between two cathode grids in a common gas chamber filled by an argon-methane, krypton-methane or xenon-methane gas mixture at atmospheric pressure. The overall spectral sensitivity of the diagnostic for different gas mixtures and different foils used in the experiments is shown in Fig.2. The main advantage of the MPX detector is the high intrinsic gas amplification (10^2-10^5, depending on the applied voltage) and the negligibly small leakage current. This allows the use of simple operational amplifiers for matching the detector signal to the acquisition system input voltage range. The amplifiers are mounted directly on the detector to minimize parasitic capacitance and noise. They convert the detector current into voltage (conversion factor 100 nA/V) and limit the signal bandwidth to 50 kHz. The signals are digitized by a 12 bit ADC at a sampling rate of 200 kHz. The voltage value applied to the detector is selected remotely from the control room and provides a flexible change of gas amplification for optimal output in different TCV operation modes.

FIRST RESULTS

The X-ray intensity as a function of time for several channels of the MPX detector shielded by a 350 μm thick beryllium foil is shown in Fig. 3 for a discharge with elongation κ=1.8 and plasma current I_p=390 kA. Sawtooth oscillations can be seen in the stationary stage of the discharge. A clear m=1, n=1 mode is growing just before the sawtooth crash at t =1.16 s. Periodic non-localized and localized bursts of the non-thermal X-ray radiation are observed in experiments with modulated Electron Cyclotron Current Drive (ECCD) in low density discharges (n_e=1x10^{19}m^{-3}, I_p=250 kA, P_{ECCD}=1.5MW). In these experiments the signal was filtered by an additional aluminium foil of thickness 308 μm and the detector was filled with the krypton-methane gas mixture (the spectral response is shown in Fig.2 (d)). Non-localized X-ray bursts appear at the end of the ECCD pulse and can be observed simultaneously on all channels of the MPX detector and on the hard X-ray runaway monitor (Fig 4). In some cases the ECCD pulse where followed by periodic localized X-ray bursts. These bursts appears in phase with an m=2, n=1 mode and can be observed only on the high field side channels close to the plasma center. In both cases the X-ray bursts are attributed to MHD activity which expels ECCD induced non-thermal electrons which then impinge on the plasma-facing components.

The high spatial resolution of the diagnostic allows an improved determination of the ECH power deposition profile. The ECH power deposition profile is determined from the time evolution of the X-ray intensity after the ECH power is switched on/off. In these calculations one assumes that the variations of the plasma density and effective charge are negligible during the analysis time (5 ms). It is then possible to reconstruct the variation of the electron temperature profile using the dependence on the local X-ray intensity from the electron temperature, taking the initial electron temperature from the Thomson scattering diagnostic. After Abel inversion of the line integrated X-ray signals and reconstruction of the time variation of the electron temperature the ECH power deposition profile is calculated using the COBRA code [4]. An example of such a calculation is shown in Fig.6. Fig.6(a) shows the X-ray intensity as a function of time for different chords (the ECH power is switched on at t=0.4 s). Comparison of the results of ray tracing calculations (solid line) with the ECH power deposition profiles calculated by COBRA code (dashed line) is shown in Fig.6 (b). It can be seen from Fig.6 that the experimentally determined ECH power deposition location is in good agreement with the results from ray tracing calculations. However the half-width of the experimental ECH power deposition profiles is always wider than the half-width of the profiles calculated by the TORAY code. This can be explained by noise in the experimental data and the finite number of polynomials used for solution regularization in the Abel inversion and COBRA codes.

CONCLUSIONS

A Multiwire Proportional X-ray detector has been implemented on TCV as a high spatial resolution X-ray imaging diagnostic. A vertically mounted helium-filled slot-hole camera equipped with a 64-channel planar MPX detector views the plasma core with a radial resolution of about 5 mm on the vacuum-vessel mid-plane. The diagnostic allows a considerably improved spatial resolution of the X-ray emission measurements and the study of MHD activity with a 50 kHz bandwidth. Periodic localized and non-localized bursts of the non-thermal X-ray radiation possibly caused by interaction of the ECCD induced non-thermal electrons with plasma-facing components are observed in low-density discharges with modulated ECCD. The diagnostic also allows improved experimental determination of the ECH power deposition profile.

REFERENCES

[1] M. Anton et al., Plasma Phys. Control. Fusion **38** (1996) 1849.
[2] V. Razin, V. Vershkov et al. Report INR-756/92 (in Russian).
[3] G. Charpak et al. Nuclear Instruments and Methods **62** (1968) 262.
[4] V.F. Andreev et al. 26-th EPS Conf. Maastricht, ECA Vol. 23J (1999) 853-856.

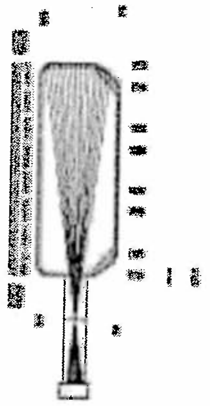

Fig.1 Geometry of the MPX diagnostic.

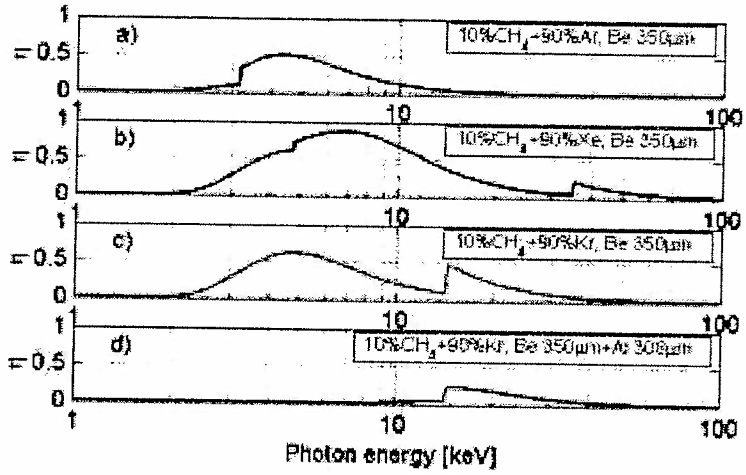

Fig. 2 Overall spectral sensitivity of the MPX diagnostic for different gas mixtures and foils.

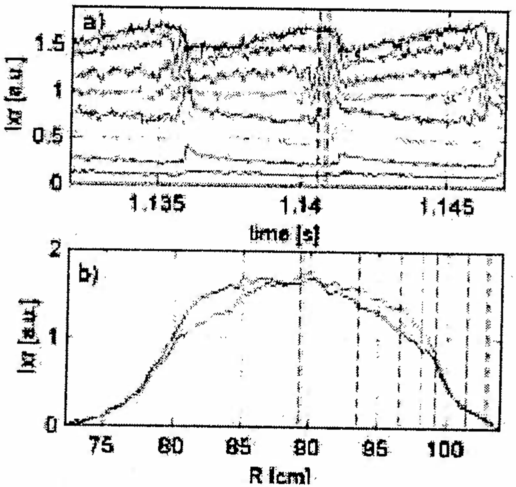

Fig. 3 X-ray intensity time traces (a) and poloidal profiles (b), dashed lines shows times and chords position (shot 22610).

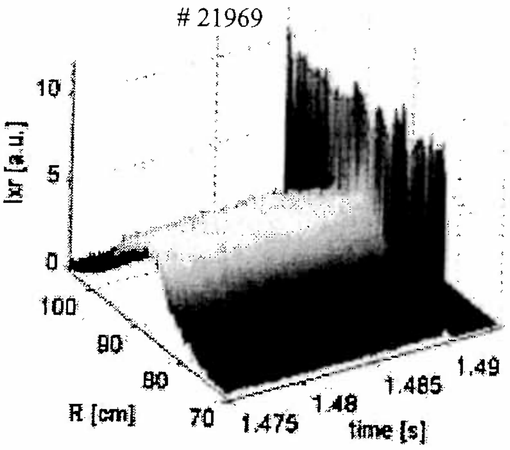

Fig.4 Non-localized X-ray burst.

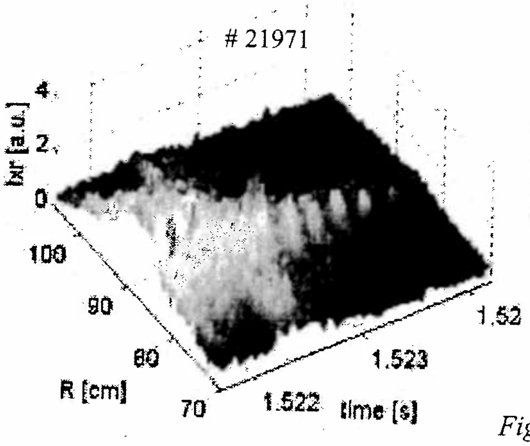

Fig.5 Localized X-ray bursts.

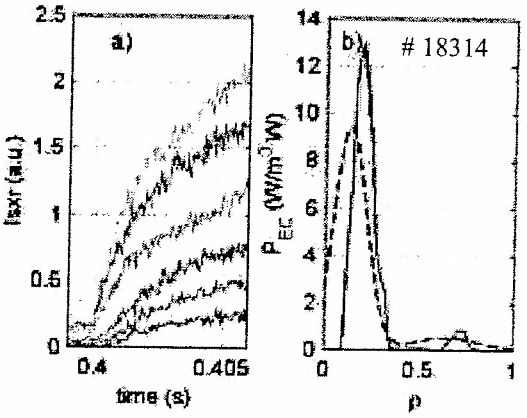

Fig. 6 X-ray intensity time traces ECH switched on t=0.4 s (a); ECH power deposition profiles (solid line TORAY, dashed COBRA) (b).

Measurement of Alfvén Waves on the JET Tokamak

D.Testa[1], A.Fasoli[1,2], D.N.Borba[3], G.Y.Fu[4], A.Jaun[5], M.Mantsinen[6], P.deVries[7],
and contributors to the EFDA-JET work programme
[1]*Plasma Science and Fusion Center, Massachusetts Institute of Technology, Boston, USA*
[2]*CRPP, Association EURATOM – Confédération Suisse, EPFL, Lausanne, Switzerland*
[3]*Associacão EURATOM/IST, Portugal; EDFA – CSU, Culham Science Centre, UK*
[4]*Princeton Plasma Physics Laboratory, Princeton, New Jersey, USA*
[5]*NADA VR-Euratom Association, Royal Institute of Technology, Stockholm, Sweden*
[6]*Helsinki University of Technology, Association Euratom – Tekes, Finland*
[7]*Association EURATOM FOM – Rijnhuizen, TEC, 3430 BE Nieuwegein, NL*

One of the main purposes of the Alfvén Eigenmodes (AEs) [1] studies on JET is to validate the existing theoretical models and identify the dominant damping mechanisms for global AEs, with the aim to obtain accurate predictions for future burning plasma experiments. As an example of this work, the dependence of the measured damping rate upon the normalized Larmor radius has been analyzed in the conventional tokamak scenario, with a monotonic q-profile, to test the predictions of the NOVA-K code [2]. The AE stability properties have been studied in the presence of the fast ion drive provided by resonant Neutral Beam Injected (NBI) ions with velocities $|\upsilon_{\parallel NBI}|\approx\upsilon_A$. We have investigated the role of the high central safety factor, $q_0\geq2$, on the AE stability in the advanced tokamak regimes, such as the JET Reversed Shear (RS) experiments with non-monotonic q-profile and internal transport barriers, where the ion diamagnetic drift frequency approaches the AE frequency, $\omega_{*i}/\omega_{TAE}\approx2nq^2\rho_*^2(R\omega_{pi}/c)$ and $\omega_{*i}/\omega_{AE}>0.1$.

1. Active Diagnostic Technique.

The JET saddle coils are used as external antennas to drive and detect stable AEs. The diagnostic technique [3,4,5] uses repetitive sweeps of the driving frequency in a pre-defined range, controlled in real-time. The plasma response is extracted from background noise using synchronous detection, and it is used to identify in real-time the resonance corresponding to a global mode. When a resonance is found, the controller locks to that frequency and tracks the mode, providing a real-time measurement of the mode frequency and damping rate γ/ω.

2. Test of the Radiative Damping Model.

The *radiative damping model*, as implemented in the NOVA-K code [2], predicts a strong dependence for the damping rate of n=1 Toroidal AEs (TAEs) upon the kinetic parameter $\lambda=4(2/5)^{3/2}(m\sigma\rho_{*i}/r)(R/r)^{3/2}(3/4+T_e/T_i)^{1/2}$: $\gamma/\omega_{RAD}\propto\exp(-\sigma^2/\lambda)$, where $\sigma=(r/q)dq/dr$ is the magnetic shear. NOVA-K also includes trapped electron Landau damping, γ/ω_{ELE}, but does not include continuum damping [6]. Figure 1 shows an example of the test of the radiative damping model, as implemented in NOVA-K, for plasmas with a monotonic q-profile and low edge magnetic shear (limiter configuration).

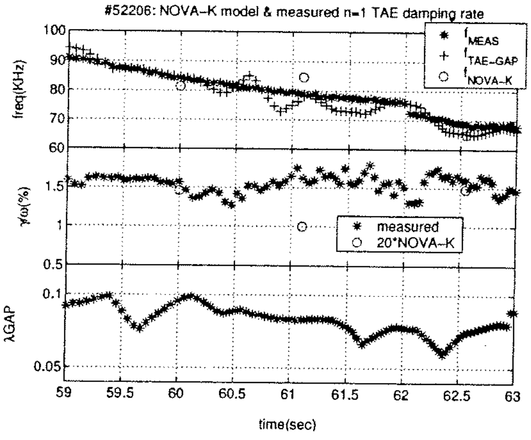

Figure 1. Test of the radiative damping model as implemented in the NOVA-K code.

The mode frequency predicted by NOVA-K agrees well with the measurement, but the predicted damping rate $\gamma/\omega_{RAD}+\gamma/\omega_{ELE}$ is a factor 2□ smaller than the measured one. A possible reason for this discrepancy is a finite continuum damping near the edge due to the global structure of the n=1 TAE. This suggests that $\gamma/\omega_{RAD}+\gamma/\omega_{ELE}$ alone may not be sufficient to predict the low-n TAE stability in JET plasmas with monotonic q-profile and low edge magnetic shear. This could also have possible implications for predicting the TAE stability of future burning plasma experiments such as ITER.

□ Measurement of the □ta□ilit□ □imits as □unction of the Edge Magnetic □hear.

A large edge magnetic shear has a strong stabilizing contribution for low-n AEs [7,□]. □sing resonant NBI ions with $|\upsilon_{\|}|\approx\upsilon_A$, we have measured the excitation threshold for TAEs with different n□ in plasma configurations with monotonic q-profile and low (limiter) and high (□-point) edge magnetic shear.

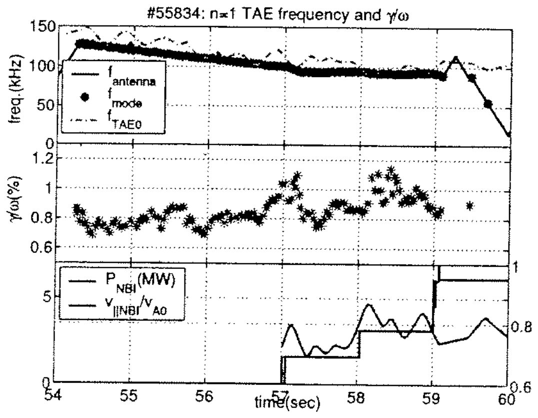

Figure 2. Measurement of the NBI ion drive and n=1 TAE stability limits.

In particular, TAEs destabilized by NBI-ions have higher toroidal mode number $n=3$ 10 [□], than those of the antenna driven (stable) TAEs, which have $n=0$ 2. The effect of the NBI ion drive on the n=1 TAE damping rate is shown in fig.2 for a limiter plasma where $|\upsilon_{\|}|\approx 0.$□$5\upsilon_A$: there is no significant variation in γ/ω. This poses a constraint on the velocity spread of the NBI ion distribution function.

Figures 3a and 3b show the results on the excitation threshold for TAEs with different n□ in limiter and X-point configurations, respectively. For similar plasma conditions, □ less NBI power (and further away from the resonant $|\upsilon_{||}/\upsilon_A|=1$ due to a different plasma density) is needed to destabilize TAEs with intermediate n□ in plasmas with low edge magnetic shear than with high edge magnetic shear.

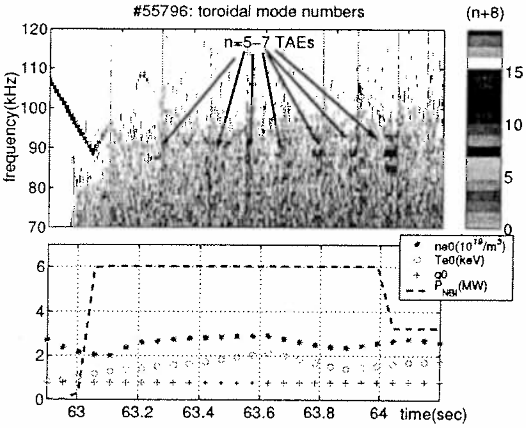

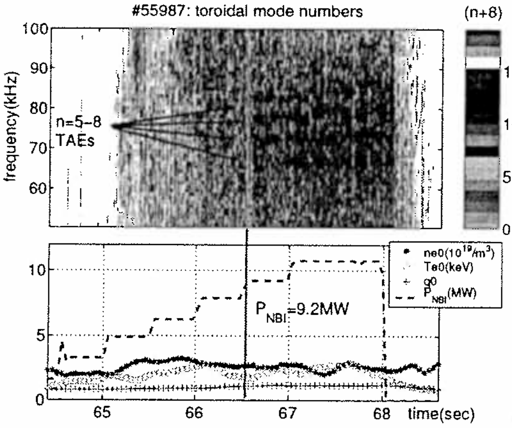

Figure 3a. *Limiter plasma□ $n=5$ 7 TAEs unstable at $P_{NBI}=6M$□, $|\upsilon_{||}|\approx 0.$□$\upsilon_A$.*

Figure 3b. *X-point plasma□ $n=5$ □ TAEs unstable at $P_{NBI}=$□$2M$□, $|\upsilon_{||}|\approx 0.$□$5\upsilon_A$.*

Conversely, for plasmas with similar low edge magnetic shear and $|\upsilon_{||}|\approx 0.$□$\upsilon_A$, $P_{NBI}=6M$□ is not sufficient to destabilize $n=0$ 2 TAEs. This result confirms earlier predictions and measurements on the importance of the magnetic shear to stabilize TAEs, but this effect appears to be weaker for $n=5$ 7 TAEs than for $n=0$ 2 TAEs [7].

□ Alfvén Mode Stability in the Advanced Tokamak Scenario.

In the advanced tokamak scenario with deeply reversed shear, coupling between kinetic and drift Alfvén waves is expected for $\omega_{*i}/\omega_{TAE}\approx 2nq^2\rho_*^2(R\omega_{pi}/c)>0.01n$, and an ITER-FEAT scenario with $q_0=4.5$ is predicted to be unstable to such modes [1□]. Figures 4a and 4b show the measurements for two JET RS discharges in X-point configuration with a non-monotonic q-profile and electron (and ion) core transport barrier. Here no MeV energy ions were present, which are needed to destabilize TAEs in similar plasmas with a monotonic q-profile. The $n=0$ modes observed in the experiment do not follow the $f_{TAE}(t)$ frequency scaling and are weakly damped even in the presence of a large edge magnetic shear, during the X-point phase. This could be related to a flat q-profile, with very small (or even negative) magnetic shear in the plasma core, since these weakly damped modes do not appear in similar plasmas with positive magnetic shear, as shown in fig.5.

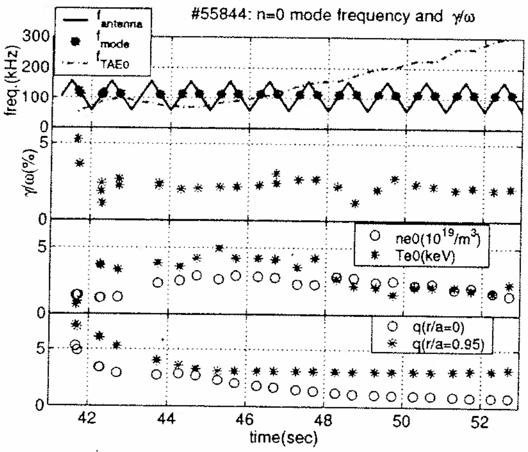

Figure 4a. *□eakly damped n=0 modes.*

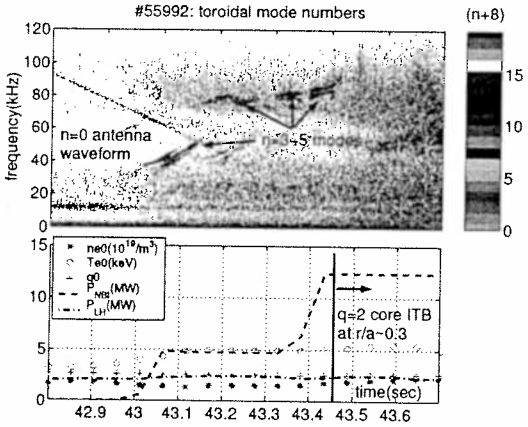

Figure 4b. *Unstable n=3 5 modes.*

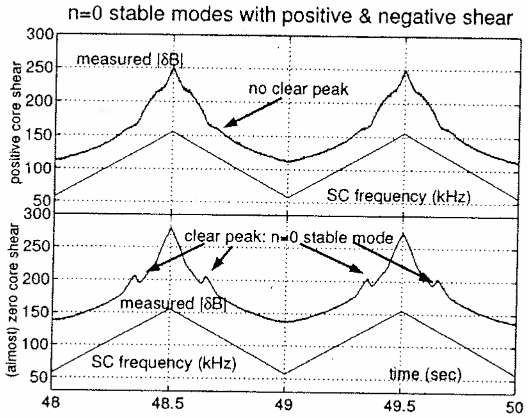

Figure 5. *Amplitude of stable n=0 modes for two discharges with monotonic q-profile and positive core magnetic shear (top) and non-monotonic q-profile with almost zero core magnetic shear (bottom).*

It should be noted that the n=□modes cannot be driven unstable by fast particles, but can serve as a useful benchmark of theory. Future work in RS plasmas will focus on the reactor relevant and potentially unstable $n>0$ modes. Intermediate and high-n AEs ($n>3$) are more easily destabilized on JET, and future burning plasma experiments are predicted to have unstable AEs with even higher n□ because of a smaller ρ_{*i}. To study the stability properties of these high-n AEs, new antennas are being designed for future installation in JET.

This work has been conducted under the European Fusion Development Agreement. D.Testa and A.Fasoli were partly supported by DoE contract No. DE-FG□2-□□ER54563.

References.

[1] □.□heng et al., *Ann. Phys.* **1□1** (1□□5), 21. [2] □.□heng, *Phys. Rep.* **211** (1□□2), 1□G.Fu et al., *Phys. Plasmas* □(1□□6), 4□36. [3] A.Fasoli et al., *Phys. Rev. Lett.* □□(1□□5), 645. [4] A.Fasoli et al., *Phys. Plasmas* □(2□□□), 1□16. [5] A.Fasoli et al., *MHD Spectroscopy*, Invited Paper I-2.□□ this □onference. [6] F.□onca, L.□hen, *Phys. Rev. Lett.* □□(1□□2), 5□2. [7] D.Testa, A.Fasoli, *Nucl. Fusion* □1 (2□□1), □□□ [□ A.Jaun et al., *Phys. Plasmas* □(1□□□), 2□52□A.Jaun et al., *Nucl. Fusion* □□(2□□□) 1343□A.Fasoli et al., *Phys. Lett.* **A2□□** (2□□□), 2□□ [□ D.Borba et al., *Nucl. Fusion* □□(2□□), 775. [1□ A.Jaun et al., *Nucl. Fusion* □□(2□□□), 1343.

Stabilization of ITG Modes and Destabilization of Trapped Particle Modes with $E \times B$ Flows

L. Villard, A. Bottino, S. Allfrey, and O. Sauter

Centre de Recherches en Physique des Plasmas
Association Euratom - Confédération Suisse
EPFL, 1015 Lausanne, Switzerland

Abstract. The development of radial electric fields (E_r) is an important mechanism leading to the formation of transport barriers through turbulence suppression when the $E \times B$ shearing rate exceeds the turbulence inverse correlation time γ_t [1]. Often a simplified stabilization criterion is used in the case of applied (equilibrium) E_r, replacing γ_t with the linear growth rate without flow γ_0, while the theory was established in the context of turbulence self-generated E_r (zonal flows) which are fluctuating quantities. In this paper, the applicability of this simplified criterion is examined for a variety of cases. Three geometries are considered: axisymmetric, helical and cylindrical. Various radial profiles of the shearing rate are studied. Full radius linear gyrokinetic simulations yield the following results: (a) the toroidal-ITG, slab-ITG and helical-ITG growth rates have a quadratic dependence on the shearing rate; (b) these modes are fully stabilized when the shearing rate is comparable to the linear growth rate, within a factor of about 2; (c) the critical gradient for marginal stability increases quadratically with the value of the shearing rate; (d) applied radial electric fields can be destabilizing when the dominant drive is from trapped ions or when the trapped electron dynamics are taken into account.

1. Global linear gyrokinetic model

We consider low β magnetic configurations with axisymmetry or helical symmetry, with given profiles of $q(\psi)$, $n_0(\psi)$, $T_e(\psi)$, $T_i(\psi)$ and applied electrostatic potentiel $\Phi_0(\psi)$, where ψ is the poloidal or helical flux. Electrostatic perturbations are assumed to follow the usual gyrokinetic ordering $\omega/\Omega \sim k_\parallel/k_\perp \sim e\delta\phi/T_e \sim \rho_L/L_n \sim \rho_L/L_T \sim \mathcal{O}(\epsilon_g)$ and $\rho_L/L_B \sim \mathcal{O}(\epsilon_B)$. With $f = f_0 + \delta f$ and $\phi = \Phi_0 + \delta\phi$, the linearized equations are

$$
\begin{aligned}
\frac{d\mathbf{R}}{dt} &= v_\parallel \mathbf{e}_\parallel + \mathbf{v}_d + \mathbf{v}_E \,, \quad \frac{dv_\parallel}{dt} = \frac{1}{2} v_\perp^2 \nabla \cdot \mathbf{e}_\parallel \,, \quad \frac{dv_\perp}{dt} = -\frac{1}{2} v_\perp v_\parallel \nabla \cdot \mathbf{e}_\parallel \,, \\
\mathbf{v}_E &= \frac{\mathbf{e}_\parallel \times \nabla\psi}{B} \frac{d\Phi_0}{d\psi} \,; \;\; \mathbf{v}_d = \frac{v_\parallel^2}{\Omega} \mathbf{e}_\parallel \times \Big((\nabla \times \mathbf{e}_\parallel) \times \mathbf{e}_\parallel \Big) + \frac{v_\perp^2}{2\Omega} \mathbf{e}_\parallel \times \nabla \ln B \,, \\
\frac{d\,\delta f}{dt} &= \frac{< \nabla \delta\phi >}{B} \\
&\cdot \quad \left[\mathbf{e}_\parallel \times \left(\nabla\psi \frac{\partial f_0}{\partial \psi} - \frac{1}{2} \nabla \ln B \; v_\perp \frac{\partial f_0}{\partial v_\perp} - \mathbf{e}_\parallel \times \nabla \times \mathbf{e}_\parallel \; v_\parallel \frac{\partial f_0}{\partial v_\parallel} \right) + \Omega \frac{\partial f_0}{\partial v_\parallel} \mathbf{e}_\parallel \right] \,, \quad (1)
\end{aligned}
$$

where the brackets <> indicate Larmor averaging. We consider small Mach numbers of v_E and have neglected terms of order $(v_E/v_{thi})^2$ and $\epsilon_B(v_E/v_{thi})$. The system is closed with the quasi-neutrality equation. Two models for electrons are considered: either all electrons are adiabatic or trapped electrons are drift-kinetic and only passing electrons are adiabatic. The equations are solved with a finite element, PIC, full radius code in magnetic coordinates [2].

The shearing rate of the applied E_r field is [1]

$$\omega_{E\times B} = (1/q)(sd\psi/ds)d^2\Phi_0/d\psi^2 \approx (\rho/q)(\partial/\partial\rho)(qv_E/\rho) \qquad (2)$$

in which $s = \sqrt{\psi/\psi_a}$ and the last expression is valid only in circular large aspect ratio configurations: it shows the combined effect of magnetic shear with the *value* of v_E.

2. Stabilization of toroidal-ITG, helical-ITG and slab-ITG modes

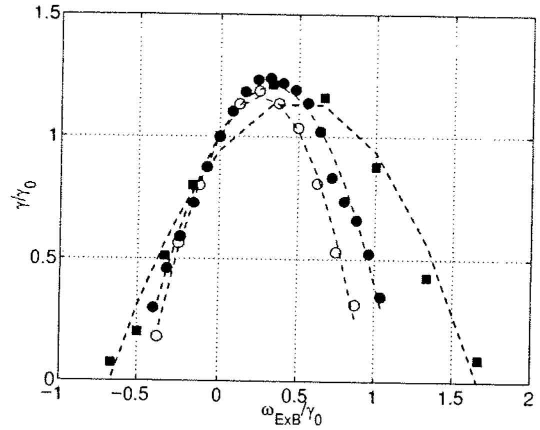

Figure 1: *Growth rates of toroidal-ITG (circles) and helical-ITG (squares) as function of the shearing rate $\omega_{E\times B}$; filled symbols with $v_E \propto s(s-s_0)$, open symbols with v_E/ρ=const. Dashed lines: quadratic fits.*

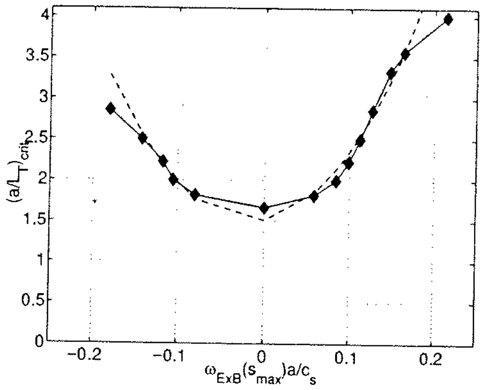

Figure 2: *Critical gradient as function of $\omega_{E\times B}$ for slab-like ITG modes.*

In this section we consider fully adiabatic electrons and gyrokinetic ions. We apply the model to 3 different configurations: (a) a circular cross-section tokamak with $R/a = 5.5$ and $q(s) = 1.25 + 3s^2$, (b) a shearless helically symmetric heliac configuration and (c) a cylinder. First, the most unstable mode in the absence of applied electric field is searched, and then an external electric field is applied. Fig.1 shows how the growth rate depends on the shearing rate of the applied E_r in the tokamak and heliac cases and for different E_r profiles. In all cases the behaviour is quadratic, and the stabilization occurs when $\omega_{E\times B} \approx \gamma_0$, the growth rate in the absence of applied E_r. Note in particular the result of the shearless v_E profile ($v_E \propto \rho$), for which the shearing rate is the product of magnetic shear times the value of v_E/ρ. It is therefore justified to use the expression of Eq.(2) for $\omega_{E\times B}$. A more detailed analysis of the cases shown here is made in Ref.[3]. Slab-ITG modes have been studied in Ref. [4], and the results confirm the generic nature of the quadratic dependence of the growth rate on $\omega_{E\times B}$. We show in Fig.2 the critical gradient $(a/L_T)_{crit}$ as a function of $\omega_{E\times B}$. There is clearly an upshift, and this upshift is proportional to the square of the shearing rate $\omega_{E\times B}$. We conclude that the often used stabilization criterion ($\omega_{E\times B} > \gamma_0$) seems to hold in all these cases. Note that a seemingly similar criterion for the suppression of turbulence has been theoretically derived [1] in which one should compare $\omega_{E\times B}$ not with the linear growth rate γ_0 but with the inverse decorrelation time of turbulence. The stabilization mechanisms are different: linear in our case and nonlinear for turbulence studies. What is common is the expression for the shearing rate, Eq.(2).

3. Destabilization of trapped particle modes

In this section we consider drift-kinetic trapped electrons and adiabatic passing electrons. All ions are gyrokinetic. The purpose of this study is to examine the effect of applied E_r on microinstabilities for which the dominant contributions to the drive come from trapped particles. We start from a tokamak configuration with $R/a = 3$, $L_T/a = 0.3$, $L_n/a = 3$, $q(\rho/a) = 1 + 2.3(\rho/a)^3$. The most unstable mode in the absence of applied E_r is a trapped ion mode (TIM). This has been verified by running a simulation in which $v_\parallel = const$ was artificially imposed: a toroidal ITG mode has been found but with a 10 times smaller growth rate.

Applying an external E_r with a shearless profile of $v_E \propto \rho$ we find the growth rates and frequencies of Fig.3. The remarkable result is an overall destabilization. In order to understand the reason for such a contrasted behaviour (as compared to the toroidal-ITG, helical-ITG and slab-ITG cases shown in the previous section), we have performed a power transfer analysis. The power transfer from the particles to the field is

$$-dE_{kin}/dt = \sum_{\alpha=i,e} \int q_\alpha \, \delta f \, (v_\parallel \mathbf{e}_\parallel + \mathbf{v}_d + \mathbf{v}_E) \cdot < \nabla \delta\phi > d\mathbf{R} d\mathbf{v} \tag{3}$$

and should be equal to the time rate of change of the field energy, dE_{field}/dt, with

$$E_{field} = (1/2) \int \left((n_0 e/T_e) < \delta\phi >^2 + (n_0/B\Omega) | < \nabla_\perp \delta\phi > |^2 \right) d\mathbf{x} \tag{4}$$

Checking this power balance is a way to verify the quality of the numerical simulation. In all results shown here it is satisfied to better than 5%. The power transfer can be broken up into its contributions (ions, electrons, parallel motion, magnetic and $E \times B$ drifts). Fig.4 shows these contributions, divided by $2E_{field}$.

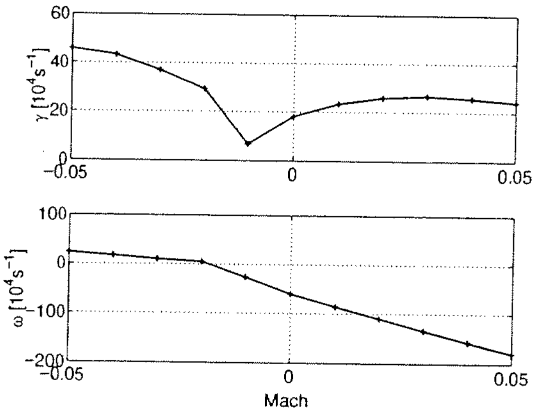

Figure 3: *Growth rate and frequency of TIM / TEM vs Mach number.*

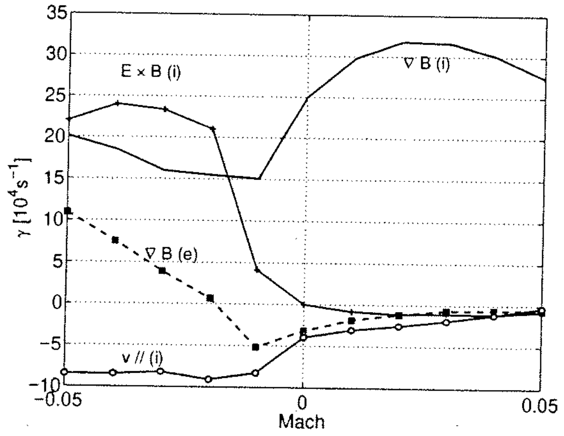

Figure 4: *Contributions to the growth rate from v_E on ions (line with +), v_d on ions (plain line), $v_\parallel$ on ions (line with o), and v_d on electrons (dashed line with squares).*

Without applied E_r (Mach=0) the dominant contribution to the instability drive comes from the magnetic drift term on ions. This is to be expected since the mode is a trapped ion mode. The parallel ion dynamics are weakly stabilizing, as is the trapped electron drive. That electrons seem to be stabilizing could be misleading. As a matter of fact, running the same simulation but with *all* electrons adiabatic results is a much lower growth rate (by a factor of about 3). Thus taking into account the trapped electron dynamics is destabilizing rather than stabilizing because the adiabatic electron response is reduced (this mechanism is similar when considering larger T_e/T_i).

When a positive E_r is applied, the main effect is to further increase the contribution to the instability drive coming from the magnetic drift term on ions. The other contributions remain small and are little modified.

When a negative E_r is applied, first the ion instability drive is reduced, but then the trapped electron contribution increases substantially and becomes destabilizing. Another striking feature is the strong destabilization contribution of the $E \times B$ drift on ions, which becomes the dominant drive mechanism. The destabilization for $E_r < 0$ is therefore a combined effect of the trapped electron dynamics and of the $E \times B$ flow on ion dynamics. Note that there is no contribution from $E \times B$ on electrons. Running simulations with all electrons adiabatic the destabilization at $E_r < 0$ disappears. We note that the frequency is positive (Fig.3), meaning that the mode rotates in the electron diamagnetic direction. But the linear behaviour of ω with Mach number is simply due to the Doppler shift due to the poloidal angular $E \times B$ velocity: running without trapped electron dynamics also results in $\omega > 0$ for Mach < 0.02. However, since the mode at $M < -0.01$ exists due to the presence of trapped electrons, it is justified to call it a Trapped Electron Mode.

In order to determine whether the *value* of v_E or its *shearing rate* is causing the destabilization of the TEM, we have run a series of simulations with a linear profile of v_E having zero value at the maximum temperature gradient position s_0, $d\Phi_0/d\psi \propto (s - s_0)$. In this case the TEM destabilization does not occur. We conclude that the *value* of v_E, combined with the indirect effect of trapped electron dynamics, is responsible for the TEM destabilization for $E_r < 0$ in this case.

Conclusion. While the simplified stabilization criterion $|\omega_{E\times B}| > \gamma_0$ appears to be verified for toroidal-ITG, helical-ITG and slab-ITG modes, it can be clearly violated when trapped particle effects dominate the instability drive, in which case the destabilization comes from the *value* of v_E rather than its shearing rate.

Acknowlegements. This work was partly supported by the Swiss National Science Foundation. The computations were performed on the ORIGIN-3000 of the SIC-EPFL.

References

[1] T.S. Hahm and K.H. Burrell, Phys. Plasmas **2**, 1648 (1995). T.S. Hahm, Phys. Plasmas 4, 4074 (1997).
[2] M. Fivaz, *et al.*, Comput. Phys. Commun. **111**, 27 (1998).
[3] L. Villard, *et al.*, Phys. Plasmas **9**, (to appear in June 2002).
[4] S.J. Allfrey, *et al.*, New Journal of Physics **4**, 29 (2002) (http://www.njp.org)

Particle Transport and Density Profile Behaviour in TCV

A.Zabolotsky, H. Weisen and TCV Team

Centre de Recherches en Physique des Plasmas,
Association EURATOM - Confédération Suisse,
Ecole Polytechnique Fédérale de Lausanne
CH-1015 Lausanne, Switzerland

The observation of peaked density profiles in tokamak plasmas, which are dominated by turbulent transport, is still eluding a satisfactory theoretical description. The aim of this paper is to present and temptatively interpret density profile behaviour in a wide range of conditions in the TCV tokamak in the framework of two potential turbulent particle transport mechanisms, Turbulent Equipartition (TEP) and Turbulent Thermodiffusion (TTD).

Electron temperature and pressure profiles, as well as sawtooth inversion radii in L-mode tokamak discharges are known to scale with $1/q_a$ in plasmas with circular cross sections [1]. This generalises to a scaling with$\langle j\rangle/(q_0j_0)$ in shaped plasmas [2,3] such as exemplified in fig.1. This parameter is easily evaluated with an equilibrium code, or alternatively, can be accurately approximated from global plasma parameters, even for extremely shaped plasma cross sections [2].

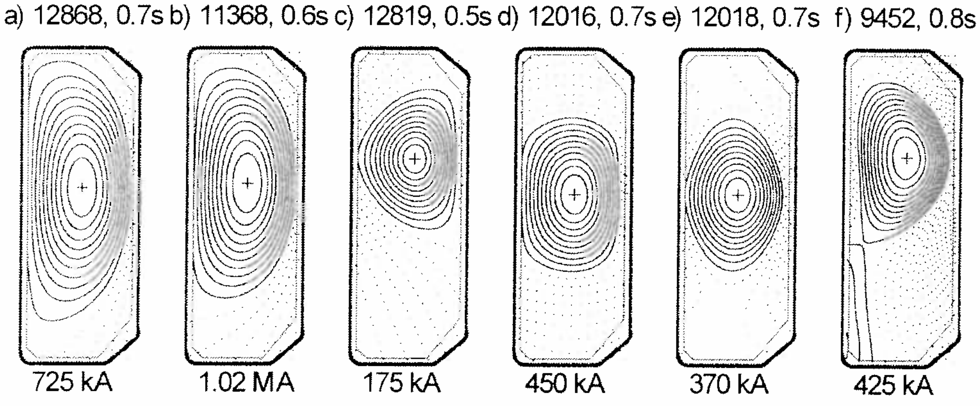

Fig. 1 Examples of discharge cross sections in the dataset under investigation

A scaling with $j\rangle/(q_0j_0)$ is also observed for the electron density profile peaking in TCV, implying the existence of an inward particle pinch and a dependence of particle transport coefficients on this scaling parameter. Fig.2 shows typical density and temperature profiles in

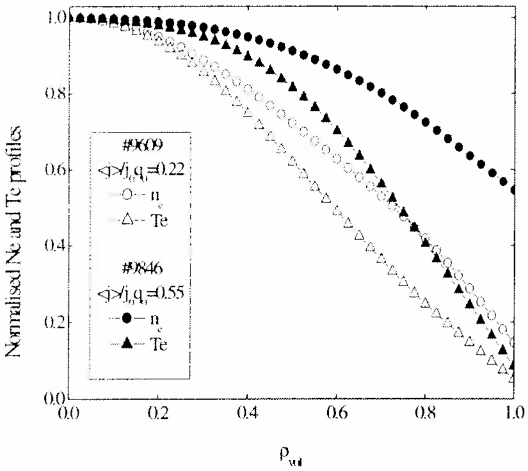

Fig. 2 Examples of electron density and temperature profiles at different values of $<j>/(q_0j_0)$ in Ohmic L-modes.

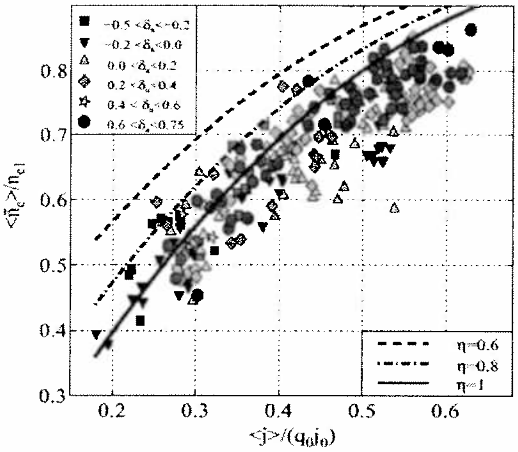

Fig. 3 Density profile widhts from experiment- for Ohmic L-mode discharges and expected for $n_e \propto 1/(qd\Phi/dV)^{\eta}$

Ohmic L-mode plasmas as a function of $\rho_{vol} = \sqrt{V/V_{LCFS}}$, where V is the volume enclosed by the flux surface. The data were taken using a repetitively pulsed Thomson Scattering system and mapped to ρ_{vol} as smooth functions. The scaling of the widths (inverse peaking factors) $\langle n_e \rangle / n_{e1}$ of the density profiles is shown in fig.3 for a wide variety of discharge conditions in TCV: $1 < \kappa_a < 2.6$, $0.5 < \delta_a < 0.7$, $2 < q_{95} < 7$, $1.2 \cdot 10^{19} m^{-3} < n_e < 12 \cdot 10^{19} m^{-3}$, $0.1 < \nu^*_{75} < 10$, where κ_a and δ_a are the elongation and the triangularity at the LCFS and ν^*_{75} is the electron collisionality at 75% of the poloidal flux.. The normalisation is made with respect to the density n_{e1} at the sawtooth inversion radius, $\rho_{inv} \approx \langle j \rangle / j_0 q_0$, rather than at the magnetic axis, in order to make it independent of the moment at which the sample was taken during the sawtooth cycle.

This result can be interpreted as being due to Turbulent Equipartition (TEP), which assumes conservation of the magnetic moment and the longitudinal invariant J during transport. According to TEP, particles spread evenly over the poloidal flux, i.e. $\partial N / \partial \Psi \approx const$, where N is the total number of particles within a given flux surface. Fig.4 shows, for each subplot, a superposition of about 130 normalised total particle number profiles as a function of poloidal flux, calculated from an equilibrium code, establishing that N increases roughly linearly with Ψ, irrespective of other discharge parameters.

TEP is expected to lead to density profiles roughly proportional to $(1/q)^{\eta}$ with $0.3 \leq \eta \leq 1$, depending on the relative contributions of trapped and passing particles to transport [4]. TEP implies a scaling of inverse peaking factors with $<j>/(q_0j_0)$ in shaped plasmas, in rough agreement with observations for $\eta \sim 1$ (lines in fig.3). Note that for many cases values of η

larger than unity would be required in order to account for the peaking. These are unphysical from the TEP point of view. Density profiles also depart from TEP predictions in the case of ECH heating in the confinement zone (off-axis power deposition) and in all cases in the vicinity of the LCFS, where fuelling is likely to be important. Possible reasons are the non conservation of the above mentioned invariants in the presence of intense sources of heat and the influence of electrostatic potentials, which enter in the definition of J, but are not considered in the derivation of TEP predictions. Particle expulsion from the plasma core ('pumpout'), as observed with strong central ECH in the presence of a (1,1) island, is also at odds with TEP expectations, presumably because the low levels of turbulent particle diffusivity in the central region allow neoclassical effects to compete [5].

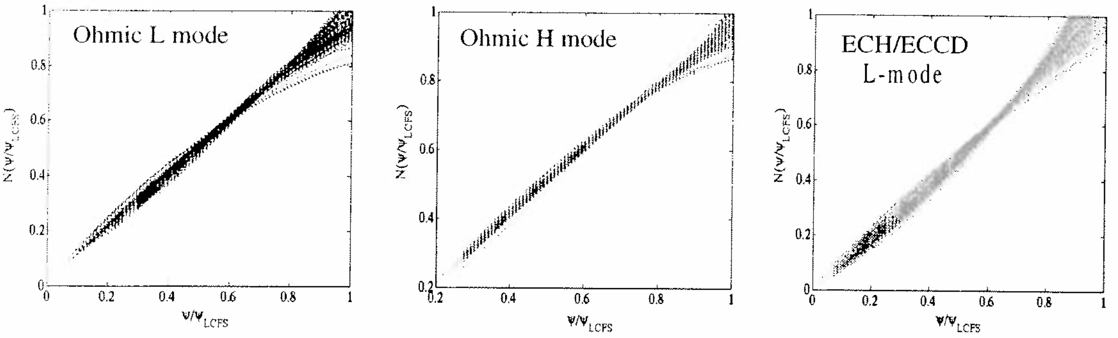

Fig. 4 Integrated, normalised particle content versus normalised poloidal flux in OH-Lmode, OH H-mode and ECH/ECCD L-mode datasets. Each line corresponds to a density profile. Only the portion corresponding to the confinement zone is shown

An alternative explanation of the observed density profile behaviour is offered by turbulent thermodiffusion by (TTD). This process is based on an energy dependent phase space diffusivity of the particles or more precisely decrease of the diffusion coefficient with velocity within the velocity distribution. Such diffusion behaviour is expected to lead to steady-state density gradients, which, in source-free regions and in the absence of other pinch mechanisms, are proportional to the temperature gradients, such that $\nabla n/n = \alpha_T \nabla T/T$ [6], with $\alpha_T<0.5$ [6]. Fig. 5 shows the normalized density gradient as a function of normalised temperature gradient in the region $0.2<\rho<0.75$ for Ohmic L-modes with three different values of $<j>/(q_0 j_0)$. No convincing comparison with thermodiffusion has so far been obtained in ECH plasmas, possibly owing to the poor signal to noise ratio of Thomson Scattering at the low densities necessary for ECH in TCV. For most of the confinement zone in Ohmic L- and H-modes, a single value of α_T provides a satisfactory fit of the density profile, when the temperature profile is known. The value of however varies as a function of $<j>/(q_0 j_0)$ from around 0.8 to around 0.4 over the database range and exhibits considerable scatter, not accounted for by measurement errors (fig.6).

Assuming a single value of α_T does not allow to account for the observed scaling of density peaking with $<j>/(q_0 j_0)$. In addition, the degree of peaking appears to exceed TTD expectations in many cases, making it unlikely that TTD alone can account for the observations.

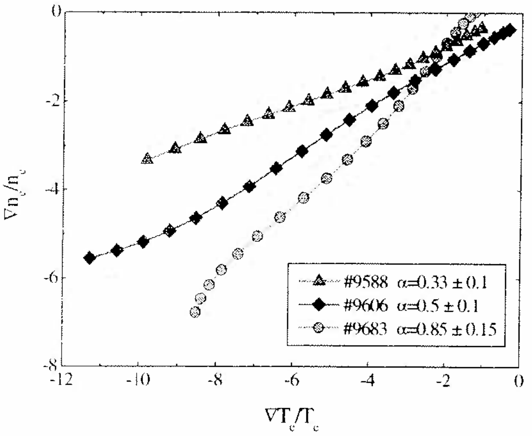

Fig. 5 Relation between electron density and temperature gradients in three different Ohmic L-modes in the region 0.2<ρ<0.75.

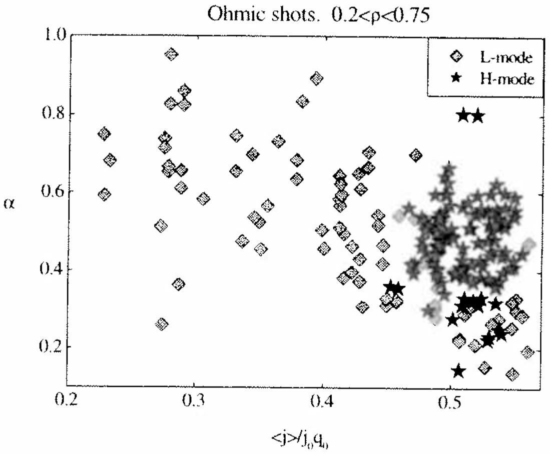

Fig. 6 Ratio of density to temperature gradient lengths versus $<j>/(q_0 j_0)$ in Ohmic L- and H-modes.

In principle density peaking can also result from a combination of TEP and TTD. Since bothtemperature profiles and poloidal flux profiles are strongly correlated (being parameterised by$<j>/(q_0 j_0)$ in normal magnetic shear discharges), it is however difficult to seperate the two effects on the basis on the available dataset. Since at least part of the density profiles are more peaked than predicted by TEP and TTD, additional pinch effects, such as the Ware pinch, may have to be considered.

References:

[1] Arunasalam V. *et al.*, *Nuclear Fusion* **30** (1990) 2111

[2] Weisen H et al., *Nuclear Fusion* **42** (2002) 136 and references therein

[3] Weisen H. and Minardi E., *Europhysics Letters* **56** (2001) 542

[4] Baker D.R. and M.N. Rosenbluth, *Phys. Plasmas* **5** (1998) 2936

[5] Weisen H., I. Furno, TCV Team, *Nuclear Fusion* **41** (2001) 1227

[6] Miskane F. and Garbet X., *Phys. Plasmas* **7** (2000) 4197